University of Strathclyde

Department of Naval Architecture, Ocean and Marine Engineering

Analysis of ship performance in deep and shallow waters using CFD

Momchil Terziev

A thesis presented in fulfilment of the requirements for the degree of Doctor of Philosophy

2020

This thesis is the result of the author's original research. It has been composed by the author and has not been previously submitted for examination which has led to the award of a degree.

Signed: Date:

Acknowledgements

It is with great joy that I write this section because it not only represents the culmination of my studies at the University of Strathclyde, but also because I am reminded of the many individuals who have tremendously enriched my life during this time.

I would like to begin by expressing my deepest gratitude to my supervisors, Professor Atilla Incecik, and Dr Tahsin Tezdogan. Without a doubt, I am indebted to your mentoring, encouragement, and help, without which I would never have imagined reaching the stage where I am ready to submit my thesis. I whole-heartedly appreciate the confidence you placed in me during this time. To this day I continue admiring your professionalism, which will endure in being an example to me. This has definitely enriched my personal worldview. Finally, I would like to thank you for giving me opportunities for independent work, and for including me in a wide range of activities both inside and outside the department. These have definitely helped my development. Undoubtedly, I have learned tremendously many things from you.

I gratefully acknowledge for the funding provided by the Faculty of Engineering at the University of Strathclyde, which fully supported and made my PhD studies possible.

I would also like to thank Dr Zhiming Yuan, for always having the time to discuss my project with enthusiasm, and engaging constructively with me.

My thanks go to all administrative and academic staff at the Department. I would like to specifically thank the postgraduate research administrator, Susan Pawson, and the IT officer, Ross Gilmour, for always being extremely helpful.

My thanks also go out to my friends from the postgraduate research centre at the department, who have made my time here very enjoyable. I wish the best

of luck to Guangwei Zhao and Mohammed Baba Shehu in pursuing their PhDs. Similarly, I would like to thank the members of the IEEE-OES student branch at the Department, who occasionally provided a very welcome distraction from my daily routine. I am in no doubt that they will continue to run the branch successfully.

I would like to thank Dr Khaled Elsherbiny for his friendship. I would also like to thank him for his hospitality upon my visit of his home country of Egypt. This is not something I will ever forget! I sincerely hope we stay in touch, and wish you a successful career at the Arab Academy for Science, Technology, and Maritime Transport.

Additionally, I would like to thank Dilyana Hristova for proofreading part of this thesis, and Zlatina Plamenova for helping me with life in Glasgow – I appreciate your friendship very much, and I am sure both of you will have brilliant successes in whatever endeavour you embark on.

My thanks also go to James Nicolson for his continuous support in all aspects during the last several years. I have no doubt that without your patience, help, and motivation, my life in Glasgow would not have been anywhere near as enjoyable as it has been.

My siblings also deserve thanks for their support and for always being willing to listen to me talk about my studies. I am very grateful to my brother for devoting time to help me proofread this thesis. I would also like to wish my sister the great success she deserves in her studies.

Finally, I would like to thank my parents for their support throughout my studies. I am privileged to have been raised with a love for continuous learning, which has undoubtedly helped me reach this moment. Thank you for your enduring patience.

TABLE OF CONTENTS

LIST OF FIGURES

LIST OF TABLES

ABSTRACT

Historically, the prediction of ship resistance has received its fair share of attention by the scientific community. Although there is a significant body of literature devoted to the study of ship hydrodynamics, several open research questions of great practical relevance remain unanswered. Among these are the extrapolation of ship resistance from model to full-scale in restricted, and unrestricted waters, as well as shallow water ship flows.

Most approaches used to predict the performance of a ship have typically relied on the assumptions inherent in potential flow theories, namely, the fluid is treated as inviscid and irrotational. In many cases, these are justifiable assumptions, yielding accurate predictions. However, there are equally many occasions, in which the analyst may not obtain a correct picture of the performance of a ship when relying on the assumptions of potential flow theory. Predicting scale effects, and shallow water influences on ship performance are prime examples of such cases.

Numerical techniques based on the Navier-Stokes equations can be thought of as a solution in cases where it is important to model a greater proportion of the physical phenomena. The numerical simulation of ship flows has evolved into a highly practical approach in naval architecture. The main advantages of using such an approach relate to the fact that it accounts for the action of viscosity and turbulence, and can therefore model scale effects and shallow water ship flows.

However, with the rapid advent of computational methods in all fields of engineering, several areas have emerged as significant sources of ambiguity. Amongst these are the best approach to modelling turbulence, the numerical

uncertainty induced as a result of mapping the continuous governing equations onto a discrete grid, and boundary conditions within the computational domain.

This thesis aims to address all of these issues using a commercially available Reynolds averaged Navier-Stokes solver. Firstly, a detailed literature review on the current methods and approaches to circumventing the problems mentioned above, both numerically and through the use of potential flow theory, is given. Then, studies on scale effects in deep and shallow waters are performed, supplemented by investigations into turbulence modelling and numerical uncertainty. Following these, the thesis' focus shifts towards shallow water phenomena. In particular, the modelling of ship flows without the use of Galilean relativity, and the determination of the Kelvin half-angle in restricted waters. Abrupt changes in the cross-section of the canal in which a ship propagates are also explored, with focus on ship resistance and the properties of the wave field.

Finally, the main results obtained from each chapter are summarised and compared against the aims and objectives of this thesis, before recommendations for future work are suggested.

1. INTRODUCTION

This chapter will provide a brief overview of the issues and topics this thesis aims to address. Then, the rationale behind the motivating factors for each subsequent chapter will be given. Following this, the research aims and objectives will be detailed. Finally, the thesis structure will be described.

1.1 Background

The prediction of ship resistance is a fundamental issue with great importance. If a naval architect does not have an adequately accurate estimate of the hydrodynamic forces, acting on a particular hull, the resulting decisions can prove to be wrong, with detrimental consequences.

Several considerations should be taken into account when endeavouring to predict the resistance of the ship. A useful starting point is to utilise potential flow theories, which can be used to assess a great number of different designs quickly, even on modern day standard computers. However, over-reliance on potential flow theories should be avoided due to their limitations. The vast majority of these methods, some of these are formulated to treat the fluid flow as linear, irrotational, and inviscid (Beck and Reed, 2001). Although these assumptions may well be suitable in some situations, and are to a certain degree, able to achieve engineering accuracy, they never represent the full picture.

The complexity of the problem is predominantly expressed in the mathematics required to numerically describe the flow around a ship. Particularly elusive are the vorticity and turbulence components. The latter is a very active field of research in itself, which has made great strides in recent years. However, a substantial number of the most state-of-the-art theories and methods are not

capable of providing the full mathematical description of the flow around a ship. Instead, Computational Fluid Dynamics (CFD) is used, particularly Reynolds Averaged Navier-Stokes (RANS) solvers. This approach allows the analyst to solve for the fully nonlinear viscous flow around the ship.

Naturally, physical experiments are of immense value to the field of ship hydrodynamics. The problem here lies with the cost, time, and technological equipment which is a necessary prerequisite for such a study. A towing tank is an expensive facility itself, however, it is an absolute necessity for the rapid advancement of the field of hydrodynamics. Furthermore, high-accuracy sensors and high-speed processing units are also necessary in order to detect features such as flow velocity, free surface elevation, etc. in a towing tank experimental setting.

The advances in modern computational processing power and speed, on the other hand, have resulted in the favourable situation where a model-scale RANS simulation can be performed on standard computers within a reasonable timeframe. Of course, the computational requirements frequently necessitate the use of high-performance computers (HPCs), especially when full-scale simulations are performed in CFD. HPCs are not only becoming more widely available, but the number and complexity of tasks they can handle is increasing exponentially (Slotnick et al., 2014). It is therefore reasonable to expect that RANS, and more widely used CFD methods will become the norm for routine analyses and standard hydrodynamic problems in the foreseeable future. In this thesis, a commercially available RANS solver, Star-CCM+, is used to perform analysis of ship hydrodynamics in deep and shallow water.

1.2 Motivating factors

The continued acceleration of the use of RANS methods calls for best practice approaches to be identified, especially in the fields currently identified as bottlenecks in ship hydrodynamics, and in CFD simulations of ship hydrodynamics. The present thesis attempts to use the strengths of CFD RANS simulations when compared to potential flow in the following areas:

- **Scale effects**: Due to the fact that a ship operates at the air-water boundary interphase, there are both Reynolds number and Froude number dependencies on the flow. Since these two components scale differently, it is not possible to achieve full similarity experimentally, using a scaled model. Compounding on this issue is the fact that scale

effects on different components are not fully understood. There is also strong evidence that constituent components of ship resistance might not, strictly speaking, exist in the form currently assumed (that is, linearly decomposable components). This may be deduced by observing interdependencies between different components of ship resistance, which suggest nonlinear relationships between those components. CFD methods are well-placed to address these issues since they are capable of modelling the full spectrum of physical phenomena. In particular, RANS methods are fully nonlinear, inherently taking into account vorticity and an approximate description of turbulence. The present thesis will evaluate scale effects on a ship in deep and shallow waters following a geosim approach. Emphasis is placed on understanding the physical reasons behind the observed interdependencies (Chapters 3 and 5).

- **Turbulence dependence**: Although there are many approaches to modelling turbulence, with alternatives emerging on a regular basis, the field of ship hydrodynamics is slow to adopt these new methods. A survey of over 100 studies concerning maritime CFD revealed that virtually all work is concentrated solely on two modelling approaches when it comes to closing the Navier-Stokes equations. Simultaneously, it was discovered that ship sinkage and trim have been identified as particularly difficult to simulate accurately as seen in the findings of several workshops focused on numerical ship hydrodynamics. The increased relative importance of these metrics on ship performance suggests that shallow and confined water cases require further research. Therefore, a turbulence dependence study in restricted waters is warranted and necessary to help settle the debate regarding which turbulence model, if any, is superior (Chapter 4).
- **Numerical uncertainty at full-scale**: High Reynolds number flows are difficult and expensive to measure experimentally, often resulting in the lack of full-scale measurements used to validate numerical predictions. In such cases, the analyst has no choice but to rely on best practice approaches. One difficulty relates to constructing an adequate grid onto which to solve the governing equations. Finite availability of computational resources also dictates that allocating solution nodes cannot be uniform across the entirety of the computational domain. This results in areas within the solution which one can discretise with different mesh densities. Parameters produced in the course of the

simulation also require different levels of mesh refinement. To begin addressing these issues, a study on local spatial numerical uncertainty within the domain was performed. Specifically, the elevation of the free surface and the skin friction of the ship were assessed (Chapter 6).

- **Ship-generated waves in restricted waters**: The impact of ship-generated waves, particularly in restricted waters, can lead to bank erosion and infrastructure damage. Their high degree of nonlinearity presents a challenge for potential flow methods. To assess the capability of CFD to model ship waves, a Fourier method was used to analyse the wavefield and compare the numerical output with a theoretical estimation of the Kelvin wake angle. In an attempt to reduce the modelling assumptions used in the study and be as consistent as possible with a physical towing tank, all open boundaries within the computational domain were removed. These were replaced with no-slip walls, rendering a greater degree of similarity and conceptual consistency to the physical towing tank. The newly constructed virtual towing tank is used to simulate a ship advancing through a rectangular canal and the New Suez Canal at model-scale. The analysis of the ship-induced disturbance reveals that the Kelvin half-angle is modelled with a discrepancy of less than two degrees when compared to a linear theory for the rectangular canal. However, the inflection wavenumber at which the Kelvin half-angle occurs is shown to deviate from the theory (Chapter 7).
- **Depth transitions in shallow water**: Restrictions in shallow water are in fact rarely maintained constant in shape over long distances as bathymetry may vary substantially over the track of a ship. Yet the majority of studies in shallow water ship hydrodynamics examine different conditions sequentially, and consequently treat them as independent. It is therefore prudent to numerically construct a towing tank featuring an abrupt change in the water depth, which the ship encounters and advances over, as it propagates in the tank. The characteristics of the wavefield were compared to analytical methods to provide a kind of validation to the study. Transmission of the ship-induced disturbance over the depth discontinuity was also evaluated alongside the viscous dissipation of the generated waves (Chapter 8).

1.3 Research aims and objectives

The research aim of this thesis is to evaluate the performance of ships in deep and shallow waters via CFD, to use the RANS method's strengths, to the challenges, and seek to provide practical recommendations for improvement of modern methods.

The specific objectives of this thesis have been designed to address the issues raised previously. The objectives are as follows:

- To perform a thorough review of the literature on computational ship hydrodynamics and identify open research questions.
- To perform a geosim analysis in deep and shallow waters.
- To investigate the scale effects on ship resistance and identify the sources of these scale effects.
- To identify the best turbulence model to close the RANS equations, providing consistent predictions over a range of parameters, at a small computational cost.
- To demonstrate the application of numerical uncertainty estimators on different parameters and their use in full-scale CFD simulations.
- To determine the performance of computational grids in terms of proximity to the asymptotic range.
- To determine the Kelvin half-angle of a ship in restricted waters based on a numerical free surface analysis method.
- To predict the impact of an abrupt change in the water depth on the resistance of a ship and its wavefield in shallow waters.

1.4 Thesis structure

This thesis is organised in accordance with the motivating factors, aims and objectives. The layout is summarised below.

- Chapter 2 (Critical Review) is dedicated to a review of the literature. To begin with, a brief historical overview is presented, focusing on important contributions in the wider field of hydrodynamics. Then, recent work in the field of ship resistance prediction in deep and shallow waters is critically reviewed. The current understanding of scale effects is then summarised and further need for research is identified. Finally, a review is given on the modelling of ship-generated waves.

- Chapter 3 (A Geosim Analysis of Ship Resistance Decomposition and Scale Effects with the aid of CFD) presents a study on the scale effects of a ship in unrestricted waters. The analysis is performed within Star-CCM+, and compared to experimental data at three different scales model-scale factors. Following this, a full-scale simulation is performed. The generated results suggest there is an interdependence between frictional and wave resistance, and demonstrate a Reynolds number influence on the latter. The form factor is shown to depend to the scale factor at which the analysis is ran.
- Chapter 4 (Application of Eddy-Viscosity Turbulence Models to Problems in Ship Hydrodynamics) presents a thorough investigation into the best choice of modelling turbulence in shallow water ship hydrodynamics. A simple statistical approach is proposed to rank the turbulence models from 3 families to determine which candidate performs both accurately and consistently across case studies, while consuming the least computational resources in CFD.
- Chapter 5 (A Numerical Assessment of the Scale Effects of a Ship Advancing Through Restricted Waters) presents an analysis of the scale effects of ships in restricted waters. The source of scale effects in a canal are identified as the presence of viscosity, and vorticity. These are generalised to the case of unrestricted waters, and the consequences of including those parameters are discussed. The results are shown to conform to theoretical estimations of the scale effect. An examination of the generated data in terms of frictional resistance coefficient and boundary layer profiles reveal that lateral restrictions of the waterway are not as significant as the level of vertical confinement for the examined case.
- Chapter 6 (A Posteriori Error and Uncertainty Estimation in Computational Ship Hydrodynamics) presents an assessment and comparison of numerical uncertainty estimation procedures in CFD. The application of a local error approach is examined in detail, as well as the additional data, resulting from its application. A less-known approach to estimate the numerical error is applied, and its confidence interval is assessed. The results reveal that distinct metrics within the domain, are located at different distances from the asymptotic range. Therefore, the applicability and performance of uncertainty estimators varies significantly depending on the parameter chosen for the verification study.

- Chapter 7 (Virtual Replica of a Towing Tank Experiment to Determine the Kelvin Half-Angle of a Ship in Restricted Water) presents a virtual towing tank, physically consistent with model testing facilities. Specifically, the numerical simulation features no open boundaries. It is demonstrated that the approach can provide satisfactory predictions in terms of resistance, and can model the wavefield accurately. The wavefield is validated by means of a Fourier representation of the numerical free surface, which is compared to theoretical relations, derived from the linear dispersion relation. Differences between the theoretical and numerical Kelvin half-angle are demonstrated. These are found to stem from the magnitude and location of the wavenumber inflection point, at which the Kelvin half-angle is evaluated.
- Chapter 8 (Modelling the Hydrodynamic Effect of Abrupt Water Depth Changes on a Ship Travelling in Restricted Waters Using CFD) presents an evaluation of the increase in resistance of a ship due to a step change in the water depth. The numerical simulations, performed at model-scale, showed that magnifications of ship resistance of up to 226% are predicted when the depth Froude number is near the critical value past the transition. As the velocity is increased, the wavefield is shown to interact less with the depth discontinuity. The numerical data show very good agreement with analytical relations of wave transmission past a depth discontinuity and viscous dissipation of waves in canals. A strong formation of a boundary layer at the canal bottom is observed, which persists a significant time after the ship has passed.
- Chapter 9 (Conclusions and Future Work) summarises the findings of this thesis and lays out directions for future research. A discussion is given on the findings and how they relate to the aims and objectives.

2. CRITICAL REVIEW

This chapter is dedicated to an overview of the discipline to which this thesis pertains, i.e. numerical ship hydrodynamics. The origins of the field are briefly explored, before focus is shifted to the evolution of the discipline into its present form, its successes, challenges, and future directions. Then, each subset of problems examined in the following chapters is given a separate section, where the relevant literature is reviewed. Naturally, prevalence is given to the contributions made in the area of ship hydrodynamics.

2.1 The origins of ship hydrodynamics

The problem of ship resistance prediction has a long and rich history spanning over centuries, and forms a cornerstone in the field of hydrodynamics. The discipline itself, however, did not emerge as a result of the fundamental questions regarding ship resistance, asked by both Newton and Euler (Gotman, 2007). Nevertheless, so important was the study of fluid motion around ships that Newton devoted a significant section of his *Principia Mathematica* to it, where he asserted the proportionality of inertial resistance of a body to the square of its velocity (Darrigol and Frisch, 2008). Though Newton's contributions are important, da Vinci is thought to have produced the first treatise of fluid motion many years earlier (Gotman, 2007).

However, it was Daniel Bernoulli who first gave the present area of study its formal designation (Darrigol and Turner, 2006). He discovered the universally known law carrying his name. Hydrodynamics was then capable of explaining highly practical phenomena that seem counter-intuitive at first. For instance, Bernoulli's equation described why the pressure drops in a pipe when its cross-section is reduced. This found applications in describing blood flow and

advanced the understanding of blood pressure within the cardiovascular system. Unfortunately, hydrodynamics could not maintain the perception of being a practical science for long. This is best explained by one of Daniel Bernoulli's contemporaries, d'Alembert, whose contributions to science are many, particularly as they relate to fluid flow.

Hydrodynamics ended up being seen by many researchers as a purely theoretical study of immense complexity with little to no bearing on the real world. This is best exemplified by d'Alembert's paradox, stating that a body would encounter no resistance in an incompressible, inviscid fluid. Of course, the paradox, as interpreted at the time, contradicted everyday experience by precluding the possibility of, for example, bird flight. This was partially responsible for a fundamental split in the field itself, resulting in the two sciences of hydrodynamics and hydraulics (Darrigol and Turner, 2006).

The primary reason behind the perceived fracture between the practical and theoretical was likely driven by the fact that Euler's equations, describing fluid motion, presented not only the first nonlinear field theory, but remain shrouded in mystery even today. In effect, Euler's equations are still thought to be sufficient to model ship-generated waves (Torsvik, 2009). This likely contributed to the confusion regarding d'Alembert's paradox, which can be resolved as soon as one considers the complete description of the governing equations.

There are many critical contributions to the field, without which hydrodynamics would not be as rich a science. Some of the important names include those of Navier, and Stokes, who derived the equations of motion in a viscous fluid; Rankine, who developed the theory of sinks and sources; Helmholtz, who founded the theory of vortex motion and introduced the velocity potential; Reynolds, who formulated the ideas of laminar and turbulent flow (Milne-Thomson, 1962); Froude (1874), who conceptualised the first scaling law in ship hydrodynamics; and Michell (1898), whose integral (or variations thereof) is still used extensively in practical and academic contexts to predict the wave resistance of a ship, despite being overlooked by his contemporaries.

2.2 Contemporary perspectives

The idea that it is practically relevant to obtain a good estimate of the resistance of a ship emerged when the first machine-powered craft were built (Gotman, 2007). The mathematics of ship resistance prediction remains a highly active

field even today. In the last century, the linear description of the scientific problem at hand matured significantly. For instance, Havelock (1908) and Inui (1954, 1936a, 1936b) derived methods to predict the location of wave crests and the corresponding kelvin half-angle in deep and shallow waters.

In recent years, the volume and pace of research in linear methods has reduced dramatically. However, linear methods remain of high regard and use due to their utility (Beck and Reed, 2001). Nevertheless, the 21st century, has seen an explosion of academic literature concerned with the application of the Navier-Stokes equations. Largely driven by the exponential growth in available computational resources, the numerical solution of the fully nonlinear governing equations has become commonplace. However, there are still many problems in the application of all forms of the Navier-Stokes equations.

Ranging from purely mathematical to fundamentally practical, the Navier-Stokes equations offer a wealth of open research questions. The problems in applying the governing equations span many disciplines. For instance, it is still unknown whether the Navier-Stokes equations produce unique solutions in three dimensions (Carlson et al., 2014). Luckily, most of these issues do not concern practical applications of the Navier-Stokes equations (or more accurately, the Reynolds averaged form of the governing equations). From an engineering point of view, all that is required is consistent provision of results within some predefined measure of accuracy, which has been extensively demonstrated for ships in academic contexts.

The remaining challenges relate to how one can guarantee that a solution satisfies the predefined measure of accuracy. This is particularly of concern when performing novel case studies. Efforts to improve predictions have been ongoing for many years. Their evolution in the field of ship hydrodynamics is best exemplified in a hierarchal form, as shown in Figure 2.1, adapted from Witherden and Jameson (2017). The main difference between the present interpretation of the hierarchy of fluid flow models and that of the above reference is that Large Eddy Simulation (LES) and Direct Numerical Simulation (DNS) have been incorporated at the top of the pyramid. This was done in light of recent publications on the matter, which demonstrated that LES can be used in practice, albeit subject to restrictions. An in-depth discussion on these can be accessed in the open literature (Fureby et al., 2016; Kornev et al., 2019; Kornev and Abbas, 2018; Liefvendahl and Fureby, 2017; Shevchuk and Kornev, 2017). Although DNS remains outside researchers capabilities for high Reynolds number flows at present, it can be anticipated

that this would not be the case indefinitely, keeping in mind the rapidly increasing availability of computational resources and improvements in algorithm efficiency.

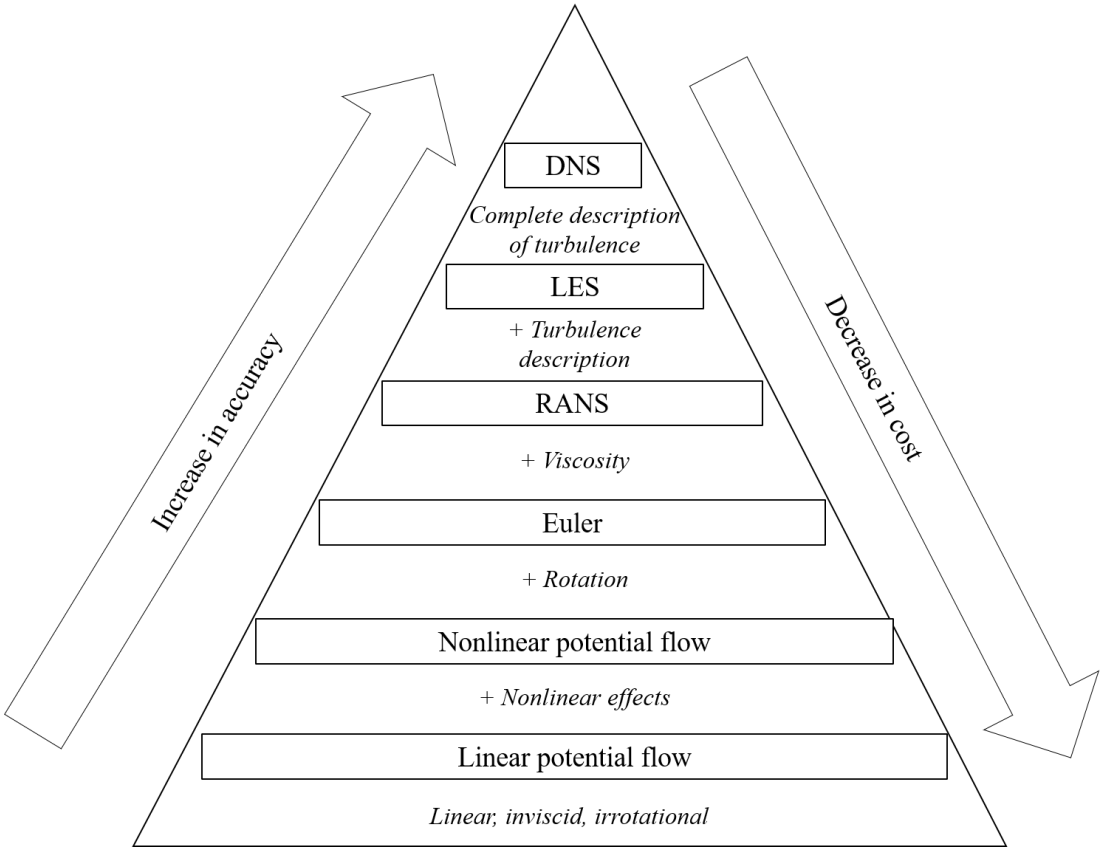

Figure 2.1. Hierarchy of fluid flow models, adapted from Witherden and Jameson (2017).

The issues not addressed by Figure 2.1 relate to potential difficulties and their underlying sources relevant to each method. As one progresses towards the top of the hierarchy, different conceptual issues must be overcome. To elaborate, although the practicality of, for example, linear potential flow is not questioned, practitioners are aware of the situations where its use is admissible. The range of parameter definitions, computational resource and ease of implementation suggest that it is trivial to compare solutions obtained with linear potential flow solvers and experiments to build confidence.

Near the top end of the complexity scale, RANS-based flow predictions feature dozens of parameters, models, sub-routines, and more generally, modelling approaches. These range from turbulence modelling, through boundary conditions, to numerical wave damping/definition, and interface tracking/capturing to name but a few. Each category mentioned above has

emerged as a field of study in its own right, rendering it practically impossible for the practitioner to have adequate expertise simultaneously in all fields. For this reason, studies have emerged aimed at providing specific recommendations to alleviate the burden. The required levels of technical knowledge can be reduced upon familiarisation with relevant research work for a wide spectrum of problems. For instance, Wackers et al. (2011) have given the most in-depth overview of strategies to model free surfaces in ship CFD, while Eca et al. (2015) provide an overview of the application of wall functions.

Although they are highly valuable, guides, best practices, and reviews are insufficient to increase physical understanding in ship hydrodynamics. For this reason, the majority of studies are concerned with specific phenomena, i.e. a subset of the physics. These are typically carried out under idealised conditions to isolate a certain aspect of the solution and analyse it suitably in view of increasing the conceptual understanding of the underlying physics.

2.3 Scale effects on a ship hull

When designing a ship, its performance is usually assessed against a variety of parameters. One of these is the expected value of resistance that the ship will experience in calm waters. Having a good estimate of this value is crucial because it determines the power delivered by the propulsion plant. In some cases, the naval architect may choose to seek alternative hull forms if the resistance falls within an unfavourably high range. It is therefore of critical importance to obtain an accurate estimate of ship resistance in full-scale. Unfortunately, at the design stage, one rarely possesses full-scale data. To address this, towing tests are performed to predict the resistance in model-scale, which is then extrapolated to full-scale.

The earliest procedure for ship resistance extrapolation was devised by Froude (1874). It begins by assuming that ship resistance, in non-dimensional form, can be decomposed into frictional and residuary components. Central to the present argument is the latter being constant with scale, which is known not to be correct (Toki, 2008). On the other hand, the frictional components vary with Reynolds number (Re), and can be approximated by the skin friction of a flat plate with an equivalent submerged surface.

The second and more widely used approach was proposed by Hughes (1954), who suggested the form factor approach. Within this approach, the resistance is decomposed into viscous and wave-making components. The latter is hypothesised to remain constant for geometrically similar ships, because, at

any scale, the ship is expected to produce a geometrically similar wave pattern. On the other hand, viscous resistance is further split into frictional and viscous pressure components by use of the form factor. Again, the frictional resistance approximated as that of an equivalent flat plate. Several problems plague this method, the most important of which is perhaps that the form factor (1+k), used in accounting for 3D effects, is assumed invariant with scale. To estimate (1+k), a model is towed at a low speed, where the wave resistance is supposed to be negligible, also known as the Prohaska test. Alternatively, the ITTC'78 method introduces a factor to be determined via regression analysis to account for the wave resistance in the form factor calculation, shown in Eq. (2.1):

$$C_T = (1 + k)C_F + cF_r^N \tag{2.1}$$

where c is a constant, chosen to fit as many C_T (total resistance coefficient) measurements as possible, while N normally attains a value between 4 and 6 (van Mannen and van Oossanem, 1988), and C_F is the frictional resistance coefficient.

Although the 2D and 3D extrapolation procedures, summarised graphically in Figure 2.2, can provide a good estimate of the resistance prediction, they are just that – estimates. Differences between the two methods are expected to stem from a variety of sources. The obvious ones are associated with the assumptions mentioned above: in the first case, the residuary resistance, whereas in the second – the wave resistance, both assumed constant with scale.

The problem becomes worse because, while a linear decomposition is assumed, it is well-known that resistance is a nonlinear problem (van Mannen and van Oossanem, 1988). Furthermore, this falls within the category of processes in which linearly breaking up physical phenomena and treating each part separately cannot adequately describe reality. This is due to the inability of linear systems to account for interactions between the different components in a nonlinear system, yielding properties not exhibited by the linear system (Saaty and Bram, 1964). An example of this problem is the interaction between frictional and wave resistance.

Underpinning the field of engineering is dimensional analysis, defined by White (2010) as the practice of reducing the number and complexity of variables upon which a physical process depends. Consequently, dimensional analysis rests on scientists' ability to define proper relationships between variables. Having established the difficulty in achieving this fully implies that one can never predict exactly the full-scale resistance of a ship with precision,

using model experiments. To tackle this, towing tank facilities rely on experience and large databases of model and full-scale data recorded during sea trials.

It should be noted that the use of sea trial measurements for validation purposes is used infrequently. This is the case because the equipment and cost, required to perform such an activity tend to be prohibitive. A testament to this fact is the scarcity of full-scale validation work in the literature. However, in 2016, the Lloyd's Register organised a blind workshop on full-scale ship hydrodynamics. The findings, and anonymised results from participants were published in Ponkratov (2016). The aforementioned report begins with an extensive summary of the 3D laser measurements of the hull, performed during dry docking. Then, the experimental equipment is detailed, before the aggregated results are given. These highlight the difficulty in performing full-scale simulation, as only 3 participants achieved an error of approximately 3% or less.

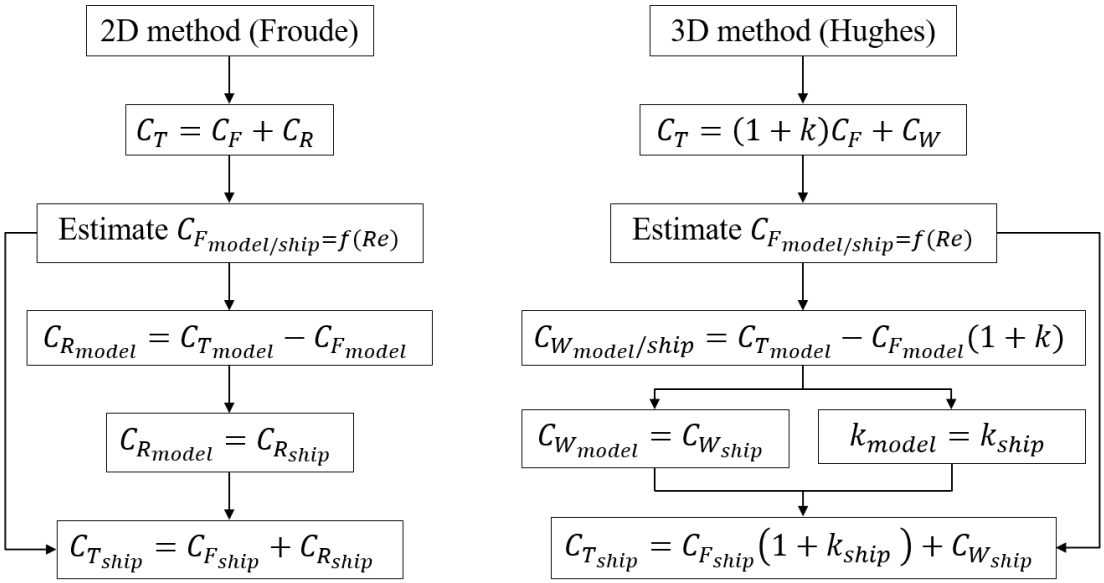

Figure 2.2. Resistance extrapolation

One of the most fundamental problems in model tests, and the subsequent extrapolation is that the intrinsic physical properties of the medium (air and water) have not been scaled down along with the ship. In this respect, potential flow can be a useful starting point. Specifically, linear potential flow theories predict no scale effect in the wave pattern, generated by a ship for a given Froude number. To reveal scale effects, the physical phenomena not modelled by the abovementioned approach should be taken into account, specifically,

the action of viscosity. Therefore, it can be stated that the action of viscosity in the fluid is responsible for scale effects.

In his experiments, García-Gómez (2000) demonstrated changes in the form factor of a ship as a result of scaling on several different hull forms. He also suggested an empirical correction to account for the difference in the model and full-scale ship form factors. It is important to note that according to García-Gómez, (2000), scale effects are due to Reynolds number-dependency only, and they are due to the friction line used.

It is well documented that the form factor (1+k) changes with *Re*, as demonstrated by many researchers (García-Gómez, 2000; Kouh et al., 2009; Lee et al., 2018; Terziev et al., 2019a; Zeng et al., 2019), but its use is still endorsed as part of the ITTC extrapolation procedure (ITTC, 2017a). However, placing all scale effects on the skin friction line is not correct, because every component of ship resistance is expected to be associated with a scale effect in its own right. This may be confirmed by examining the non-dimensional form of the Navier-Stokes equations. Specifically, the effect of viscosity is represented as $1/Re$ (Fox et al., 2015). Therefore, any viscous fluid will change its behaviour with varying Reynolds number. This implies that at a change from model to full-scale, where the Reynolds number changes order of magnitude from $O(10^6)$ to $O(10^9)$ may induce palpable scale effects.

The wave resistance is also typically assumed invariant of *Re*, but boundary layer physics suggests otherwise. To elaborate, Brard (1970) predicted that viscosity and vorticity act on near-field waves as $1/(Re \times F_n^2)^{1/3}$, while on far field waves as $1/(Re \times F_n^4)$, where F_n is the Froude number. Thus, rendering the effect of near-field waves more significant. Coincidently, these are also of greater practical importance in the low speed regime, where ships are tested according to the Prohaska test, used to determine the form factor. This is because ships generate predominantly near-field disturbances at low speeds.

The influence of turbulence is also known to impact on ship-generated waves (Brard, 1970; Tatinclaux, 1970). Since it is not possible to achieve both Reynolds and Froude similarity simultaneously in practice, one retains different flow properties in terms of turbulence and vorticity when extrapolating from model to full-scale. Here, it is useful to introduce the concept of an "equivalent ship". This is sometimes used in potential flow theories in an attempt to account for boundary layer displacement thickness and its impact on flow properties (Gotman, 2002; Lazauskas, 2009). In this concept, an "equivalent ship" is the

ship's underwater geometry, plus the displacement thickness of the boundary layer. Now, the displacement thickness being different at each scale, inevitably means that this equivalent ship is different in shape at each scale.

One could consider the aforementioned statements from the classical point of view of source strength distribution used by potential flow to model the ship as a wave maker. If boundary layer physics are taken into account, then the source strength, assigned to the stern is not the same at different scales. This is true because the boundary layer is relatively thicker at model scale than at full-scale. Moreover, a higher Reynolds number implies a broadening of the turbulent kinetic energy spectrum (Durbin and Pettersson Reif, 2011). The net effect of this is the presence of eddies of different characteristic lengths and time scales. All of the above serve to point towards the existence of a viscous effect on the wave resistance, as suggested by Brard (1970) and Tatinclaux (1970), and therefore, scale effects.

The arguments laid out so far must also be considered in conjunction with the fact that in each scale factor of a geosim series, the fraction of the ship over which a laminar boundary layer may be observed is different. Furthermore, knowledge that a thickening of the boundary layer occurs with an increase in scale factor (decrease in linear dimension) suggests that one may expect wave resistance coefficient to decrease as one moves up the Reynolds number scale in a geosim series. This was one of the conclusions of Ferguson (1977), who observed this effect experimentally. More recently, studies on ship hull roughness demonstrated the that a thicker boundary layer, resulting from surface roughness increases wave resistance (Song et al., 2019). However, Brard (1970) discovered that turbulence and vorticity supress ship waves. Indeed, the presence of turbulence is typically interpreted mathematically as a "sink" for large scale motions (Golbraikh et al., 2013). It is therefore not straightforward to predict whether the wave resistance will be higher or lower *a priori.* This is the case because the combined effect of turbulence, vorticity, and change of boundary layer properties on ship waves are difficult to quantify. Moreover, the relationship between these components, and their relative impact may alter for different shapes.

Flow separation is also known to play an important part in model-scale, but not in full-scale (Kouh et al., 2009; Raven et al., 2008). Vortex formation is typically delayed in full-scale, and when it occurs, vortices encounter higher damping than in model-scale (Hochkirch and Mallol, 2000). Both of these effects are likely related to the change in the laminar-turbulent boundary layer

transition location. This causes the different flow properties generated at each scale to cascade and snowball towards the stern and into the wake itself.

At this stage, it is important to make some brief observations regarding the frictional component of ship resistance. As stated earlier, this is assumed to be one of the independent components of the total resistance. Its prediction has received its fair share of attention form the scientific community, resulting in numerous approaches.

Methods to calculate the frictional resistance coefficient can be classified into three categories, all of which define the frictional resistance coefficient as a function of the Reynolds number. The first category consist of correlation lines, such as that of White (2006), as well as Prandtl-Schlichting and Schultz-Grunow, reported in Schlichting (1979). The second category consists of formulae, derived using integrated analytical two dimensional boundary layer equations expressing the local frictional resistance of a flat plate, such as those of Schoenherr (1932), Hughes (1954), Grigson (1999), Katsui et al. (2005), and Lazauskas (2009). The third category is numerical lines, such as those of Eça and Hoekstra (2008), who developed three formulations by fitting curves to data obtained via a RANS solver - one based on the of Hughes (1954) line (in rational form); and two in polynomial form (one linear and one cubic). More recent numerical friction lines include that of Wang et al. (2015) and Korkmaz et al. (2019).

While there is a plethora of available friction lines, it is important to keep in mind that the vast majority do not take into account free-surface effects. The analytically derived ones use the integral value of two-dimensional boundary layer equations to express the friction coefficient. Even the numerical friction lines were established with the use of double body models. However, as pointed out by Stern (1985), the presence of a free surface causes a highly complex three-dimensional flow. Thus, not only does one expect differences due to the presence of a free surface in the frictional coefficient, but also, the wave resistance is modified as a result of the different nature of the boundary layer (Marquardt, 2009).

So far, primarily analytical and experimental studies aiming to determine the resistance of a ship have been mentioned. However, an approach of rapidly emerging popularity in the context of ship hydrodynamics is the use of Reynolds averaged Navier-Stokes methods, as shown in Figure 2.3. Some of the early work in which scale effects using a CFD approach have been

examined includes the work of Oh and Kang (1992). They modelled viscous flow over the stern of a ship by invoking the double body approximation. According to Gotman (2007), Foettinger first described the double body idea by replacing the free surface with a symmetry boundary in 1924. Since then, tests in wind tunnels using the underwater shape of a ship and its mirror image have been performed, for example, by Patel and Sarda (1990). They studied the turbulence and boundary layer characteristics of the Wigley parabolic hull. The contribution of the abovementioned work is that it describes features of the 3D flow used for numerical turbulence modelling.

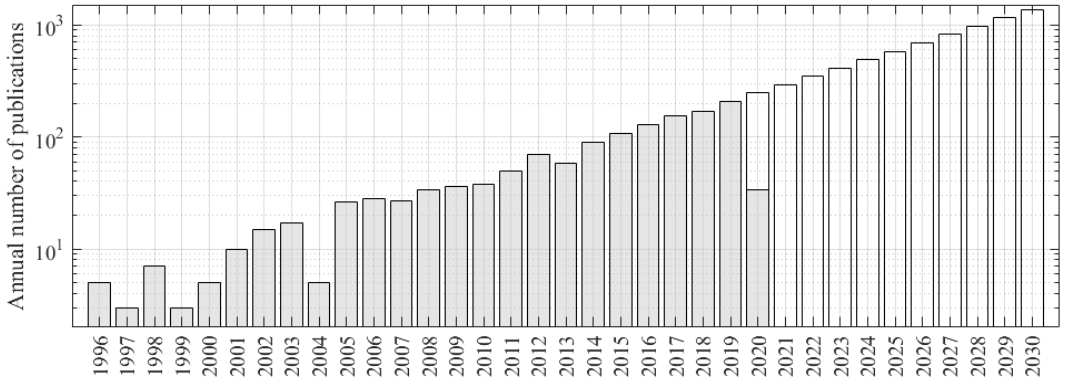

Figure 2.3. Annual publications listed under the category "ship CFD" according to Web of Science (2020) as of 26.04.2020. Extrapolated numbers based on the trend[1] up to 2030 are represented by empty bars.

Researchers were constrained for several years to modelling only a part of a ship's hull. Using the double body approach and placing the inlet amidships, Eca and Hoekstra (2001) predicted the scale effect on a tanker by varying the Reynolds number. One of the problems highlighted in their study is the scarcity of experimental data for comparison. Although the problem is still unresolved today, Kim et al. (2001) performed a systematic series of experiments to alleviate this. Their motivation for performing the study was specifically to provide validation data for CFD codes. Later, Tahara et al. (2002) investigated the appropriate numerical setup applicable to full-scale ship hydrodynamic performance prediction. Their findings include that one of the key issues "for full-scale ship flow simulation is to maintain the accuracy in the resolution of the flow within a viscous and turbulent boundary layer of decreasing thickness."

[1] The data and associated fit to extrapolate the number publications to the year 2030 can be found in Appendix A

In RANS solvers, turbulence modelling has been shown to be one of the main factors in modelling scale effects. Duvigneau et al. (2003) performed a study on hull form optimisation in both model and full-scale. Their findings indicate the calculated parameters are highly dependent on the turbulence model chosen. Indeed, Visonneau (2005) reported the same finding within the European Full-scale Flow Research and Technology (EFFORT) project (Bugalski, 2007). He also pointed towards free-surface effects as a potential source of difficulties for RANS solvers in full scale. However, the main problem remains the lack of full-scale data for validation.

Later, Raven et al. (2008) examined the capabilities of an inviscid solver and a viscous solver to predict the full-scale performance of a ship. They found that the wave resistance coefficient is up to 20% higher in full-scale when compared to model-scale. However, the scaling of viscous resistance was computed via a double body model. Continuing the trend of using the double body method, Kouh et al. (2009) demonstrated the Reynolds number dependence of the form factor. Their study featured several hull forms, including the KRISO containership (KCS), which allowed them to draw comparisons between different shapes. They demonstrated that the form factor decreases with Reynolds number for all examined shapes.

Min and Kang (2010) questioned the basic assumptions of the extrapolation procedure recommended by the ITTC (2017). Their paper represents the end of the sequence of studies confirming that the form factor is Reynolds number-dependent. However, they went further, suggesting the form factor be treated as a function of Froude number as well, and called on other researchers to investigate this. Min and Kang (2010) also provided a correction formula to be used in the determination of the form factor.

An interesting approach to resolving the scaling problem was presented by Guo et al. (2015), who utilised a non-geometrically similar approach, namely, a similar ship, whose flow characteristics at model-scale match the parent hull in full-scale. Although this method would be very useful if refined, it is yet to be implemented elsewhere.

As recently as 2016, researchers opted to use the double body method to study ship performance. For instance, Wang et al. (2016) chose this approach to examine the effect of different draughts on the form factor. However, the main event of 2016 in this respect was the publication of the Lloyd's Register's workshop on ship scale hydrodynamics (Ponkratov, 2016), in which the

problems of CFD predictions in full-scale could be seen more easily. Although attention is limited to the bare-hull submissions in the workshop in this thesis, it is worth noting that only 3 participants achieved an acceptable level of accuracy between the full-scale CFD result and the sea-trial data in terms of total resistance and propeller rotation rate (3% deviation). For the purposes of the workshop, sea trials were conducted post-docking of a general cargo ship between Istanbul, Turkey and Varna, Bulgaria. The results indicated that air resistance (cranes and superstructure) plays a much more important role in the total resistance (7% contribution) than trim (3% contribution) for the particular ship investigated. The Ponkratov (2016) report highlights the differences between numerical setups. For instance, Starke et al. (2017), who were one of the participants, showed that a level-set method for free surface capturing is not capable of modelling the overturning bow wave.

The main obstacles to be overcome prior to the routine use of CFD in full-scale computations require further research as suggested by the literature. One of the issues frequently pointed out is the large number of cells. However, Tezdogan et al. (2015) demonstrated that it is possible to carry out RANS numerical simulations directly in full-scale. Alternatively, Haase et al. (2016) proposed to verify a numerical grid in model-scale (based on Froude similarity). Then, by altering the value of viscosity, the Reynolds number can be changed to match the corresponding full-scale ship.

Recent work in the field of computational ship hydrodynamics has concentrated on tackling the problem referred to above, directly (Niklas and Pruszko, 2019a, 2019b). For instance, Sun et al. (2020) performed a numerical analysis in model and full-scale and compared the latter with sea trial data. Their work features double body and multiphase in for both model and full-scale conditions. Incorporating a spinning propeller allowed Sun et al. (2020) to determine that vortex formation is noticeably damped at full-scale when compared at model-scale.

Other researchers have opted to focus on the action of turbulence in full-scale. Turbulence modelling is typically a source of modelling errors, which are difficult to quantify at full-scale (Bhushan et al., 2009, 2007; Duvigneau et al., 2003; Pereira et al., 2017). Thus, alternatives to RANS techniques, which resolve at least part of the turbulent kinetic energy spectrum, have emerged and are rapidly gaining popularity. In this respect, Liefvendahl and Fureby (2017) estimated that a full-scale Large Eddy Simulation (LES) for the Japan Bulk Carrier (JCB) would require between 9.7×10^{9} and 6.7×10^{12} cells,

depending on the approach (wall-modelled LES vs. wall-resolved LES). Such grids are difficult to handle, even in academic contexts, demonstrating that resolving the turbulent kinetic energy spectrum in full-scale is not currently practical.

According to Pena et al. (2019), the bridging alternative (resolving part of the turbulent kinetic energy spectrum), known as Detached Eddy Simulation (DES), can be successfully employed to predict full-scale ship performance. In their study, the aforementioned authors performed full-scale simulations on the cargo ship investigated within the Lloyd's Register workshop. The novelty within their study is expressed in the fact that they opted to use the DES approach. Although this is typically associated with considerably higher requirements in cell numbers and lower time-steps, the authors achieved high predictive accuracy. More importantly, they demonstrated that an accurate solution can be achieved not only for integral properties, such as resistance, but for the flow field near the ship as well.

Grid numbers are currently of some interest to the academic community. For instance, Jasak et al. (2018) performed grid sensitivity studies in full-scale. Their results suggest that full-scale simulations may be performed with a relatively low number of cells while achieving high accuracy. Specifically, simulations on a car carrier in the aforementioned work were performed with approximately 6.4 million cells and achieved 0.24% deviation from the sea trial result.

It is clear that full-scale simulations are possible even with current computational power availability. However, best practice approaches should be established to avoid the scenario observed in the Lloyd's Register report, where a relatively low number of participants obtained the desired level of accuracy.

2.3.1 Shallow water effects

In many cases, instead of isolating a certain part of the physics to analyse it separately, it is worthwhile to do the opposite in order to magnify certain parameters, thereby making them stand out for easier analysis. In essence, this results in seeking more challenging case studies which will accentuate sought after phenomena. Shallow water studies can be thought to represent a such reasoning. This is thought of in the sense that many phenomena, and their interactions are highlighted due to the proximity of the seabed in the case of shallow waters. Therefore, in carefully constructed experiments (physical or

numerical), one can deduce effects that may be obscured in deep waters due to their small magnitude, for example, scale effects.

It is also important to have an appreciation that although a ship may spend large parts of its operational life in unrestricted waters, it inevitably must enter shallow/restricted waters. Therefore, to obtain a complete picture of a ship's performance, the designer must also understand how the ship will react to a reduction in underkeel clearance (Tuck and Taylor, 1970). This may occur whilst entering a port, or traversing one of the famous man-built waterways (the Panama and Suez canals (Tuck, 1966)). It is known that an increase in ship resistance can be expected when operating in shallow waters. Typically, this is offset by a reduction in speed, also used to ensure against groundings, which are the most frequently occurring accidents in the Suez Canal. While a grounding at low forward speed may not damage the ship from a structural point of view, it creates congestion. The low speed requirement has also meant that the abovementioned waterways have become bottlenecks, restricting the amount of freight passing through.

In fact, while the average annual vessel traffic has remained largely constant in the past four decades, freight has increased in an exponential fashion (Suez Canal Authority, 2018). Therefore, ship size must have increased proportionally. This has meant that the main task of the Suez Canal Authority is to now perform bathymetric surveys, since larger vessels require greater under keel clearance and safety margins. Moreover, disproportionately many incidents occur in shallow water according to EMSA (European Maritime Safety Agency, 2019, 2018, 2017, 2016, 2015).

The principal phenomena, occurring in shallow waters are related to the reduction in underkeel clearance and lateral extent of the waterway (in rivers and canals, for example). These cause sinkage and trim of the ship, the combined effect of which is termed ship squat. Unlike deep waters, waves propagate at a single speed, $\sqrt{gh}$, where h is the water depth. In such conditions, wave resistance is known to be nonlinear. Consequently, Michell's (1898) integral, and variations thereof predict no resistance in shallow water for subcritical speeds (Beck et al., 1975; Tuck, 1967, 1966). A ship propagates at a subcritical speed when its velocity smaller than $\sqrt{gh}$. Conversely, when U>$\sqrt{gh}$, the regime is called supercritical, whereas when the two quantities are equal, the flow is termed critical.

By analogy to aerodynamics, and the associated wave resistance emanating as sound when crafts break the sound barrier, Michell's (1898) integral predicts a non-vanishing resistance for supercritical speeds. However, the sustained generation of waves by sub-critically propagating objects in water of finite depth suggests some energy transfer must occur from the object to the wave system. Therefore, a result to the contrary defies physical experience, and was part of the reason why Michell's (1898) integral was overlooked by his contemporaries.

The reasons behind the non-existing predictions for subcritical speeds are rooted in the linear nature of the aforementioned integral. In essence, wave resistance in shallow water is non-linear. Obviously, such phenomena cannot scale linearly. Therefore, understanding how wave resistance scales in shallow water can increase knowledge of the deep-water equivalent, which contains a substantial, if not dominant, linear component. This is true because the two phenomena have the same origin and therefore share the physical mechanism producing them. If one were to couple this fact with Tuck's (1978) forecast of greater relative scale effect in shallow water, it is easy to see why the examination of such cases is worthwhile.

The origins of scale effects in shallow water have several additional dimensions. Firstly, the boundary layer changes in relative thickness with scale, as discussed earlier. Its interaction with the seabed and/or sides causes greater scale effects. For instance, Gourlay (2006) predicted that a ship's boundary layer may intersect the seabed. This may be the case even when the depth-to-draught ratio (h/T) is not very small. For instance, Terziev et al. (2019b) showed this to be the case for h/T=1.6. A study by Shevchuk et al. (2016), and subsequently Böttner et al. (2020) examined the narrow gap between a ship hull and seabed numerically and experimentally.

The findings of the aforementioned studies include the formation of a boundary layer on the seabed. Knowing that a boundary layer will not scale linearly implies that in full-scale, the ship operates under different conditions than those in towing tanks. The extent to which this is impactful is yet to be determined. In any event, scale effects are expected as a result of the disparity between the 'equivalent' ship in different scales. Since the forces acting on the hull will also be different, stemming from the scale-inconsistent boundary layers, it is reasonable to forecast differences in ship squat as well. Indeed, numerical and experimental studies have shown this assertion to be justifiable (Duffy, 2008; Ferguson, 1977; Shevchuk et al., 2019).

However, in contrast to the above-mentioned studies a recent paper suggested that scale effects on ship squat are negligible (Kok et al., 2020). Examining the results presented in the aforementioned paper, it becomes apparent to the author that such scale effects are actually predicted. For instance, the authors of the previously mentioned paper state that "at h/T= 1.23 and F_h= 0.53, the difference between the full scale and the model scale non-dimensional squat is only 5.32%". However, this may be a substantial difference when carried to full-scale and could realistically cause grounding.

A systematic geosim series in shallow waters would likely to resolve the questions posed above. However, when devising such an experiment, the equivalent ship concept should be taken into account. A vessel at different scales operates at different effective underkeel clearances due to changes in the boundary layer thickness. It is therefore not immediately apparent how a meaningful comparison should be carried out if the conditions are to be maintained identical for all Reynolds numbers. The proximity of lateral boundaries will also scale nonlinearly, inducing further effects.

Frictional resistance in shallow water is also of some importance for ships. Studies have shown that the proximity of the seabed causes an increase in C_F, which according to the most recent research on the matter, is unique for each ship (Zeng et al., 2019). This is caused as a result of three-dimensional effects on the frictional resistance (Raven, 2019). In deep waters, these are relatively mild, and cause a tolerable deviation from the well-known friction relations used to predicting C_F. Since scaling behaviour of the 3D contribution is unknown, the use of relationships expressing C_F should be scrutinised further.

Three-dimensional effects on the frictional resistance are an inherent aspect of the tangential force itself (Dand, 1967). To the best of the author's knowledge, there are no methods to remove the 3D contribution of the frictional component on a ship's hull from the flat plate equivalent. Indeed, the boundary layer of a ship is fundamentally different from that of a plate. Therefore, there are many aspects in which a ship's hydrodynamic behaviour differs from that of a simpler body.

2.4 Ship waves

One fascinating consequence of operating at the air-water interphase is the continuous production of waves. It is convenient to begin by examining the deep-water case first. In deep waters, the ship generates a wave system, confined within a semi-infinite wedge, extending aft of the ship. To gain a

picture of the waves generated by a surface-piercing disturbance, one must simply place one wedge of half-angle ≈19° 28′ at the bow and one at the stern. The entire wave system will be confined within these regions regardless of the speed or underwater shape. This was described for the first time by Kelvin, after whom the half-angle is named (Thomson, 1887).

The interesting phenomena occur once again in shallow water, where the half angle which the wave system makes with the ship's trajectory is speed dependent. The shallow water case causes the previously described wedges to be confined between the deep water limit (19° 28′) and 90° increasing as the depth Froude number approaches to unity (Havelock, 1908; Inui, 1936a, 1936b). In other words, the waves fill the entire half-plane aft of the ship and propagate in the same direction as the ship. The prediction of the Kelvin half-angle is an active field of study even today, with regular new contributions being published (Jiang et al., 2002; Lee and Lee, 2019; Rozman, 2009; Tunaley, 2014). That is, despite the fact that it has been over a century since the Kelvin half-angle's value in deep waters was first documented and subjected to mathematical analysis (Thomson, 1887). This serves to highlight the wealth of phenomena associated with ship-generated waves, rather than an inability to describe the system.

Scientists have the habit of advancing hypotheses, which are either confirmed or discredited experimentally. However, the opposite occurred in the study of ship waves. John Scott Russel observed solitary waves in Scotland's canals years before they were subjected to appropriate mathematical analysis successfully (Darrigol, 2003). Russel's observations that a solitary wave may cause a drop in the resistance at high speeds was belittled at first, only to be vindicated years later.

Today, significant advances have occurred in the modelling of ship waves at all water depths (Dias, 2014; Pethiyagoda et al., 2014; Rozman, 2009; Soomere, 2007). The methods range from Thomson's (1887) ray argument, through the stationary phase method of Newman (1970) and Lighthill (1990), up to more recent approaches reminiscent of Thomson's (1887) reasoning (Lee and Lee, 2019). These deep water relationships are also studied in a towing tank (Gomit et al., 2014), and via satellite imagery (Rabaud and Moisy, 2013; Wu, 1992).

Using RANS solvers, one can simulate cases of arbitrary underwater cross sections. For instance, an asymmetric canal was investigated by several researchers as part of the PreSquat workshop (Mucha et al., 2014). Gourlay

(2014) modelled the required case studies using the slender body theory. However, this method cannot recreate the free surface, which produces highly intricate and complex patterns, as demonstrated by Tezdogan et al. (2016b). Later, Terziev et al. (2018) simulated a set of horizontally unrestricted shallow waters alongside dredged channels and a canal case. All of these studies highlight that a ship's wavefield will be highly influenced by any change in the bathymetry. Even if the seabed is perfectly flat, the nonlinear effect in ship waves is not fully understood. For this reason, many researchers have used the RANS approach to model the problem at hand (Kinaci et al., 2016; Li, 2003; Pacuraru and Domnisoru, 2017; Rotteveel and Hekkenberg, 2015; Schweighofer, 2004; Song et al., 2019; Wackers et al., 2011; Wilson et al., 2006).

However, the extent to which a ship-generated wave is modelled by RANS solvers in accordance with linear dispersion properties is yet unknown. That is although significant demonstration of the accuracy of RANS solvers has been demonstrated in a series of workshops on numerical ship hydrodynamics, for example, Larsson et al. (2014). Human perception of differences in between experimental and numerical free surfaces is notoriously unreliable. For this reason, within this thesis, a study is performed to assess the degree of agreement between the linear dispersion relation-based Kelvin half-angle in shallow water and its numerical counterpart (Chapter 7). The dispersion relation for canals of sloping sides is also of some interest in practice due to their geometric similarity to riverbeds, used extensively for navigation even nowadays.

Ship waves can cause erosion and infrastructure damage in many cases. This is particularly relevant for ships operating in otherwise low-energy coastal areas or lakes (Bourne, 2000; Hofmann et al., 2008; Schoellhamer, 1996). Another equally important concern relates to the impact ship waves on fish and their assemblages, a review of which is given in Wolter and Arlinghaus (2003). More severe events are reported in Soomere (2009) where, firstly a case where holidaymakers were being "forced to flee for their lives when enormous waves erupted…", and secondly, a case where ship waves caused a fatal incident on the East coast of England. It is therefore important to understand how ship waves transform over a sloping wall, representing a beach or a canal/river side. This problem is reminiscent of that investigated by Tezdogan et al. (2016b), Torsvik et al. (2009), Bechthold and Kastens (2020), Terziev et al. (2020), Kok et al. (2020), and Elsherbiny et al. (2020, 2019a, 2019b) to name but a few.

It is also important to note that RANS-based predictions of ship waves have attracted some mixed opinions from researchers in terms of utility for the present context. Although there does not seem to be any objection to using this modelling approach *per se,* there is an awareness of the computational expense at which such predictions come (Jiang et al., 2002). Even in cases where ship hydrodynamics and the resulting waves are investigated, the wavefield is destroyed at no more than 4~5 ship lengths aft of the stern, at most. This occurs at the outlet boundary and is irreversible. From a naval architect's perspective, this may not be of great consequence, but in coastal engineering practice, these waves need to be captured a long distance aft of the ship. Their interactions with infrastructure can occur several miles from the ship track (Grue, 2017; Soomere, 2009).

An economical approach to modelling ship waves is found in the Korteweg-de Vries (KdV) equation, which accounts for dispersive and weakly nonlinear effects. This has been used to model ship waves by many researchers (Cole, 1987; Hur, 2019; Katsis and Akylas, 1987, 1984). If the ambient pressure term is retained in the formulation of the KdV equation, one obtains its forced version (fKdV), which is only valid for waves propagating in a single direction (Torsvik, 2009). An extension of the fKdV equation, capable of accounting for waves propagating at a small angle relative to the ship's track is the Kadomstev-Petvianshili (KP) equation. This approach has also been extensively used to model ship waves(Beji, 2018; Mathew and Akylas, 1990; Sharma, 1995). These equations are frequently used in the present context because they are susceptible to producing closed form solutions (Whitham, 2011). By contrast, the Euler form of the governing equations admits this for simple, and therefore predominantly unrealistic cases (Torsvik, 2009).

Unlike the fKdV or KP equations, the Boussinesq equations, also members of the long wave family of theories, have no known closed forms. In this respect, they are related to the Euler equations. However, Boussinesq-type solutions can account for motion in any direction. Moreover, they can handle intermediate wavelengths, as opposed to solely long ones. Their derivation also does not rely on a balance between dispersive and nonlinear phenomena, as is the case with the two earlier types of equations. For this reason, the Boussinesq form is frequently preferred (Dam et al., 2008; David et al., 2017; Grue, 2017; Jiang et al., 2002; Torsvik et al., 2006; Wu and Wu, 1982). For instance, according to Nwogu (1993), the Boussinesq equations, as derived by Peregrine (1967) can model nonlinear transformations in shallow waters.

Nwogu's (1993) derivation, was used to examine ship waves recently by David et al. (2017) to study ship waves propagating over an irregular bathymetry. They compared their model with measurements made in the port of Hamburg to demonstrate the validity of the Boussinesq approach.

The utility of Euler-based methods is indisputable. That is the case especially when viscosity is of little to no importance and solutions can be obtained at low cost. However, there are cases where the subtle action of viscosity has only recently been uncovered. Specifically, as stated earlier, Böttner et al. (2020) and Shevchuk et al. (2016) demonstrated the formation of a boundary layer on the seabed in very shallow waters. It is in such cases that RANS methods can be used, showcasing their strengths. For vessels with high block coefficients, i.e. non-slender shapes, the action of viscosity may be significant. This would be expressed as an influence in the near-field pressure distribution, which can impact on the far-field waves.

On the other hand, in very shallow and/or narrow canals and rivers, the reflection of waves would unavoidably interact with the aforementioned boundary layer, found at the river or canal bottom, thus altering the wave-induced velocity of water particles. In such cases, an Euler-based method would not necessarily be suited for the modelling of ship-induced waves and related wave fields.

2.5 Summary and conclusions

This chapter examined several, widely studied as independent, but fundamentally linked topics. Firstly, a brief historical overview of the broader discipline of ship hydrodynamics was given. This illustrated that as is typical of phenomena within the field itself, the evolution of hydrodynamics was frequently nonlinear. That is, great strides were made by, for instance, Euler in describing the inviscid form of the governing equations. However, his contributions present such levels of complexity, that even today, the Euler equations carry open research questions.

Then, conceptual difficulties and challenges were summarised. Following this, scale effects were described in some detail for deep and shallow water cases sequentially. It was illustrated that phenomena observed in the latter cases can exist in a generalised form within the former cases. Thus, it may be frequently desirable to examine cases of greater complexity to enable a better understanding of the physics. Shallow water flows past ships are

representative of such cases due to the amplification in relative importance of nonlinear phenomena.

In line with the research aims and objectives, a survey of the literature was performed. This suggested that scale effects in the context of ship resistance originate from the nonlinear nature of the problems, which are treated linearly. This is true for both deep and shallow waters. To overcome this obstacle, one could perform simulations directly in full-scale. However, as demonstrated by the literature, validation data for such cases is scarce. To make matters worse, the computational cost associated with full-scale simulations currently tends to be high.

Several aspects requiring further research were identified. These can be summarised as follows, and are addressed in subsequent chapters:

- Scale effects on the wave resistance coefficient, form factorhave not been investigated simultaneously in any previous study.
- Interactions between different components of ship resistance, specifically wave and frictional resistance, have not been investigated using a RANS solver in previous studies.
- Turbulence dependence is a source of ambiguity, therefore requiring a separate investigation.
- Restricted water effects on the scaling of ship resistance have not been examined in sufficient detail.
- Ship waves modelled via RANS solvers have not been extensively compared against other methods.
- Cases where a ship advances over a change in the water depth have not been investigated using a RANS solver.

3. A GEOSIM ANALYSIS OF SHIP RESISTANCE DECOMPOSITION AND SCALE EFFECTS WITH THE AID OF CFD

This chapter examines the scale effects on a ship in deep, unrestricted waters. The analysis is performed for the KCS hull in three different model-scale factors, forming a geosim series, which culminates in a full-scale set of simulations. The specific condition to which the analysis is performed reflects the operational speed of the ship. Simulations are performed in multiphase and double body regimes with and without sinkage and trim. Moreover, the viscous scaling approach is applied to gauge its performance when compared to the linear scaling method.

3.1 Introduction

In 2011, the International Maritime Organisation (IMO) introduced the first mandatory measure since the Kyoto Protocol (UNFCCC, 1998) to improve the energy efficiency of ships and accelerate innovation in the maritime sector (IMO, 2011). This regulation requires every ship that has been built after January 1st, 2013 to be certified using the Energy Efficiency Design Index (EEDI). EEDI can be broadly thought of as a measure of the energy efficiency per tonne-mile. As such, ship resistance is one of the primary parameters used in its calculation. Hou et al. (2019) discussed the two sources of uncertainty that arise when calculating the EEDI of a ship: aleatory uncertainty, which exists objectively due to the operating environment, for example; and

epistemic uncertainty, which relates to lack of knowledge. Here, the latter is examined only.

The source of epistemic uncertainty lies with the complexity of estimating ship resistance – a problem that remains unsolved despite the fact that scientists have been attempting to overcome it for several centuries. For instance, Gotman (2007) reported that both Newton and Euler had devised approximations based on different mathematical approaches. Even with the advent of Computational Fluid Dynamics (CFD) methods, one cannot *guarantee* that a calculated value for the resistance of a ship will match experimentally obtained data. Instead, the uncertainty is estimated and reported on, for knowledge of the exact value of the error would allow us to simply correct results accordingly. For this reason, expensive experiments are routinely performed in towing tanks around the world.

While one is free to geometrically scale down a ship to a convenient size, the physical properties of water do not change (Tropea et al., 2007). Therefore, the troubles of the naval architect do not end once the experiment has run its course. One may only keep the ratio of inertial and viscous forces (the Reynolds number – *Re*), or the ratio of gravitational and inertial forces (the Froude number – *Fr*) the same between model and ship (Lee et al., 2018). Extrapolation procedures have been devised to keep these ratios, the earliest by William Froude in the 1870s (Molland et al., 2017). Theoretically, these allow us to predict the resistance of the full-scale ship using a model experiment in any scale.

This chapter will attempt to establish a better understanding of the epistemic uncertainty involved in calculating full-scale ship resistance using a Reynolds Averaged Navier-Stokes (RANS) solver. To achieve the task at hand, experimental data for the well-known KCS hull form in three different scale factors were collected. At each scale factor, numerical simulations are performed in three different ways to predict the components of bare hull resistance. Specifically, the ship is scaled geometrically and simulated in both double body and multiphase conditions. Additionally, by modifying the value of dynamic viscosity only, the ship's Reynolds number is changed to match its respective value at higher scale factors without a change in characteristic length.

The novelty in this part of the thesis is expressed in the unique approach adopted to predicting ship resistance. While a plethora of researchers have

examined scale effects in the present context, to the best of the author's knowledge, none have performed this with a variety of methods incorporating all physical phenomena, simultaneously validating numerical predictions against experimental data. Specifically, the adopted methodology enables prediction of interactions between the linearly decomposed components of ship resistance and examine scale effects on each individually.

Of particular interest is wave resistance, which is typically assumed scale invariant at a constant Froude number. Although the work of Raven et al. (2008) suggested otherwise, this assumption is still applied widely. In this context, it will be attempted to confirm and further examine the presence of scale effects in wave resistance in an attempt to stimulate more research in this area.

The remainder of chapter first justifies the adopted research methodology in section 3.2, and gives the ship geometry and examined conditions in section 3.3. Then, the numerical modelling is presented in section 3.4, before the resulting data is shown in section 3.5, accompanied by a discussion on its significance. Finally, section 3.6 provides summary and conclusion.

3.2 Methodology

The adopted methodology revolves around the capabilities of Star-CCM+, an extensively used, validated, and verified commercially available RANS solver (Siemens, 2018). Making this choice allows the exploitation of the versatility inherent in numerical simulations. In reality, one is limited to performing 'multiphase experiments', unless the underwater shape of a ship and its mirror image are tested in a wind tunnel. The wider literature suggest that such experiments are extremely rare, even in an academic context (Lee et al., 2003). However, numerically, not only is this a possibility, but it is an approach capable of substantially accelerating convergence characteristics of the numerical solution.

In particular, some aspects of a simulation requiring attention are the decay of ship motions (in steady state cases) and the convergence of the wave field. In other words, the wave pattern must become invariant with respect to the ship. Invoking the double body assumption implies replacing the free surface with a symmetry plane as well as eliminating the rigid body motions of the ship. This is thought to be the main reason why the earlier studies cited in Chapter 2 use the double body approach: insufficient computational power to fully simulate the flow field and ship motions. Alternatively, researchers have

sought to predict the form factor via double body simulations. Naturally, deviating from the actual physics of the problem examined renders predictions less reliable.

Keeping in mind the inherent consequences present in performing simulations under the double body assumption, it should also be mentioned why applying it here is beneficial. The resistance decomposition of a ship according to the ITTC (2017) is shown in Eq. (3.2):

$$C_T = (1 + k)C_F + C_W \tag{3.2}$$

Where (1+k) is the form factor, while C_T, C_F, and C_W are the total, frictional, and wave resistance coefficients, respectively. These constitute the measured force, non-dimensionalised by $0.5\rho SV^2$, where ρ (997.561 kg/m^3) is the freshwater density, S is the wetted surface area in m^2, and V is the ship speed in m/s.

Replacing the free surface with a non-deformable symmetry plane renders $C_W = 0$, therefore Eq. (3.2) becomes $C_T = (1 + k)C_F = C_{VP} + C_F$, where C_{VP} is the viscous pressure resistance coefficient. This matches the resistance definition in all RANS solvers. Namely, the total resistance is the sum of tangential and normal components. In multiphase simulations, RANS solvers compute the total as $C_T = C_P + C_F$, where C_P is the pressure resistance. Clearly, all components are interrelated and calculating each presents its own challenges. Here, relying on methods can be avoided, whether potential (in the case of C_W) or otherwise (for (1+k) and C_F), to predict their value by defining the wave resistance coefficient as shown in Eq. (3.3) and form factor in Eq. (3.4):

$$C_W = C_{T_{\text{multiphase}}} - C_{T_{\text{double body}}} \tag{3.3}$$

$$(1 + k) = C_{T_{\text{double body}}} / C_{F_{\text{double body}}} \tag{3.4}$$

The definitions of Eq. (3.3) and (3.4) are used in to predict scale effects on each component of ship resistance.

Additionally, seeking to confirm the assertion that sinkage and trim do not contribute much to the total resistance in deep waters, double body simulations are run in both level and translated conditions, the latter matching the multiphase orientation of the ship. To isolate Reynolds number effects on resistance coefficients and the form factor, a single Froude number is used (Fr = 0.26, which corresponds to the service condition), chosen to match available experimental data.

Finally, an explanation is owed to the assertion that a change fluid viscosity can be used to scale the ship without altering its dimensions. The term 'viscous scaling' is used to describe the altering of the value of dynamic viscosity (μ) that changes the Reynolds number. This approach was adopted following Haase et al. (2016), where it was applied on a catamaran. The method relies on verifying the mesh in model-scale versus experiments and changing the viscosity value to match the full-scale *Re*. Here, this is performed in steps, which match the examined scale factors to more accurately gauge its performance. It is only applied on the double body simulations after the orientation of the ship has been adjusted according to the running trim and the sinkage, calculated using the multiphase approach.

Naturally, the most economical simulations are sought in terms of computational power and time. For this reason, viscous scaling is applied to the hull form in the 75th scale. Therefore, the values for μ shown in Table 3.1 correspond to those needed to make the $Re^{(75)}$ match $Re^{(52.676)}$, $Re^{(31.599)}$ and $Re^{(1)}$, where the bracketed superscripts indicate the scale factor ($Re^{(\lambda)}$). To account for the geometric scaling, all results are multiplied by λ^3 (Haase et al., 2016b). To elaborate, the resistance values are multiplied by the ratio of scale factors, raised to the third power. Specifically, using λ=75→ λ=31.599 as an example, after modifying μ according to the value shown in Table 3.1 ($\mu^{(31.599)} = 2.431\times10^{-4}$ Pa-s) each constituent component of the measured resistance would be multiplied by $(75/31.599)^3$=13.371 at the end of the simulation. This procedure is applied analogously at each scale factor examined.

3.3 Ship geometry and conditions

There are many examples of research that attempt to resolve the ship scaling problem. Some significant contributions to the field were discussed in Chapter 2. Here, the aim is to elaborate on the selected case-studies.

The best way to determine scaling effects is to test the same ship at different scales while measuring parameters of interest. By doing this, the scope is limited to a single hull form, and therefore, it would put into question the generalisations that one might be tempted to make about other hulls forms. Still, the literature on this subject suggests that incorporating multiple hull forms is not advantageous. For instance, García-Gómez (2000), Min and Kang, (2010), and Lee et al. (2018) showed scattering in results produced by different hull forms, even when considering non-dimensional quantities, such as the form factor. Although one is by no means insured against the same outcome,

it is maintained that a more in-depth study is possible considering a single hull form.

The only choices worth considering in detail in terms of hull forms are those created for numerical benchmark purposes. From the large number of experiments conducted on them in different scale factors, the most attractive proves to be the KCS, because resistance measurements (for Fr=0.26) have been performed in a scale factor (λ) of 75 by Shivachev et al. (2017), 52.667 by Simonsen et al., (2013) and 31.599 by Kim et al. (2001). Table 3.1 shows the principal dimensions and case-studies in each scale. Here, the value of dynamic viscosity in the 75th scale is in bold to highlight it as the default value for the simulations. By contrast, viscous scaling has been performed in the places where other values are listed.

Table 3.1. KCS Principal characteristics and case-studies

Quantity	Symbol	Value				Unit
Scale factor	λ	1	31.599	52.667	75	-
Length	L	230	7.279	4.367	3.067	m
Beam	B	32.2	1.019	0.611	0.429	m
Depth	D	19	0.601	0.361	0.253	m
Draught	T	10.8	0.342	0.205	0.144	m
Displacement	∇	51990.120	1.649	0.356	0.123	m^3
Block coefficient	C_B	0.6505	0.651	0.651	0.651	-
Wetted area with rudder	S	9539	9.553	3.439	1.696	m^2
Longitudinal centre of gravity	LCG	111.603	3.532	2.119	1.488	m
Vertical centre of gravity	VCG	7.28	0.230	0.138	0.097	m
Metacentric height	GM_T	0.6	0.019	0.011	0.008	m
Velocity	U	12.350	2.196	1.702	1.426	m/s
Froude number	Fr	0.26	0.26	0.26	0.26	-
Reynolds number	Re	3.188×10^{9}	1.794×10^{7}	8.342×10^{6}	4.909×10^{6}	-
Dynamic viscosity for scaling	μ	1.368×10^{-6}	2.431×10^{-4}	5.229×10^{-4}	$\mathbf{8.887\times10^{-4}}$	Pa-s

Selecting the KCS as the case study for this chapter and the remainder of the thesis is justifiable for two reasons. Firstly, one ought to use realistic hull forms for numerical investigations. For instance, if an alternative benchmarking hull were to be selected, for example, the parabolic hull, the results may not be equally applicable, restricting the possible findings and discussions. This is the case due to the fact that the Wigley hull is a simple shape, and lacks some

prominent features many ships possess. Specifically, the bulbous bow, a concave-convex variation in the surface curvature between the bow and stern, as well as a flat bottom. The second aspect, worth considering is the wealth of available experimental data. These were hinted at earlier in this chapter, and will be detailed in the results sub-section. Moreover, the numerous experiments performed with the KCS allow for validation potential in the remaining chapters of this thesis as well. Therefore, the KCS is considered an ideal case for the purposes of this thesis.

As mentioned earlier, a single Froude number is used. This approach is adopted in order to isolate Reynolds number effects in the examined parameters. The Reynolds number changes several orders of magnitude between the smallest and largest scale factors used herein. It is therefore anticipated that the Reynolds number would produce the most noticeable. While Froude number effects may also be present in the scaling of ship resistance, their effect is not forecast to be as significant as that stemming from the Reynolds number change, since the Froude number solely changes by a considerably smaller amount.

3.4 Numerical set-up

In this section, the relevant details regarding the numerical setup are discussed. Prevalence is given to parameters likely to affect the computed results. Where possible, a discussion is included on the potential effect each decision could have.

3.4.1 Physics modelling

The RANS solver used, Siemens' Star-CCM+, version 13.4.011, employs a Finite Volume Method (FVM) to discretise the integral form of the Navier-Stokes equations. Continuity and momentum are linked via a predictor-corrector scheme.

As mentioned in Chapter 2, turbulence modelling is suspected to play a crucial part in scale effects. Here, the realisable k-ε turbulence model with the all y^+ wall treatment is used. There are several advantages of selecting this two-equation turbulent kinetic energy-dissipation model. Primarily, interest lies in accuracy and economy. The findings of Larsson et al. (2014) indicate that there is no discernible change in resistance predictions with more complex models. On the other hand, Salim and Cheah (2009) performed systematic RANS simulations using ANSYS on the frictional resistance of a flat plate and

compared their results with a variety of turbulence models. The k-ε model was shown to deliver better predictions than the k-ω model, provided that the viscous sublayer is resolved. In other words, the y^+ value should be lower than 1. Indeed, the accuracy of the result depends strongly on the ability to maintain $y^+<1$.

Eça et al. (2015) showed that values of y^+ within the buffer zone ($5<y^+<30$) may lead to an error in the region of 10% when calculating the frictional resistance. For grids featuring cells within the viscous sublayer ($y^+<1$), a single difficulty is reported by both Eça et al. (2015) and the ITTC (2011): large number of high-aspect-ratio cells, which make convergence problematic. In other words, resistance predictions are vastly superior in terms of accuracy when $y^+<1$ is maintained over the wetted area of the ship, as long as convergence is not compromised. Stern et al. (2013) reported that a challenge for full-scale computations would be the number of near-wall cells. Indeed, Piomelli and Balaras (2002) predicted that wall-normal cell numbers would have to vary with $Re^{0.4}$ only within the outer boundary layer. Thus, the y^+ value is allowed to exceed unity in full-scale due to the prohibitively large cell number needed otherwise. The impact of this choice is yet unknown, requiring further investigation.

The k-ε turbulence model, widely used for full-scale flows (Schweighofer, 2004; Tezdogan et al., 2016b), is also advantageous due to its relative computational economy. Quérard et al. (2008) found that a reduction of up to 25% in computational time is possible compared to more sophisticated models. Furthermore, the simulations of Simonsen et al. (2013) were performed using the k-ω model in Star-CCM+ and CFDSHIP-IOWA, which will allow comparison of turbulence models.

In the case of multiphase simulations, the Volume of Fluid (VOF) method, introduced by Hirt and Nichols (1981), is used to model the free surface, and the movement of the water. This is done via the flat wave concept. The VOF method describes the two phases by assigning a scalar value of 0 to air and 1 to water. The interface between the two, i.e. cells containing equal parts of air and water attain a value of 0.5. Therefore, the inlet and outlet boundaries have a field function associated with them. At the inlet, the velocity and direction of the flat wave is specified, whereas the outlet is set to maintain the hydrostatic pressure. The VOF model depends on both fluids accounting for large parts of the domain, while maintaining a relatively small contact area. For the double-body simulations, the movement of water cannot be modelled

in such a way. Instead, the velocity is defined at the inlet boundary, whereas at the outlet, a pressure of 0 Pa is preserved.

The segregated flow model is used to solve the equations of state in an uncoupled manner. In all simulations, the convective terms are solved via a second order scheme, while the overall solution is obtained using a SIMPLE algorithm. The dynamic trim and sinkage of the ship is captured using a Dynamic Fluid-Body Interaction (DFBI) model, where only heave and pitch modes of motion are allowed. More information on the aforementioned choices may be found in Siemens (2018).

3.4.2 Time step selection

The Courant-Friedreichs-Lewy (*CFL*) number is sometimes used as a condition to assess the convergence of simulated flows. It expresses the idea that if a flow is moving across a discrete spatial grid, one must choose a suitable time step Δt and spacing Δx to guarantee that the properties of the fluid (velocity, pressure) are solved for at each grid point. In such a case, $CFL \leq 1$. The ITTC (2011) recommends the use of Δt=0.005~0.01L/U, where L and U are the ship's length and speed, respectively. Tezdogan et al. (2016) and Terziev et al. (2018) demonstrated that the use of Δt=0.0035L/U showed little error due to the discretisation of the temporal term in the Navier-Stokes equation, which was set as first order, and is therefore chosen as well.

3.4.3 Mesh generation

Mesh generation was performed using the automatic facilities of Star-CCM+, which allows the user to make use of several operations. The trimmed cell mesher is used to fabricate predominantly hexahedral cells. The alternative, using tetrahedral cells, has been shown to deliver unreliable results by Jones and Clarke (2010). The near-wall cells were generated using the prism layer mesher, which is used to fabricate orthogonal cells near the hull surface. Star-CCM+ automatically places these cells using a geometric progression to determine their dimensions. The prism layer thickness is set to equal the approximate value of the turbulent boundary layer thickness, derived by the 1/7 power law, found in White (2006).

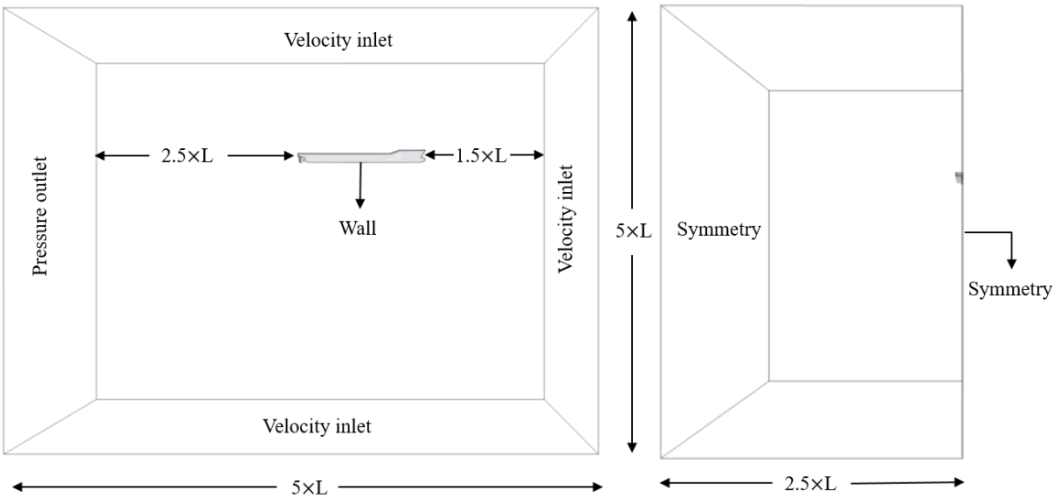

Figure 3.1. Domain boundary conditions and dimensions for the typical multiphase simulations

3.4.1 Computational domain and boundaries

According to Date and Turnock (1999), the boundary conditions of a CFD simulation play a critical role in both the accuracy and convergence of the solution. Their position as relative to the ship is equally important because, in rare cases, wave reflections may occur and that would invalidate the solution. To insure against this, the computational domain is constructed following the recommendations of the ITTC (2011). The resulting dimensions and boundary conditions are shown in Figure 3.1. A numerical beach model, the VOF damping length, is also applied to the outlet boundary equal to approximately 1.24L in each scale. This allows the wavefield to develop prior to reaching the damping zone, and guarantees no reflections will occur.

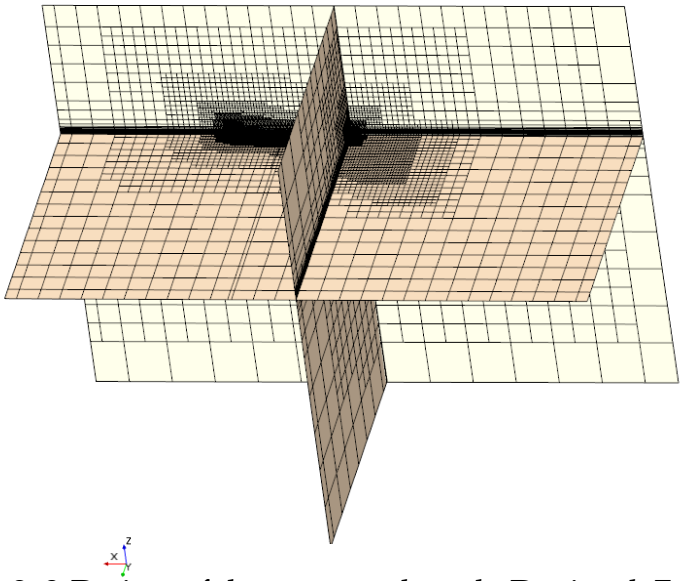

Figure 3.2. 3-D view of the generated mesh. Depicted: Full-scale

Only half of the ship is simulated, thus, a symmetry plane is applied to all case studies to alleviate the computational load and allow a larger number of cells to be used. The side boundary is set as symmetry because it does not allow changes in velocity or pressure across it to occur, i.e. it approximates an infinitely wide, deep sea. In any case, it is reasonable not to expect the Kelvin wake to reach the side boundary. The computational domain, shown in Figure 3.2, is scaled with the ship linearly to minimise numerical scale effects. The resulting three-dimensional grid properties are shown in Table 3.2. Here, the cell count for the translated double body simulation in λ=75 have been highlighted to indicate their use in the viscous scaling procedure.

Table 3.2. Number of cells in each scale

Scale		1	31.599	52.667	75
Number of cells	Multiphase	20,554,263	12,343,685	5,832,169	3,338,447
	Double body: level	5,166,585	3,750,965	2,703,735	1,615,244
	Double body: translated	5,532,073	3,491,712	2,739,160	**1,632,931**

3.4.2 Time-history of the numerical solution

Calm water ship resistance is a steady state-problem. In other words, the solution is not affected regardless of how long the computation is performed for. However, in CFD, the ship experiences a well-known shock at the beginning of the simulation (Mucha, 2017). This can be mitigated by hydrostatic balancing (also referred to as 'equilibrium'), but is not implemented here to avoid contaminating the solution with deficiencies of

numerical algorithms. According to Siemens (2018), the equilibrium option is a purely mathematical procedure that has no basis on physical rigid body motion. The alternative offered by the RANS solver consists of 'free motion', where the body is translated and rotated as a result of the forces acting on it at each time step, and is implemented here.

To reduce the shock effect, the ship is constrained in all directions for the first 5 seconds of the simulations. In Figure 3.3, the time-history is illustrated for the three components of resistance for λ=31.599. A ramp time of 10 seconds is also adopted, which gradually applies the forces on the hull to help reduce oscillatory motions. The combined effect of these two settings can be seen in Figure 3.3.

Transient effects in CFD have a potential to invalidate the results, which is why, as explained earlier, the domain boundaries must also be placed suitably. Figure 3.3 also demonstrates that the placement of the boundaries in the computational domain was successful, as well as the adequate decay of transient solution characteristics.

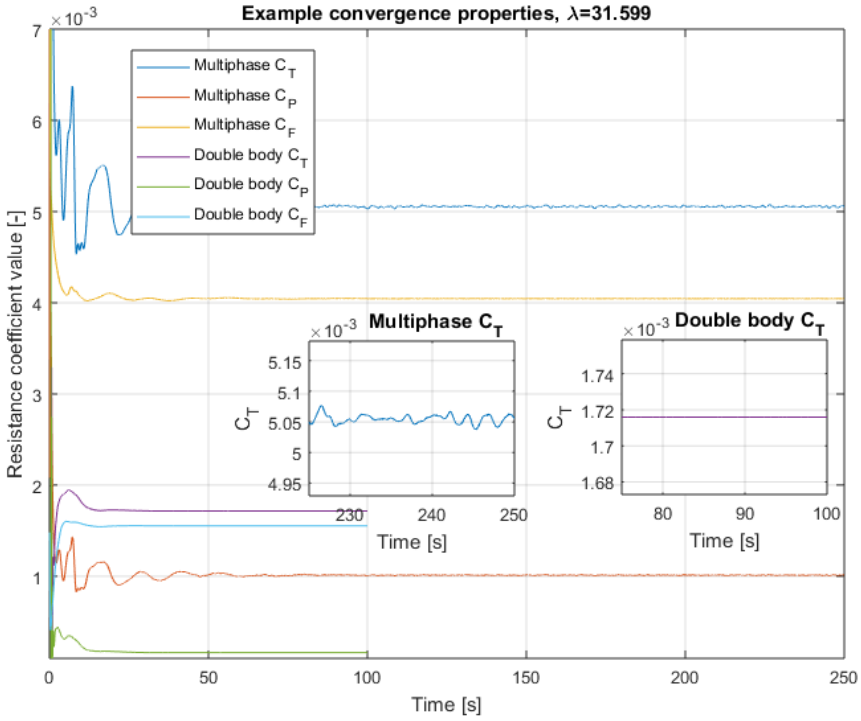

Figure 3.3. Example time-history of resistance and sinkage for case λ=31.599

To evaluate the iterative errors, the procedure of Roy and Blottner (2006) was used on the total resistance coefficients in multiphase and double body

regimes. The analysis showed an absolute error of approximately 5.504×10^{-4} % and 2.112×10^{-6} % for multiphase and double body C_T values, respectively, which was representative of other cases as well. These are used to justify the use of the numerical verification procedure, which assumes that iterative errors must be at least two orders of magnitude smaller than discretisation errors. In any case, all final values reported here are averaged over the last 25 seconds to ensure the final value is affected as little as possible by the iterative error.

Convergence properties can also be judged based on residuals. The residual of a numerical scheme can be broadly thought of as the (usually scaled) difference between the iteratively approximated solution and the perfect conservation of mass and momentum (ITTC, 2014). Typically, these are required to reduce by several orders of magnitude for the simulation result to be accepted. However, this is strictly dependent on how close the initial state of the simulation is to satisfying perfectly the discretised form of the governing equations (Siemens, 2018). This true is because if the initial state of the simulation is very close to satisfying the laws of conservation perfectly, the residuals will not reduce at all (Siemens, 2018). In other words, residual time-histories should not be used on their own to assess for convergence, although they are a powerful tool in any numerical analysis problem. Furthermore, the observed reduction in residual values is highly case-specific: a large reduction can still lead to a high validation error.

The double body residuals were found to reduce quickly by about five orders of magnitude (to 10^{-5} ~ 10^{-6}) within approximately the first 4000 iterations (the ITTC's (2011) recommendation is a reduction of three orders of magnitude). This is a highly attractive feature of this type of set-up. It is also the reason why ship CFD simulations were performed in double body mode in the early days of the field. In the case of multiphase simulations, all residuals decreased by two orders of magnitude within the first 8000 iterations (considerably later than in the double body case). Reducing the magnitude of residuals further proved difficult. This is not considered problematic, as stated by the ITTC (2011) A representative case for the residual behaviour in both multiphase and double body modes is shown in Figure 3.4 (λ=31.599).

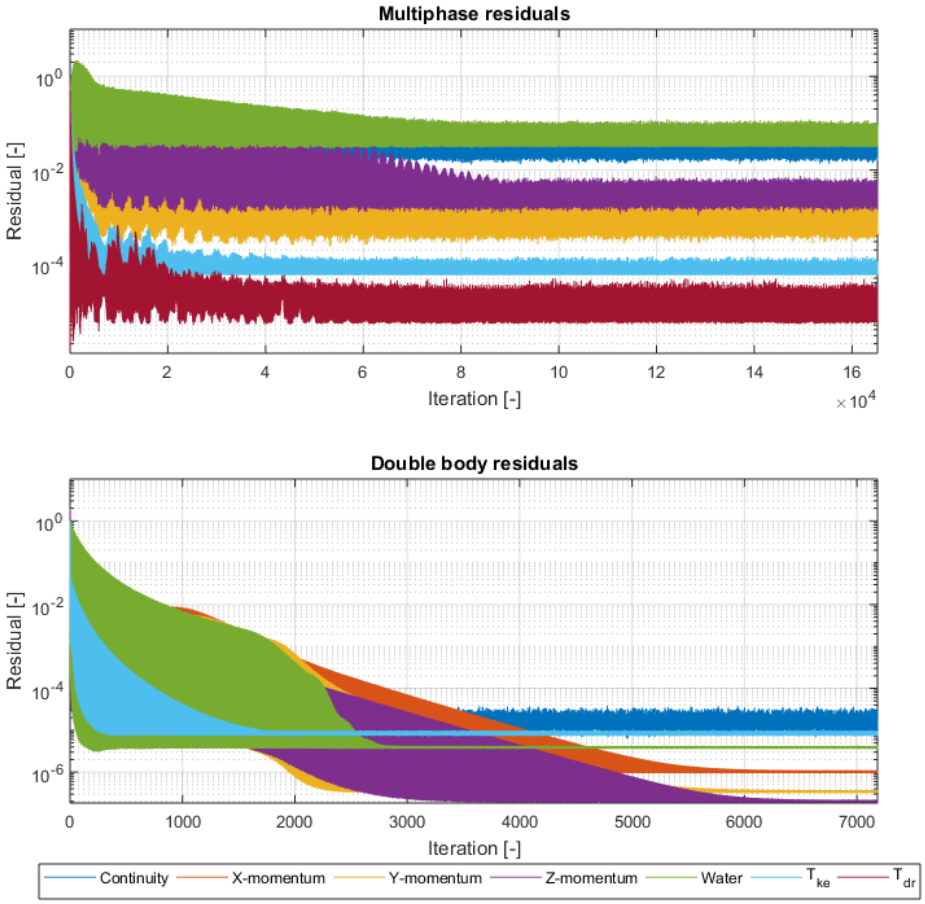

Figure 3.4. Residual time-history ("Water" refers to the volume fraction residual). Depicted: λ=31.599

In all cases, following the end of the transient oscillatory motion, residuals did not exhibit signs of reducing further. This is because the flow had fully developed at this stage. This is not problematic *per se*, because ship CFD – especially towed, calm water predictions – are not characterised by large ship motions or deformations of the free surface. Thus, while it is desirable to achieve a magnitude of the residuals that is as low as possible, a small reduction does not imply a 'bad' solution by itself.

According to ITTC (2014), even if the recommended three order of magnitude residual reduction cannot be achieved, integral values can be used to assess convergence of the solution, in particular, forces and moments acting on the hull (this is primarily in view of the complexity associated with the numerical simulation of ship flows). This was done earlier in this section in the case of iterative errors in resistance for λ=31.599. The following section presents the numerical verification study, which expands on the expected uncertainties due to spatial and temporal discretisation.

3.4.3 Verification study

It is inevitable to induce errors when temporally or spatially discretising the Navier-Stokes equations. Since the governing equations cannot be modelled continuously, it is assumed that errors decay rapidly as Δt and Δx decrease. In other words, the continuous equations should match the discretised versions as Δt, $\Delta x \rightarrow 0$.

The current method of estimating uncertainty in CFD simulations is based on expanding the error as a power series with integer powers of Δt or Δx (Xing and Stern, 2010), introduced by Richardson (1911). The four types of conditions which govern whether a solution is convergent or divergent as Δt and Δx are refined can be summarised as follows:

1. Monotonic convergence: $0 < R < 1$
2. Oscillatory convergence: $R < 0$; $|R| < 1$
3. Monotonic divergence: $R > 1$
4. Oscillatory divergence: $R < 0$; $|R| > 1$

For conditions 3 and 4, neither error nor uncertainty can be estimated. Here, R is the convergence ratio, defined in Eq. (3.5):

$$R_k = \varepsilon_{21}/\varepsilon_{32} \tag{3.5}$$

where ε_{21} is the difference between the medium (f_2) and fine (f_1) solutions, while ε_{32} is the difference between the coarse (f_3) and medium (f_2) solutions. These ($f_{1,2,3}$) are obtained by systematically coarsening (by using the refinement ratio $r = \sqrt{2}$, recommended by the ITTC, (2008)) the respective input parameter – time-step or mesh (Stern et al., 2006). In other words, the base size is multiplied by $\sqrt{2}$ while maintaining the smallest time step. The resulting cell counts are 1,674,346 and 880,876 for the medium and coarse mesh study for λ=75, respectively. The same procedure is applied to the time step, which is lessened by the same factor on the finest grid to isolate errors due to changes in temporal discretisation.

Since r is maintained constant, the order-of-accuracy (p) takes the form of:

$$p_k = \ln(\varepsilon_{k32}/\varepsilon_{k21})/\ln(r) \tag{3.6}$$

Thus, one arrives at the extrapolated value (f_{ext}^{21}), according to Celik et al. (2008):

$$f_{ext}^{21} = (r^p \times f_1 - f_2)/(r^p - 1) \tag{3.7}$$

Next, the approximate relative error, defined in Eq. (3.8), and extrapolated relative error, defined in Eq. (3.9), can be estimated.

$$e_a^{21} = |(f_1 - f_2)/f_1| \tag{3.8}$$

$$e_{ext}^{21} = |(f_{ext}^{12} - f_1)/f_{ext}^{12}| \tag{3.9}$$

Table 3.3. Grid convergence for trim and total resistance coefficient

	Trim at CoG (with monotonic convergence)	C_T (with monotonic convergence)
r	$\sqrt{2}$	$\sqrt{2}$
f_1	0.1642	4.2908×10^{-3}
f_2	0.1653	4.2794×10^{-3}
f_3	0.1693	4.2454×10^{-3}
R	0.2963	0.3600
p	3.5102	2.9480
f_{ext}^{21}	0.1637	4.2972×10^{-3}
ε_a^{21} (%)	0.6914	0.2673
ε_{ext}^{21} (%)	0.3010	0.1486
GCI_{fine}^{21} (%	0.3638	0.1879

Finally, the grid convergence index (*GCI*) can be calculated, shown in Eq. (3.10). This marks the end of the error estimation, mentioned earlier.

$$GCI_{fine}^{21} = 1.25\varepsilon_a^{21}/(r^p - 1) \tag{3.10}$$

Table 3.4. Time step convergence for trim and total resistance coefficient

	Trim at CoG (with monotonic convergence)	C_T (with monotonic convergence)
r	$\sqrt{2}$	$\sqrt{2}$
φ_1	0.1642	4.2908×10^{-3}
φ_2	0.1612	4.3002×10^{-3}
φ_3	0.1566	4.3315×10^{-3}
R	0.6716	0.2983
p	1.1483	3.4904
f_{ext}^{21}	0.1703	4.2868×10^{-3}
ε_a^{21} (%)	1.8436	0.2180
ε_{ext}^{21} (%)	3.6346	0.0927
GCI_{fine}^{21} (%)	4.7147	0.1158

Table 3.3 and Table 3.4 collectively show the numerical uncertainty is bound within acceptable limits (arbitrarily set as 5%). The adopted numerical set-up is more sensitive to changes due to the time step than due to cell number variations in the case of trim, as shown in Table 3.3 and Table 3.4. The results suggest the opposite is true for the computed total resistance coefficients. The suspected cause for this is the turbulence model: even in the coarse mesh condition, the $y^+ \lesssim 1$ condition is not deviated from, where the k-ε turbulence model is known to perform well. It is not difficult to see that the y^+ condition has been maintained because the number of wall-normal cells, as well as the thickness of the prism layer are independent of the base size, although the cell aspect ratio changes dramatically as the mesh is coarsened. On the other hand, trim is tied to the dynamic behaviour of the ship, where the lessening of Δt has greater potential for impact. This, coupled with the uncertainty described previously regarding the effect turbulence modelling has on sinkage and trim is thought to be the root cause of the elevated GCI indices for trim.

3.5 Results and discussion

In this section, the obtained results are presented and compared against experimental values where possible. At the onset of this chapter, the parameters of interest were defined as the total resistance and its constituent components. Although prevalence will be given to these, running trim and sinkage are also considered.

3.5.1 Error evaluation

Experimental data were collected for three different scale factors. For λ=75, Shivachev et al. (2017) performed both tests, and CFD computations on the KCS without appendages. Simonsen et al. (2013) modelled the rudder, but not the propeller of the KCS in λ=52.667. Kim et al. (2001) performed experiments on the KCS without the rudder or propeller, and did not allow the ship to trim or sink. While the aim is to present results that are as realistic as possible, it is not possible to satisfy all three experimental set-ups. The decision made for the purposes of this thesis is that the ship should be modelled with the rudder, since it has the potential to modify substantially the flow field near the stern. On the other hand, the propeller was omitted so as to avoid deviating too much from the experiments, the majority of which omitted the propeller. Finally, as explained in the previous section, the DFBI method is used to model sinkage and trim.

Table 3.5 shows the numerical and experimental total resistance coefficients. The error in λ=31.599 is based on the results of Kim et al. (2001). In all model scales, the error is bounded within an acceptable limit (3% deviation). An easily observed trend is that C_T values are always under predicted, albeit slightly, by the adopted numerical set-up.

In the cases of sinkage and trim, the numerical calculations show a greater scatter. In λ=75, the trim was predicted within 1.3% of the experimental value (Table 3.6), which the present CFD set-up suggests remain largely unchanged as the ship is scaled. However, the experimental results show a greater trim in λ=52.667. The opposite seems to be suggested by the limited sample points for sinkage, which has been non-dimensionalised by ship length, shown in Table 3.7. Here, the results predict a reduction in sinkage with scale. Despite the aforementioned errors in trim and sinkage, the results presented suggest the principle of dimensional similarity holds to a greater degree than experiments do.

The errors reported could stem from a variety of sources. In model-scale experiments, turbulence stimulators are mounted near the bow of the ship. Thus, the numerical and experimental flows around the hull in each scale would have exhibited different turbulence characteristics. Furthermore, some variability is expected in the approach to turbulence stimulators between testing facilities. While their effect cannot be accounted for in sinkage and trim, the induced parasitic drag is subtracted. As reported in Larsson et al. (2014), turbulence modelling has a pronounced effect on sinkage, and one could, therefore, speculate that it could also have a similar effect on the trim. Factoring in the small uncertainty reported in each experimental study, it can be said that the resistance values have been predicted very well.

Although an acceptable level of error was established in all model-scale case studies examined, it would be wrong to generalise this to full-scale. Indeed, without full-scale measurements one should be wary of making such a claim. The choice of the adopting the KCS provided the possibility of comparing against experiments at each model-scale λ. However, it also prohibits us from attempting to carry this forward to full-scale since no real, full-scale equivalent of the KCS exists. Therefore, the full-scale wave resistance coefficients and form factors for the highest Reynolds number should be considered as an estimation rather than a concrete prediction. Furthermore, it is not practical to achieve $y^+ \lesssim 1$ in full-scale due to the prohibitively large number of cells doing so would entail. Hence, the numerical set-up, where it can confidently be

claimed that the results are accurate, strictly speaking, is not identical to the implemented full-scale set-up. Keeping this in mind, there are sufficient grounds and indeed verifiable data samples in model-scale to justify every conclusion drawn in the following sub-sections.

Table 3.5. Numerical and experimental total resistance coefficients, $Fr = 0.26$

Method or source	Scale (λ)	Re	Software package	Numerical	Experimental	Error (%)
Shivachev et al. (2017), no appendages	75	4.909×10^{6}	Star-CCM+	4.32×10^{-3}	4.41×10^{-3}	2.041
				4.3×10^{-3}		2.494
				4.23×10^{-3}		4.023
The current CFD: multiphase				**4.291×10^{-3}**		**2.703**
Simonsen et al. (2013)	52.667	8.342×10^{6}	CFDSHIP-IOWA	4.07×10^{-3}	4.31×10^{-3}	5.568
			Star-CCM+	4.42×10^{-3}		-2.552
The current CFD: multiphase				**4.232×10^{-3}**		**1.818**
The current CFD: multiphase	31.599	1.794×10^{7}		**3.51×10^{-3}**	3.557×10^{-3}	**1.312**
Tezdogan et al. (2015)	1	3.188×10^{9}		2.295×10^{-3}	-	-
The current CFD: multiphase				**2.294×10^{-3}**	-	-

Table 3.6. Numerical and experimental trim, $Fr = 0.26$

Method or source	Scale (λ)	Re	Software package	Numerical (deg)	Experimental (deg)	Error (%)
Shivachev et al. (2017), no appendages	75	4.909×10^{6}	Star-CCM+	0.198	0.162	-22.222
				0.198		-22.222
				0.195		-20.370
The current CFD: multiphase				**0.164**		**-1.330**
Simonsen et al. (2013)	52.667	8.342×10^{6}	CFDSHIP-IOWA	0.178	0.185	3.940
Simonsen et al. (2013)			Star-CCM+	0.18		2.860
The current CFD: multiphase				**0.165**		**10.708**
The current CFD: multiphase	31.599	1.794×10^{7}		**0.163**	-	-
The current CFD: multiphase	1	3.188×10^{9}		**0.153**	-	-

Table 3.7. Numerical and experimental sinkage/length, Fr = 0.26

Method or source	Scale (λ)	Re	Software package	Numerical	Experimental	Error (%)
Shivachev et al. (2017), no appendages	75	4.909×10^{6}	Star-CCM+	-1.957×10^{-3}	-2.283×10^{-3}	14.286
				-1.950×10^{-3}		14.571
				-1.924×10^{-3}		15.714
The current CFD: multiphase				**-1.890×10^{-3}**		**17.218**
Simonsen et al. (2013)	52.667	8.342×10^{6}	CFDSHIP-IOWA	-2×10^{-3}	-2.100×10^{-3}	4.762
Simonsen et al. (2013)			Star-CCM+	-2.706×10^{-3}		-9.524
The current CFD: multiphase				**-1.897×10^{-3}**		**-9.667**
The current CFD: multiphase	31.599	1.794×10^{7}		**-1.907×10^{-3}**	-	-
The current CFD: multiphase	1	3.188×10^{9}		**-1.902×10^{-3}**	-	-

3.5.2 Resistance decomposition

Here, the form factor approach is adopted, because it contains one parameter more than the Froude's approach on which scale effects can be examined: the form factor itself. As explained in earlier, by making use of the double body approach, there is no free surface (C_W=0) which modifies the form factor equation to yield $(1+k) = C_T/C_F$. In this form, $(1+k)$ can be calculated directly using CFD (under the double body assumption), whether scaled geometrically, or via a modification to the value of dynamic viscosity (μ).

An initial estimate of the form factor during the early design stage can be as valuable as a precise calculation down the line. Therefore, three empirical relations to predict $(1+k)$ have been adopted from Molland et al. (2017). Alongside these, the corrections of García-Gómez (2000) and Min and Kang (2010) are applied.

3.5.2.1 Wave resistance

While Reynolds number effects on the form factor are practically uncontested, scale effects on wave resistance are largely unexamined. Doctors et al. (2007) suggested a 'wave resistance form factor' $(1+k_w)$, but did not provide a recommendation regarding its value. Doctors (2007) and Lazauskas (2009) defined this as $|k_w| < 1$, and $k_w < 0$: a fundamentally different concept from the 'traditional' form factor. Unfortunately, a sufficiently large dataset for the KCS to establish a value for k_w using a regression procedure is not available. Even if

that were the case, many hull forms must be examined under the same criteria to achieve a meaningful estimation applicable in general.

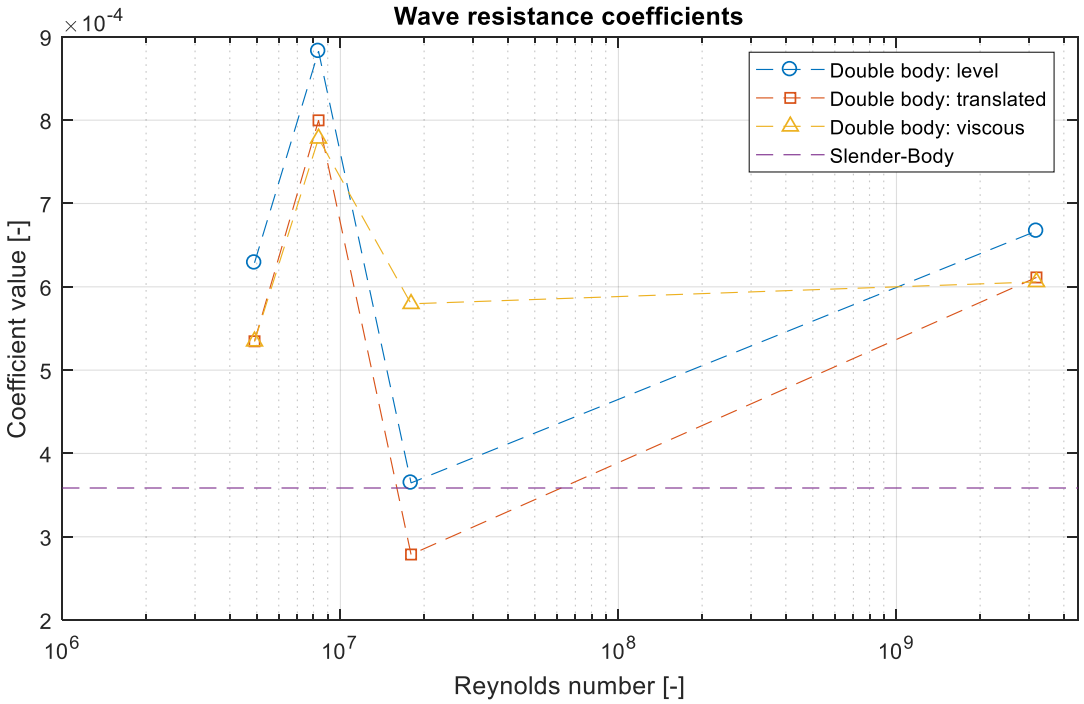

Figure 3.5. Wave resistance coefficients.

Figure 3.5 shows the predicted wave resistance coefficients for each scale according to the three different methods using CFD (calculated as the difference in total resistance of the multiphase and double body simulations). Here, the Slender-body prediction, calculated using Bentley's Maxsurf Resistance software, is represented by a flat line because it is invariant with a change in Reynolds number. This figure presents the first indication that it may not be possible to achieve a smoothly varying curve for which general predictions can be made when large changes are applied to the *Re*. While all methods agree the general direction of the curve in every examined scale, there are disagreements between them at every examined *Re*. It is worth mentioning that the first point of the viscous scaled values, i.e. λ=75, is the same as the translated double body value.

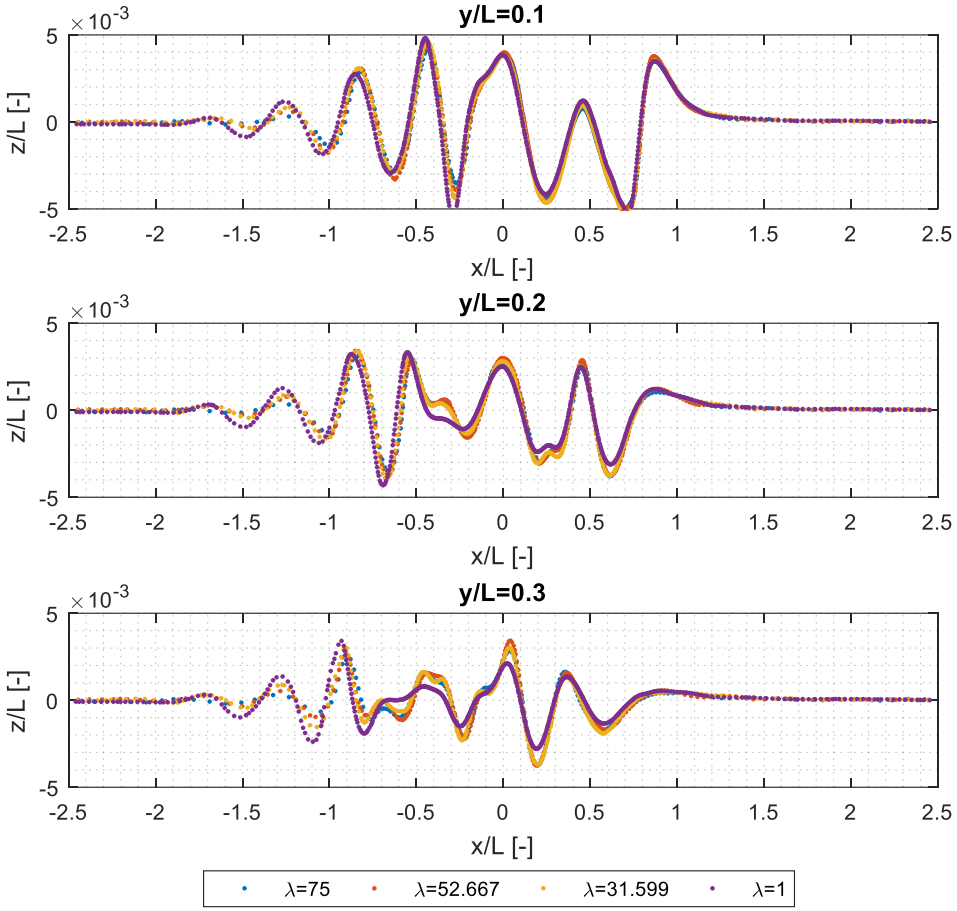

Figure 3.6. Wave cuts at y/L=0.1, 0.2, 0.3 for all examined scale factors. The ship is located at $0 < x/L < 1$, whereas the flow is in the negative x direction.

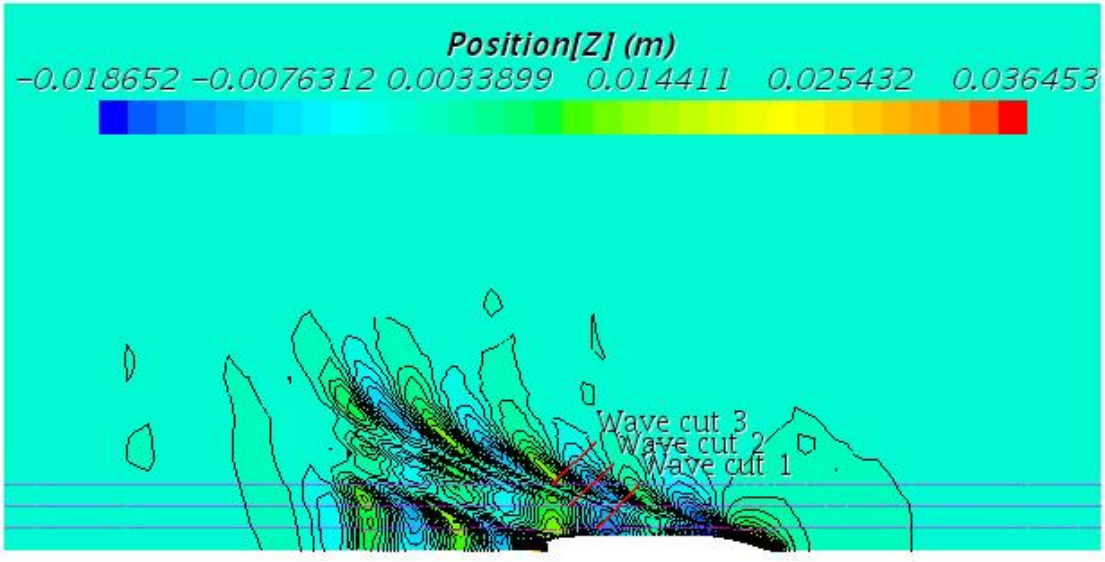

Figure 3.7. Relative locations of the wave cuts. Depicted: λ=75.

The change in wave resistance coefficient implies a geometrically non-similar wave pattern between scale factors. Here, these are not examined, as

identifying differences is difficult and subjective. Instead, to reveal differences, wave cuts are used, shown in Figure 3.6, at three different locations next to the ship. The relative positions of the wave cuts are shown in Figure 3.7. In all λ>1 examined, the curves are sufficiently close to make them largely indistinguishable from each other. In full-scale, the differences become more pronounced. This is the suspected source of differences in wave resistance coefficient. It is interesting that changes are magnified as one moved further away from the ship centreline, i.e. into the fully developed wake. In other words, changes to the wave field with scale require time to propagate some distance from the wave maker before differences become apparent. Therefore, the geometric scaling of the ship's bulbous bow, whose primary function is to modify the wave field is responsible for the observed differences in the wake. Indeed, the laminar portion of the boundary layer at the bulbous bow is appreciably stronger in model scale than that at full scale, inevitably creating discrepancies (Hochkirch and Mallol, 2000). On the other hand, the stern, being the second main source of wave-making, together with the interaction from the bow wave cause the dominant features observed between $-2.5 < x/L < 0$ in Figure 3.6.

Albeit small, errors in the predicted total resistance coefficient and their influence on the wave resistance should not be disregarded. Nevertheless, once decomposed, it is reasonable to expect that these are distributed, to some extent, among the constituent components of the total resistance. Thus, it could be argued that the predicted error, spread over the frictional resistance, wave resistance, and form factor, is insignificant (in the 3D extrapolation case). Therefore, scale effects on wave resistance have been proven, conclusively rendering it a function of both the Reynolds number.

In reality, the boundary layer's interaction with the wave field, and therefore wave resistance, is expected to resemble an iterative process, where the former modifies the latter and vice versa. Although this is largely ignored, several studies have documented such effects, for example Stern (1985). The effects of free surface flow effects on flat plates were examined in Longo et al. (1998), who reported changes in Reynolds stresses and mean velocity components. Marquardt (2009) stated that wave effects on the boundary layer are proportional to wave steepness and may influence the boundary layer up to half a wavelength (in the $-z$ direction). Suh et al. (2011) also identified deformation of vortical structures as a consequence of the presence of a phase interphase.

3.5.2.2 Frictional resistance

To quantify free surface effects on the frictional component of resistance, Figure 3.8 contains all CFD simulations performed as part of this chapter as well as the friction lines used for extrapolation. Although not frequently used in the literature, (in full-scale) the Telfer (1927) line passes just below the CFD predictions, while the Grigson (1999) method slightly overpredicts the multiphase result. The method proposed by Gadd (1967), on the other hand, passes through the predicted frictional resistance coefficients. The ITTC'57 line also provides a good approximation, underpredicting the values slightly.

The results of Figure 3.8 reveal that in the low *Re* range (high λ), free surface effects are much more pronounced than in full-scale. There are several reasons for this. Primarily, the boundary layer affected by the free surface grows much more slowly than the skin friction of a fully submerged body. The latter increases with the wetted area (λ^2), while the former changes approximately with the reciprocal of the 7^{th} root of the Reynolds number. Clearly, the boundary layer length will be equal to the length along the waterline, whereas the vertical distance at which it is disturbed can be estimated by the wavelength of the Kelvin wake. Methods to calculate this vary in complexity and robustness. Such a computation is not attempted, instead leaving it as a piece of future work. Such a study could seek to establish a relationship expressing the exact volume of the disturbed boundary layer by the generated waves. Simultaneously, the contribution of air resistance to the total friction was calculated as less than 0.3% of in all cases using the multiphase simulations.

Naturally, at low Froude numbers, the free surface is hardly disturbed (which also forms the basis for calculating the form factor), and double body approximations can provide good predictions (Landweber and Patel, 1979). Since the relative importance of free surface effects on the boundary layer decay rapidly with scale (similar to the displacement thickness), the aforementioned approximation can be used successfully at full-scale without significantly compromising the accuracy of the desired solution. That is, provided one is equipped with a tool capable of estimating the wave resistance separately with sufficient fidelity directly at full-scale.

Mitchell's integral is used for many theoretical predictions of wave resistance, and forms the basis for the slender body method used in Figure 3.5. Its accuracy in full scale, however, is not as well documental as in model scale.

Gotman (2002) asserted that if the ship has a convex transom, the wave resistance is over predicted. The opposite was suggested to be the case for concave transoms, while if the waterline is straight, or near straight, the values agree well with experiments in the range $Fr < 0.29$. The results presented earlier suggest that the above is only true in λ=31.599 (the KCS transom is convex). Thus, while confidence in numerical tools is largely lacking, it should also be questionable to use a single wave resistance coefficient for all scales.

It is a well-reported fact that the Schoenherr line matches almost exactly experimental values for the skin friction of plates (Bertram, 2012). The reason why a deviation is observed here between the friction lines and CFD results was partially examined by Magionesi and Di Mascio (2016). They focused their attention on flows over ship bulbous bows, because, while a flat plate is characterised by a 0 pressure gradient (Peltier and Hambric, 2007), this is not the case for large parts of the ship's wetted area. Bulbous bows in particular exhibit pressure gradients, the boundary layer is three dimensional, and they are subject to free surface effects, which cannot be ignored (Ciappi and Magionesi, 2005). Ishihara et al. (2015) stated that turbulent boundary layers not only influence the large-scale wake behind a structure, but also the location of separation. In the case of a ship, the boundary layer at the bulbous bow, being different from that of a flat plate, causes changes to cascade astern, and likely into the wake itself.

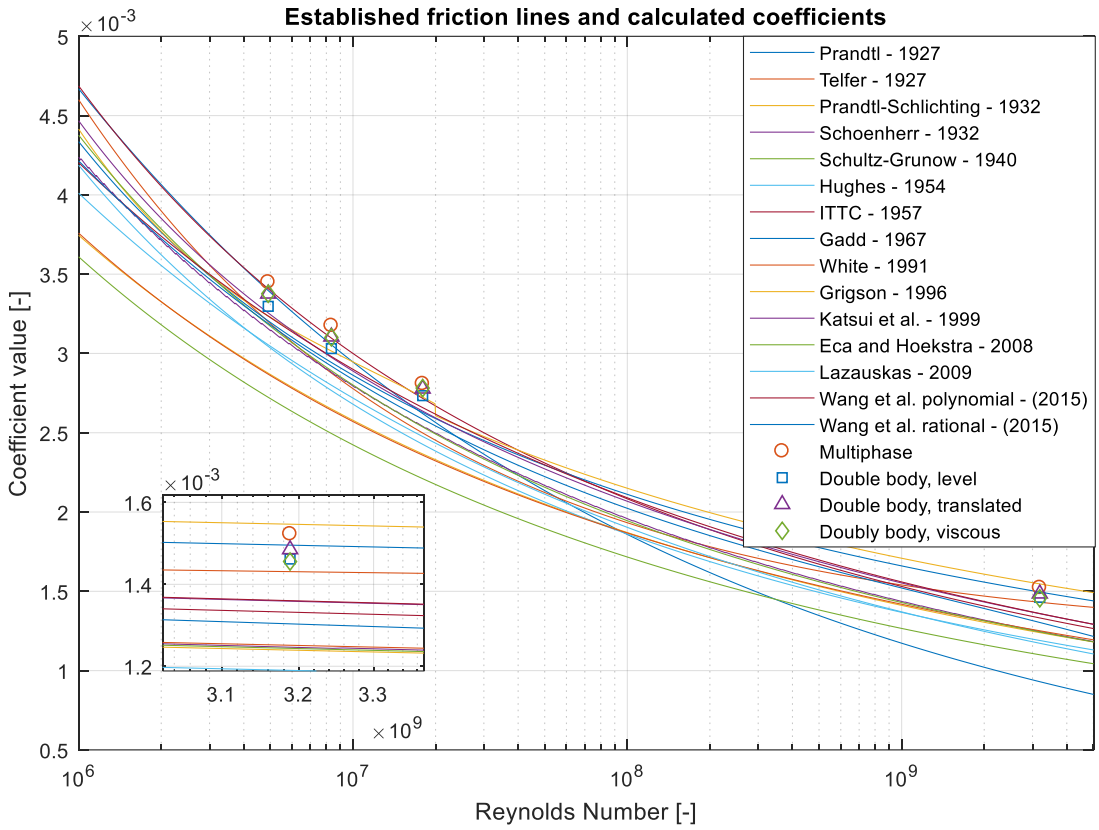

Figure 3.8. Frictional resistance coefficients

One final point to consider here is the Froude number. Having used a single *Fr* (0.26) in all simulations allowed the isolation of the effects of *Re*. Froude number effects on wave resistance are well documented. What is lacking in particular is its effect on the form factor. To resolve this, a larger scale study is required, featuring both numerical and experimental geosim analyses from a single institution to eliminate variability across testing facilities. This is suggested as a piece of future work.

3.5.2.3 Form factor

It is now appropriate to introduce the calculated form factors, shown in Figure 3.9, against Reynolds number. Surprisingly, the (1+*k*) values do not exhibit a well-defined trend. Instead, some scatter is evident as the Reynolds number increases. A similar trend was discovered by Min and Kang, (2010), whose empirical correction depends solely on the *Re*. García-Gómez (2000) on the other hand, devised a formulae based on the scale factor. Both of these are shown in Figure 3.9 with the dashed, and dotted lines, respectively. What is most evident here is their change with scale factor or Reynolds number.

Indeed, the error between the empirically corrected, translated double body form factor and multiphase (1+k) value found is approximately 8.6%. In the level double body case, this is even higher, reaching 10.9%. It should be noted that the empirical form factors are placed for a λ=31.599. The abovementioned corrections are applied to them in order to demonstrate how they perform compared to the full-scale CFD results.

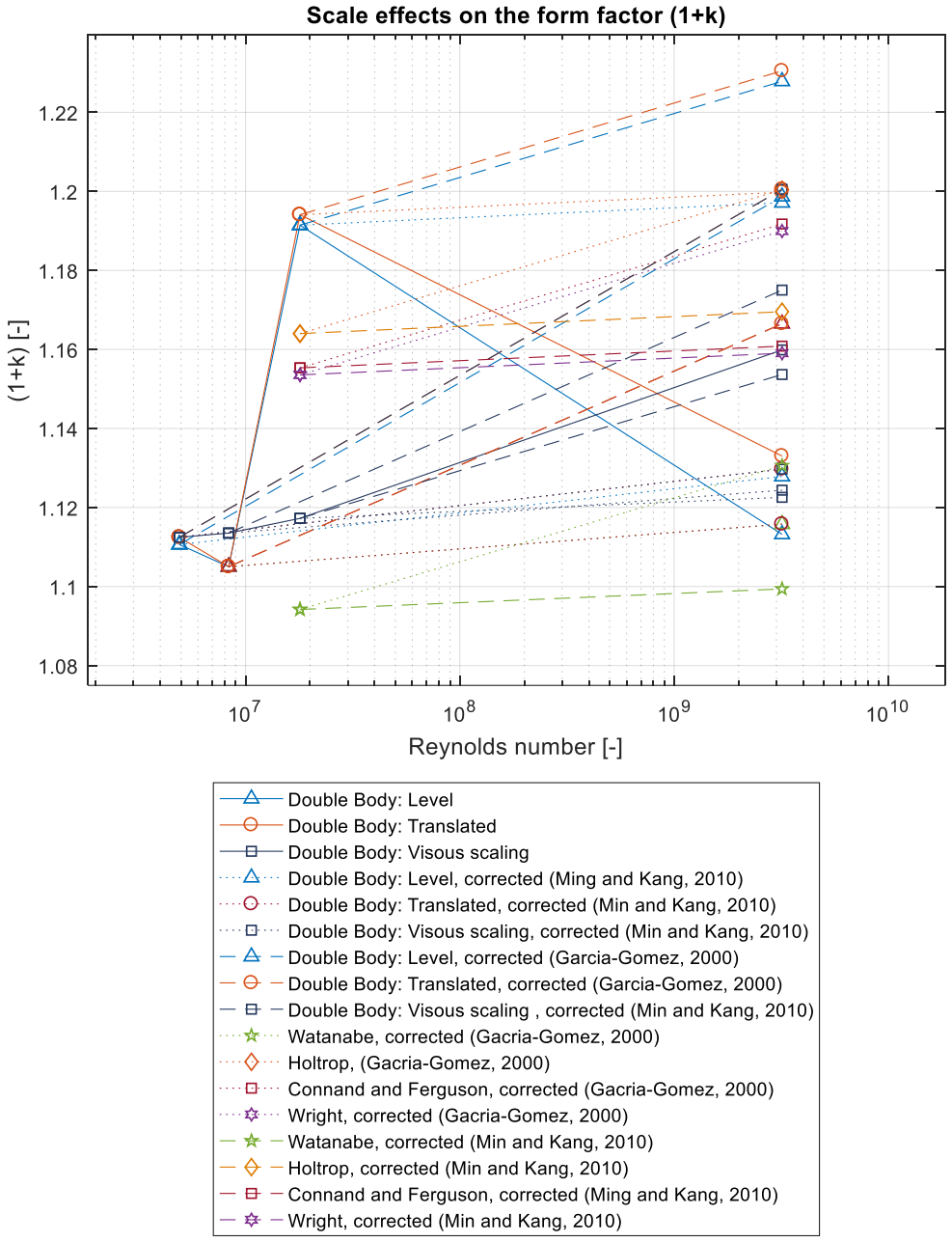

Figure 3.9. Calculated form factors

3.5.2.4 Extrapolation to full-scale

The presence of the scatter in values described previously implies there is a high degree of variability in the possible extrapolated value of the total resistance coefficient in full-scale. For example, two testing facilities using different scale factor to determine the wave resistance would find inconsistent C_T values. To illustrate this, Figure 3.10 was compiled using all combinations of wave resistance coefficients (CFD and slender body), form factors (CFD and empirical, with and without the corrections of Min and Kang (2010) and García-Gómez (2000)), yielding 126 unique predictions for each friction line. Clearly, it is not possible to show the corresponding category for each point. Instead, the average of each friction line, global average, and the multiphase CFD prediction for C_T are shown in Figure 3.10. Now, it is imperative to highlight the importance of reliable predictions for each component of the total resistance. For instance, although the Telfer (1927) line showed excellent predictions for the frictional resistance, its use may be questioned depending on the values chosen for the form factor and wave resistance. Of course, this is also the case for all other methods used. Figure 3.10 suggests a 'band' of possible values for each friction line exists. Therefore, a large degree of uncertainty can be expected depending on the adopted methodology to calculating each component of C_T.

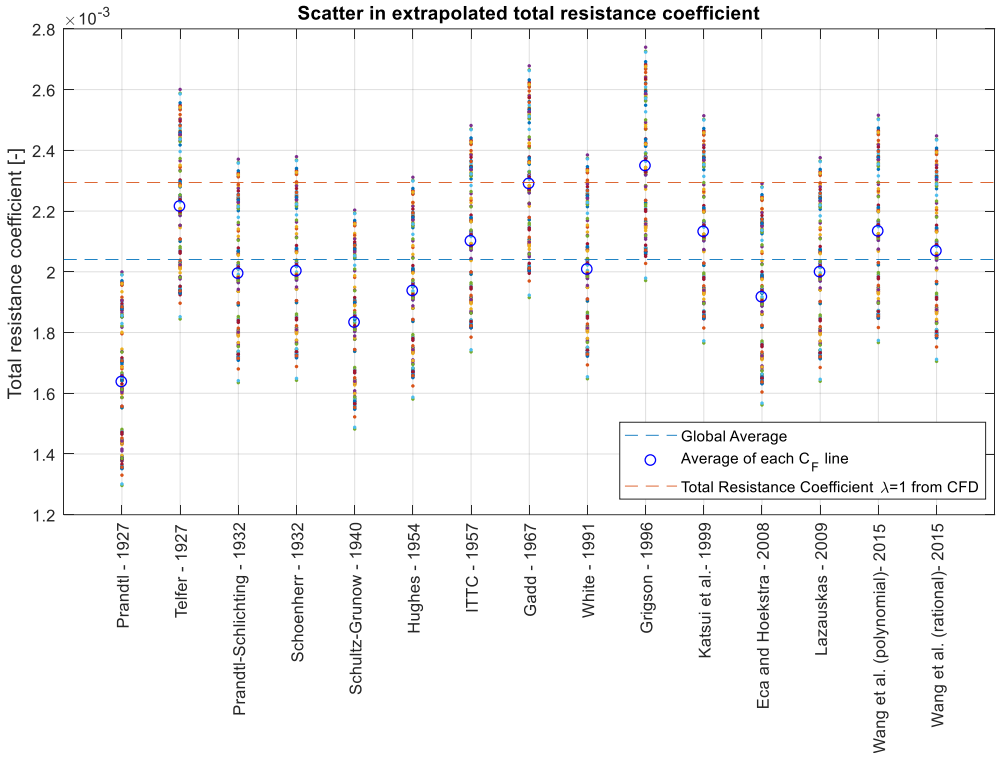

Figure 3.10. Extrapolated total resistance coefficient based on the results obtained in this chapter

The assertion that a small error in the total resistance coefficient is decomposed into even smaller errors over each constituent component worked advantageously earlier. However, if the process is reversed, the effect is magnified to yield a high degree of uncertainty. Thus, the importance of high-fidelity methods cannot be overstated. One possible problem is that virtually all of the available literature treats these problems (the evaluation of the total's constituent components) separately. For example, one may determine a method to calculate the exact frictional resistance for a specific Reynolds number. Indeed, the available methods perform very well, as shown in this chapter. However, if free surface effects are not accounted for in the extrapolation procedure from a Reynolds number in the region of 10^6, to one near 5×10^9, the results will not resemble reality. This would influence all parameters present in the decomposition of the total resistance coefficient and would likely be amplified when carried to full scale. An analogous argument can be made for the estimation of wave resistance, although there is uncertainty in its estimation due to the degree of complexity associated with ship wave making.

A more fundamental problem arises from the ambiguity resulting from the amplification of errors discussed above: it becomes difficult to justify

validating the estimation of each constituent component of the total resistance when calculated separately. Perhaps the best example in this context is the prediction of wave resistance by potential flow methods. These are typically validated by subtracting the viscous resistance $(1+k)C_F$ from the experimentally obtained total, for instance, Tuck and Lazauskas (2008). Now C_F is usually obtained via one of the friction lines in Figure 3.8 (typically the ITTC57 line), while $(1+k)$ – experimentally using the procedure stated in earlier. As demonstrated, both of these are susceptible to scale effects and therefore contain a certain amount of error when carried to full-scale. Consequently, the use of wave resistance estimations using potential flow methods in extrapolation procedures should be approached with caution, not least because they fail to model scale effects. Referring to validation versus experiments, the problem is not confined to the use of methods based on Michell's (1898) integral. Instead, wave cut methods (Janson and Spinney, 2004) and panel methods (Newman, 1992), both of which are deemed reliable and robust, must suffer from the above issue. To circumvent this obstacle, wave probes can be used during tank testing (Kim et al., 2001; Townsin, 1971, 1968; Troesch and Beck, 1974).

Alternatively, a recently emerging method is to capture high quality optical images of the free surface around the ship (Gomit et al., 2014). Applying this method, Caplier et al. (2016) estimated the energy contained in a ship's wake by using its spectrogram, defined as a heat map used to visualise the time-dependent height of the water surface in terms of a frequency spectrum (Pethiyagoda et al., 2018, 2017). Here, only half of the obstacle has been addressed. The remainder (scale effects) seems insurmountable with present methods, especially with the apparent scatter of C_W observed in Figure 3.5.

The use of CFD methods undoubtedly increases understanding of the underlying phenomena and their relative importance. However, there is still a fundamental source of uncertainty present in their use: the statistical modelling of turbulence, usually referred to as turbulence modelling. In this chapter it was shown that it is the most probable source of errors in sinkage and trim, whose effect cannot be neglected. One could argue along the lines of Moore (1965) with regards to the availability of computational power, and claim that Direct Numerical Simulation (DNS) will solve the problems in this respect if one allows sufficient time to increase the available computational power. However, even today, the use of DNS is limited to a narrow range of Reynolds numbers, which is far from sufficient even for model-scale

computations (Beck and Reed, 2001). Simultaneously, the field of wall function derivation is very active (Kiš and Herwig, 2012). Even if one chooses to accept the use of turbulence modelling, Pereira et al. (2017) found that different models are best suited for hull resistance prediction and propeller dynamics.

3.6 Summary and conclusion

In line with the research aims and objectives, this chapter focused on scale effects on ship bare hull resistance in unrestricted waters. Several hypotheses were tested using a commercially available RANS solver. Emphasis was placed on challenging the widely used assumption of geometric similarity in ship wave patterns with scale, and thus a scale invariant wave resistance, which was shown to be untrue, confirming the results of Raven et al. (2008). Scale effects on all examined parameters were shown to be magnified with large changes in the Reynolds number. This was accomplished by maintaining the Froude number constant throughout all adopted case-studies (Fr = 0.26).

It was demonstrated that the relative importance of free surface effects of frictional resistance decay rapidly with an increase in Reynolds number, but can substantially influence extrapolated results if not properly accounted for. Several sources for this have been identified, including boundary layer thickness and flow separation. These are also the likely cause of non-geometrically similar wave patterns observed.

An alternative path worth exploring is to perform all computations directly in full-scale. While the resources required to perform a full-scale computation seem to be limited, experience suggests that time improves computational availability. It could then be argued that it is only a matter of time before it becomes commonplace to routinely perform full-scale CFD simulations. One of the main issues academia must seek to resolve is that of turbulence modelling, which is a very active field of research where strides of progress are being made.

In performing numerical simulations, the intention was to maintain the highest possible degree of similarity with the real-life physics of the problem. However, incorporating propeller effects was omitted. The complex, non-uniform flow, generated by the presence of a rotating propeller is responsible for stark changes in the overall pressure and velocity fields near the ship's stern. While by ignoring such effects, representing the overall problem may have been deviated from, it is thought that isolating the bare hull resistance is a worthwhile endeavour. Indeed, to the best of the author's knowledge, the

work presented herein is the first to examine scale effects on the wave resistance and free surface effects on the frictional resistance using CFD.

4. APPLICATION OF EDDY-VISCOSITY TURBULENCE MODELS TO PROBLEMS IN SHIP HYDRODYNAMICS

This chapter examines different approaches to close the Reynolds averaged form of the Navier-Stokes equations. This is identified as the most widely used method to model flows in marine hydrodynamics. A comparative assessment is performed on two families of two-equation eddy viscosity turbulence models and a one-equation closure. The time per iteration characteristics of each model is also recorded to determine which model is most economical. A statistical approach is proposed to rank the turbulence closures.

4.1 Introduction

Since the beginning of the 19th century, the fields of science and engineering have been underpinned by the concept of determinism. Its principle was first articulated by Pierre-Simon Laplace (van Strien, 2014) to express the idea that every event is causally determined by previous occurrences. Therefore, if one possesses sufficient information about these causes, it is possible to predict the state of a system at any point in the future. This idea likely feels natural to engineers in particular.

Mathematically, determinism is merely an expression that a unique solution of the Navier-Stokes equations exists. In fact, this has been shown to be the case in two dimensions, but for three-dimensional cases it holds for finite times

only (Lesieur, 2008). In other words, it is not always possible to obtain sufficient knowledge of antecedent events in order to determine the exact state of the system at some future time. In practice, the engineer is rarely, if ever, interested in the level of detail referred to above. Hence, the use of statistical modelling of physical processes is justified as long as an accurate mean, or integral, value can be obtained.

The question then shifts from the ability to capture the physical interaction of every molecule of the fluid, to its overall properties, such as velocity and pressure. In other words, the fluid is treated as a continuum. The difficulty here is associated with the complexity of turbulent phenomena. Although these can be observed in everyday life, modelling exact statistical averages of fluctuations inherent in turbulence has proven impossible (Durbin and Pettersson Reif, 2011). Thus, every time the numerical solution to a problem involving turbulent properties is invoked, it contains a degree of empiricism. This empiricism is required due to the averaging process, whether temporally or spatially, applied to the Navier-Stokes equations. Upon performing what is known as Reynolds averaging, additional terms are introduced as a consequence of nonlinearities in the governing equations. Perhaps surprisingly, the degree of empiricism (the number of empirically defined coefficients, or lack thereof) is not always an indication of accuracy.

The addition of new unknowns to the governing equations means that the Reynolds Averaged Navier-Stokes (RANS) equations no longer form a closed set. In simple terms, there are now more unknowns than there are equations, which is why turbulence modelling is also referred to as providing closure. The additional (partial differential) equations introduced define the type of turbulence model. Hence, zero, one, or two-equation closures will be referred to. Now, the topic of investigation can safely be shifted to identifying which turbulence model is optimal for the particular case it is applied to. The optimal solution must exhibit several characteristics:

1. The solution must lie within some predefined measure of accuracy.
2. The effort required to obtain the solution must not be excessive.
3. There should be no simpler method to achieve the same, or reasonably similar result.
4. The method used should represent the underlying physical phenomena correctly.

In most cases, one can gain an idea of the expected level of accuracy depending on the method used. For example, it is well-known that linear potential flow theories do not perform well in extreme cases, where nonlinear phenomena dominate. However, the above (or any other) classification of turbulence models, cannot be used to establish such a hierarchy. Indeed, one-equation models can, and do perform better than two equation models in certain cases. This is true because the derivation of most of the currently available models are not rooted in the physics of the problem *per se* (Argyropoulos and Markatos, 2015). Simply put, some of the empirical constants contained within the turbulence models are determined by fitting data to simple experimental observations. There is no telling what their effect would be if they were applied to a different problem, as is often the case. Moreover, the mathematical formulation of the equations used to provide closure are rarely related to the physics of the problem either (Markatos, 1986).

This chapter is addressed to practitioners as well as researchers of RANS-based ship hydrodynamic analysis, with the goal of reducing some of the ambiguity inherent in the field. The aim is to analyse the issue of optimal turbulence model selection as applied to problems pertaining to the realm of ship hydrodynamics. Complex problems in the field are sought to test the turbulence models robustly. To elaborate, it would be counterproductive to select a simple, two-dimensional case since the aim is not to improve on the selected models. The parameters of interest are ship bare hull resistance, sinkage, and trim, due to the difficulties associated in with their prediction. Furthermore, Larsson et al., (2014) reported a scatter in sinkage and trim results when examining submissions to the Gothenburg numerical ship hydrodynamics workshop, justifying the above selections. Deliberately accentuating the effect each of these has on the remaining parameters as well as their overall importance implies the selection of a shallow water case study.

In shallow water, the sinkage, trim, and resistance are influenced by the adverse pressure gradient acting longitudinally on the hull, generated as a result of the hull's proximity with the seabed. Additionally, in terms of turbulence, pressure gradients present an extra layer of complexity, superimposed of the already difficult problems of predicting highly three-dimensional boundary layers inherent in ship underwater shapes. The hull form selected is the benchmark KCS container ship, while the analysis is performed using Star-CCM+, version 13.01.011.

The remainder of this chapter will continue with an overview and identification of selected turbulence models. Then, the case studies and numerical implementation are presented in Section 4.3 and 4.4, respectively. Results and their analysis follows form these in Section 4.5, while a summary and conclusions are given in Section 4.6.

4.2 Background

This chapter is motivated partially by the findings of Larsson et al., (2014), who observed a scatter in sinkage and trim predictions, as mentioned previously, and partially by recent work undertaken within Chapter 3. Sinkage and trim proved more difficult to simulate accurately than resistance in CFD (Terziev et al., 2019a). In deep waters, the combined effect of sinkage and trim is known to be small on resistance and in some cases may even be neglected (Ponkratov, 2016). However, their magnitude and influence are accentuated by the proximity of the seabed in shallow water cases. This not only represents a case where the underlying physics are not well understood, but also, an everyday situation all ships must cope with. More importantly, groundings, where the combined effect of sinkage and trim (termed ship squat) play a central role, are consistently in the top five incident categories of EMSA (European Maritime Safety Agency, 2018, 2017, 2016, 2015) since records began in 2011. In fact, the annual figures published by EMSA suggest more than half of all incidents occur in shallow water, where ship squat is always a contributing factor. Thus, the accurate prediction of ship squat is of critical importance.

While ship squat is a phenomenon requiring further research, turbulence modelling is a 'known unknown', which contributes to the present levels of ambiguity inherent in shallow water predictions. Greater levels of attention are typically attributed to the prediction of resistance. However, there is less ambiguity in its predictions. This has led to rule of thumb approaches even in CFD by international bodies, such as the International Towing Tank Conference (ITTC, 2014). On the other hand, sinkage and trim have proved more evasive. The results from the present research will enable generalisations to be carried into deep water cases for enhanced predictions, even when running trim and sinkage are of little importance. The remainder of this section will proceed by examining the turbulence models.

4.2.1 Turbulence

Attempts to bring turbulence under mathematical scrutiny begin with Boussinesq's concept of eddy-viscosity (Wilcox, 2006), which he developed from ideas expressed by Saint-Venant (Darrigol, 2017). This makes it possible to express the Reynolds stress tensor, which is the additional term introduced in the process of Reynolds averaging, as a function of mean flow properties (such as the eddy-viscosity). Here, Reynolds averaging refers to the process of averaging the decomposed total velocity (mean and fluctuating parts) (Durbin and Pettersson Reif, 2011). The eddy-viscosity is a property of the flow, i.e. a function of space and time, unlike the molecular viscosity, which is an intrinsic physical constant (Bailly and Comte-Bellot, 2004).

The first turbulence model was introduced by Prandtl (1925) using the mixing length concept to compute the eddy-viscosity. This model did not contain any Partial Differential Equations (PDEs), and is therefore known as zero-equation or algebraic. In practice, an n-equation model refers to the number of additional PDEs introduced to close the Reynolds Averaged Navier-Stokes (RANS) equations (Wilcox, 2006). Twenty years passed before the next conceptual leap was made by Prandtl, when he modelled a PDE to express the turbulent kinetic energy, k, thereby creating the first one-equation turbulence model. Fundamentally, this allowed the local flow properties to be dependent on antecedent events. Then, van Driest (1956) devised a viscous damping modification to the mixing length model, which has been applied to virtually all algebraic closures since (Wilcox, 2006). A noteworthy example of a zero-equation model includes that devised by Baldwin and Lomax (1978).

Since the first one-equation model was born, an explosion of competing turbulence closures has occurred. Here, prevalence is given to those, used in the assessment. Thus, attention will be confined to the main eddy-viscosity models and their significant variants as implemented in the commercial RANS solver, Star-CCM+, version 13.01.011. The fundamental purpose of this class of closures is to predict an eddy-viscosity. Since this was first introduced by Boussinesq, it has since become the underlying hypothesis used to derive the vast majority of turbulence models.

Although the Reynolds Stress turbulence (RST) model boasts as the most physically sound closure strategy (Sarkar and Lakshmanan, 1991), there are problems related to computational stability in its implementation (Parneix et al., 1998). Furthermore, for the present class of problems (ship

hydrodynamics), eddy-viscosity models dominate the literature, despite the fact that Rotta (1951) derived the first RST model decades prior to the first practical application of eddy-viscosity-type models. The prevalence of eddy-viscosity models in the field is illustrated at the end of this section.

Broadly speaking, the problem of closure is solved via two main classes of turbulence models. These are the *k-ε, k-ω* models and their variants. Here, k is the turbulent kinetic energy, ε is the dissipation rate, and ω is the dissipation frequency. Before each class is examined sequentially, a qualitative description of a one equation turbulence model is given. It should be noted that the underlying mathematical relations, expressing all turbulence models utilised in this thesis can be found in Appendix C.

4.2.1.1 One equation Spalart-Allmaras turbulence closure

A popular alternative to two-equation turbulence models is presented in one-equation closures. The most successful of these is the formulation proposed by Spalart and Allmaras (1992). Breaking precedent, this closure uses a diffusivity equation in place of the turbulent kinetic energy to establish an eddy-viscosity. All prior work on models of this type had used the turbulent kinetic energy instead (Baldwin and Timothy, 1990; Johnson and King, 1984). The original formulation presented in Spalart and Allmaras (1992) was specifically designed for unstructured codes. Due to its ability to model separated flows and its popularity in the field of aerodynamics (Siemens, 2018), this model is incorporated.

4.2.1.2 The k-ε model and its variants

The *k-ε* model's foundations were laid by Jones and Launder (1972). It is interesting to note that it the *k-ε* model does not owe its popularity to robustness or accuracy, but to the fact that it was the first two equation model applied in practice (Durbin and Pettersson Reif, 2011). That is, even though Kolmogorov's (1942) *k-ω* model had been described decades earlier. In Star-CCM+, the original coefficients proposed have been replaced with those suggested by Launder and Sharma (1974) in the case of the standard formulation. However, the standard *k-ε* model cannot be applied on low Reynolds number (LRN) type cases due to the occurrence of a singularity near solid boundaries. Here, low Reynolds number refers to turbulent Re_T, which is a function of wall distance ($Re_T = \sqrt{k}d/v$, where k is the turbulent kinetic energy, d is the distance from the wall to the nearest cell, and v is the viscosity,

as opposed to $Re = UL/v$, where U is the speed, and L represents the length of the ship). Thus, when $y^+ \sim 1$, models capable of coping with LRN must be used. On the other hand, if $y^+ > 30$, high Reynolds number (HRN) models are required.

Jones and Launder (1972) originally formulated the k-ε model for HRN-type cases. However, in such a scenario, the use of wall functions is required, which are not compatible with complex flows (Pettersson Reif et al., 2009). Therefore, researchers use either a LRN or realizable versions, discussed below. According to Durbin (1996), two equation turbulence models have a tendency to overpredict turbulent kinetic energy in stagnation points. Realizability refers to the imposition of a suitable constraint to the model to alleviate this shortcoming. Additionally, Star-CCM+ offers the two-layer method, where a PDE is solved for k near the wall, but ε is algebraically prescribed based on the wall distance (Chen and Patel, 1988). The wall proximity indicator is then used to patch the two solutions onto each other, as suggested by Jongen (1998). On the other hand, the length scale and turbulent viscosity ratio, used to calculate ε, are adopted from Wolfshtein (1969) in the two layer approach.

The realizable, two layer k-ε model, hereafter referred to as "*k-ε 2l*" for brevity, has been extensively used for practical applications (Cakici et al., 2017; Liu et al., 2018; Ozdemir et al., 2016; Song et al., 2019; Terziev et al., 2018; Tezdogan et al., 2016a, 2016b, to name but a few), making it an ideal candidate for this chapter's purposes. However, there are a large number of variants of the k-ε model put forth by researchers, each claiming superiority. The motivation behind the plethora of alternatives lies with the shortcomings on the model. While its inability to model near-wall effects in the original form can be circumvented easily, the implicitly assumed linear stress-strain relationship poses further problems: linearity may be violated in strongly 3D boundary layers (Durbin and Pettersson Reif, 2011). This is certainly the case for ship boundary layers, as asserted by Magionesi and Di Mascio, (2016). Despite these shortcomings, the *k-ε 2l* has enjoyed considerable success and widespread implementation for industrial applications. It is therefore interesting to compare the performance of some k-ε variants available in Star-CCM+. Alternatives include proposals by Shih et al. (1995), which cannot be incorporated since it is not offered by the RANS solver.

Abe et al. (1994) proposed a modification of the standard k-ε model, henceforth referred to as 'AKN' (after the authors of the paper – Abe, Kondoh, Nagano), claiming their variant can predict flow reattachment better than the original.

As such, their model is of the LRN-type. The authors also altered the coefficients of the original model in their derivation. According to Siemens (2018), the AKN model is a suitable choice for flows over complex geometries, which is undoubtedly representative of a ship underwater shape. For these reasons, this model is selected for the present examination. Additionally, flow reattachment following separation is a crucially important parameter in the prediction of ship resistance, trim and sinkage.

A widely discussed closure in turbulence research is the k-ε-v^2-f model, hereafter referred to as 'v^2-f' (Durbin, 2017a), where v^2 is the wall-normal stress component and f is the elliptic relaxation parameter. This model solves two additional equations in order to predict the eddy-viscosity. Its origins can be traced to work done by Durbin (1996, 1995, 1993, 1991), whereas some recent extensions and modifications include Pettersson Reif et al. (2009), Pettersson Reif, (2006), Laurence et al. (2004), Davidson et al. (2003), and Lien et al. (1998). While this model cannot be classified as a two-equation model for obvious reasons, it retains its larger classification (eddy-viscosity-type model). The benefits of utilising the v^2-f model include its ability to handle wall effects, simultaneously accounting for flow nonlocality. Thus, it can be applied directly to LRN-type meshes, without any modifications, or the need to patch regions of different solutions as was the case earlier. Siemens (2018) stated that selecting this model "is known to capture the near-wall turbulence effects more accurately, which is crucial for the accurate prediction of heat transfer, skin friction and flow separation." Thus, it is included in the investigation within the k-ε-class models. The fundamental advantage in implementing the v^2-f model is related to its ability to account for anisotropy of turbulence stresses, which are not addressed in the variants examined so far (Gorji et al., 2014).

The final two models incorporated within the present category are elliptic blending closures, henceforth referred to as '*EB*'. Both of the variants integrated in this chapter solve for the turbulent kinetic energy, the dissipation rate, the normalised reduced wall-normal component, and the elliptic blending factor (α, rather than f). This is thought to be beneficial due to its inclusion of nonlocal, and pressure echo effects. The latter, observed near impermeable boundaries, are solved for via the method of images. The wall-normal component is defined as the ratio of v^2 and k, and therefore requires the solution of v^2 in a similar manner to the v^2-f model. The concept of elliptic relaxation was first introduced for the RST-class models by Durbin (1993b). As

such, it mandated the solution of six equations to provide closure, which was later simplified to a single equation (α). Later, Manceau and Hanjalić (2002) further simplified the *EB* model rendering it more industry friendly, which is the form utilised by Star-CCM+. The elliptic blending model's conception can be traced to being a consequence of the development of the v^2-f model.

Up to this point, linear eddy-viscosity models have been the focus. Although, the v^2-f has been extended to incorporate nonlinearities, Pettersson Reif (2006) found its linear variant to perform equally well, which is the version employed here. On the other hand, non-linear eddy-viscosity models, specifically of the elliptic blending-type have recently emerged and gained popularity. The main contributors to their development other than Manceau and Hanjalić (2002) include Manceau (2015) and Manceau et al. (2001), however, the conceptual origins of 2nd order closures can be traced to Chou (1945). In the present work, the standard and lag *EB* (referred to as '*Lag-EB*') are adopted. The former, according to Billard and Laurence (2012), circumvents the k-ε *2l* models near-wall issues, while it exhibits stable performance for practical applications.

The alterative, the *Lag-EB* model of Revell et al. (2005), was devised to address a fundamental shortcoming of almost all eddy-viscosity models. Namely, their imposition of a linear relationship between the stress tensor and rate-of-strain tensor, which follows directly from the Boussinesq hypothesis. Revell et al. (2005) implemented a phase lag, or angle between these two parameters to express their misalignment. In Star-CCM+, the implementation of *Lag-EB* follows the modifications suggested by Billard and Laurence (2012) for stability reasons (Siemens, 2018).

This marks the end of the description of the five k-ε variants used. The next class of turbulence models replace the dissipation rate, ε, with ω – the dissipation frequency.

4.2.1.3 The k-ω model and its variants

The second most widely used strategy to close the governing equations involves the adoption of a k-ω type turbulence model. Here, only a brief overview of the variants used is given. Wilcox (2006) can be consulted for a comprehensive overview of the subject. It is worth noting that without having prior knowledge of the Kolmogorov (1942) k-ω model, Saffman (1970) formulated a k-ω model to close the RANS equations. The latter was applicable down to the wall, immediately showing distinct advantages over the k-ε model.

The modern version of the *k-ω* variant, here referred to as the standard '*k-ω Wilcox*' model, can be traced to Wilcox (1988), although earlier work provided its basis (Saffman and Wilcox, 1974), it was later revised several times by the same author. Most notably, by Wilcox (2008, 2006), the most recent of which is incorporated in Star-CCM+. Siemens (2018) advise that the model coefficients of Wilcox (2008) have not been extensively verified for flows, other than two-dimensional parabolic cases. Therefore, these corrections are included as an optional add-on. Since the objective of the present work is to test well-established closures, these have not been made use of.

The *k-ω Wilcox* model has faced primarily the criticism of free-stream sensitivity (Cazalbou et al., 1994). This refers to the fact that turbulent statistics must vanish at some distance from an impermeable wall. In the free-stream, their influence on the irrotational region (the region not affected by viscosity) is thought to decay as $(y^+)^{-4}$ (Phillips, 1955) which is not always the case when employing the *k-ω* closure. This problem was addressed by Wilcox (2008) and is thought to have been resolved in the latest version of his model. Menter (1994) transformed the transport of ε from the *k-ε* model to resolve the free-stream sensitivity by a variable substitution in the *k-ω Wilcox* model. The formulation Menter (1994) arrived at is similar to the standard *k-ω Wilcox* model, but contains an additional term expressing the cross-diffusion of *k* and ω.

In other words, the form derived by Menter (1994), referred to as the '*k-ω SST* model' (where SST stands for Shear Stress Transport), could potentially provide identical results to the *k-ε* model. By incorporating a blending parameter, expressed as a function of wall distance, the *k-ω SST* model is thought to preserve the advantages inherited by both main closures used today (*k-ε* and *k-ω*). This is also one of the models gaining popularity in the field of ship hydrodynamics (Deng et al., 2015; Farkas et al., 2018; Haase et al., 2016b; van Wijngaarden, 2005; Wang et al., 2018; Wnęk et al., 2018). As such, it is important that it is incorporated it within the set of case studies.

The final aspect of turbulence research considered in this sub-section is associated with the concept of transition. This term is used to describe the change of a boundary layer from laminar to turbulent (Saric et al., 2002). This change is of practical importance because a turbulent boundary layer imparts a greater skin friction to the surface from which it is shed, than when in laminar state. Thus, the onset of turbulence, and its possible delay, is of great importance, especially considering that skin friction is one of the main

contributing components of ship resistance. According to Durbin (2017b), the primary modes in which transition occurs are:

1. Natural
2. Bypass (as a response to external disturbances)
3. Separation-induced

Transition models are required because most turbulence closures are by definition applicable to the fully turbulent part of a flow (HRN-type models). A related example is the difference and range of applicability of the Blasius (1908) and any other friction lines, for instance, the well-known Schoenherr (1932) line. The *AKN* model and the standard k-ε model, for example, contain empirical damping functions, which allow them to exhibit transition properties. However, this is a consequence of solution bifurcation, resulting from the use of damping functions rather than physical insight into the phenomenology of the process itself (Lesieur, 2008). Their use has also been widely criticised (Patel et al., 1984), in part because the only similarity between different empirical damping functions is the presence of exponentials in their derivation (Durbin, 1991; Shih, 1990). Some notable examples include Chien (2008) and Launder and Sharma (1974), to name but a few.

The RANS solver employed, Star-CCM+, offers a variety of methods of modelling transition. The first, and arguably more difficult to implement (the turbulence suppression model) requires prior knowledge of the location of transition. Thus, it is not applicable in many cases. An alternative solution was provided by Abu-Ghannam and Shaw (1980), which is based on the concept of intermittency. This parameter can range from 0 to 1, describing the time the flow is in a turbulent state (in percentage values). The reason this is not implemented is related to its requirement of nonlocal quantities, which cannot be evaluated at cell centres. A local alternative was suggested by Langtry (2006). Since the formulation was originally incomplete, its adaptation in Star-CCM+ requires user programming and definition of additional functions. Recognising that it is highly unlikely for the average user to accomplish this, the simpler 'γ' transition model has been opted for. Selecting the γ transition model activates the solution of an additional intermittency equation (γ) and couples its solution with the k-ω *SST* model via the kinetic energy – k (Menter et al., 2015). Non-local effects are handled via an approximation of the three-dimensionality of boundary layer by using the concept of helicity, which is a measure of the cross-flow within a turbulent boundary layer (Müller and Herbst, 2014).

4.2.1.4 Potential alternatives

As has been illustrated thus far, research and development of turbulence models has been rather chaotic, featuring small steps and large conceptual leaps. For instance, while elliptic blending-type models are thought to be superior, the development of one, and two-equation closures has continued since the former's inception. One way to characterise the field would be via additions of small theoretically and empirically acquired pieces of information to existing models. Indeed, this sort of 'tinkering' is a defining feature of the field of turbulence research (Roache, 2016).

Initially, model constants were calibrated against experiments. When Direct Numerical Simulation (DNS) data became available, the validation procedure shifted. Nowadays, the aim is to match DNS data instead of experiments. Regardless, due to the complexity and limitations of the DNS approach, the possible benchmarks are limited to simple two, or three-dimensional cases at best (a classical example is the backward facing step (Darrigol and Turner, 2006)). Thus, the coefficients selected for each model have been calibrated to perform best for these specific cases. It is therefore not possible to determine the precision, accuracy, or even tendency to over or underpredict values of any one turbulence model when applied elsewhere. The matter is worsened by the previously illustrated fact that all turbulence models contain a large degree of empiricism (arrived at by a process of tinkering), compounded by the simple truth that the mathematical formulations used do not represent real, physical processes.

The degree of empiricism is a reflection of the complexity of the processes occurring in turbulent flows. If analytical solutions were possible, turbulence models would be exact, and empirical coefficients would not be required (Durbin and Pettersson Reif, 2011). Contrary to expectation, empiricism is not necessarily a drawback. The problem addressed here is the inability to establish a hierarchy in the modelling of turbulence in any meaningful way other than complexity. For this reason, research of the type of Gorji et al. (2014), and El-Behery and Hamed (2011) have emerged attempting to provide specific recommendations with regards to the use of different turbulence closures in a particular context.

Turbulence models described thus far model statistically almost the entirety of the turbulent kinetic energy spectrum. This expresses a concept similar to wave spectra (St Denis and Pierson, 1953), where components of different

wavelength coexist simultaneously (turbulent eddies replacing waves in the present context). Richardson (1922) and Kolmogorov (1941) are chiefly attributed with the conceptualisation of the turbulent energy spectrum and its cascade into smaller scales. It is this cascading process that gives rise to nonlinear interactions, and thus inhibits its description. Researchers have devised a way to statistically model part of the spectrum via the turbulence models described above, leaving the remainder to be captured in the simulation. This is known as Large (or Very Large) Eddy Simulation (LES or VLES, alternatively, Detached Eddy Simulation - DES). Alongside the twofold increase of the order of magnitude in computational power requirements, Kornev et al. (2019) reported several difficulties when applying the LES technique to ship hydrodynamics problems. The main issue was related to the region used to patch the statistically averaged and resolved solution together. In light of this, the adoption of LES will not be considered. Studies, detailing the use of hybrid RANS-LES techniques in marine hydrodynamics include the work of Bhushan et al. (2013), Carrica et al. (2010), Posa et al. (2019), and can be consulted for further information.

Before the case study description is given, it is worth examining which turbulence models tend to be preferred in marine hydrodynamics. Here, the term 'marine hydrodynamics' is used in reference to research encompassing all aspects of ship and offshore research that includes the simulation of fluid flow using a RANS solver. Additionally, investigations centred on propeller performance are incorporated.

The compiled dataset presents a sample of research work done during the past two decades using RANS solvers in the related field. The sample, collected from two of the biggest academic publishers (*ScienceDirect*, and *Taylor and Francis*), is split into categories corresponding to the turbulence model used in each work. No differentiation is made between different subtypes of models (e.g. realizable vs standard k-ε). Figure 4.1 presents the breakdown of the turbulence models among the same categories and provides a graphical representation of their cumulative use over the past roughly two decades. The results shown in Figure 4.1 demonstrate that the k-ω *SST* model has gained increasing popularity in the past decade, and that virtually all work done is concentrated in two categories. The purpose of this chapter will then serve to introduce some of the newer turbulence models (v^2-f, *EB*, and *Lag-EB*) to the field of marine hydrodynamics.

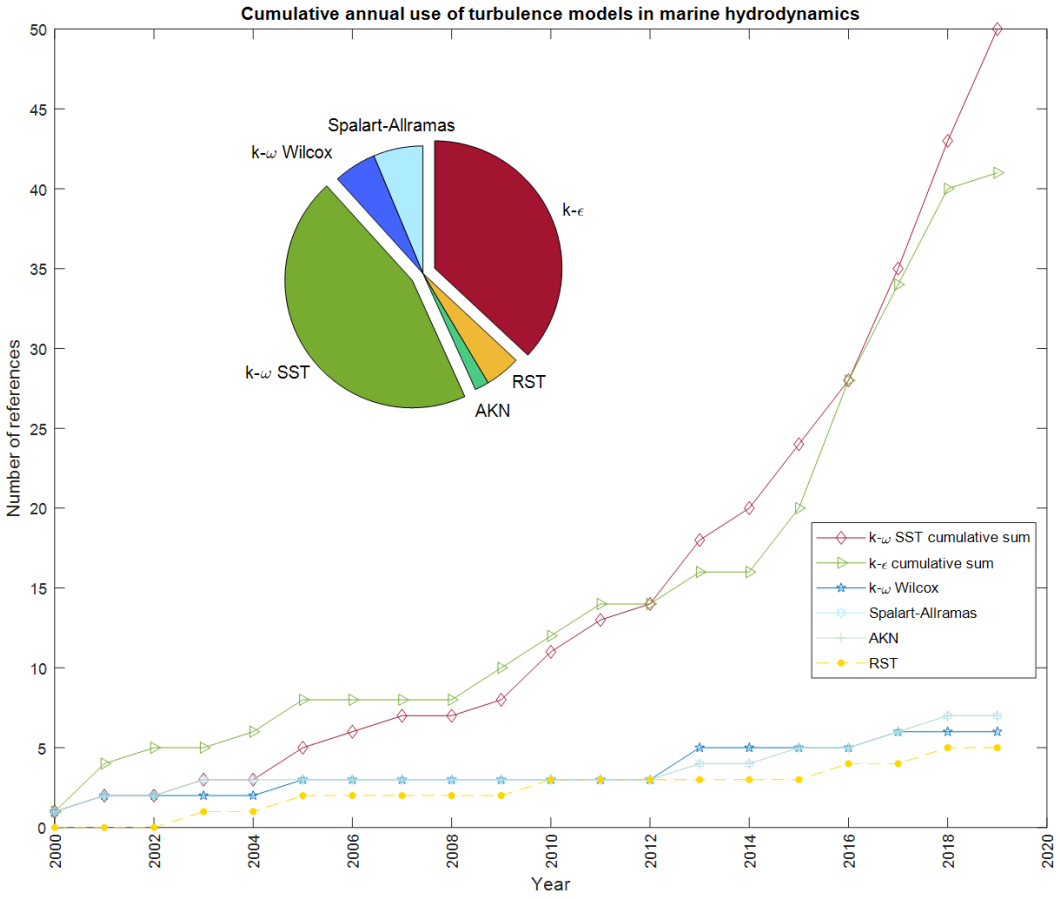

Figure 4.1. Graphical representation of the use of turbulence models in marine hydrodynamics[2].

4.3 Case-studies

An integral part of testing the performance of any turbulence model or numerical set-up involves comparing results against experimental data. Having established shallow water ship hydrodynamics will be focused upon due to the innate complexity of the field, restricts the choices available. In a recent study by Elsherbiny et al. (2019), the behaviour and performance of the well-known benchmark KCS container ship were tested. Although focus was placed on the new Suez Canal in the abovementioned work, a rectangular canal case study was investigated as well, and is adopted here. Doing so will allow the reduction in cell numbers because simulating the thin layer of water near the intersection of the sloping seabed and sides (as was the case in Tezdogan et al. (2016b)) is bypassed. Thus, the computational mesh can be refined in the vicinity of the ship, and gradually coarsened in every direction

[2] The full list of references used to construct Figure 4.1 can be found in Appendix B

without compromising the solution. Indeed, doing so is a mainstay in the practice of computational hydrodynamics.

The case-studies examined by Elsherbiny et al. (2019) allow us to vary the speed of the ship and test the turbulence models while keeping all other parameters constant. However, one could argue that in shallow water ship hydrodynamics, a change in the depth can have an effect, comparable to the change in speed. Limiting the case-studies in such a way would prevent the results from being generalised to a wider pool of problems in the field. For this reason, two case studies adopted from Mucha and el Moctar (2014) are also replicated numerically. In their work, the authors used the same ship as in Elsherbiny et al. (2019), with a different draught (T=10m, rather than T=10.8m full-scale equivalent) and scale factor (λ=40, rather than λ=75 in Elsherbiny et al. (2019)). For the purposes of the present research, two ratios of depth and draught have been selected for a single ship speed. This translates into a different Depth Froude number (F_h=$U/\sqrt{g \times h}$, where U is the speed, g is the gravitational acceleration and h is the depth), although the speed has been maintained constant. In shallow water, waves are nondispersive and can attain a single propagation speed defined by the denominator of the depth Froude number.

The KCS principal characteristics are summarised in Table 4.1, while the case studies are graphically depicted in Figure 4.2. The conditions, against which the turbulence models are assessed are given in Table 4.2. All nine turbulence models are tested against each of the four case studies delineated jointly in Table 4.1 and Table 4.2, yielding a total of 36 simulations.

Table 4.1. Principal characteristics of the KCS

Quantity	Elsherbiny et al. (2019)		Mucha and el Moctar (2014)	
	Full-scale	Model-scale (1:75)	Full-scale	Model-scale (1:40)
L [m]	230	3.067	230	5.75
B [m]	32.2	0.429	32.2	0.805
T [m]	10.8	0.144	10	0.25
C_B [-]	0.651	0.651	0.64	0.64
S [m^2]	9530	1.694	8992	5.62

Table 4.2. Case-studies description

ID	Reference	λ	h/T	h [m]	F_h [-]	Re [-]	U_{model} [m/s]	U_{ship} [kn]
1	Elsherbiny et al. (2019)	75	2.2	0.32	0.303	1.8297×10^6	0.534	9.0
2					0.57	3.4759×10^6	1.005	16.9
3	Mucha and el Moctar (2014)	40	1.3	0.325	0.37	4.7116×10^6	0.73	8.1
4			1.6	0.4	0.41	4.7116×10^6		8.1

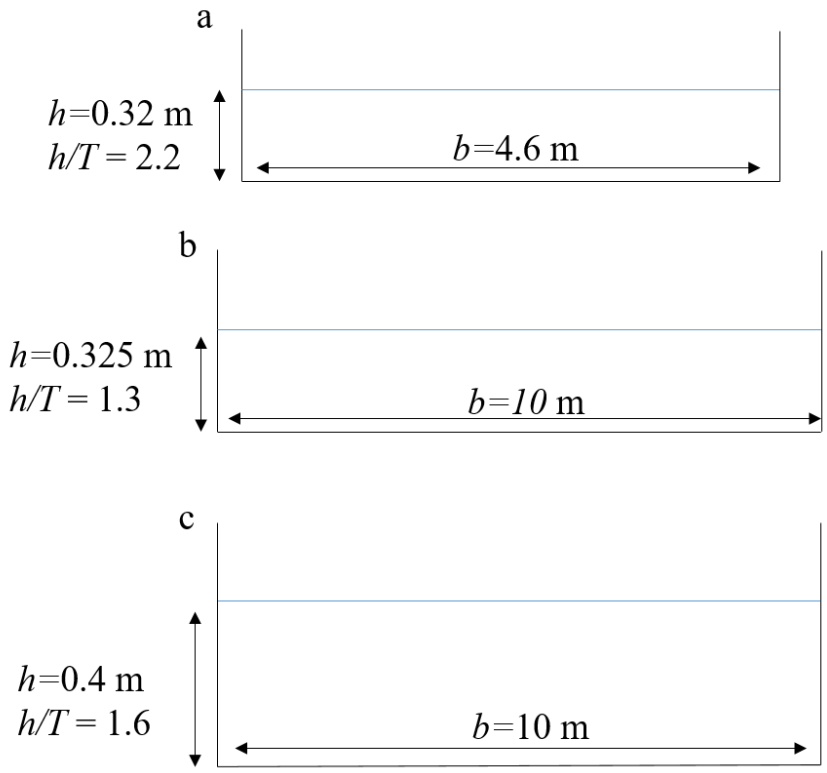

Figure 4.2. Graphical depiction of the adopted case-studies (not drawn to scale): (a) refers to the study of Elsherbiny et al. (2019), (b) and (c) refer to Mucha and el Moctar (2014).

4.4 Numerical implementation

The RANS solver used, Star-CCM+, employs the Finite Volume Method (FVM) to model the problem at hand by using the integral form of the governing equations and by discretising the computational domain into a finite number

of adjoining cells. Within the framework of Star-CCM+, pressure and continuity are linked via a predictor-corrector scheme.

To simulate turbulent properties within the fluid, the closures described in Section 4.2.1 are applied. These are summarised in Table 4.3, where Roman numerals are used to assign each case with a number.

Table 4.3. Summary of the tested turbulence models.

ID	Class	Identifier
I	*k-ε*	*AKN*
II		v^2*- f*
III		*EB*
IV		*Lag-EB*
V		*k-ε 2l*
VI	*k-ω*	*k-ω γ*
VII		*k-ω SST*
VIII		*k-ω Wilcox*
IX	One-equation	*Spalart-Allmaras*

4.4.1 Physics modelling

The motion of the fluid is modelled via a flat wave by the Volume of fluid (VOF) method (Hirt and Nichols, 1981). Alternatives include the Level-Set method. However, Starke et al. (2017) showed that some features of the bow wave generated by the ship could not be captured using the Level-Set method. In some deep-water cases, the presence of the free surface may be omitted. However, in shallow water flows, the energy imparted onto the waves due to the disturbance caused by the ship has a higher relative importance than in deep waters. Thus, it is not admissible to neglect the presence of the water surface. A third approach was proposed by Carrica et al. (2007), where a single phase level set method is introduced. This eliminated the need to account for the air-filled part of the domain, reducing cell numbers. Unfortunately, it has not been incorporated within the solver used. Therefore, it cannot be applied for the here-examined conditions.

The phase interface is captured by the RANS solver by assigning a scalar value between 0 and 1 to every cell in the domain. A value of 1 implies the cell is filled with water, conversely, 0 means the cell is in the air-filled part of the domain. A value of 0.5 indicates a cell is half full of air and water, thereby defining the location of the free surface. The adoption of the VOF method

requires that both immiscible fluids account for large parts of the domain, while their contact area should be relatively small (Siemens, 2018). To prevent reflections from the outlet, a VOF damping zone, equal to 1.25L is implemented in all cases.

A critical feature of the simulation is the type of convection scheme, which was selected as second order upwind. This choice is made because reducing the order (to 1st order) compromises the accuracy, whereas increasing the order (to 3rd order) can potentially lead to problems related to stability (Siemens, 2018). This is applied to all turbulence models in all case-studies. The segregated flow solver is used solve the Navier-Stokes equations in an uncoupled manner with the aid of a SIMPLE (Semi-Implicit Method for Pressure Linked Equations) algorithm.

To model the motions of the ship, the Dynamic Fluid-Body Interaction (DFBI) module offered by Star-CCM+ is used. The ship is allowed to sink and trim only, which occur as a result of pressure (normal) and shear (tangential) forces acting on the hull. To avoid a large initial shock, resulting when the simulation is initiated, the ship is constrained during the first 5 seconds in all simulations. Implementing this constraint on the motions of the ship reduces the transient oscillatory motion typically observed in the early stages of the simulation. Since the type of problem is pseudo-steady, it is desirable to reduce the time taken to achieve a steady state. The time taken for the solver to complete a single iteration is also reduced during these first 5 seconds, since an update to the position of the ship is not required at the end of the inner loop, which is set to comprise of 10 iterations. It is important to note that the free surface is updated at every iteration, while sinkage, trim, and resistance are recorded and updated once the inner iterations loop has competed.

4.4.2 Time step selection

At the end of the inner loop of iterations, the time step must be updated. This is selected in all cases as $\Delta t = 0.0035L/U$, following Terziev et al., (2018), and Tezdogan et al. (2016b), where the efficacy of this method of setting Δt has been demonstrated. This value is calculated for each case study, but is not changed across turbulence models. An advantage of using this method of setting the time step is that a change in the mesh is not necessary when the speed is altered. Thus, for the four case-studies, only 3 meshes are required. Cases 1 and 2 can be used with the same computational mesh (whose properties are examined in the following sub-section), while the time step is

altered according to the formula above. Case study 4 requires a slight increase in cell numbers due to the different depth, when compared to case 3 (see section 4.4.4, Table 4.4). All other characteristics, including the time step for cases 3 and 4 is the same because the speed is not changed. Alternative approaches to setting the time step include the ITTC's (2011) Δt=0.005 ~ 0.01L/U. Throughout all examined cases, the temporal discretisation is set as first order, and the solution is allowed to develop for a minimum of 150 seconds of physical time to ensure convergence of the results.

4.4.3 Computational domain

The computational domain has been structured according to the recommendations of ITTC (2011) and Siemens (2018). Namely, the inlet boundary in resistance computations should be located between one and two ship lengths from the ship bow, while the outlet – between two and three ship lengths downstream. The velocity inlet is placed 1.5 ship lengths upstream from the forward perpendicular, while the pressure outlet – 2.5 ship lengths downstream from the aft perpendicular. The domain width and depth are dictated by the case studies, which are summarised in Table 4.2. The side boundary is set as a wall, while the domain bottom is a velocity inlet. The latter choice is made because the cells in the domain are linked to the ship's centre of gravity (CoG), which is set as the origin of the local coordinate system. As the CoG translates and rotates, some cells cross the domain bottom. To ensure that the same amount of water flows past the ship, the domain bottom is allowed to introduce the lost amount of water back into the domain. This is done adding the same VOF flat wave speed to the domain bottom in the negative x – direction. In other words, the bottom acts as a reflective boundary, without developing a boundary layer as a result of the relative motion between it and the fluid, while simultaneously ensuring the h/T condition is maintained.

To alleviate the computational cost, a symmetry boundary is imposed, coincident with the ship and canal centreline. Finally, the domain top is located 1.25 ship lengths from the undisturbed water level, where a velocity inlet condition is imposed. The domain is graphically shown in Figure 4.3.

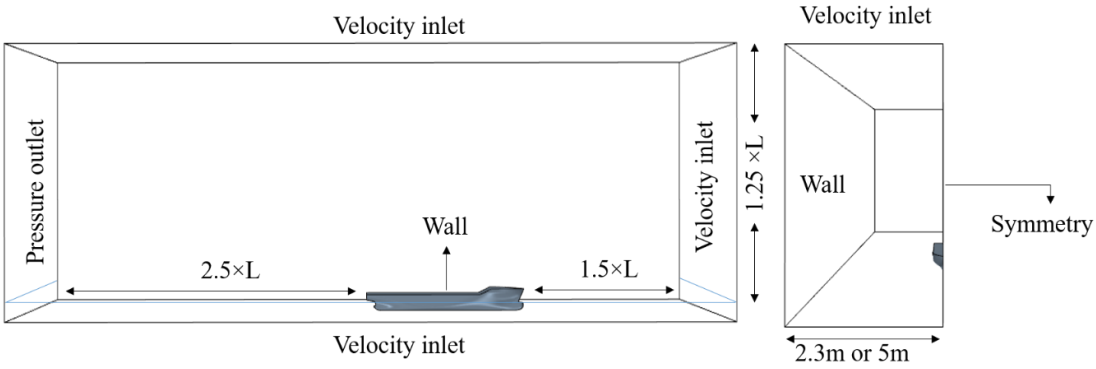

Figure 4.3. Boundary conditions and dimensions for all computational domains.

4.4.4 Mesh generation

The mesh was generated within the facilities of Star-CCM+, which allow the user to make full use of the software's automatic operations. The static, region-based mesh comprises mainly of hexahedral cells with minimal skewness, generated via the trimmed cell mesher. According to the findings of Jones and Clarke (2010), tetrahedral cells can compromise the accuracy of the solution. Concentric local volumetric refinements are imposed in the vicinity of the hull, ensuring the accurate representation of flow phenomena. Furthermore, the location where the free surface is expected to deform has been systematically refined.

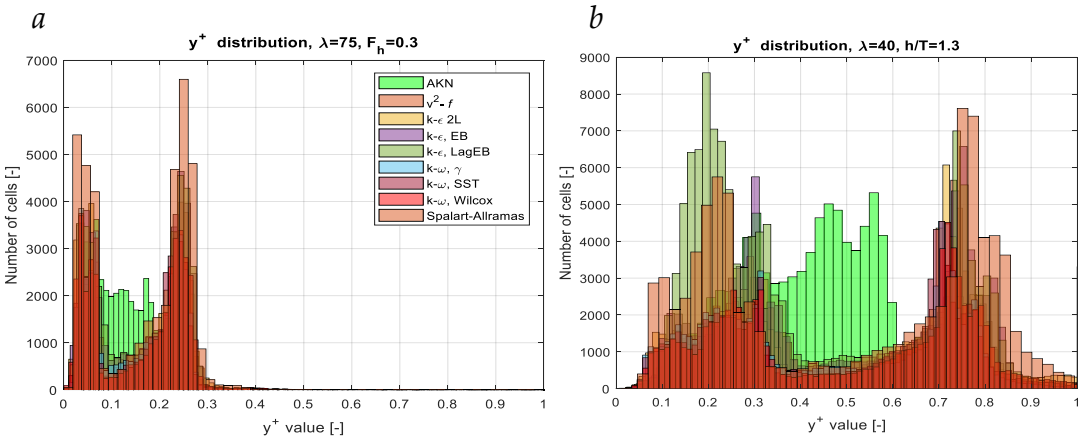

Figure 4.4. Sample y+ value distribution along the wetted hull: (*a*) refers to the study of Elsherbiny et al. (2019), (*b*) refers to Mucha and el Moctar (2014) – case 2.

The prism layer mesher is used to capture the ship boundary layer by creating orthogonal prismatic cells. Resolving near-wall flow accurately is of critical

importance, which is why the y^+ values are monitored, ensuring the average values remain below 1 in all cases (Eca et al., 2018). The distribution of y^+ values along the wetted part of the hull are shown in Figure 4.4 for cases 1 and 3.

While the vast majority of turbulence models predict the same y^+ values, the *AKN* model (bright green) deviates significantly. In the next section, it will be shown that such behaviour leads to a compromised accuracy. For case 1 (of Elsherbiny et al. (2019)) the large scale factor (λ=75) allows an increased resolution to be imposed without the need to resort to an excessively large number of cells. The second case is not as straightforward, which is why the y^+ values are allowed to reach 0.9, although the average in all cases is smaller than 1, despite the two-fold increase in cell numbers (Table 4.4). The resulting computational mesh, mirrored using the central symmetry for illustration purposes, is shown in Figure 4.5, where the local volumetric refinements are clearly visible, including the Kelvin wedge. The properties of the computational domain for all case-studies are shown in Table 4.4.

Strictly speaking, the imposition of a symmetry plane has the potential of invalidating the results presented herein. However, Mucha and el Moctar (2014) demonstrated a negligible difference resulting from the presence of a symmetry plane. For this reason, it is deemed safe to proceed directly with the computational mesh, as described previously. Finally, to enable a reliable comparison of the results, free of unregistered unknowns, all parameters described in this section have been kept identical across the case-studies.

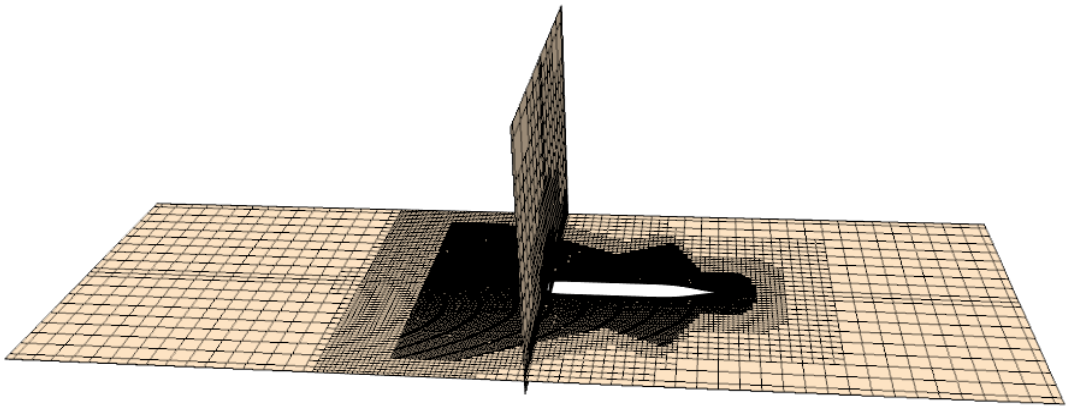

Figure 4.5. 3-D view of the computational mesh. Depicted: case 1 (mirrored using the central symmetry plane).

Table 4.4. Computational domain cell properties.

Case study number	Number of cells	Number of faces	Number of vertices
1 and 2	1,446,076	4,281,940	1,491,537
3	2,995,685	8,868,880	3,087,140
4	3,032,015	8,984,576	3,125,549

4.5 Results and discussion

In this section, the results are presented and compared, both against each other and against the relevant experiments. The first sub-section is dedicated to the numerical uncertainties and error estimations against experiments. Presenting these first will later allow a fuller discussion of the results.

4.5.1 Comparison against experimental data

The first step taken in this section is to present the results in tabular form alongside the experimentally obtained values (EFD – Experimental Fluid Dynamics) and calculated error (E). This step is used to validate the solution. The error is defined as E=(EFD-CFD)/EFD×100, and is shown in Table 4.5. The values, highlighted in red were not used in the computation of averages shown in the same table. This is done in an attempt to allow the global average (shown in bold) of the error to represent the values in a meaningful way. If the error values for trim were taken into account, the global average error would be much higher.

The first conclusion drawn from the errors shown in Table 4.5 suggest that resistance can be predicted by almost all turbulence models effectively. This is true especially considering the experimental force measurement uncertainty, which is up to 2.20% in Elsherbiny et al. (2019). As referred to previously, sinkage and trim present an additional layer of complexity. The numerical set-up has not predicted values within acceptable margins for one row (case 3), in the case of sinkage and three (cases 1, 3, and 4) in the case of trim (discussed further in the following sections). This is the case for two reasons, which include numerical and experimental uncertainty.

Table 4.5. Numerical results and error calculations

Description				ID	Type	*AKN*	*v^2- f*	*EB*	*Lag-EB*	*k-ε 2l*	*k-ω γ*	*k-ω SST*	*k-ω Wilcox*	*SP-All*	Average
	λ	*F_h*	*h/T*												
Resistance coefficient [-]	75	0.303	2.2	1	EFD	5.775×10^{-3}									-
					CFD	4.401×10^{-3}	5.559×10^{-3}	5.559×10^{-3}	5.614×10^{-3}	5.439×10^{-3}	5.298×10^{-3}	5.340×10^{-3}	5.505×10^{-3}	5.596×10^{-3}	5.489×10^{-3}
					E	*23.79%*	*3.74%*	*3.75%*	*2.79%*	*5.83%*	*8.26%*	*7.53%*	*4.67%*	*3.10%*	4.96%
		0.570		2	EFD	5.224×10^{-3}									-
					CFD	4.087×10^{-3}	5.212×10^{-3}	5.199×10^{-3}	5.247×10^{-3}	5.096×10^{-3}	5.034×10^{-3}	5.014×10^{-3}	5.138×10^{-3}	5.239×10^{-3}	5.147×10^{-3}
					E	*21.77%*	*0.24%*	*0.49%*	*-0.44%*	*2.46%*	*3.64%*	*4.02%*	*1.65%*	*-0.27%*	1.47%
	40	0.370	1.3	3	EFD	2.784×10^{-3}									-
					CFD	1.120×10^{-3}	2.802×10^{-3}	2.668×10^{-3}	2.869×10^{-3}	2.851×10^{-3}	2.587×10^{-3}	2.559×10^{-3}	2.661×10^{-3}	2.842×10^{-3}	2.730×10^{-3}
					E	*59.76%*	*-0.64%*	*4.15%*	*-3.06%*	*-2.42%*	*7.07%*	*8.09%*	*4.42%*	*-2.07%*	1.94%
		0.410	1.6	4	EFD	4.74×10^{-3}									-
					CFD	1.80×10^{-3}	5.02×10^{-3}	4.67×10^{-3}	4.99×10$_{-3}$	4.97×10^{-3}	4.49×10^{-3}	4.45×10^{-3}	4.66×10^{-3}	4.98×10^{-3}	4.781×10^{-3}
					E	*62.02%*	*-5.86%*	*1.50%*	*-5.27%*	*-4.79%*	*5.28%*	*6.24%*	*1.89%*	*-5.01%*	-0.75%
Sinkage [m]	75	0.303	2.2	1	EFD	-2.09×10^{-3}									-
					CFD	-2.09×10^{-3}	-2.00×10^{-3}	-2.00×10^{-3}	-2.01×10^{-3}	-2.01×10^{-3}	-2.02×10^{-3}	-2.03×10^{-3}	-2.02×10^{-3}	-2.01×10^{-3}	-2.015×10^{-3}
					E	-0.07%	4.10%	4.18%	3.58%	3.54%	3.23%	2.97%	3.09%	3.65%	3.14%
		0.570		2	EFD	-8.85×10^{-3}									-
					CFD	-8.48×10^{-3}	-8.18×10^{-3}	-8.20×10^{-3}	-8.22×10^{-3}	-8.19×10^{-3}	-8.25×10^{-3}	-8.28×10^{-3}	-8.25×10^{-3}	-8.18×10^{-3}	-8.221×10^{-3}
					E	4.15%	7.52%	7.29%	7.09%	7.41%	6.76%	6.45%	6.78%	7.57%	7.11%
	40	0.37	1.3	3	EFD	-6.16×10-3									-
					CFD	-7.73×10^{-3}	-7.60×10^{-3}	-7.54×10^{-3}	-7.56×10^{-3}	-7.69×10^{-3}	-7.61×10^{-3}	-7.61×10^{-3}	-7.60×10^{-3}	-7.51×10^{-3}	-7.591×10^{-3}
					E	-25.46%	-23.35%	-22.47%	-22.72%	-24.83%	-23.59%	-23.59%	-23.34%	-22.00%	-23.24%
		0.41	1.6	4	EFD	-6.16×10^{-3}									-
					CFD	-6.01×10^{-3}	-5.83×10^{-3}	-5.85×10^{-3}	-5.83×10^{-3}	-5.88×10^{-3}	-5.86×10^{-3}	-5.89×10^{-3}	-5.88×10^{-3}	-5.77×10^{-3}	-5.848×10^{-3}
					E	2.49%	5.28%	5.11%	5.37%	4.58%	4.85%	4.37%	4.60%	6.38%	5.07%

Table continued on the next page

Trim [°]															
	75	0.303	2.2	1	EFD	-2.2×10^{-2}									-
					CFD	-3.79×10^{-2}	-3.56×10^{-2}	-3.52×10^{-2}	-3.58×10^{-2}	-3.55×10^{-2}	-3.58×10^{-2}	-3.54×10^{-2}	-3.59×10^{-2}	-3.64×10^{-2}	-3.568×10^{-2}
					E	-69.15%	-58.78%	-56.92%	-59.82%	-58.38%	-59.67%	-57.84%	-60.35%	-62.29%	-60.36%
		0.570		2	EFD	-1.03×10^{-1}									-
					CFD	-1.07×10^{-1}	-9.95×10^{-2}	-9.75×10^{-2}	-9.96×10^{-2}	-9.95×10^{-2}	-1.02×10^{-1}	-1.01×10^{-1}	-1.02×10^{-1}	-1.03×10^{-1}	-1.005×10^{-1}
					E	-4.49%	3.22%	5.20%	3.12%	3.21%	1.27%	1.82%	0.67%	-0.62%	1.49%
	40	0.37	1.3	3	EFD	-2.24×10^{-2}									-
					CFD	3.97×10^{-4}	-5.39×10^{-3}	-6.01×10^{-3}	-5.67×10^{-3}	-4.81×10^{-3}	-5.44×10^{-3}	-4.97×10^{-3}	-4.99×10^{-3}	-6.23×10^{-3}	-5.438×10^{-3}
					E	101.77%	75.93%	73.16%	74.69%	78.49%	75.70%	77.77%	77.73%	72.19%	75.71%
		0.41	1.6	4	EFD	-2.24×10^{-2}									-
					CFD	-9.10×10^{-4}	-5.37×10^{-3}	-5.48×10^{-3}	-4.86×10^{-3}	-4.98×10^{-3}	-5.42×10^{-3}	-5.03×10^{-3}	-4.88×10^{-3}	-6.54×10^{-3}	-5.319×10^{-3}
					E	95.93%	76.03%	75.53%	78.27%	77.74%	75.78%	77.55%	78.19%	70.79%	76.24%
Average						24.57%	2.20%	3.96%	1.65%	2.48%	5.05%	5.19%	3.47%	1.59%	**3.13%**

Particularly in the case of trim for case-studies 3 and 4, no turbulence model has adequately predicted the experimentally measured results. This can stem from a variety of sources. One interesting observation is that in Mucha and el Moctar (2014) the reported Longitudinal Centre of Gravity (LCG) is different from what is typically reported elsewhere. In the numerical work done here, the LCG is located as prescribed in the relevant reference. However, this serves to highlight a problem in the results: the two pieces of research found a disagreement in a metric as fundamental as the LCG. In the presence of such uncertainties, it is imperative that an inter-facility test is conducted and assessed via a Youden (1972) style technique.

4.5.2 Numerical verification

The numerical verification adopted herein follows widely used procedures in the ship hydrodynamics community (Xing and Stern, 2010). Specifically, the Richardson Extrapolation (RE) procedure (Richardson, 1911). This consists of expressing the error as an expanded power series with integer powers of grid spacing (Δx) or time step (Δt) as a finite sum. If one assumes the solutions lie within the asymptotic range, it is admissible to take only the dominant term into account, leading to the so-called grid triplet study. Following Xing and Stern (2010), the Grid Convergence Index (GCI) is used, devised by Roache (1998). This method can be used to establish the uncertainty due to grid spacing and time step errors, as demonstrated in Terziev et al. (2018), Tezdogan et al. (2016b). This step is a crucially important part of any numerical solution, and its omission in computational science and engineering is not admissible (Roache et al., 1986). On the other hand, the iterative errors are calculated as being virtually zero in all cases following the procedure of Roy and Blottner (2001).

The GCI procedure begins by calculating the convergence ratio (R), defined as the ratio between $\varepsilon_{21} = (f_2 - f_1)$ and $\varepsilon_{32} = (f_3 - f_2)$. Here, f_i refers to the solution obtained via the respective input parameter (mesh or time-step) using the i^{th} solution. The solutions (i) are obtained by systematically coarsening each parameter by a factor of $\sqrt{2}$ (also known as the refinement ratio – r), as recommended by ITTC (2008). Thus, in the case of grid dependence, the base size is magnified by the above factor, whereas in the case of time dependence, the time step is lessened by r. This procedure yields a total of four extra solutions, used to define four possible scenarios for R for time and grid dependence (Stern et al., 2006):

1. Monotonic convergence, if $0>R>1$
2. Oscillatory convergence, if $R<1$ and $|R|<1$
3. Monotonic divergence, if $R>1$
4. Neither error nor uncertainty can be evaluated

Once the type of convergence is known, the order of accuracy (Celik et al., 2008), p is calculated as shown in Eq. (4.1). A monotonic convergence is assumed in all equations presented herein.

$$p = \ln(\varepsilon_{23}/\varepsilon_{21})/\ln(r) \tag{4.1}$$

The next step is to find the extrapolated solution – Eq. (4.2), relative error – Eq. (4.3), and extrapolated error – Eq. (4.4):

$$f_{ext}^{21} = (r^p \times f_1 - f_2)/(r^p - 1) \tag{4.2}$$

$$\varepsilon_a^{21} = |(f_1 - f_2)/f_1| \tag{4.3}$$

$$\varepsilon_{ext}^{21} = |(f_{ext}^{12} - f_1)/f_{ext}^{12}| \tag{4.4}$$

Finally, the grid convergence index can be calculated as shown in Eq. (4.5):

$$GCI_{fine}^{21} = 1.25\varepsilon_a^{21}/(r^p - 1) \tag{4.5}$$

To obtain the solutions in the grid convergence study, the smallest time step is used while coarsening the grid. On the other hand, to obtain the time step convergence study results, the finest grid is used while lessening the time step. Throughout the numerical verification procedure, surface mesh characteristics were kept constant to maintain the accurate representation of the ship geometry. The convergence studies are summarised in Table 4.6. The results suggest that simulations are subject to greater uncertainty stemming from the grid, rather than the time step. Although a GCI of 12.47% (for sinkage) may seem high, Elsherbiny et al. (2019) report a 90% uncertainty for sinkage and trim. In other words, the simulations exhibit uncertainty, with an order of magnitude smaller than the experiment. The reason why this is the case is related to experimental measurement equipment. The displacements used to calculate sinkage and trim are too small to be reliably measured. Even in the case of resistance, the numerical uncertainty (1.94% and 0.01%) is smaller than the experimental uncertainty – 2.2%. This also explains the observed errors in Table 4.5. While the resistance has been predicted reasonably well in all cases, sinkage and trim are harder to capture, both experimentally and numerically.

Table 4.6. Convergence study for sinkage, trim, and resistance for case 1, λ=75, h/T=2.2, F_h=0.303, EB model.

Parameter	Grid dependence			Time dependence		
	Sinkage [m]	Trim [°]	Resistance [N]	Sinkage [m]	Trim [°]	Resistance [N]
r	$\sqrt{2}$	$\sqrt{2}$	$\sqrt{2}$	$\sqrt{2}$	$\sqrt{2}$	$\sqrt{2}$
f_1	-2.002×10^{-3}	-3.516×10^{-2}	1.252	-2.002×10^{-3}	-3.516×10^{-2}	1.252
f_2	-2.181×10^{-3}	-3.402×10^{-2}	1.269	-2.000×10^{-3}	-3.510×10^{-2}	1.252
f_3	-2.655×10^{-3}	-3.209×10^{-2}	1.316	-1.946×10^{-3}	-3.498×10^{-2}	1.251
R	0.380	0.591	0.360	0.367	0.575	0.111
p	2.792	1.519	2.900	9.536	1.599	6.334
f_{ext}^{12}	-1.822×10^{-3}	-3.630×10^{-2}	1.235	-2.004×10^{-3}	-3.523×10^{-2}	1.252
ε_a^{21}	8.99%	3.25%	1.37%	0.10%	0.18%	0.01%
ε_{ext}^{21}	9.88%	3.14%	1.39%	0.10%	0.18%	0.00%
GCI_{fine}^{21}	12.47%	7.56%	1.94%	0.19%	0.38%	0.01%

Finally, the modelling errors induced by a change in turbulence models are known to differ depending on the closure selected (Pereira et al., 2017). Therefore, the results presented in Table 4.6 are not uniform across all case-studies. However, having compared the solution against experimental data, it is not though necessary to verify the numerical solution for each turbulence model. The number of additional solutions required per case study (four) implies an unreasonably high number (140) of additional simulations necessary to bind the numerical error completely, as would be desirable. In consequence, due to the extreme computational expense associated with the procedure, this is left as a piece of future work.

4.5.3 Results comparison

Having established that resistance is predicted reasonably well by all turbulence models (with the exception of *AKN*), it is worthwhile examining its constituent components in more detail. In CFD assessments the resistance of a body subject to fluid flow is defined as the sum of tangential (shear) and normal (pressure) components. Each of these is non-dimensionalised by division by $0.5\rho U^2 S$, where ρ=997.561 kg/m^3 is the water density, and S is the wetted surface area (C_F and C_P, respectively). Figure 4.6-Figure 4.9 show the distribution of resistance among the two categories (shear and pressure) as well the experimental values and error calculated for each turbulence model.

In the figures, the errors calculated by the *AKN* model have not been included in order to preserve the y-scale of the error within reasonable values for the remaining turbulence closures.

4.5.3.1 Pressure resistance

The results (Figure 4.6-Figure 4.9) suggest that all turbulence models predict the pressure component of resistance well, with little disagreement between the different approaches to closing the governing equations. This may seem a trivial observation, since the pressure resistance is not strongly coupled with viscous flow behaviour near impermeable walls. This has been widely used as a justification for the coupling of RANS and potential flow solvers (Tahara and Stern, 1994). However, this observation has wider implications: it suggests the wave resistance, which is part of pressure resistance, is computed with good accuracy regardless of the turbulence model. Wave resistance has been a particularly important and difficult metric to accurately capture in the past for several reasons. These include the complexity of the flow surrounding a ship. In some cases, the deep-water wave resistance problem is thought to be addressed reasonably well by potential flow. However, the vast majority of theories break down for shallow waters. A good example illustrating this is Michell's (1898) integral. As shown by Tuck and Lazauskas (2008), Beck (1977), Beck et al., (1975), Tuck (1967, 1966), Michell's (1898) integral can be extended to a large variety of shallow water problems, including deep water wave resistance, but not to the prediction of shallow water wave resistance.

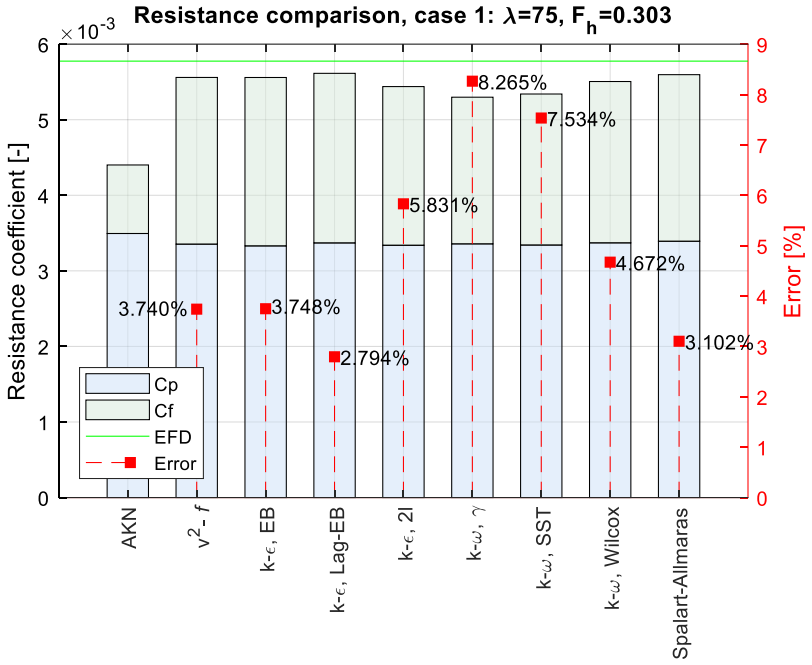

Figure 4.6. Resistance coefficient comparison for case 1

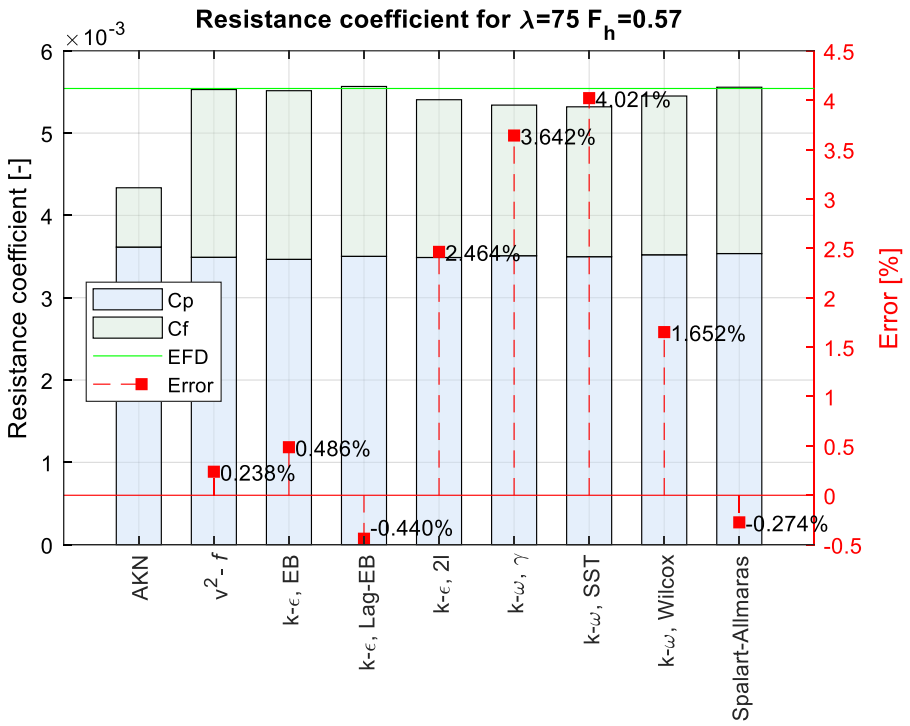

Figure 4.7. Resistance coefficient comparison for case 2.

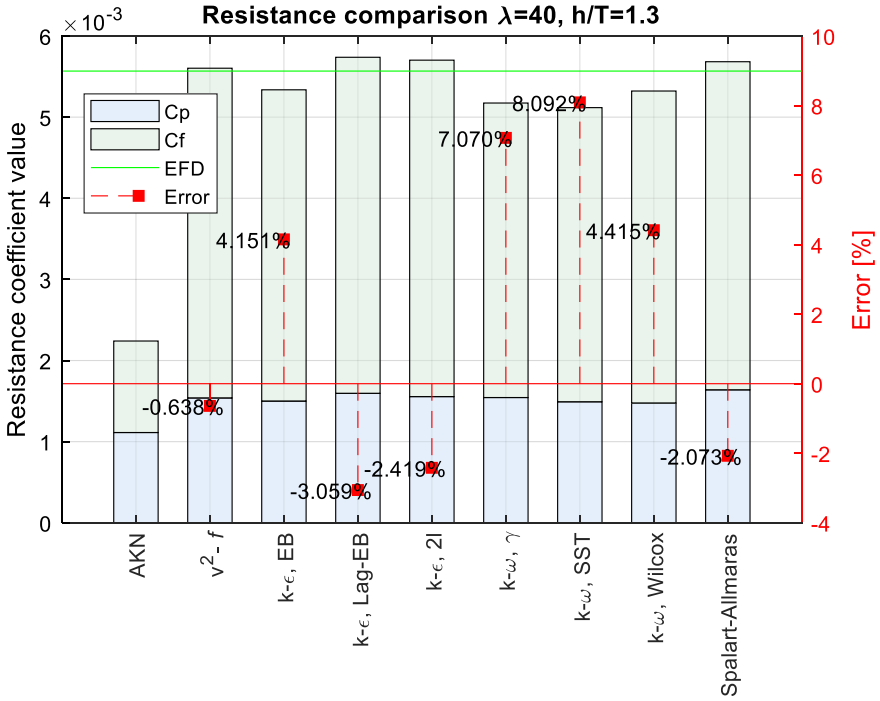

Figure 4.8. Resistance coefficient comparison for case 3.

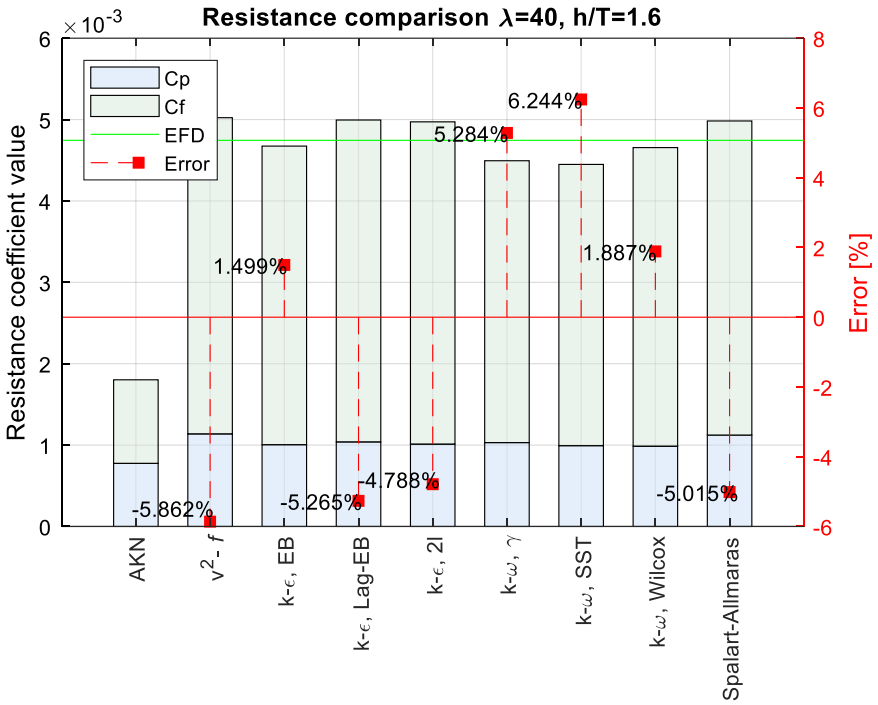

Figure 4.9. Resistance coefficient comparison for case 4.

Traditionally, ship resistance is extrapolated from model to full-scale following a towing tank experiment (Molland et al., 2017). Once the total resistance has been obtained, it is decomposed into a frictional component, a component due to wave making, and a viscous component. The assumption is that a ship's form factor and wave resistance components remain constant with scale, while friction varies as prescribed by the friction line of choice (Grigson, 1999; ITTC, 1999; Katsui et al., 2005). The findings presented herein suggest the wave resistance (if assumed constant with scale) can be established with sufficient accuracy regardless of the turbulence model employed at a high scale factor, where the computational expense is small (refer to Table 4.4 for cell numbers). Finally, the well-established trend of increase in pressure resistance with decreasing depth is observed in Figure 4.8 and Figure 4.9.

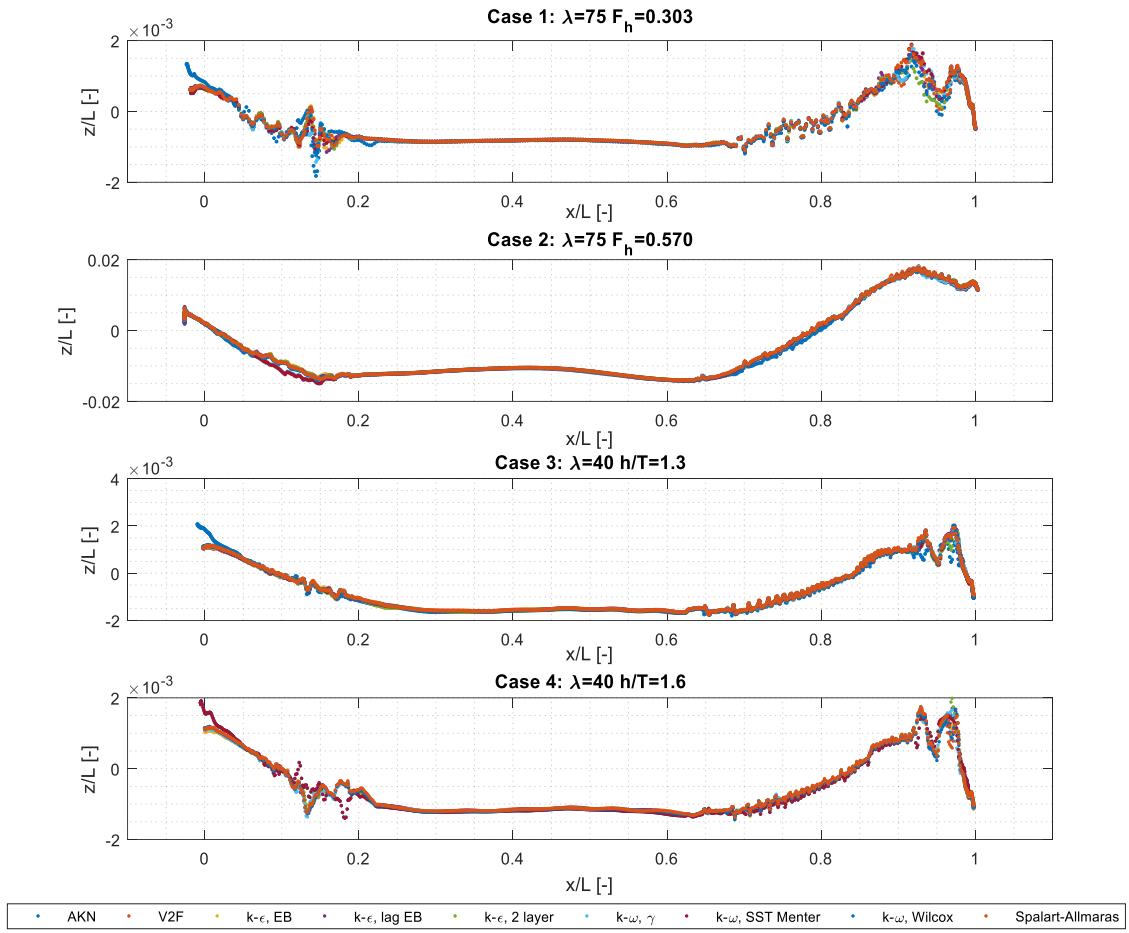

Figure 4.10. Free surface profile along the hull for all case-studies.

One way to confirm that wave resistance is predicted well is to examine whether any differences are present in the location of the waterline along the hull. In this respect, in Figure 4.10, all wave-hull profiles are shown. The first observation made here is the agreement established between all turbulence models. The *AKN* closure seems to deviate slightly in cases 1 and 3. In case 2, the *k-ω SST* model diverges from the other turbulence models near the stern of the ship. Furthermore, it exhibits a slight oscillatory behaviour in case 4, not predicted by other closures. Indeed Table 4.5 can be consulted to confirm the presence of a systematic deviation in the predicted resistance values obtained via the *k-ω SST* model. This is surprising considering its popularity among the ship hydrodynamics research community. The reasons for this are explored later in this chapter.

4.5.3.2 Friction resistance

The difference between the smallest and largest skin friction coefficient prediction, excluding *AKN*, is 2.7×10^{-3} for cases 1 and 2, and 2.9×10^{-3} for cases 3 and 4. This an interesting observation, because it serves to highlight that depending on the turbulence model, vastly different results can be obtained in terms of friction. Naturally, this has a strong influence on the total resistance, since friction is one of the main contributing components. Keeping in mind the y^+ distribution shown in Figure 4.4 (Section 4.3.1), it seems unlikely that predictions made by different turbulence models will collapse into a single value were the grid to be refined further. The skin friction coefficients are graphically compared to established friction lines in Figure 4.11. With the exception of the two variants based on the *SST* model (*k-ω SST*, and *k-ω γ*), the closures predict a significantly higher skin friction than any friction line would suggest. This can be used to highlight the shortcomings of form factor and wave resistance extrapolation techniques, since a reliable frictional resistance is integral to the procedure (Terziev et al., 2019a). Confidence in the predictions can be established due to their systematic predictions, as shown in Figure 4.11, in terms of their relative location on the plot. To elaborate, *k-ω SST*, and *k-ω γ* models are consistently the lowest predictions, whereas *k-ε Lag-EB* – the highest.

There are several likely sources of error in the solutions presented herein associated with the RANS technique. Stern et al. (2006) identify these errors as turbulence modelling (which is being here), artificial compressibility (also a part of some turbulence models), domain size (dictated by the experimental facilities), and round off errors. It is generally accepted that the latter are negligible. In Section 4.5.2 the numerical uncertainty was bound for an example test case. This allows for the turbulence model to be identified as the dominant contributor to all errors found.

In terms of C_F, Fukagata et al. (2002) derived a relationship between skin friction and the Reynolds stress distribution across a surface. Their results confirm experimental observations suggesting that the Reynolds stress within 80 wall units (y^+ <80) accounts for the vast majority of skin friction (up to 90%). This region is viscosity-dominated and coincides with the location where turbulence modelling can have the greatest impact. Indeed, one of the aims of turbulence modelling is to predict a Reynolds stress. The three-dimensionality of ship boundary layers is also a critically important fact, since closures are

calibrated for two dimensions in almost all cases . In fact, the skin friction is known to consist of pressure development, laminar contribution, spatial development, and Reynold stress components (Stroh, 2016). Shallow waters amplify the three-dimensionality of boundary layer, which was one of the motivating factors cited in the adoption of the case-studies (Zeng et al., 2018).

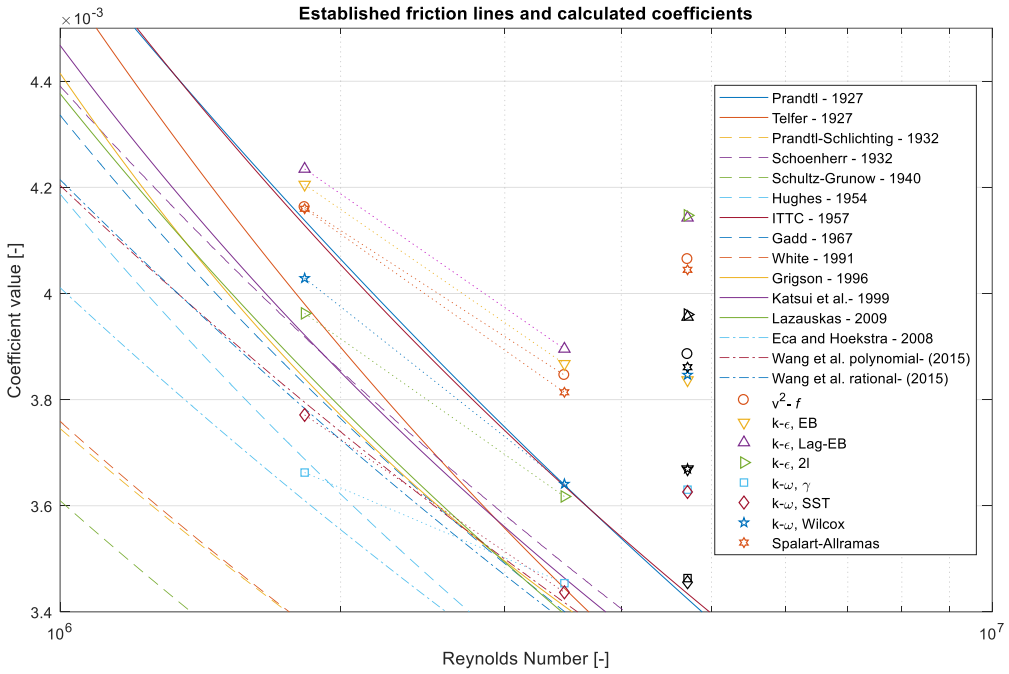

Figure 4.11. Skin friction comparison. Shapes connected via dotted lines correspond to cases 1 and 2. Solitary coloured shapes correspond to case 3, while the black shapes – case 4.

Finally, the results shown in Figure 4.11 suggest that a change in water depth can have influence skin friction substantially. The mechanism by which this occurs is not well understood. Zeng et al. (2018) presented a modification of the ITTC friction line for shallow waters (ITTC, 2017a). Their derivation is based on flat plates, and is only applicable to the flat region of a ship's bottom, whereas the friction line proposed by Katsui et al. (2005) is used for the remainder of the wetted area. There are obvious problems with this, mainly due to the fact that the KCS was allowed to sink and trim, rendering the boundary layer on the flat bottom highly three-dimensional, unlike that of a flat plate. The flow is also forced past the sides of the ship in virtually all shallow water cases, which avoids the violation of the Bernoulli principle. Figure 4.12 depicts the boundary layer and wake generated by the KCS in case 4. The top half of the figure was generated to represent 90% of the free stream

velocity ($U_{90\%}$=0.657 m/s)., while the bottom half – 99% of the free-stream velocity ($U_{99\%}$=0.7227 m/s). Figure 4.12 shows the boundary layer is highly three-dimensional, especially near the bow and stern, where the 99% free-stream iso-surface is in contact with the seabed over a significant area. In the figure, the dynamic pressure is used to colour the surfaces. This is done to highlight the differences in pressure, acting longitudinally and transversely due to the proximity of the seabed. Finally, the waves resulting from the disturbance, caused by the ship also register in the plot.

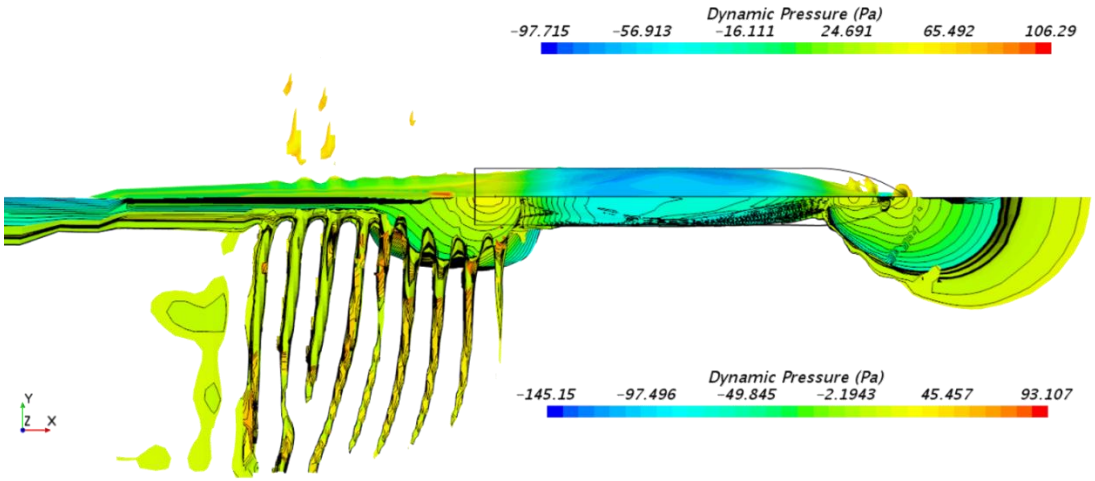

Figure 4.12. Boundary layer and wake (top view), depicted: case 4. Top: iso-surfaces for 0.9×U. Bottom: iso-surfaces for 0.99×U.

4.5.3.3 An attempt to identify the optimum turbulence model

The problem of consistency can be addressed via a modified Youden (1972) plot. Although the original purpose of the technique proposed by the abovementioned author was to establish experimental biases, it can also be used to provide an indication of accuracy and consistency. The required modification is that instead of dimensional quantities, plotted in the x and y axes, the error is used, calculated in Section 5.1.1, Table 4.5.

The modified technique begins by plotting the error for each parameter in an x-y plane. As shown in Figure 4.13, the y-axis is chosen to represent error in resistance as calculated for case-studies 2 and 4, whereas the x-axis: the error in case-studies 1 and 3. Thus, the empty shapes in Figure 4.13 represent the points with coordinates [x, y] = [E_1, E_2] where the subscripts refer to case study number, and E is the error. The filled shapes correspond to points with coordinates [E_3, E_4]. For example, the empty blue circle (v^2 – f model) in Figure 4.13 has an x – coordinate equal to the total resistance error for case 1 (3.74%),

and a y – coordinate equal to the total resistance error for case 2 (0.24%). Similarly, the filled blue circle has x – coordinates equal to the C_T error for case 3, and y – coordinate equal to C_T error for case 4.

As described by Youden (1972), the next step is to construct the straight lines, representing the median x and y values. Depending on the location of each point within the plot, a systematic bias, or lack thereof can be established. For instance, a point lying in the first quadrant (the standard convention is adopted), established via the intersection of the median values, suggests a systematic overprediction. Using the intersection of the median x and y values, a 45-degree diagonal is drawn. This diagonal can be useful in giving a measure of consistency each turbulence model provides in its predictions. In other words, points close to the diagonal perform in a similar manner in all four case-studies, i.e. systematically. An extra layer of information can be extracted due to the fact that the error was made use of in Figure 4.13.

By requiring that the error is the metric against which the points are assessed, it is possible to simultaneously take into account the closures' performance against the relevant experiment. An additional consequence of the above choice is that the experimental uncertainty can be drawn directly onto the plot. For case-studies 1 and 2, this is 2.20%. For cases 3 and 4, the uncertainty is not reported, therefore, the same magnitude as in cases 1 and 4 is assumed. Armed with this information, a circle, centred at [0, 0], with a radius of 2.20 can be drawn, giving a graphical interpretation of the error and biases in all four cases (the red circle in Figure 4.13). If all experimental uncertainties were known, an ellipse would be required, as is the case with modified versions of the plot (Velázquez and Asuero, 2017).

The mathematics behind different turbulence models cannot provide any information that could forecast whether the values will under or overpredict the experiment prior to running the simulation. If all turbulence models were made equal, the values would be scattered evenly in each quadrant around the median x-y intersection. This is true because all models are calibrated against a similar set of experiments, and therefore should be equally robust. Therefore, displacement along the diagonal can be interpreted as bias, whereas offset from the diagonal is an indication of erratic behaviour.

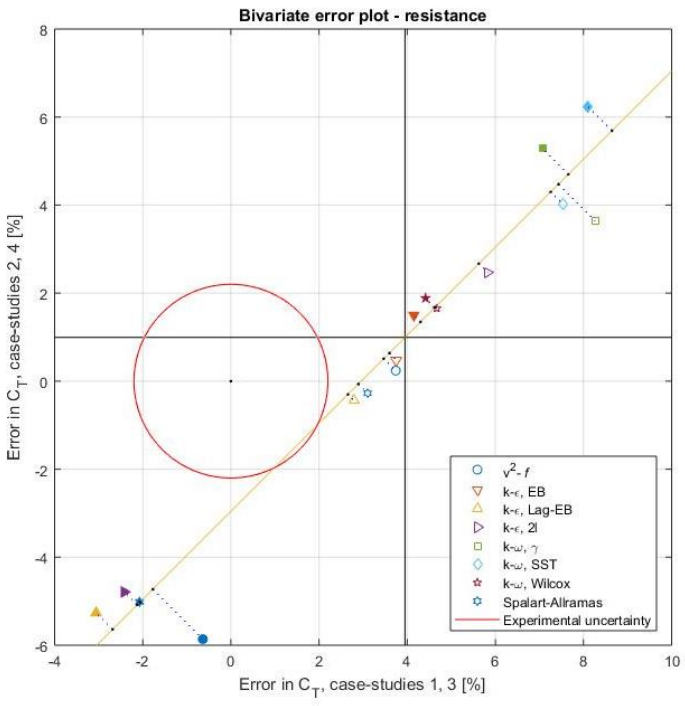

Figure 4.13. Bivariate error plot for resistance.

A high deviation from the circle (representing the experimental uncertainty) indicates a turbulence model's inability to cope well with the case it is applied to. Thus, the proximity of *k-ω Wilcox*, and *k-ε EB* (and its *Lag* extension) models, coupled with their small distance from the diagonal, indicates they perform well, consistently, and reliably. By contrast, the *k-ε 2l* model shows erratic behaviour, over and underpredicting results by a large margin depending on the case study. Thus, the results suggest that applying this closure, the user cannot hope to predict with any confidence what the outcome of a simulation will be. If either of the well-performing models mentioned above were to be used, one could expect to achieve results with a small, positive error. That is, provided the numerical set-up is reasonably similar to that presented herein.

Unfortunately, Figure 4.13 takes into account only resistance. Thus, no information regarding the turbulence models' behaviour in sinkage and trim can be deduced from it. For this reason, Figure 4.14 was constructed using case-studies 1, 2 and 4. On the x-axis, the error in sinkage is plotted, while on the y-axis – the corresponding case study's error in resistance. As before, the empty shapes represent case 1, the filled shapes – case 2, and the black shapes

– case 4. Case 3 is omitted due to the large errors in sinkage, which would push the x scale too far for any meaningful discussion.

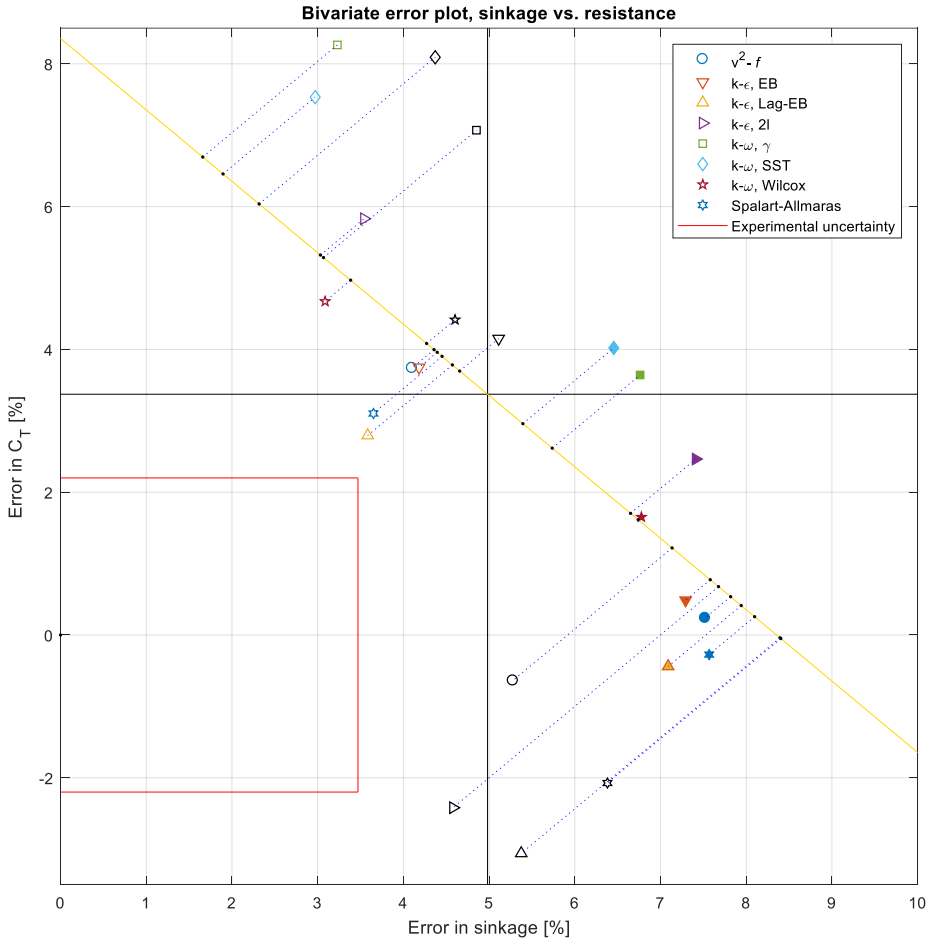

Figure 4.14. Bivariate error plot: sinkage vs. resistance.

A consequence of the arrangement of the points is that the diagonal, constructed from the intersection of the median x and y values has a negative slope. Since different experimental uncertainties are reported in Elsherbiny et al. (2019) for each axis, the shape constructed in Figure 4.14 is a rectangle with dimensions 3.47×2.2, matching the uncertainties in sinkage and resistance, respectively. As before, the lack of reported data for case-studies 3 and 4 means a uniform cross-experimental uncertainty is assumed.

All turbulence models seem to follow certain tendencies in Figure 4.14, where k-ε type models tend to fall beneath the diagonal, while k-ω based models are located above it. A notable exception to this is the k-ε *2l* model, which has two points above, and one below the diagonal. Figure 4.14 happens to be constructed so that points below the diagonal are closer to the limits of the rectangle, and therefore closer to the experimental uncertainty bounds.

It is important to keep in mind that the 'distance to the diagonal' metric is purely artificial. However, since it depends on the overall scatter of the predictions, it serves as a good indication of erratic behaviour. As mentioned previously, if all turbulence models were equally robust, they would all lie within a small circle, centred at the median x and y values. Large deviations, prevalent to the k-ε-class models, point towards unreliable predictions. This is not in reference to the accuracy itself. Indeed, in some cases their predictions fall within the experimental uncertainty (e.g. $v^2 - f$, *EB*, and *LagEB* models in resistance for case 2). Instead, reliable turbulence models are those that preform similarly across all case-studies they are applied to.

For Figure 4.14, the set of criteria used to establish a hierarchy of performance follow from the assessment performed for Figure 4.13. Namely, the quadrant in which each point lies, as well as the distance to the diagonal, and origin are taken into account. These metrics, in addition to their overall Root Mean Square (RMS) values have been constructed graphically in Figure 4.15, where only the results depicted in Figure 4.14 are used. Here, the k-ω *Wilcox* model exhibits the desired characteristics to greater extent than the remaining candidates. Firstly, the distance to the diagonal is small throughout, relative to other cases. This is an indication the turbulence model is not an outlier in the scatter of predictions. Secondly, the distance to the origin is reasonable. Finally, two out of three points predicted via this model fall within the same (2^{nd}) quadrant, indicating a degree of consistency.

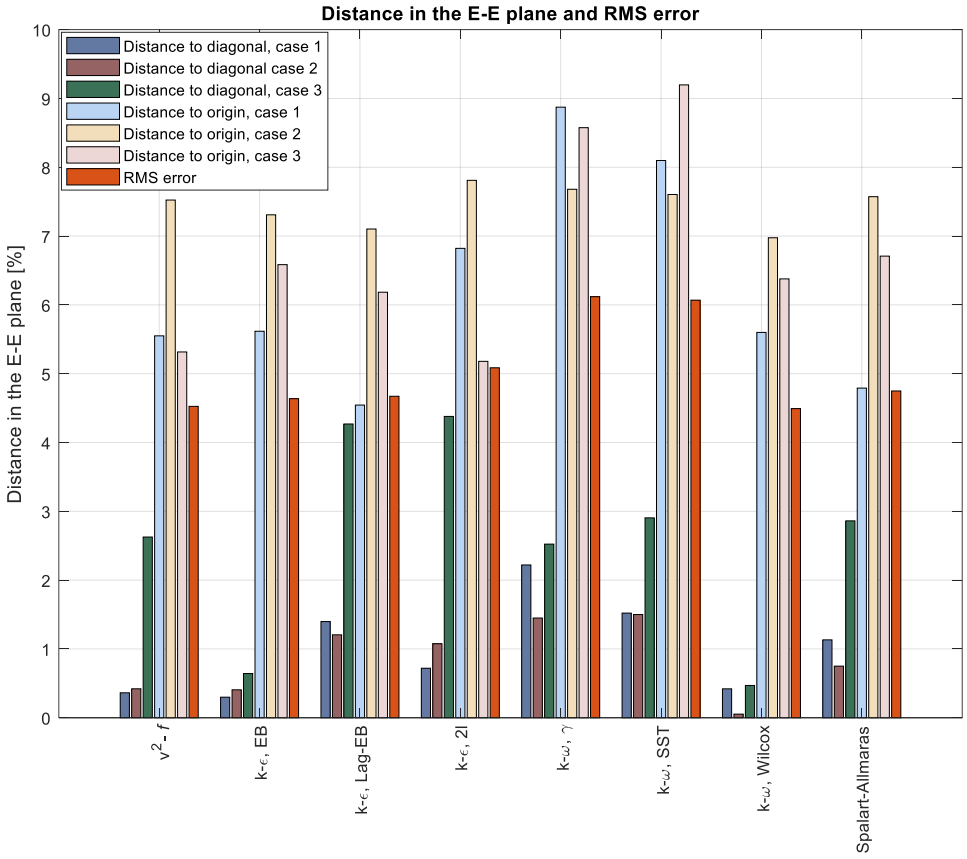

Figure 4.15. Distances in the Error-Error plane and RMS error for case-studies 1-3.

The *k-ε EB* model performs marginally worse, with all three points within different quadrants. Other strong candidates include the $v^2 - f$ model, whose predictions tend to lie close to those obtained via the *k-ε EB* closure. Perhaps surprisingly, the results suggest that the two models accounting for over 80% of all research done in the field of ship hydrodynamics should be ruled out (based on the dataset established earlier). Namely, the *k-ε 2l* and *k-ω SST* models (see Figure 4.1). On the other hand, the *SPAL* model performs almost as well as the more complex, recent closures, such as *k-ε EB* and *Lag-EB* models. In part, the findings of Eça et al. (2018) have been echoed, who found that for the *k-ω SST* model, a $y^+ \approx 0.1$ is required to achieve the same level of accuracy as other turbulence models. This requirement restricts the use of the *k-ω SST* closure, because of the difficulties related to the constraint. Specifically, the cell numbers would increase substantially, as well as the their aspect ratio, which compromises the solution's stability and convergence properties (Eca et al., 2015; ITTC, 2011).

4.5.3.4 Quantification of the computational resource

The final metric, against which turbulence models are evaluated is time per iteration. Although the solver's time per iteration has been recorded throughout the entire duration of the simulation, only values achieved during the first 5 seconds are reported. This is done because once the ship is allowed to translate and rotate, the time history is contaminated with the numerical algorithms responsible for doing this. Additionally, the auto save function of Star-CCM+ was employed to routinely save the simulation (every 5 seconds of physical time), which registers as a spike in the time per iteration monitor. Therefore, global averages would not be a suitable metric.

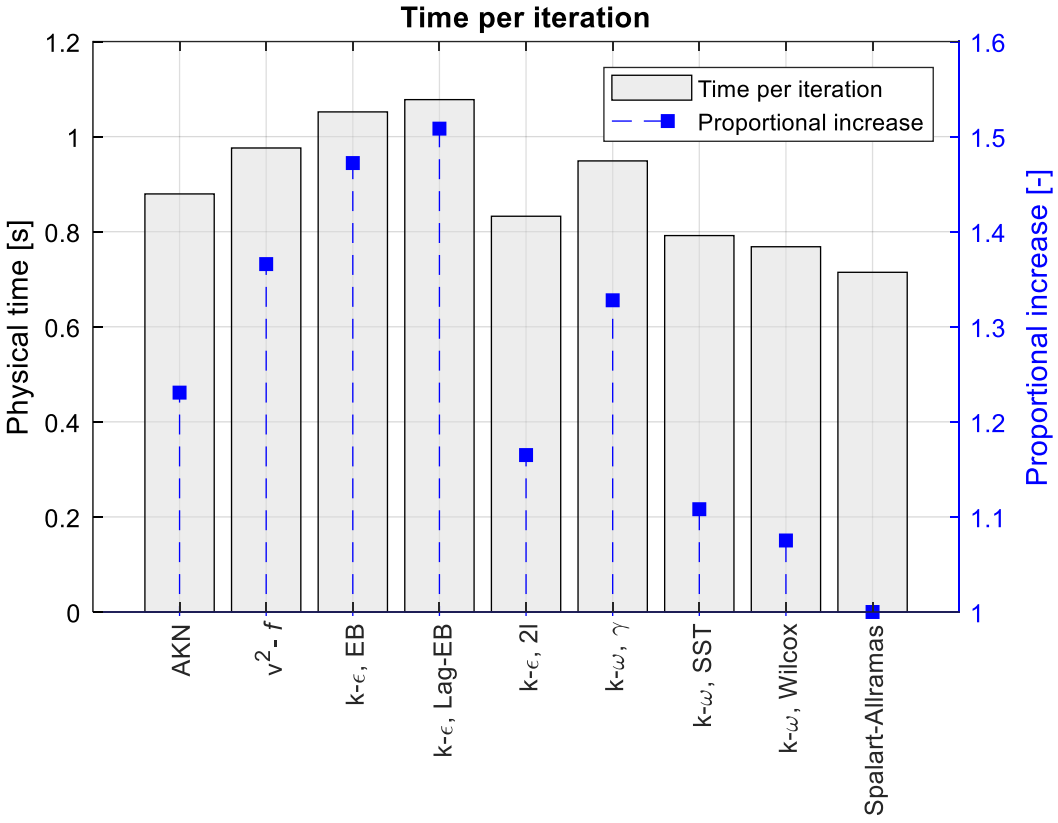

Figure 4.16. Time per iteration for case 1.

All simulations were performed using the high performance computer facilities at the University of Strathclyde, Archie-WeSt. The facility features 2 Intel Xeon Gold 6138 20 core 2.0GHz CPUs, with 40 cores per node, and 192 GB RAM allocated per node. To run the simulations described herein, one node (with 40 cores) was used per case per turbulence model (i.e. per simulation). The resulting time per iteration is shown graphically in Figure 4.16 for case 1. It should be stressed that all results presented in Figure 4.16 are

highly dependent on the solver employed. The relationship between different closures would most likely be maintained if carried forward to a case using Star-CCM+ featuring different cell numbers. However, scalability is not uniform across all RANS solvers, as discussed by Robertson et al. (2015).

The relationship between core numbers and efficiency in obtaining the solution is known to be inverse in nature (Axtmann and Rist, 2016). Therefore, as the cell numbers increase, the difference in computational time will likely decrease. For this reason, case 1, with the smallest number of cells, is chosen for this assessment. In this respect, the development of algorithms tasked with optimising parallelisation is an active field of research, although its relationship with DNS is stronger than RANS approaches (Cifani et al., 2018; Kooij et al., 2018; van der Poel et al., 2015).

As expected, the *SPAL* model provides the smallest computational time requirements, and is used to establish a proportional increase metric for all other models. The *k-ω Wilcox* model provides the smallest time after the *SPAL* closure, closely followed by *k-ω SST.* All *k-ε* variants exhibit a higher time per iteration due to the additional near-wall treatments or extra equations introduced. For instance, the main source of differences between *k-ω Wilcox* and *k-ε 2l* in terms of time is the realizability requirements for the latter. On the other hand, the imposition of a γ transition is shown to increase substantially the computational requirements, while providing little, if any improvements in terms of accuracy, consistency or reliability of the solution. Furthermore, introducing additional equations into the turbulence closure implicitly destabilises the solution. Specifically, more ways in which the numerical calculation could fail are introduced. This is sometimes thought of as numerical stiffness of the solution, and was the reason given for employing a 2nd order convection scheme, rather than the more accurate 3rd order option. In this respect, the practitioner must have a sense of the accuracy, consistency, and computational resource required. Improving the latter is normally associated with a detrimental effect in the former two. The results suggest this trade-off may not always be necessary. That is, provided a suitable numerical set-up is employed.

One final aspect requiring discussion is associated with the solver itself. Research has shown that it is dangerous to generalise outcomes achieved in one software to another. Specifically, the same mesh and set-up can lead to different solutions depending on the solver employed. This problem was highlighted by Iaccarino (2002), who found significant deviations across

RANS software. In consequence, the hierarchy established in this thesis would, in all likelihood differ if repeated using a different solver. This is true because software providers do not disclose all information related to the algorithms and sub-routines used. It is therefore not possible to predict what the effect of replicating the work reported in this chapter elsewhere would have.

4.6 Summary and conclusion

This chapter has focused on reducing the uncertainty in turbulence model selection for a class of problems in ship hydrodynamics. Nine turbulence models were identified as potential candidates for the assessment based on a literature survey. Emphasis was placed on devising a hierarchy depending on performance, since it is not possible to use any other meaningful metric. The adopted case-studies, attempting to replicate a set of shallow water experiments, were specifically selected to challenge the turbulence models.

The validity of the implemented numerical set-up was demonstrated by validating the solutions against experimental data and by estimating the numerical uncertainty for an example case study. The results indicate that pressure resistance and its constituent components are predicted well by all turbulence models. This finding has wider implications in the extrapolation of ship resistance from model to full-scale, as it implies wave resistance is largely independent of turbulence modelling. Friction resistance was shown as the main source of errors. There are several identified areas contributing to the observed discrepancies, other than those due to the numerical set-up, which are bound within acceptable levels. While turbulence models tend to be calibrated against two dimensional cases, a strong three-dimensional boundary layer is observed in the investigated cases.

The observed difference between the highest and smallest frictional resistance prediction was calculated to be nearly constant across all case-studies. This indicates that a strong turbulence modelling sensitivity should be prevalent for full-scale computations, as forecasted by Duvigneau et al. (2003). The difficulties in creating sufficiently fine meshes to resolve the boundary layer at full-scale is also a suspected contributor to the here-described uncertainty. Specifically, the work presented herein can be said to have established a hierarchy for similar numerical set-ups. If the y^+ values are varied significantly, the ranking establishing could well be different.

An attempt to rank turbulence models with respect to their accuracy and consistency was performed, which identified the *k-ω Wilcox* and elliptic blending models as exhibiting the best performance. The assessment was carried out via a modified Youden bivariate plot, where the error in relation to the experimental values was plotted on both axes. The performance criteria included are thought to be capable of providing an initial estimate of the outcome prior to completing the simulation. Coupling these findings with the time per iteration characteristics of each turbulence model suggests the optimal choice is the *k-ω Wilcox* turbulence model for bare hull ship resistance computations.

5. A NUMERICAL ASSESSMENT OF THE SCALE EFFECTS OF A SHIP ADVANCING THROUGH RESTRICTED WATERS

This chapter uses the findings of the previous two chapters of this thesis to assess scale effects in restricted waters. A geosim series analysis is performed on a containership advancing through a canal. Multiphase and double body simulations are performed as part of the assessment. Viscous scaling is also explored for the adopted case study. Numerical estimates of the scale effects are shown to conform to theoretical analysis of the impact of viscosity and vorticity on the flow around the ship.

5.1 Introduction

Historically, naval architecture has primarily relied on Experimental Fluid Dynamics (EFD) due to the lack of consistently reliable theoretical predictions in the field. The advent of analytical and computational methods has not done enough to encourage naval architects to adopt theoretical predictions in their toolkit. Even where this has been the case, computational work usually takes a secondary place. While experimental work has its distinct advantages, the tendency of overreliance on the EFD predictions has some major drawbacks.

Experiments are expensive, especially shallow water cases (Jiang, 2001), they require time, as well as facilities with adequate equipment. Even if all of these requirements are satisfied, one can run into the assumptions of the

extrapolation procedures used to determine the full-scale parameters. Specifically, scale effects have been documented in every component of ship resistance (García-Gómez, 2000; Kouh et al., 2009; Raven et al., 2008).

The case of shallow water presents an additional layer of complexity, because scale effects are expected to be greater than in unrestricted waters (Tuck, 1978). Here, it is important to distinguish between inland ships, which spend their entire operational lives in restricted waters, and seagoing ships. Shallow water studies merit investigation because even seagoing ships enter shallow waters multiple times each voyage. It is precisely in these cases that a significant proportion of accidents occur according to EMSA (European Maritime Safety Agency, 2019, 2018, 2017, 2016, 2015). However, this does not represent the full picture. Inland transportation will play a major role if carbon dioxide emissions due to transportation are to be reduced. This has led to policies aimed at encouraging the use of navigable rivers and canals (Caris et al., 2014; European Commission, 2018; Mihic et al., 2011).

To facilitate the transition to safer operations in shallow waters, the underlying hydrodynamic phenomena must be better understood. An action taken by the ship in deep water can have counter-intuitive consequences in shallow water (Tuck, 1978). These consequences are caused by the hydrodynamic interaction between the ship's hull and the surrounding bathymetry. Effects include a reduction in under keel clearance which translates into a grounding hazard. Additionally, the resistance is known to increase, and the manoeuvrability characteristics are compromised (Fujino, 1976; Millward, 1996). Faced with the above challenges, many analysis methods are either inapplicable, or perform poorly in shallow water.

The primary goal of this chapter is to examine scale effects of the total resistance and its constituent components in confined water. It is important to mention that there have been reports of scale effects in sinkage between model- and full-scale measurements in shallow water (Dand, 1967; Duffy, 2008; Ferguson, 1977; Shevchuk et al., 2019; K. Song et al., 2019). The fact that external parameters, such as wind and waves are impossible to control, as well as the difficulties one faces in full-scale measurements might preclude the identification of the specific root these scale effects experimentally. It may not always be possible to ascertain whether a true scale effect is observed, or if the apparent differences are due to uncontrolled parameters, such as surface roughness, bathymetry irregularity, etc. The adopted case-studies therefore neglect the effects of sinkage ad trim.

The lack of experimental data at different scale factors (i.e. a geosim series in a controlled, laboratory environment) for the same ship in confined water motivates a purely numerical study in all but the smallest scale factor, where data is available. The geosim analysis is applied on the well-known KCS hull form, with conditions replicated from recent experimental work, reported in Elsherbiny et al. (2019). To reveal scale effects, double body and multiphase simulations are performed. In the present context, double body simulations refer to the modelling approach where the free surface has been replaced by a symmetry plane. This has the effect of eliminating the wave resistance component from the total resistance. The novelty the work presented in this chapter is expressed in the approaches used to determine the parameters of interest, as well as the adopted case study.

The remainder of this chapter proceeds with a brief description of the methodology in Section 5.2, which also contains the ship geometry and case-studies. Section 5.3 contains the results and relevant discussion, whereas a summary and conclusion is given in Section 5.5.

5.2 Methodology

This section is split into two major parts. In the first part, the overall procedure and case studies are presented. The second section contains a description of the numerical set-up used, together with details regarding its implementation.

5.2.1 Approach to the problem at hand

The approach to the problem adopted herein is to perform a numerical simulation in a single scale factor, where experimental data is available. In particular, the work of Elsherbiny et al. (2019) was selected. Verification is performed to demonstrate the efficacy of the numerical set-up for this case. Specifically, the well-known KCS ship, without appendages was used, in a depth to draught ratio of 2.2 and a depth Froude number (F_h) of 0.303. Although different speeds are also available, as a result of the experiment, F_h=0.303 was selected as it guarantees a reasonable speed when full-scale is reached (approximately 9 knots). This is chosen to increase the practical relevance of the presented numerical simulations.

The choice of the next, higher scale factor (λ) is trivial in the absence of experimental data. For this reason, it was decided to divide λ by 2, followed by a full-scale simulation to arrive at the scale factors and ship properties shown in Table 5.1. In Table 5.1, the field labelled as “Dynamic viscosity” is

used to reproduce the approach of Haase et al. (2016). In the aforementioned study, the authors devised a procedure whereby a modification of the value of viscosity, a ship may satisfy both Reynolds and Froude similarity simultaneously. The value highlighted in bold is the default used in all simulations, whereas the fields corresponding to the remaining scale factors contain the value used to push the Reynolds number its corresponding value for each λ. This is performed while the linear dimensions are maintained the same. The approach allows one to use a single grid for scale effects assessments.

Table 5.1. Case-studies

Quantity	Symbol	Value			Unit
Scale Factor	λ	75	37.5	1	-
Length	L	3.067	6.133	230	m
Beam	B	0.429	0.859	32.2	m
Draught	T	0.144	0.288	10.8	m
Depth	D	0.253	0.507	19	m
Water depth	h	0.317	0.634	23.760	m
Block coefficient	C_B	0.651	0.651	0.651	-
Longitudinal Centre of Gravity	LCG	1.488	2.976	111.593	m
Wetted area	S	1.694	6.777	9530	m^2
Speed	U	0.535	0.756	4.630	m/s
Reynolds number	Re	1.840×10^{6}	5.205×10^{6}	1.195×10^{9}	-
Dynamic viscosity	μ	$\mathbf{8.8871\times10^{-4}}$	3.1421×10^{-4}	1.3683×10^{-6}	Pa-s
Depth Froude number	F_h	0.303			-

In Chapter 3, the same approach alongside linear scaling and demonstrated that the approach provides results that are close to those obtained by a traditional double body simulation (Terziev et al., 2019a). Sezen and Cakici (2019) performed a similar study, but arrived at the opposite conclusion. This is the case for several reasons. Firstly, in Chapter 3, solely double body simulations were performed using the approach referred to as "viscous scaling". This eliminates the issue of viscous effects on the free surface, resulting from the change in the physical properties of the fluid surrounding the ship. However, in the evaluation the performance of the viscous scaling approach, the authors (Sezen and Cakici, 2019) assumed that the residuary coefficient must remain constant. Moreover, the initial methodology of Haase et al. (2016a) validates a grid in model scale, then repeats the simulation with a change in the viscous properties of the fluid. No change in mesh was originally envisioned. Although it is true that the y^+ values cannot remain the

same between the different case-studies, a change in mesh characteristics voids the first step, in which validation is performed. In addition, the approach's appeal is expressed in the fact that low cell numbers can be used to perform a full-scale simulation. Reconstructing the mesh and matching the y^+ values negates this appeal as it corresponds to a drastic increase in cell numbers.

Once the viscously scaled simulation has run its course, the results are multiplied by the ratio of scale factors to the third power, thus correcting the discrepancy in linear dimensions.

5.2.1 Numerical implementation

The placement of the inlet and outlet boundaries follows the recommendations of ITTC (2011) and is shown in Figure 5.1. The domain top is placed at 1.25×L from the undisturbed water surface, where a velocity inlet condition is imposed. The domain bottom is set to match the experimental condition of h/T=2.2 in all scales, specified as a velocity inlet. Such a boundary condition guarantees that there will be no relative motion between the fluid and the seabed. A velocity inlet may also be preferable due to the fact that open boundaries have a stabilising effect on the numerical solution. In any case, the use of velocity inlets to represent the domain bottom has been validated in recent studies (Elsherbiny et al., 2020). The side boundary is also positioned following the experiment, at 2.3m from the ship centreline in λ=75, and is scaled accordingly. The accompanying mesh for the full-scale multiphase simulation is shown in Figure 5.2, whereas Table 5.2 contains the resulting cell numbers for all simulations. It should be noted that the multiphase simulation for λ=75 corresponds to the cell numbers used for viscous scaling. To ensure that the longitudinal extent of the computational domain does not impact detrimentally the solution, the domain was extended by one ship length on either side of the ship and the simulation repeated. This revealed no discernible change in the results. The near-wall mesh is set to maintain an average of y^+<1 in all model-scale computations, whereas its average value in full-scale is approximately 300.

The latter value is thought to provide sufficiently accurate results for full-scale simulations (Peric, 2019).

The simulations which contain both air and water and represent the experimental set-up as accurately as possible are labelled as multiphase. Here,

the interphase between the two mediums is modelled by the Volume of Fluid (VOF) method (Hirt and Nichols, 1981). This is a standard approach adopted in the vast majority of marine CFD where the resolution of the free surface is important. The VOF method is also used in Star-CCM+ to model air and water currents and therefore the ship's speed. This is done via the concept of a flat wave, and is set appropriately for each scale, as shown in Table 5.1. The velocities specified at the inlet boundary, while the outlet is required to maintain the hydrostatic pressure.

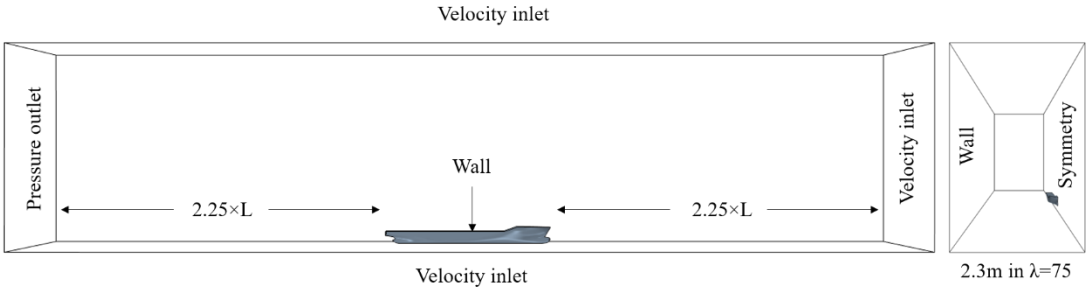

Figure 5.1. Domain characteristics and boundary conditions

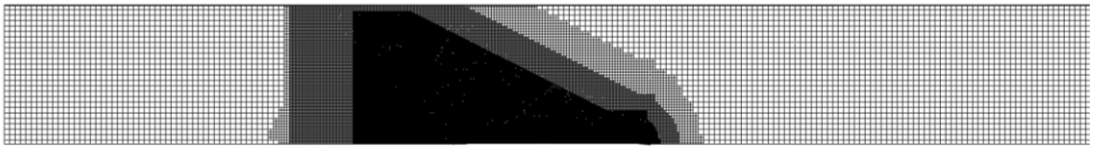

Figure 5.2. Full-scale mesh generated in Star-CCM+

Table 5.2. Cell numbers for all simulations.

Scale factor	1	37.5	75
Multiphase	26644375	7938801	4046168
Double body	14339889	2387454	1050032

To enable the assessment of scale effects, an estimate of the wave resistance and form factor is necessary. In CFD, these can be extracted by performing what is known as a double body simulation. In essence, this is equivalent to replacing the free surface with a symmetry plane. Thus, wave resistance is no longer a component of the total, as shown in Eq. (5.1a) for multiphase regime, and Eq. (5.1b) for double body regime:

$$C_T = C_F \times (1+k) + C_W \quad (5.1a)$$

$$C_T = C_F \times (1+k) \quad (5.1b)$$

In Eq. (5.1a) and Eq. (5.1b), all resistance parameters are shown in non-dimensional form, achieved by division by $0.5 \times S \times U^2 \times \rho$, where S is the wetted

area in m^2, U is the ship velocity in m/s, and ρ is the water density (997.561 kg/m^3). To obtain the wave resistance, one must simply subtract the total resistance in double body mode from the multiphase condition, while the form factor $(1+k)$ is obtained by division of C_{Tdb} by C_{Fdb} (Eq. (5.1a) and Eq. (5.1b): C_{Tdb}/C_{Fdb}) (Molland et al., 2017), where the m subscript refers to multiphase solutions, while db indicates double body. It is important to note that CFD predicts ship resistance (C_T) as the sum of normal (pressure resistance C_P – which contains 3D effects (viscous pressure) as well was wave resistance (C_W)), and tangential (frictional resistance C_F) components. It should be noted that in this chapter, flat plate friction lines are not used to determine the form factor as is typically done according to the ITTC (1999). This done in favour of the frictional resistance coefficient obtained from CFD because this matric has been shown to be highly sensitive to ship underwater form as well as depth, rendering the usually used friction lines inapplicable to shallow waters. In other words, the approach of Zeng et al. (2019) is followed.

The standard k-ω model (Wilcox, 2006) is adopted, as implemented in Star-CCM+ version 13.06.012. The stability and consistency of the k-ω model for the class of problems examined here was demonstrated in Chapter 4 (Elsherbiny et al., 2020). Moreover, it proved the least computationally expensive two-equation turbulence model. The k-ω model showed an increase in solution time of 8% compared to a one-equation turbulence model, whereas the k-ε model increased the wall time by approximately 16%. As a result of the high relative importance of turbulent properties, the convective term is set to 2nd order.

The temporal evolution of the solution is resolved via a first order implicit unsteady scheme, with a time step (Δt) equal to $\Delta t = 0.0035 \times L/U$. This has been demonstrated to be a good choice in several works, and is adopted (Tezdogan et al., 2016a). However, it is important to state that any discretisation of the temporal term of the Navier-Stokes equations will inevitably result in some numerical error. These are explored in the following section. The remaining physics, modelled by the incompressible RANS equations, are solved for numerically via the segregated flow solver offered in Star-CCM+. More details can be accessed in Siemens (2018).

5.3 Results and discussion

5.3.1 Verification study

As mentioned previously, the first step in the procedure is to determine the uncertainties of the numerical set-up of λ=75. The predicted multiphase total resistance coefficient (5.123×10^{-3}) shows reasonable agreement with the experimental value (5.505×10^{-3}), underpredicting the result by -6.85%. This is thought to be sufficiently accurate, especially considering that in the experiment, the ship was allowed to sink and trim, whereas during the numerical simulation it was kept fixed. The verification study is presented in Table 5.3 for spatial and Table 5.4 for temporal discretisation, respectively. It should be noted that the relevant equations and relationships used in the production of Table 5.3 and Table 5.4 are omitted. Instead, the reader is referred to the report by the ITTC (2017b). To compute the numerical uncertainty, the Grid Convergence Index (GCI) is used, which is typically treated as the standardised approach to reporting numerical uncertainties.

Table 5.3 and Table 5.4 contain the grid and time-step studies for the numerical simulations in both physics regimes (multiphase and double body). The results indicate that the largest uncertainty can be expected from the multiphase RANS simulation (3.348%). In terms of temporal dependence, the simulations do not show significant errors. According to Table 5.3 and Table 5.4, the numerical simulations (regardless of physics approach) are more sensitive to grid refinement than they are to a change in the time step.

The choice of refinement ratio is of critical importance in verification studies (Phillips, 2012). This is used as a multiplicative factor to the grid size or time step to coarsen the grid. The choice of $\sqrt{2}$ is chosen in line with the recommendations of the ITTC (2008). In general, the refinement ratio should be chosen to attain a value between 1.1 and 2, as suggested by ASME (American Society of Mechanical Engineers, 2009).

The achieved grid numbers were as follows. The double body cell numbers for the medium and coarse solution numbered 679,472 and 480,040, respectively. Similarly, the multiphase cell numbers were 2,384,829 and 1,395,411. In the process of coarsening the mesh for the verification study, the properties of the mesh used in defining the surface of the ship have been maintained identical. This is done to preserve an accurate representation of the ship geometry in the

process of determining the numerical uncertainty. Such an approach was adopted by Tezdogan et al. (2016b, 2015) and is followed here as well.

The wave resistance coefficient's numerical uncertainty characteristics are also shown in Table 5.3 and Table 5.4 for spatial and temporal discretisation, respectively. Here, C_W is calculated as the difference of the multiphase and double body resistance values at each refinement level. In the case of time dependence, the double body simulations exhibit a smaller variation in resistance characteristics than the multiphase results. Therefore, C_W is predicted to exhibit an oscillatory behaviour. For this case, the modified relationships, as given in the recent work of Song et al. (2019) are used to predict the uncertainty, since they can cope with oscillations in the data.

Table 5.3. Spatial discretisation-induced numerical uncertainty (for λ=75). The wave resistance coefficient listed in this table was arrived at by subtracting the double body resistance from the multiphase resistance.

Parameter	Multiphase resistance	Double body resistance	C_w
Refinement ratio	$\sqrt{2}$	$\sqrt{2}$	$\sqrt{2}$
Fine	5.123×10^{-3}	4.752×10^{-3}	0.371×10^{-3}
Medium	5.607×10^{-3}	4.745×10^{-3}	0.862×10^{-3}
Coarse	6.877×10^{-3}	4.720×10^{-3}	2.157×10^{-3}
Convergence	Monotonic	Monotonic	Monotonic
Order of accuracy	2.792	3.377	2.798
GCI (%)	3.348	0.020	0.014

Table 5.4. Temporal discretisation-induced numerical uncertainty (for λ=75). The wave resistance coefficient listed in this table was arrived at by subtracting the double body resistance from the multiphase resistance.

Parameter	Multiphase resistance	Double body resistance	C_w
Refinement ratio	$\sqrt{2}$	$\sqrt{2}$	$\sqrt{2}$
Fine	5.123×10^{-3}	4.752×10^{-3}	0.371×10^{-3}
Medium	5.215×10^{-3}	4.793×10^{-3}	0.422×10^{-3}
Coarse	5.293×10^{-3}	5.010×10^{-3}	0.289×10^{-3}
Convergence	Monotonic	Monotonic	Oscillatory
Order of accuracy	2.472	4.79	2.8930
GCI (%)	1.109	0.016	0.0012

The uncertainty estimation technique also requires that other sources of error are small. These include round-off error and iterative error (Ferziger and Peric, 2002). The former is thought negligible in most cases, whereas the latter can have a significant impact. Iterative errors are assessed via the procedure of Roy and Blottner (2006). The results suggest that the smallest iterative errors are found in the case of double body simulations are negligible. On the other

hand, the RANS multiphase simulation demonstrated an iterative error of *circa* 0.08%, which is considered sufficiently small. To ensure that the solution has converged, the resistance time-history is monitored alongside the residuals. The former are allowed to decrease by at least three orders of magnitude before the solution is stopped.

5.3.2 Numerical results

In this section, the computed skin friction data are shown for each scale factor according to the three different methods in Figure 5.3 along some established friction lines. Here, it is evident that the viscous scaling procedure may be used with good accuracy to determine the frictional resistance coefficient. This conclusion may be drawn from the fact that the difference between the linearly scaled multiphase predictions and their viscously scaled counterparts are not substantial. These seem to increase as the Reynolds number approaches its full-scale value, where the viscously scaled simulation predicts the skin friction within 0.1% of the double body result.

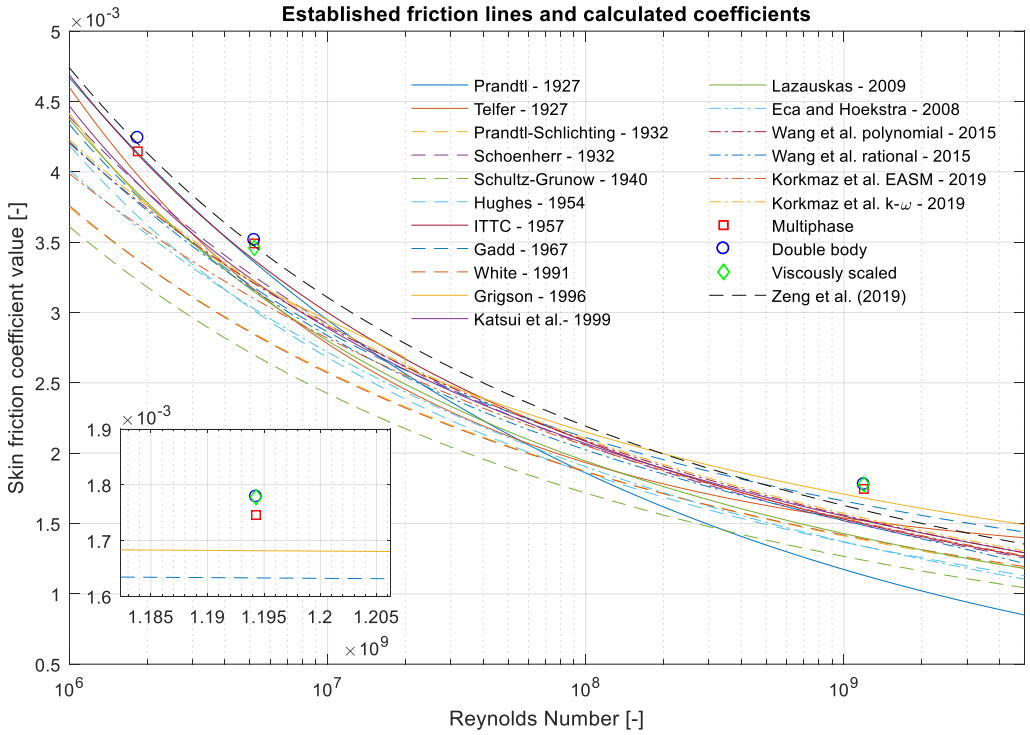

Figure 5.3. Skin friction coefficients calculated at each scale and established friction lines, used to demonstrate the relative difference between the shallow water line of Zeng et al. (2019) compared to other predictions.

Discrepancies between double body and multiphase results may stem from a variety of sources. These include the small changes of the wetted surface area resulting from the deformation of the free surface. Such effects have been neglected in the present study. Alternatively, research has shown that vortex shedding is modified as a result of the presence of a free surface (Suh et al., 2011). Moreover, such an influence has been documented experimentally by Dand (1967). The same researcher also predicted co-dependence of wave and frictional resistance of a flat plate. Thus, the changes observed in the frictional resistance coefficients are not strictly a manifestation of numerical assumptions.

Now, it is important to put the findings presented in Figure 5.3 in context and compare the data with other research conducted recently. For this purpose, the friction line, specifically designed for the KCS in shallow water by Zeng et al. (2019) is included alongside the remaining friction lines. One may draw an immediate conclusion that the frictional coefficient is predicted with high accuracy in both model scale factors examined. Indeed, the line of Zeng et al. (2019) outperforms any of the remaining lines in the field. Naturally, this is solely due to the shallow water effect, which is not accounted for in the derivation of any other friction line. However, the full-scale results derived from the present study indicate a problematic trend.

In reaching full-scale Reynolds numbers, the friction line of Zeng et al. (2019) exhibits too great a slope. Thus, the frictional resistance coefficients do not agree well with the data found here. Simultaneously, lines with milder slopes, specifically that of Grigson (1999) and Gadd (1967) are closer to the full-scale data. This suggests that at full-scale, the frictional resistance coefficient may be affected by the depth restriction to a lesser extent (especially considering the fact that Gadd's (1967) line was also found to be in good agreement with deep water predictions in Chapter 3). The information presented here also points towards the fact that lateral restrictions might not impact the ship resistance significantly in terms of frictional resistance. That is at least at the restriction level posed by the adopted case study. However, one may expect that upon reaching significantly more restricted waters, such as narrow canals, the bank effect would be noticeable in the frictional resistance coefficient. In summary, the friction line of Zeng et al. (2019) is shown to perform well in model scale. To determine if the observed discrepancy in full-scale is due to the numerical set-up adopted here requires further research.

For instance, it may be the case that in full-scale, the effect of the bank is greater than in model scale. To prove or disprove this, analysis is required for different widths, although an attempt at quantifying such an influence is made later in this section. Such assessments do not seem popular in the literature due to the fact that the water depth has a greater bearing on the parameters of interest. One final aspect of the solution that one should consider is the highly specific nature of the friction coefficients and associated line devised by Zeng et al. (2019). The solution included in Figure 5.3 was generated specifically for the KCS. Indeed, within their work, Zeng et al. (2019) produced lines for two other hull forms. Unfortunately, generalisations to other ships are not possible due to the highly specific nature of the flow in shallow water, which depends heavily on the ship form. This also points to the fact that each underwater shape influences the frictional resistance even in deep waters. Thus, the use of friction lines universally might not be the best approach.

To further support the argument laid out previously, that a free surface modifies the boundary layer, Figure 5.4 depicts the numerical boundary layer extents in the smallest and largest scale factors. Typically, the extent of the boundary layer is taken as the location where the velocity near a body reaches 99% of its free stream value. In the present case, it was found that such a condition does not lead to a single line, rather, to a small area where the flow attains practically the same speed. For illustration purposes, the boundary layer definition has been slightly altered to 90% of the free stream velocity. This is sampled at four locations, namely, at the forward perpendicular, amidships, at $0.25\times L$ and at the aft perpendicular.

Even after restricting the definition of the boundary layer, it is apparent that amidships the flow velocity near the free surface exhibits several z/L points with the same velocity for a single y/L position. However, it is not thought necessary to restrict the boundary layer definition further as this may impact the resulting data detrimentally. Specifically, the difference in distribution of velocities within the boundary layers of different speeds will reduce as one approaches the solid boundary, where the flow is stationary with respect to the body.

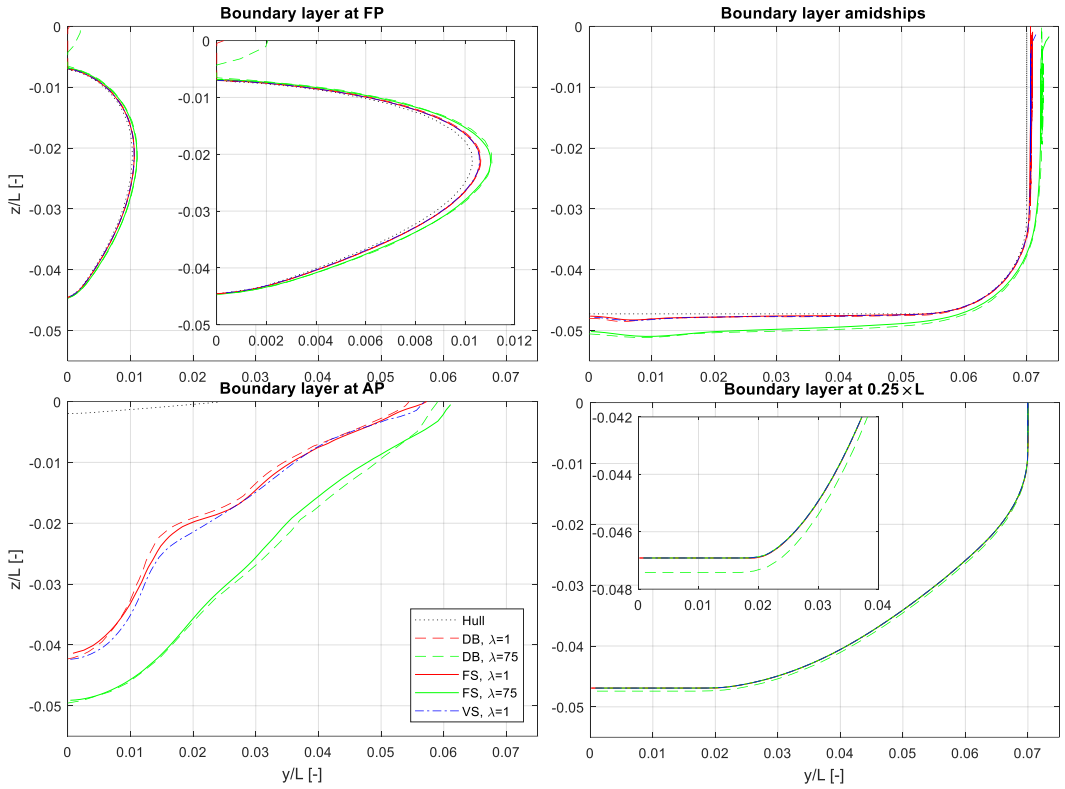

Figure 5.4. Predicted boundary layer thickness at different scales.

As asserted earlier, all subplots within Figure 5.4 confirm that at full-scale the boundary layer is thinner. However, the reduction in thickness at the aft perpendicular is seen as the largest. The well-known keel vortex is prevented from forming in the present case study likely due to the proximity of the seabed. This causes the flow to accelerate as the water is passes beneath the ship. Nevertheless, amidships in model scale, connotations of an increasing boundary layer thickness are observed. This phenomenon is predicted by both the free surface and double body method in λ=75. However, the full-scale results exhibit an even weaker vortex (Zeng et al., 2019), this specific feature being hardly discernible in both multiphase and double body simulations for λ=1. It should be noted that in their recent work, Song et al. (2019) obtained similar results in terms of boundary layer thickness variations.

In terms of viscous scaling, it is evident that the method performs adequately. To elaborate, the boundary layer seems to follow the full-scale prediction closely. It is also important to note that in model-scale, the free-surface effect is visible at the forward perpendicular, amidships and at the aft perpendicular, where the boundary layer broadens as it approaches z/L=0. The same locations

are characterised by the absence of the viscously scaled method's boundary layer, in agreement with the full-scale data.

The fact that the viscously scaled predictions model similar behaviour near the free surface is encouraging. However, there is an apparent difference between the frictional resistance coefficients predicted by this method and the linearly scaled simulations. This may stem from a difference in the wetted area, which has been assumed constant (in non-dimensional form) throughout all cases. To further elucidate the potential influence of such an effect, Figure 5.5 contains the free surface elevations for the largest and smallest scale factors on the ship hull. The intermediate scale has been omitted to allow a clearer depiction of the generated results.

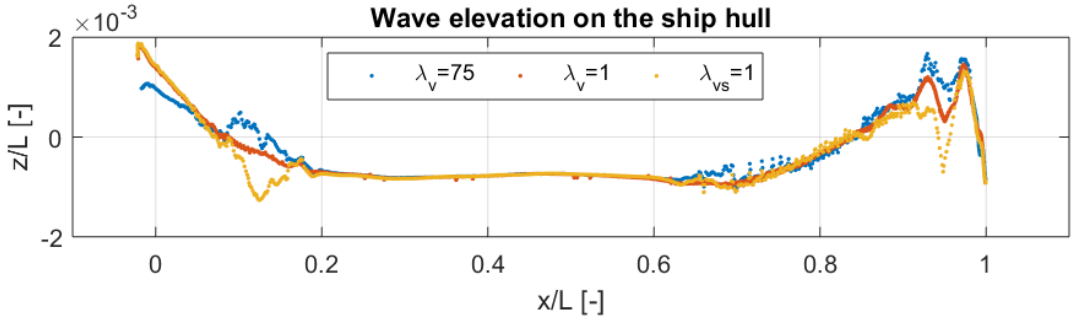

Figure 5.5. Comparison of the wave elevation on the ship hull.

For consistency, all dimensions have been normalised by the ship length in Figure 5.5. Here, the result label with a "vs" subscript indicates the viscously scaled result in full-scale. Figure 5.5 shows that better agreement with the full-scale result is achieved near the stern of the ship via the viscously scaled model, rather than λ=75. Therefore, viscous effects are of lesser consequence in full-scale. This may be deduced by considering the fact that the viscously scaled simulation features a value of viscosity, that is significantly lower than one would normally observe (Table 5.1 may be consulted for the values).

To provide supporting evidence for the observed phenomena, the reader is directed to the work of Brard (1970) and Tatinclaux (1970), who demonstrated that the action of viscosity, vorticity and turbulence are expected to have an impact on the flow properties. The abovementioned authors studied the effects of viscous, vortical flows on the wave resistance of a ship. Their findings include that a viscous contribution may be identified as part of the wave resistance of a ship.

At this stage, it is worthwhile exploring the reason why potential flow theories do not account for wave elevation changes and the related consequences. According to Brard (1970), vortical and turbulent effects act on the ship in a manner proportional to $1/(Re \times F_h^2)^{1/3}$ in terms of local waves and $1/(Re \times F_h^4)$ in terms of far field waves. Unfortunately, the analysis presented in Brard (1970) is for deep, unrestricted waters. The relative magnitude of the aforementioned terms is shown graphically in Figure 5.6. However, one may reasonably expect the above effects to be of greater significance in restricted shallow waters. Thus, no logical contradiction is expected when carrying the above relationships to the present analysis. Since the depth Froude number has been maintained constant, it is not though necessary to examine the specific relationships as a function of this particular parameter. Instead, Figure 5.6 depicts the relative contribution of each wave component (far-field and near-field) with increasing Reynolds number.

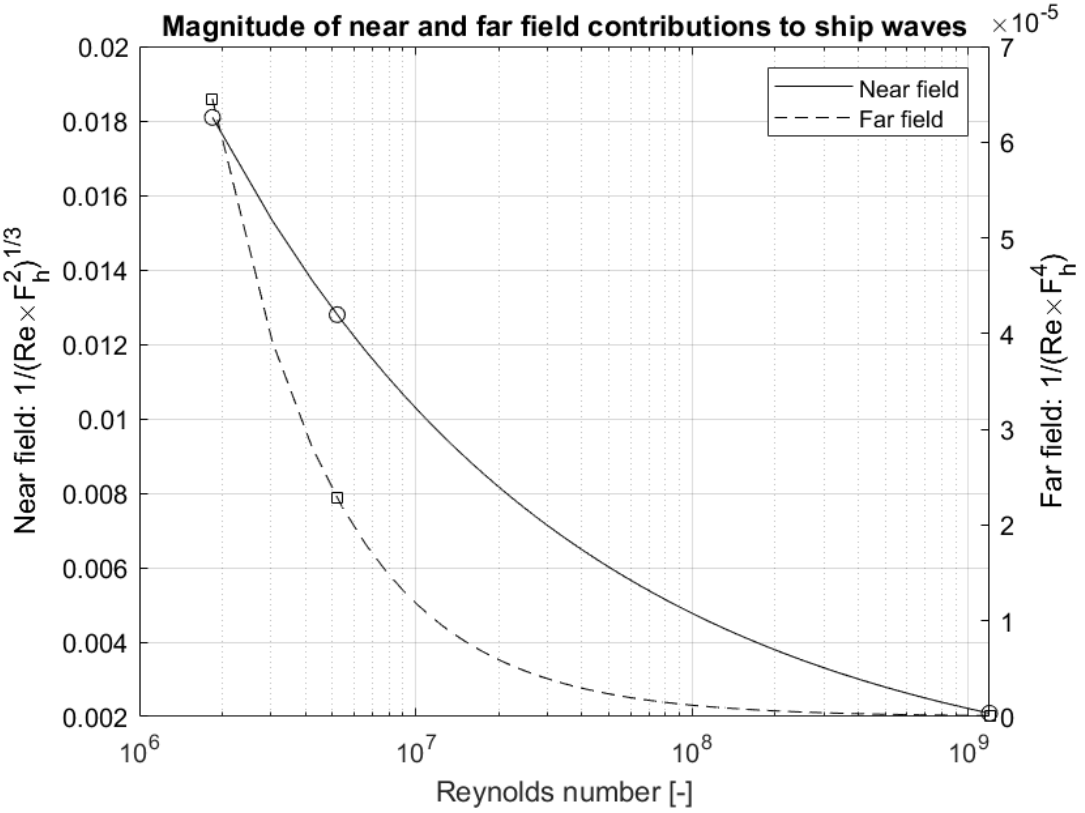

Figure 5.6. Effect of viscosity and turbulence on near and far field waves according to Brard (1970).

Figure 5.6 suggests the assertion that viscous effects are of lesser consequence at full-scale in Figure 5.5 is justified according to the mathematical analysis of Brard (1970). Although the present case studies are restricted to a single speed

for which no far field waves are present, it is worthwhile to comment on their potential effect. If a ship propagates at a speed where far field waves are generated, regardless of the water depth and/or restriction, the effect in the far field waves is expected to be greater than that in the near field disturbance. This follows because although the region where viscous effects dominate has become smaller, it has not completely disappeared. Thus, significant proportions of the near field disturbance will be generated and will lie within this region. Conversely, the far field waves will be impacted by a smaller wake, as demonstrated in Figure 5.4.

As a certain Reynolds number (~10^7) is passed, the relative difference between the model and full-scale waves decreases rapidly. This may be confirmed by examination of Figure 5.6, where it is apparent that the slope of the far field effect is nearly zero for Reynolds numbers past 10^8. A small effect may be expected because the majority of changes in the wake occur in the region Reynolds numbers in the region of $10^6 – 10^7$. Coincidently, this is the region where all model tests are performed due to size limitations. Thus, it may be an inescapable fact that such effects cannot be negated completely by adopting a model with greater linear dimensions. This is also augmented by the fact that as one enters the lower range of Reynolds numbers, both curves increase in magnitude rapidly.

The effects demonstrated in Figure 5.6 are typically omitted from potential flow theories, even when a nonlinear vortical flow is sought. This is the case because of the small relative magnitude both the near and far field disturbances exhibit, as well as their nonlinear nature. Therefore, an analysis where terms to, say, second order are sought would justifiably not take these terms into account (Brard, 1970; Tatinclaux, 1970).

The next step is to examine the predicted wave resistance. This is shown in Figure 5.7, using the aforementioned methods (viscous and viscous scaling). The viscously scaled wave resistance coefficient is estimated by subtracting the total resistance as scaled (viscously) and the double body resistance at the specific scale factor.

Figure 5.7 clearly shows that the methods agree in terms of trend – an overall reduction as the scale factor approaches full-scale is observed. Not surprisingly, the predictions follow a pattern closely resembling that of Figure 5.6, characterised by a sharp decline in the low Reynolds number range, followed by a mild slope. As demonstrated previously, the smallest linear

dimensions coincide with those where the viscous effect is expected to be highest. Therefore, the difference between the wave resistance observed at the two adjacent model scale factors is justified. The source of the persistent discrepancy between the methods is likely related to the assumptions in terms of viscosity and double body approximation, although one would expect this to decline further if the Reynolds number were to be increased.

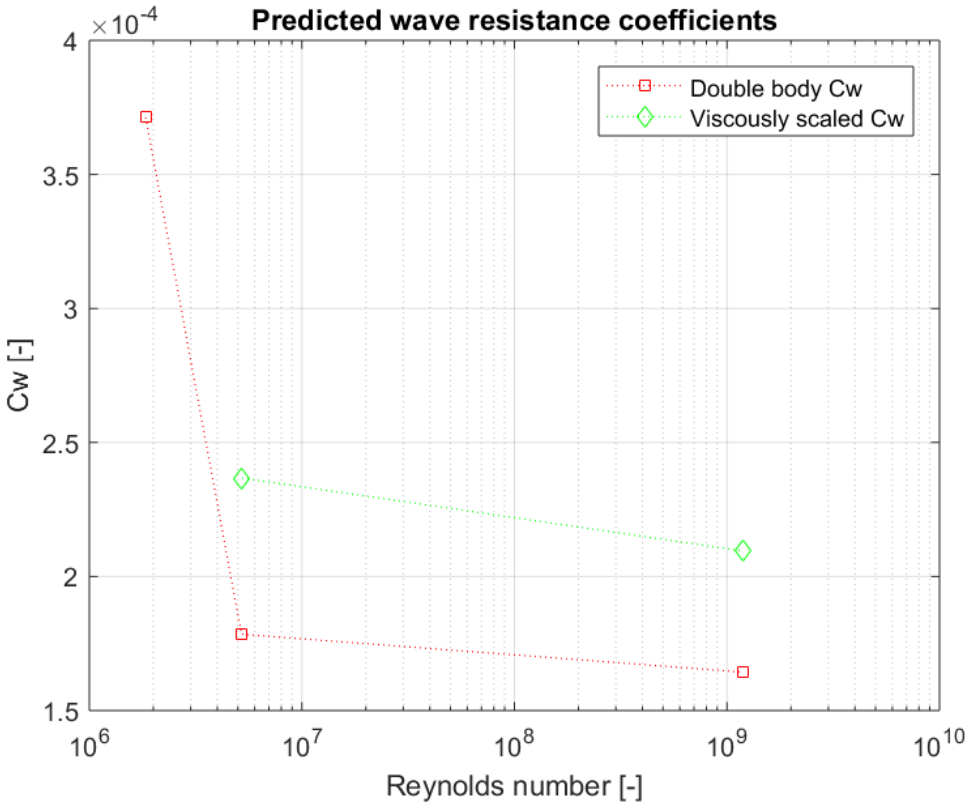

Figure 5.7. Predicted wave resistance coefficients.

Prior to providing further justification of the results shown thus far, the final set of data is presented. Specifically, Figure 5.8 depicts the predicted form factors. The overall trend observed in the figure is that of reduction in (1+k) with higher Reynolds numbers. The best-behaved curve is that calculated via the multiphase method. Indeed, the experimental work of Elsherbiny et al. (2019) suggested the form factor should be in the region of 1.16. The double body prediction seems to resemble this to a lesser extent, and as the scale factor is increased, the data do not decrease monotonically as is the case with the multiphase results.

However, it is not possible to asses scale effects in (1+k) in the absence of experimental data for each scale factor. Moreover, the multiphase method is not characterised by an increase for λ=37.5. This points to the fact that the

double body simulation at λ=37.5 may be inaccurate rather than the multiphase one. The change in form factor may be justified by referring to the recent work of Zeng et al. (2019). In the aforementioned work, the authors derived a similar shape for (1+k). The authors also defined a new relationship for the form factor of the KCS sailing in shallow waters, which is employed in Figure 5.8.

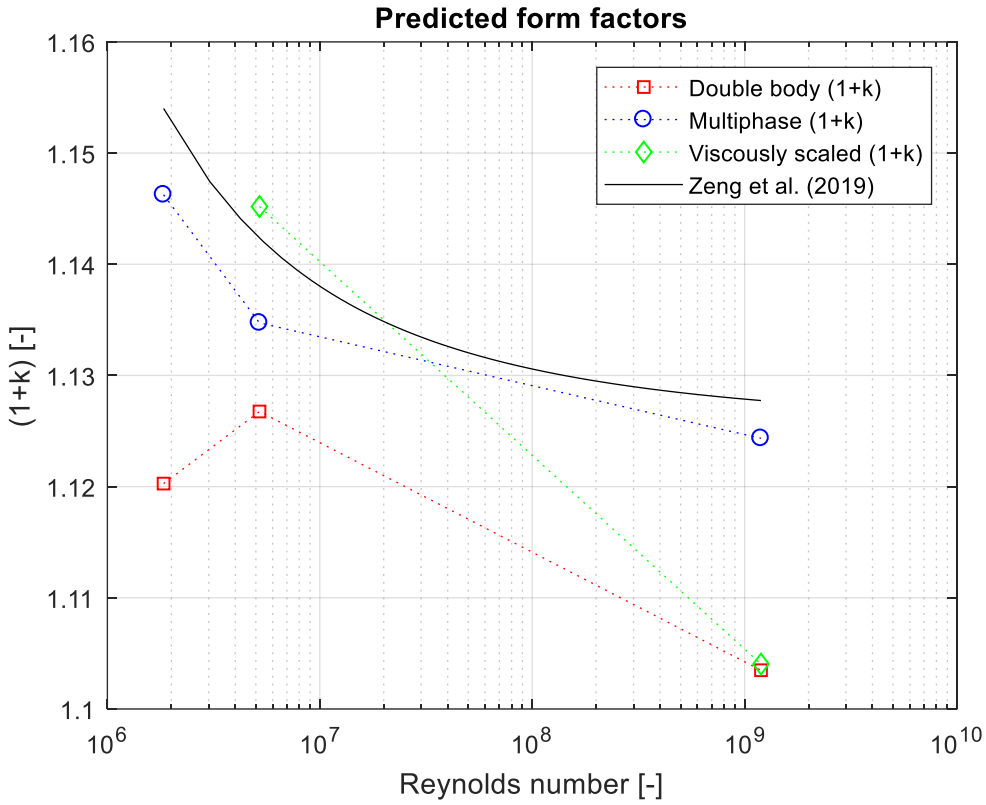

Figure 5.8. Predicted form factors.

The relationship defining the solid line in Figure 5.8 due to Zeng et al. (2019) does not take into account the lateral confinement, which is the suspected cause of the observed difference. However, the agreement between the multiphase data and the approximation of Zeng et al. (2019) is seen to be good. Thus, the results confirm the efficacy of the method determined in the previously mentioned reference. Unfortunately, the curve fitting approach used to derive the relationship must be performed anew for each ship. This is because no method is known to determine such an equation for any ship without the presence of data to fit. To prove that the lateral confinement's effect is not as significant as the depth restriction, the velocity distribution along a line in the x –z plane at the aft perpendicular is used. An example of this for [x/L, z/L]=[0, 0.5T] is shown in Figure 5.9, where the velocity has been

normalised by the free-stream velocity. In the present context, this is defined as the flow velocity specified at the inlet. The specific location is chosen in line with the significant difference in boundary layer thickness observed in Figure 5.4.

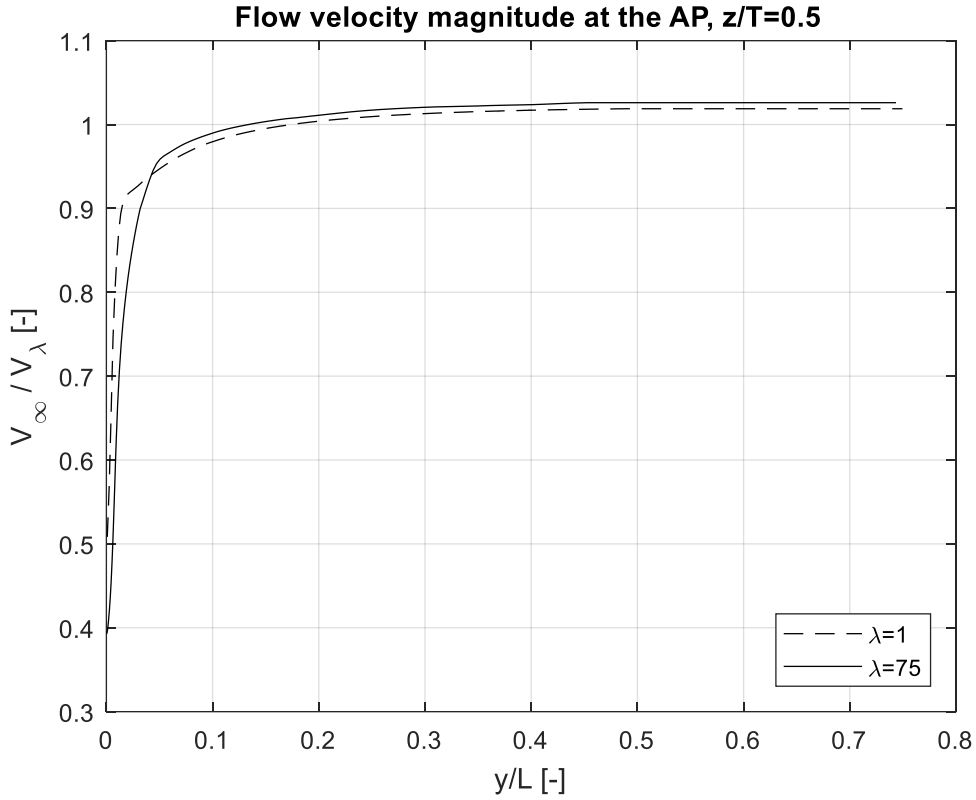

Figure 5.9. Velocity distribution along a line at the aft perpendicular, z=0.5T. Depicted: multiphase simulations, λ=75 and λ=1.

It is apparent in Figure 5.9 that the flow is accelerated in a different manner in the two scale factors. More importantly, the flow speed achieved near the tank wall (which is set as a slip wall and therefore does not impact the flow velocity as a no-slip wall would) is higher than the free-stream velocity. In λ=75, the flow velocity is 2.6% higher, whereas in λ=1 – 1.9% higher than that specified at the inlet. In other words, a net difference of 0.7%. Although one may argue that this is not a significant difference, its impact is nonetheless of some, albeit small importance to the ship, particularly on the frictional resistance. The manner in which the different scale factors achieve their maximum flow speeds near the wall is different from one another. Thus, the results from can be used to signify that in full-scale, side wall effects are of (slightly) smaller influence than in model scale factors.

Importantly, Figure 5.9 suggests that flow properties do not scale linearly in highly restricted waterways. Had this been the case, no difference would be present in the curves shown in Figure 5.9. Therefore, forming a geosim series in such conditions is not as straightforward as simply scaling the tank dimensions. In practice, tanks equipped with false bottoms could be used effectively in this respect. However, if one is to accept the results associated with Figure 5.9, then the tank dimensions should scale non-linearly. The manner in which this should occur is not known at present, but correction methods similar to Raven (2019) could be considered as a starting point. The issue with such corrections is that they are inherently designed to remove side wall effects, whereas one might wish to maintain this influence when designing, say, a canal boat, or river cruise ship.

The results presented in Figure 5.9 should also be considered in conjunction with the boundary layer thickness assessment carried out in Figure 5.4. These jointly suggest that the influence of the water depth scales non-linearly as well as the width. Thus, rendering the possibility of forming a geosim series in shallow water of infinite width equally complex. In fact, the greater proximity of the seabed amplifies the influence of the boundary. Effects of this kind were used as a justification for at the onset. It could be considered that these have been proven to a sufficient extent.

The collapsing difference between an infinitely wide water case-study, where the velocity ratio would reach unity, and the canal case explains the discrepancies observed between the present CFD method and the data of Zeng et al. (2019). Specifically, in the low Reynolds number range, the relative difference between the predicted (1+k) and the method of Zeng et al. (2019) is larger than at high Reynolds numbers. This observation fits neatly with the presented data.

5.4 Summary and conclusion

This chapter presented a numerical assessment of scale effects of a ship advancing through a canal. To assess the scale effects, a geosim series was formed and evaluated at three different scale factors. The numerical methods used comprise RANS-based multiphase and doubly body simulations. These enabled the assessment of the form factor and wave resistance.

Comparison with recently developed equations describing the frictional resistance revealed excellent agreement with the present CFD set-up in model-scale. For high Reynolds numbers, the large slope of the curve terminated at

too low values according to the present CFD method. The aforementioned equations were developed for an infinitely wide shallow water case. Results quantified the influence of the particular canal as small. The flow being accelerated by less than 3% in locations near the wall as a result of the reduced clearance in model scale.

Scale effects on the accelerated velocity were demonstrated in the case of flow near the ship and canal walls. This amounted to 0.7% difference between model and full-scale. In terms of boundary layer, the CFD set-up captured the well-known decrease in thickness. A measurement of the velocity profiles at the aft perpendicular also suggested that the wake volume as a fraction of the ship's displacement is also significantly reduced from model to full-scale.

The predicted form factor showed good agreement with recently established relationships for the KCS. This parameter, along with the wave resistance exhibits a monotonic decline until full-scale. This was confirmed by invoking well-known mathematical analysis which suggests the influence of vorticity and turbulence on the ship decay rapidly with increasing Reynolds number.

6. A Posteriori Error and Uncertainty Estimation in Computational Ship Hydrodynamics

This chapter presents the application of local and global numerical uncertainty estimators and provides a framework to interpret solution data and what it suggests with regards the computational grid's performance in view of demonstrating a small numerical error. The analysis is performed on a set of full-scale simulation because high Reynolds number flows are difficult and expensive to measure experimentally. Therefore, it is frequently the case that one lacks validation data for full-scale flows. Such conditions are where numerical error estimation has the highest value in simulation-based design.

6.1 Introduction

The year 2014 saw the publication of NASA's study on the future directions of Computational Fluid Dynamics (CFD) (Slotnick et al., 2014). Although their focus was predominantly on aerospace applications, several aspects overlap significantly with the field of computational ship hydrodynamics. This prompted Hawkes et al. (2018) to address one of the concerns raised by Slotnick et al. (2014), specifically, scalability problems of CFD simulations with increasing cell numbers.

A second key bottleneck, identified by Slotnick et al. (2014), is associated with solution uncertainty and robustness. This is directly related to the confidence

levels one can attribute to a numerically derived solution. Such metrics are of critical importance in simulation-based design. Since computational power increases exponentially, it is reasonable to anticipate that Reynolds averaged, or other Navier-Stokes-based techniques will eventually become the norm in most forms of engineering analysis. Ship hydrodynamics is by no means an exception to this statement.

One issue that remains challenging is that of grid generation. At present, constructing a mesh, onto which the solution of the governing Partial Differential Equations (PDEs) is to be obtained is as much an art as it is a science. This is true especially in cases where the requirements in terms of accuracy are high, as is often the case in ship hydrodynamics. Specifically, with ever tightening EEDI-related (Energy Efficiency Design Index) regulations, margins of error and uncertainty are slim. It is therefore imperative that once the practitioner has invested in performing what is currently the state-of-the-art analysis method in ship hydrodynamics, he/she can obtain an adequate margin of error associated with the solution. In other words, it is critical to determine the confidence one can place in the numerical solution, and discount specific results if necessary.

Lack of robust procedures to address confidence levels in numerical data that do not require user intervention (i.e. are automatically generated) is one of the key issues hindering in the large scale adoption of simulation-based design (Slotnick et al., 2014). This is particularly true of ship hydrodynamics which inherently features turbulent flows and fluid interfaces. These require knowledge of the simulation-specific phenomena, such as wakes and free surface deformations, where the computational mesh must be refined to capture the underlying physics well. Therefore, a key issue is related to mesh definition, which is almost always the greatest source of error (Eca and Hoekstra, 2006). Although grid sensitivity studies are frequently performed in an academic context, their outcomes are not always understood according to Salas (2006). In industrial applications on the other hand, the analyst may simply consider a single mesh due to the perception that error estimation is difficult and time consuming (Freitas, 2002).

This chapter will describe in detail, and demonstrate the use of a method developed by Cadafalch et al. (2002), and supplemented by Phillips and Roy (2017). This method utilises well-known procedures to predict the numerical error in the domain, simultaneously equipping the analyst with a measure of how well the grid has performed in reducing the numerical error. Full-scale

simulations are sought in line with the fact that high Reynolds number flows are difficult to experimentally measure, and are where numerical work has the highest potential impact in simulation-based design (Stern et al., 2001). Specifically, the well-known KCS was simulated in shallow water, replicating the experiments of Elsherbiny et al. (2019) in a rectangular canal at full-scale. Use is made of the commercially available RANS solver, STAR-CCM+, version 13.06.011 to perform the present analysis.

The remainder of this chapter will continue by introducing the necessary background in section 6.2, followed by a description of the case study in section 6.3. The numerical set-up, and convergence properties of the solution are examined in Section 6.4. Finally, concluding remarks are given in section 6.5.

6.2 Background

The accuracy of CFD methods is of great interest in academia for several reasons. When compared to analytical methods, computational approaches have a greater breadth of application and are capable of addressing significantly more complex physical phenomena (Oberkampf and Blottner, 1998). The main advantage of analytical methods is expressed in the fact that they are built on sound, reproducible and traceable mathematical arguments. However, this is simultaneously their major drawback. Many processes of immense practical importance, such as the turbulent motion of a fluid, cannot be described analytically (Durbin and Pettersson Reif, 2011). If this were possible, turbulence closures would be exact, and the field of turbulence modelling would not exist in its current form.

On the other hand, by avoiding the issues relating to analytical modelling of physical phenomena, the CFD method runs into a separate set of problems. These mainly relate to the equivalence between the continuum form of the governing PDEs and their discrete approximations. Lilek and Perić (1995) separate the errors into three categories:

1. **Modelling errors**, which can be thought of as the difference between the exact solution of the equations describing the fluid flow (i.e. satisfying the conservative laws), and the actual flow. For laminar flows, the Navier-Stokes equations are sufficiently accurate, but to account for cases where turbulence is important, additional models are required (Jasak, 1996). These errors are separate from the numerical errors discussed here (Oberkampf and Blottner, 1998).

2. **Iterative errors**, which arise as a result of the nonlinearity of the governing equations. The iterative fashion in which these are solved introduces errors, also known as iteration convergence errors (Eca et al., 2013).
3. **Discretisation errors**, which stem from the mapping of the continuum PDE and their related auxiliary models (for example, the turbulence model) into algebraic equations. Formally, this 'replacement' of equations rests upon Lax's Equivalence Theorem (LET) (Lax and Richtmyer, 1956). In essence, LET contains two statements regarding the discrete approximation of the PDEs. Firstly, the numerical procedure must be consistent, i.e. as the discretisation length (or mesh length – h) approaches 0, the error must vanish. Secondly, the numerical method must be stable, i.e. if the one were to allow the solver to run indefinitely, the solution must remain bounded (Morton and Mayers, 2005). It should be noted that the LET is valid for linear initial value problems. As such, it is applied to the linearised form of the mapped governing equations.

Round-off errors are sometimes included in the above list. They can be traced to the finite digit storage on digital computers, but their influence is thought negligible (Roy, 2005). For this reason, their influence will not be discussed further. As mentioned above, modelling errors are not the primary focus and are therefore discounted. Iterative errors are thought of as a simpler problem. In any case, their approximation is important because numerical error and uncertainty estimators have a tendency of magnifying solutions with large iterative errors, or incomplete iterative convergence (Larsson et al., 2014). For the adopted case-studies, these have been estimated in the region of 10^{-4}% by using the procedure of Roy and Blottner (2006). Instead, the primary goal of is to apply to RANS-based ship hydrodynamics the discretisation error estimation procedures of local quantities and demonstrate their use. This is because the discretisation error category can account for more than 90% of all error (Xu et al., 2019). The use and application of discretisation error estimators is discussed in detail in the following sub-section.

6.2.1 Discretisation error

As stated previously, discretisation errors stem from the mapping of the continuum PDEs onto discrete locations. This is done by splitting the solution domain into a finite number of solution nodes. There are two methods to

combat discretisation errors. The usual approach is to increase the density of space or time intervals, which the region of interest is subdivided into (although spatial discretisation is of interest here). This is typically referred to as spatial or temporal refinement, but cannot guarantee the solution will be improved *per se*. The above is exemplified in the findings of Larsson et al. (2014). In the aforementioned work on numerical hydrodynamics, solutions obtained with less than one million cells were compared solutions produced by 20+ million grids from different participants. The graphical summary provided in Larsson et al. (2014) indicates that participants with low cell numbers often perform better than those with large cell counts. In other words, the arrangement, or properties of the grid are equally important in reducing errors (Salas, 2006). This is an issue that will be examined in the present work.

The alternative is to shift the focus from the subdivisions, explained above, towards equation discretisation. In the Finite Volume Method (FVM), which is used by Star-CCM+, the equation discretisation employed is 2nd order. A second order discretisation approach is typical of RANS solvers, and implies that according to Lax's equivalence theorem, the error must reduce with the square of the grid size for asymptotic grids (Roy, 2005). In other words, the formal order of accuracy of the simulation is two (p_f =2) (Roache and Knupp, 1993). Therefore, the second method to reduce the discretisation error would be to increase the formal order of accuracy, such as the 4th order accurate method, devised by Lilek and Perić (1995). In practice, the choices in this respect are limited to p_f=2. That is, unless the user is re-coding the entire RANS solver. Consequently, the focus of this chapter will be on discretisation errors, stemming from grid density. The first method devised for this purpose is the Grid Convergence Index (GCI), devised by (Roache, 1998).

The GCI method predicts an uncertainty, which is used to bracket the numerically calculated solution. The *true* solution is then expected to lie within this bracket 95 out of 100 times, i.e. with 95% confidence (Roache, 1997). The GCI method is based on Richardson's (1911) work, who devised a method to estimate a solution of fourth order accuracy based on second order finite differencing. Later, the approach, widely known as Richardson Extrapolation (RE), was improved upon by Richardson (1927). RE was originally formulated to use a refinement ratio (r) of two ($r = 2$), which translates into grid doubling. However, it can be used with any factor larger than 1.1. That is, as long as the produced solutions are both sufficiently different, and asymptotic, to enable

the validity of the method. This is in view of avoiding interference of other numerical errors (Roache, 1998).

The error of a numerical solution can be defined via a Taylor series expansion in the form shown in Eq. (6.1):

$$\varepsilon = f_{ex} - f_1 = \sum_{p=p_f}^{\infty} \alpha h^p = \alpha_{p_f} h^{p_f} + Higher\ order\ terms \tag{6.1}$$

where f_{ex} is the exact solution, f_1 is the solution of obtained on a grid with characteristic size *h*, and α is a constant. In the present context, the error is defined as the difference between the *exact* solution and the solution obtained with a grid spacing *h.* In an attempt to reasonably approximate the error, higher order terms may be neglected. Thus, reducing the form of Eq. (6.1) into:

$$\varepsilon \approx \alpha_{p_f} h^{p_f} \tag{6.2}$$

The omission of higher order terms requires that their combined effect is much smaller than the error derived at the formal order of accuracy. The implications of this are that the grid must be asymptotic.

The reason why Richardson Extrapolation is not used *per se* is that it provides a 50% confidence level, whereas GCI boasts of 95%, as stated earlier. This is achieved by magnifying the predicted numerical error by a Factor of Safety (FS). The value assigned to FS is clearly of high importance. In the GCI method, this is set as 3 when two grids are available, and 1.25 when three grids are used (Phillips, 2012).

Several methods have emerged in the recent past, many based on the GCI that attempt to modify the prediction of the FS. Some have made the FS a function of the observed order of accuracy, shown in Eq. (6.3) (Celik et al., 2008):

$$p = \ln\left(\frac{f_3 - f_2}{f_2 - f_1}\right) / \ln(r) \tag{6.3}$$

where *r* is the refinement ratio.
The fundamental notion is that if the observed and formal orders of accuracy are close, the grids are asymptotic. Otherwise, the GCI uncertainty diminishes rapidly with growing *p*, rendering unrealistically low numerical errors. Roache (1998) limited the observed order of accuracy to prevent this from occurring. Clearly, Eq. (6.3) can only be used when the argument of the natural logarithm in the numerator is positive and larger than 1. In other words, when the solutions exhibit monotonic convergence.

Unfortunately, the exact solution (f_{ext}) is known rarely, if ever, in fluid flows of practical interest. Using the order of convergence, one may re-write the error as a function of p:

$$\varepsilon(p) = (f_2 - f_1)/(r^p - 1) \tag{6.4}$$

The uncertainty, (U) is then simply the absolute error, as a function of the order of convergence, multiplied by the Factor of Safety:

$$U_{GCI} = FS \times |\varepsilon(p)|/(r^p - 1) \tag{6.5}$$

Clearly, the Factor of Safety is characterised by a step change (1.25 to 3) within the framework of the GCI method. Stern et al. (2001) implemented a correction factor (CF) approach to resolve this. In essence, their approach consists of introducing a correction factor, used to account for higher order effects. This is used to magnify the error predicted via Eq. (6.4). In the above work, the correction factor is introduced as a metric describing the distance from the asymptotic range, where Eq. (6.4) is thought to be inadequate. Thus, the error according to Stern et al. (2001) takes the form of:

$$\varepsilon_{CF}(p) = C \times (f_2 - f_1)/(r^p - 1) \tag{6.6}$$

where C is the correction factor, predicted as shown in Eq. (6.7):

$$C = (r^p - 1)/(r^{p_f} - 1) \tag{6.7}$$

Finally, the uncertainty can be estimated by:

$$U_{CF} = \begin{cases} [9.6(1-C)^2 + 1.1] \times \varepsilon_{CF} & when\ |1-C| < 0.125 \\ [2|1-C| + 1] \times \varepsilon_{CF} & when\ |1-C| \geq 0.125 \end{cases} \tag{6.8}$$

Alternatively, the Factor for Safety approach of Xing and Stern (2010) uses the normalised order of convergence (P), defined as the ratio of the observed and theoretical order of convergence ($P = p/p_f$). Based on the value, attained by P, the uncertainty can be estimated as shown in Eq. (6.9):

$$U_{REFS} = \begin{cases} (16.4P - 14.8) \times |\varepsilon(p)| & when\ P > 1 \\ (2.45 - 0.85P) \times |\varepsilon(p)| & otherwise \end{cases} \tag{6.9}$$

All methods described thus far rely, in one form or another, on the observed order of accuracy. However, approximating an error does not require any knowledge of p. Indeed, p is little more than the power, to which the grid (h) is raised to in the dominant term of the Taylor series expansion, as shown in Eq. (6.1). Following such an approach, Roy (2008) split the problem into first and second order components. Thus, the fine solution (f_1) can be expressed in

terms of the extrapolated solution and a set of error terms as demonstrated in Eq. (6.10):

$$f_1 = f_{exact} + g_1 h_1 + g_2 h_1^2 + Higher\ order\ terms \quad (6.10)$$

In this approach, the constants g_1 and g_2 are defined as shown in Eq. (6.11) and Eq. (6.12), respectively:

$$g_1 = (r^2 \varepsilon_{21} - r\varepsilon_{32})/(r \times (r-1)^2) \quad (6.11)$$

$$g_2 = (\varepsilon_{32} - r\varepsilon_{21})/(r \times (r+1)(r-1)^2) \quad (6.12)$$

where $\varepsilon_{21} = f_2 - f_1$, and $\varepsilon_{32} = f_3 - f_2$. Here, it is also useful to mention the convergence ratio (R), defined as the ratio $\varepsilon_{32}/\varepsilon_{21}$, which is also the inverse of the argument in the numerator of Eq. (3). Armed with these parameters, the extrapolated solution may be estimated by:

$$f_{exact} = f_1 + (\varepsilon_{32} - (r^2 + r - 1) \times \varepsilon_{21})/[(r+1)(r-1)^2] \quad (6.13)$$

Roy (2008) defined the above procedure solely as an error estimator and did not provide a Factor of Safety, which can be used to predict an uncertainty. Therefore, one can make no claim with regards to the confidence level the method provides. To establish the range of applicability of the method, it must be applied to cases where exact solutions are known. This would allow the introduction of a Factor of Safety, which adequately accounts for the conservatism of the scheme.

The reason why this method is included in the present assessment is twofold. Firstly, the behaviour of the error can be examined with grid refinement, separating linear and quadratic terms. This permits one to determine whether the asymptotic range is approached from above, below, or from different directions by each term in the expansion (Eq. 6.10). The implications of such an analysis are important, because one may gauge whether the solution exhibits linear or quadratic convergence depending on which constant (g_1, g_2) dominates in each range (coarse, medium, fine grids). The extracted information can then be used to assess whether further mesh refinement is warranted. This decision would rest on the approximated rate at which the error reduces. In other words, one may attempt to justify using a specific grid based on its convergence properties with greater ease than is possible with other methods.

For example, if a particular parameter exhibits second order convergence, the CFD practitioner may choose to refine the grid further. This could be a good

choice since even a small reduction in the grid size can be expected to lead to a palpable reduction in the predicted error. Such tools are especially powerful when considering cases where experimental data are not available.

In second place, the spatial error, defined in Eq. (6.13), has third order accuracy, which is independent of the observed order of accuracy (Roy, 2008). Therefore, the method does not rely on the positivity of *1/R*, or the related condition $R< 1$, in Eq. (6.3) and will produce an error estimate regardless of the parameters fed into Eqs. (6.10-6.13). In practice, provided one has a greater number of solutions, a system of equations can be constructed in the form of Eq. (6.10). The first n terms would allow the calculation of the n-1st constant (g_{n-1}). Thus, when using three solutions, as is the case in this for the present set of simulations, the linear and quadratic terms (1st and 2nd order) are computed. Since the theoretical order of accuracy of the solver is $p_f = 2$, there is little merit in seeking solutions of order 3 or higher.

It should be noted that a disagreement between the observed and theoretical order of accuracy does not necessarily imply inconsistency (Thomas and Langley, 2008). This is the case because Richardson Extrapolation was devised for structured grids. In fact, Diskin and Thomas (2010) point out that in unstructured grids, an order of accuracy near unity, or higher than two is frequently observed. They further state that this does not contradict the Lax and Richtmyer (1956) equivalency theorem, because the LET requirements are sufficient, but not strictly necessary to demonstrate the validity of a numerical scheme.

6.2.2 Local error and uncertainty

Having described the error and uncertainty estimation techniques, it is prudent to put into context the contribution of this chapter to the wider literature. Here, the local error and uncertainty estimator, originally devised by Cadafalch et al. (2002) is introduced. They began by defining Richardson and oscillatory nodes as follows:

- Richardson nodes: $(f_3 - f_2) \times (f_2 - f_1) > 0$
- Oscillatory nodes: $(f_3 - f_2) \times (f_2 - f_1) < 0$

Additionally, converged nodes can be computed, where the above product lies below some predefined measure of accuracy. For the purposes of this chapter, no such limit is defined. Therefore, it is thought prudent to proceed along the

lines of Phillips and Roy (2012) and discount converged nodes as a possibility in the numerical work.

Cadafalch et al. (2002) then ensue to use the local observed order of accuracy to produce a global average. Following a similar rationale, Phillips and Roy (2017) provide an analogous framework, which is employed here. The first step is a small modification to Eq. (6.3), shown in Eq. (6.14). Specifically, the absolute value of the quotient in the numerator is taken. This ensures that oscillatory nodes are also taken into account. Such a change has been proposed previously in, for example, Celik and Karatekin (1997) and Celik et al. (2008). In other words, the change breaks no precedents.

$$\hat{p} = \ln\left(\left|\frac{f_3 - f_2}{f_2 - f_1}\right|\right) / \ln(r) \tag{6.14}$$

The resulting order of accuracy at each location of interest is not used directly. Instead, Phillips and Roy (2017) define the global deviation from the formal order of accuracy ($p_f = 2$), shown in Eq. (6.15):

$$\Delta p = \min\left[\frac{1}{N}\sum_{i=1}^{N} \min\left(\left|p_f - \widehat{p_i}\right|, 4p_f\right), 0.95p_f\right] \tag{6.15}$$

Eq. (6.15) can be interpreted as the mean local deviation of the observed order of accuracy from the theoretical order of accuracy. The maximum deviation is restricted to $4p_f$ in an attempt to avoid skewing the average (Phillips and Roy, 2017). In the process of derivation of Δp, Phillips and Roy (2017) considered multiplicative factors of p_f of 2, 4, 6, and 8, but the choice for this particular parameter was shown to be of little consequence. To prevent values close to zero, the maximum distance of the observed order of accuracy from the formal order is limited to 95% of p_f. Having obtained Δp, one can progress to calculating the global distance from the formal order of accuracy (p^*), shown in Eq. (6.16). This enables the calculation of the Factor of Safety (FS), as a function of p^*, shown in Eq. (6.17).

$$p^* = p_f - \Delta p \tag{6.16}$$

$$FS(p^*) = \left[F_0 - (F_0 - F_1)\left(\frac{p^*}{p_f}\right)^8\right] \tag{6.17}$$

where F_0=3, and F_1=1.1. Eq. (6.17) can be used to construct a smoothly varying FS with distance from the asymptotic range.

Finally, the uncertainty can be estimated as shown in Eq. (6.18):

$$Uncertainty = FS(p^*)\left|\frac{f_2 - f_1}{r^{p^*} - 1}\right| \quad (6.18)$$

In the process of any RE-based method, a solution is extrapolated. This can be thought of as the solution, which one may expect to obtain on a grid with a cell size of 0. In other words, it approximates the analytical solution. This is done by virtue of three systematically refined or coarsened grids. Emphasis is placed on solutions achieved with uniform refinement ratios, although it is possible to vary this particular parameter. For the relevant background on this, the reader is referred to ITTC (2002) and Roache (1997). The use of an extrapolated solution as the final outcome of a simulation is inadmissible because it is not possible to prove that such a solution satisfies the conservative laws (Roy, 2008).

The methods presented thus far can be classified as *a posteriori*, because they allow the estimation of uncertainty after the simulation has run its course. However, there are *a priori* methods, which are, in theory, capable of performing the same function as soon as the grid has been generated. Since no such method is available in the RANS solver used, this course of action has not been explored further. Alternatives also include intrusive methods. For example, an error transport equation may be produced, which generates an estimate of the numerical accuracy while the simulation is running. In recognition of the fact that in practice, the average RANS practitioner will not be able to achieve this, such methods have not been incorporated. A full classification and discussion on the above methods can be found in Jasak (1996), Phillips (2014, 2012), Roache (1997) and Roy (2005).

6.3 Case-studies and numerical set-up

For the purposes of this chapter, a set of full-scale numerical simulations are used. These form a full-scale replica of the experimentally investigated case-studies of Elsherbiny et al. (2019). The refinement ratio $2^{1/3}$ was selected to avoid a sudden explosion in cell numbers. In other words, making this selection allowed the adopted simulations to have a greater number of cells while avoiding a sudden increase in cell numbers beyond which the simulations would become difficult to handle. The present simulations feature cell numbers ranging from approximately 10 million to 32 million. As explained previously, these cell numbers are achieved by a systematic, consecutive spatial refinement.

6.3.1 Spatial characteristics of the computational domain

The dimensions of the computational domain satisfy two requirements. Firstly, the width and water depth are set to represent the experimental campaign of Elsherbiny et al. (2019), as shown in Figure 6.1. To reduce the required cell numbers, a symmetry condition is imposed, coincident with the ship and canal centreline. The width of the domain was originally 2.3m in λ=75, whereas the depth (h) was 2.2 times the ship draught ($h/T = 2.2$). Naturally, these conditions are maintained to reproduce the experiment as closely as possible in full-scale. To accomplish this, the side boundary is set as a slip wall, while the domain bottom is prescribed as a velocity inlet.

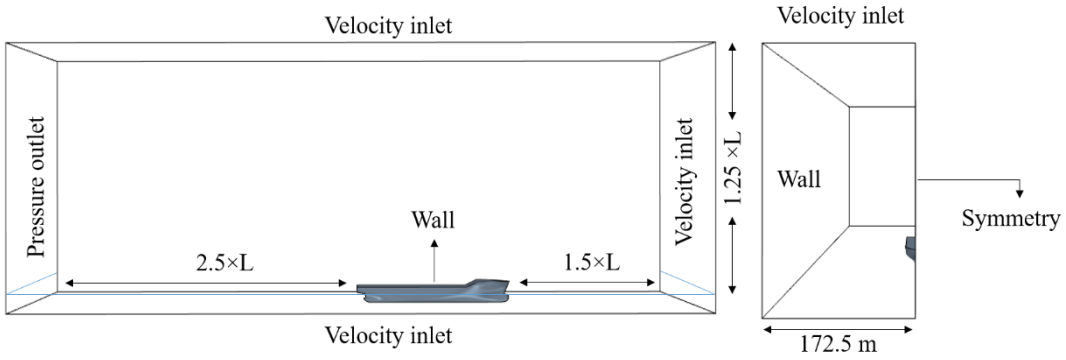

Figure 6.1. Domain dimensions and boundary conditions

The remaining boundaries are placed following widely used recommendations regarding resistance predictions in ship CFD. Specifically, the inlet boundary is positioned 1.5 ship lengths upstream of the forward perpendicular, whereas the outlet is placed 2.5 ship lengths downstream of the aft perpendicular (ITTC, 2014; Siemens, 2018). The domain top is set as an inlet, positioned 1.25 ship lengths from the undisturbed waterline. For reference, the ship and domain dimensions are shown in Table 6.1.

All simulations were performed in the commercially available RANS solver, Star-CCM+, version 13.06.011. As mentioned previously, the software uses the Finite Volume Method (FVM) to discretise the governing PDEs onto a finite number of predominantly hexahedral cells with minimal cell skewness. The latter is defined as the angle between the face area vector (face normal) and the vector connecting the centroids of two adjacent cells. The reason why this parameter is important lies in the fact that diffusion terms contain the dot product of the two vectors referred to above (Siemens, 2018). Therefore, when these are perpendicular (i.e. the mesh is non-orthogonal), the diffusive terms

are seemingly divided by zero, rendering severe convergence problems. The mesh must be as orthogonal as possible to avoid such a scenario.

Table 6.1. KCS and computational domain principal characteristics in full-scale

Quantity	Symbol	Value	Unit
Scale Factor	λ	1	-
Length	L	230	m
Beam	B	32.2	m
Draught	T	10.8	m
Depth	D	19	m
Water depth	h	23.760	m
Block coefficient	C_B	0.651	-
Longitudinal Centre of Gravity	LCG	111.593	m
Wetted area	S	9530	m^2
Speed	U	4.630	m/s
Reynolds number	Re	1.195×10^9	-
Depth Froude number	F_h	0.303	-
Water depth/Draught	h/T	2.2	-
Domain half width	w	172.5	m

In the free stream, there is little preventing the mesh from near perfect orthogonality. However, near the ship surface, the mesh must conform to the inherent curvature of the ship's underwater shape. This property, superimposed on the large aspect ratio cells, required to adequately capture boundary layer physics can create significant problems. The optimum aspect ratio of a grid was examined by Salas (2006), who concluded that it is possible to reduce the numerical error based solely on grid aspect ratio. Meshes with different aspect ratios are not manufactured, since this is too computationally expensive, considering the 32 million cells in the finest grid. Instead, the numerical error, as predicted for the finest solution will be examined against the aspect ratio of the cell, where the solution has been sampled from.

Two distinct metrics will be assessed. The first is the free surface deformation, while the second – skin friction, acting on the hull. Since the ship was allowed to sink and trim via the Dynamic Fluid-Body Interaction module, offered by Star-CCM+, one cannot take free surface samples from the immediate vicinity

of the ship hull. In the case of skin friction, the ship centre of gravity is used as the coordinate system origin, thus, automatically correcting for any differences resulting from the ship's squat. The sinkage and trim, computed from the three grids are shown in Table 6.2, while the resulting grids are shown in Figure 6.2. The free surface and skin friction are sampled at a simulation time of 500s to ensure all transient effects have decayed. Table 6.2 also contains the temporal uncertainty estimates, which where arrived at by magnifying the time-step by a factor of $2^{0.5}$ to produce the medium (f_2) and coarse (f_3) solutions.

Table 6.2. Computed integral quantities and related uncertainties

	Spatial uncertainty		Temporal uncertainty	
Parameter	Sinkage [m]	Trim [°]	Sinkage [m]	Trim [°]
f_1	-0.186	-0.0752	-0.186	-0.0752
f_2	-0.186	-0.0753	-0.186	-0.0753
f_3	-0.187	-0.0756	-0.187	-0.0754
p [-]	4.097	1.9643	2.450	0.7896
GCI [%]	0.0220	0.1852	0.42	0.877
Convergence mode	Monotonic	Monotonic	Monotonic	Monotonic

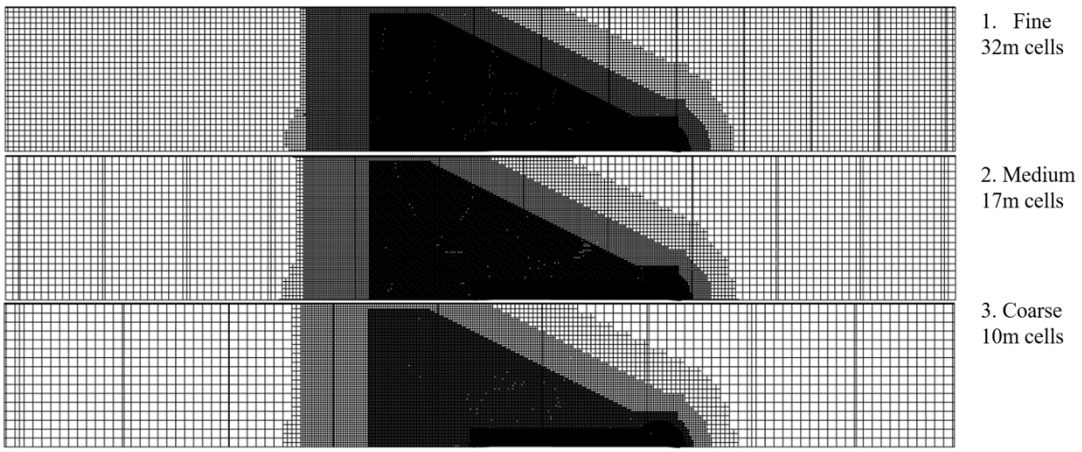

Figure 6.2. Resulting mesh

The mesh, depicted in Figure 6.2, was designed to capture the expected free surface disturbance by concentric volumetric refinements. This is done in the vicinity of the free surface, as well in the proximity of the ship hull. The top view of the mesh, shown in Figure 6.2 represents half of the computational grid. This is constructed within the automatic facilities Star-CCM+. The prism layer mesh is utilised to manufacture the near-wall mesh, which is accomplished by generating an exploded sub-surface, using the ship as input. Within the region between the sub-surface and the ship hull, a fine mesh can be imposed in order to capture boundary layer physics.

6.3.2 Physics modelling

Typically, the near-wall performance of a simulation is characterised via the dimensionless distance from the wall, the y^+ function. In model-scale computations, the desirable y^+ values are smaller than 1 ($y^+<1$). In full-scale cases, setting the y^+ values below one is a significant challenge, involving very high aspect ratio cells. These are not a desirable feature in a numerical simulations, because they destabilise the convergence properties of the solution by introducing numerical stiffness (Deng et al., 2004; Eca et al., 2015; ITTC, 2011). It is also important to consider the transition of cell size. As the flow moves between two neighbouring cells, partial reflections may occur if there are large changes in the properties of the mesh (Siemens, 2018). Additionally, mesh coarsening introduces diffusion (Perić and Abdel-Maksoud, 2016), which is not desirable in locations featuring near-wall influences. Fortunately, in full-scale applications, flow separation is less likely, and of less consequence. The question of whether employing wall functions amounts to correct flow features in the wake of a full-scale ship is yet to be determined. However, this requires experimental measurements in the wake of a full-scale ship, as well as the modelling of a spinning propeller, which is not within the scope of this thesis. The use of wall functions is therefore assumed justifiable (mean $y^+\approx200$ in the present case).

The near-wall characteristics are governed by the distribution of velocity within the boundary layer. Naturally, this is dependent on the method, selected to close the Navier-Stokes equations. Such a model is required due to the fact that in their Reynolds averaged form, the governing equations do not form a closed set. For the purposes of this thesis, use is made of the standard k-ω model. This choice is made following the findings made in Chapter 4, where the k-ω model was demonstrated to perform consistently and reliably. Moreover, the time per iteration was shown to be the smallest of all two-equation turbulence models assessed. Coupling these findings with the fact that the k-ω model can be applied seamlessly for any y^+ value without any major modifications make it a good choice for the present assessment.

The importance of turbulence modelling in full-scale ship hydrodynamics has been discussed in Deng et al. (2004), who found that the non-linear Reynolds Stress Transport (RST) model exhibits best performance. However, the RST model suffers from several problems, not encountered in two-equation turbulence models. In particular, a greater number of equations is required to

predict the Reynolds stress. Thus, the computational time is expected to be several times that achieved with the standard $k - \omega$ model. That is, albeit the solution of turbulence equations scales better than momentum equations (Hawkes et al., 2018). Although the RST model boasts of modelling turbulent physics more robustly than two-equation models, there are problems in its practical implementation (Parneix et al., 1998). The above suggest a conclusion along the lines of that made by Eca and Hoekstra (2001). Namely, two-equation turbulence models remain a good option in full-scale ship hydrodynamics. Moreover, the discrepancies between turbulence models are thought to be less significant with an increase in Reynolds number (Eca and Hoekstra, 2001), although more recent work suggests this may not be the case (Visonneau, 2005).

To guarantee that convective terms are represented as accurately as possible, a second order upwind scheme is adopted. This is done in view of the fact that upwind-biased schemes are the only available variety that can guarantee boundedness of the solution (Jasak, 1996). Moreover, adopting a higher (3rd order) scheme can destabilise the solution because it introduces significant numerical diffusion (Vanka, 1987). The use of a second order accurate method is in line with the findings of Andrun et al. (2018). The aforementioned authors recommended the use of at least 2nd order methods, although the results suggested little impact on free surface modelling. In the above reference, the authors also recommended the use of a least-squares (LSQ) approach to discretising the gradients. For all simulations performed here, the hybrid Gauss-LSQ method is used following the recommendations of software developer (Siemens, 2018). The definition of such a method is required because in addition to variable values, variable gradients must be computed at cell centres. These are used chiefly for the estimation of diffusion and convection properties.

The segregated flow method is used to solve the integral conservation laws in a sequential manner. This requires the solution of the three velocity components and pressure iteratively, one after the other. Velocity and pressure are coupled via a SIMPLE algorithm. Although the solver can cope with weakly compressible flows, the incompressible form of the governing equations is employed.

6.3.3 Time step selection and temporal discretisation

The temporal term in the Navier-Stokes equations is discretised via a first order method. This is done based the fact that the present class of problems falls within the 'pseudo-steady' category. To elaborate, the physical problem should not depend on transient terms *per se*. However, in practice, the RANS method requires the definition of temporal discretisation. Even though this may introduce an undue reliance of the computed results onto a metric they are theoretically independent of (Jasak, 1996). Time is advanced every 15 iterations by $0.0035L/U$ in the present simulations (note that this is smaller than the ITTC (2014) recommendation of $0.01\sim 0.05L/V$). This choice for the time-step has been widely used and has been proven to provide sufficiently accurate results for similar cases (Terziev et al., 2019b, 2018; Tezdogan et al., 2016a, 2015; Zhang et al., 2018).

The reason why 15 inner iterations are used relates to residual reduction. Residuals indicate the degree to which the discretised equation is satisfied in each cell. Star-CCM+ uses the root mean-square value of the absolute error of all cells in the domain to provide a single metric (Siemens, 2018). Typically, one would seek residuals that are as low as possible, say in the range $10^{-6} \sim 10^{-8}$. In the present case, the specific dissipation rate was found to be satisfied to the greatest extent, achieving values in the range of 10^{-8}. The remaining residuals, relating to the turbulent kinetic energy, x, y, z momentum equations and continuity achieved values in the order of 10^{-4}. The simulations were initially run with 10 inner iterations, but this was found to be insufficient to reduce the residuals to the desired range. This range is defined based on the recommendations of the ITTC (2014). Specifically, the residuals should decrease by 2 – 3 orders of magnitude.

6.4 Results and discussion

The first step in this section is to present the input data required. As mentioned previously, two different metrics are examined: free surface elevation and skin friction. The former is sampled 25×10^4 times, while the latter consists of 1.5×10^4 points on the ship hull.

The abovementioned points of the free surface are spaced uniformly in the x – y plane on the port side of the ship and are depicted in Figure 6.3. Here, all spatial dimensions are normalised by ship length for consistency. The final sub-plot, shown in Figure 6.3 contains the convergence ratio (R), whose extents

are limited to the range of interest, namely ±1. This is done due to the fact that if a point lands outside this range, the solution is divergent. From the figure it is immediately apparent that human visual perception of the differences with mesh refinement is by no means adequate to detect the discrepancies, highlighted by the convergence ratio.

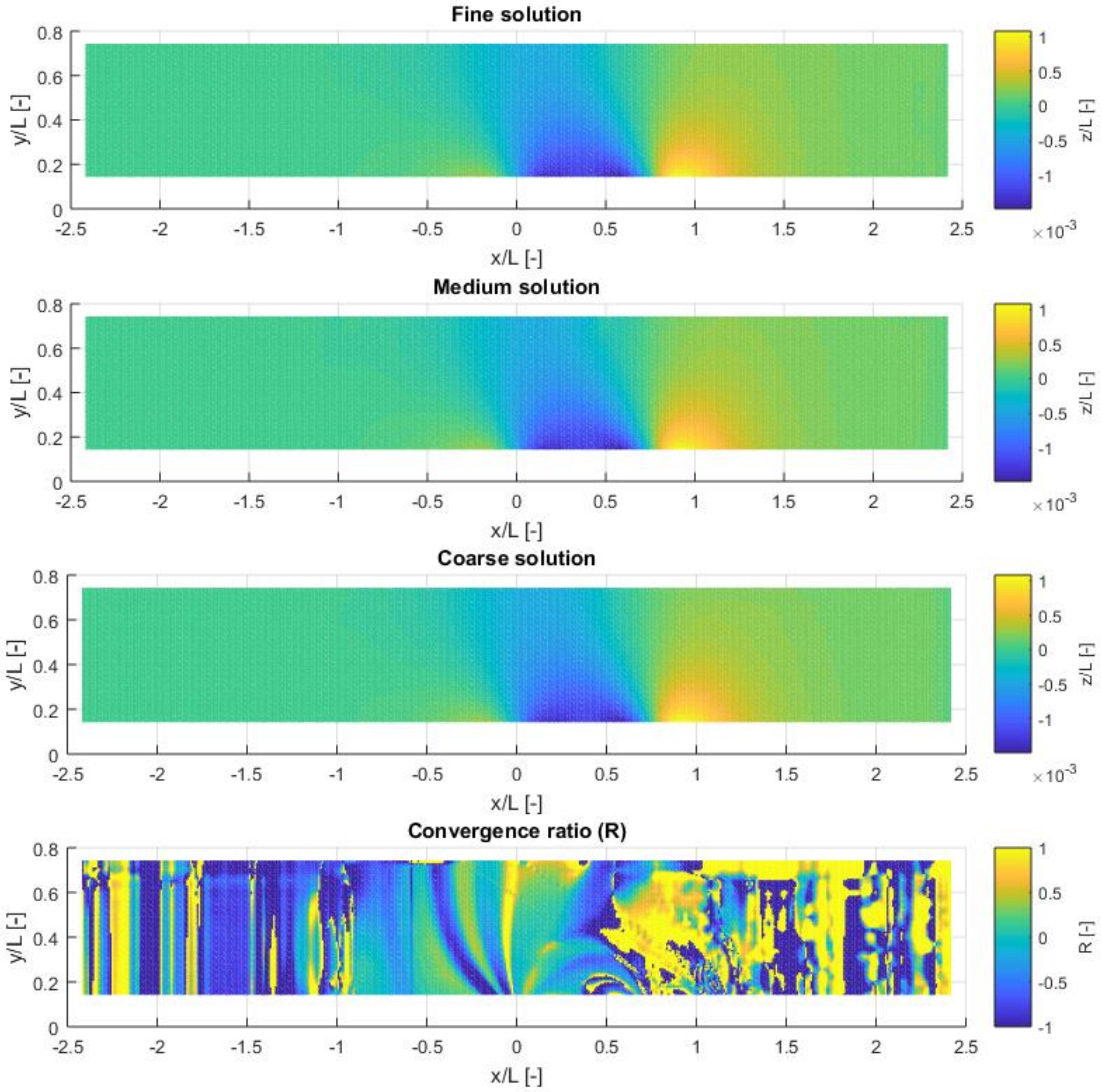

Figure 6.3. Fine, medium, coarse solutions, and convergence ratio of the free surface

It is important to mention that the use of the refinement ratio of $2^{1/3}$ means it is not possible to sample the free surface at cell centres of each grid, where the computations are performed. In cases where this is possible, the coarse grid determines the sampling locations, whereas the medium and fine grid are sampled every r^{th} cell. In other words, the grids are nested. Instead, in the work presented herein, the RANS solver interpolates the free surface at the requested locations automatically. Such interpolation, and multiple sampling

from a single cell in the coarse mesh may introduce additional errors. However, since the user is normally interested in an error estimator that is slightly leaning towards conservativeness, this is thought as an acceptable price to pay. In any case, an attempt to demonstrate the effect of sample density will be demonstrated later.

In terms of skin friction, the ship hull is sampled at ten equally spaced lines, i.e. buttock planes. In the context of ship hydrodynamics, the underwater shape is typically the main contributor to resistance. Therefore, only the submerged underwater area is normally sampled for skin friction. However, if this were to be done, it would cause a different number of samples to be acquired from each grid. This is the case because even a small variation in the water surface near the hull may have a significant effect on the number of samples. For this reason, the entirety of the ship is taken. To eliminate the different sinkage and trim effect, the coordinate system is altered in each case to match the orientation and position of the centre of gravity of the ship. This allows all differences in position, orientation, and water elevation to be accounted for.

Moreover, a change in the free surface elevation in any single grid would cause a large numerical error and consequently uncertainty in the later stages. In other words, employing the here-described technique of sampling the ship hull for points, one avoids all potential problems, simultaneously accounting for disparities in the water surface elevation on the hull which are not addressed in the free surface sampling described previously.

The resulting points on the hull are shown in Figure 6.4, along with the convergence ratios. Points lying on the above water part of the ship naturally exhibit a much smaller skin friction than the submerged points, as expected. The former are found at the bottom of the plot when examining the distribution of skin friction in the longitudinal direction. It is also important to mention that all coordinates have been normalised by ship length, as was the case for the free surface.

In the present context, skin friction is defined via the wall shear stress (τ_w). As before, the distribution of the convergence ratio in space reveals a complex pattern. It is clearly discernible that points near the parallel midbody may be responsible for significant deviations based on the value of R. This is an unexpected observation, since the curvature of the hull in this particular

location is milder than it is near the more complex structures of the underwater shape, specifically, the bulb and the stern.

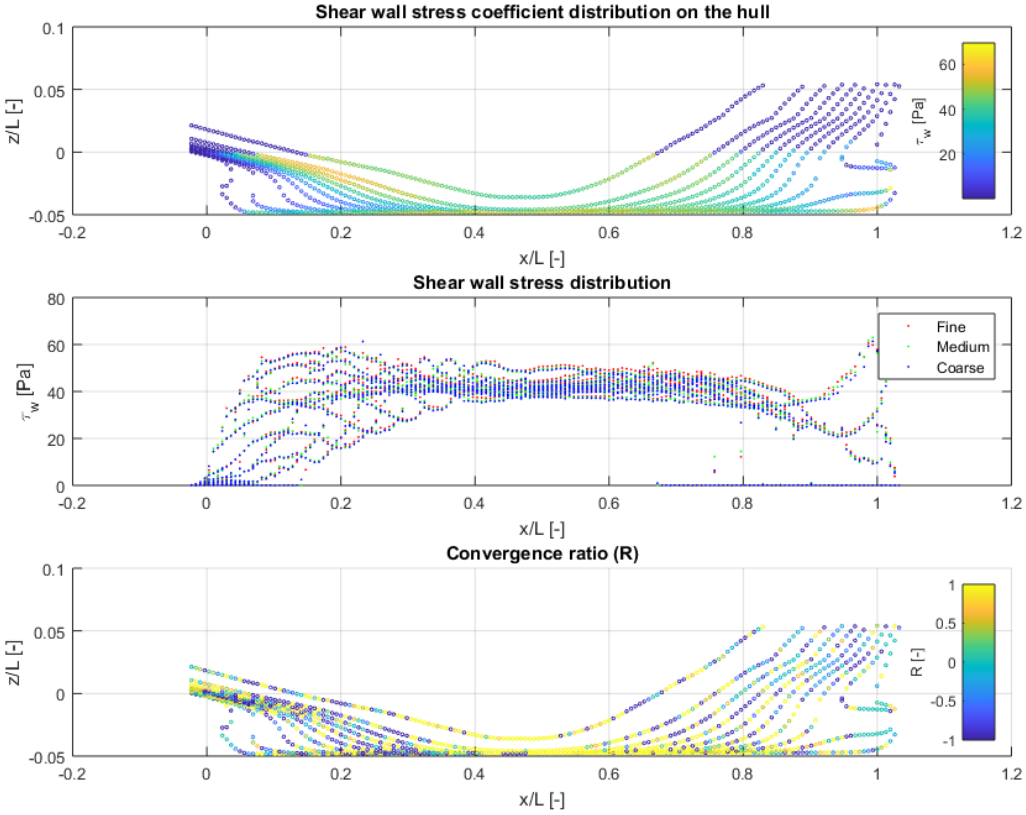

Figure 6.4. Skin friction nodes from the ship hull

6.4.1 Local classification

The next step is to determine which nodes can be classed as type 'Richardson nodes', and which are oscillatory. For illustrative purposes, this will be coupled with the local observed order of accuracy, as defined by Eq. (6.14). This is shown in Figure 6.5, where the Richardson nodes are predicted to account for approximately 43.8% of all nodes, i.e. *circa* 11×10^4 points in the case of the free surface. The remainder exhibit non-monotonic convergence or divergence. It is important to note that the local observed order of accuracy has been limited to 20. In any case, few points exceed this value. Figure 6.5 demonstrates that the computed free surface is separated into regions. The boundaries of these regions are characterised by a high observed order of accuracy.

The patches of Richardson or oscillatory nodes are clearly evident in locations, next to the ship hull, as well as up to half a ship length downstream. These locations are coincidently characterised by significant increases in mesh

density (refer to Figure 6.2). The clearly distinguishable patches coincide with the wedge, prescribed to capture the potential effect of the Kelvin wake. In the present simulations, the low depth Froude number (0.303), coupled with the lateral restrictions allow for near-field waves only, as shown in Figure 6.3.

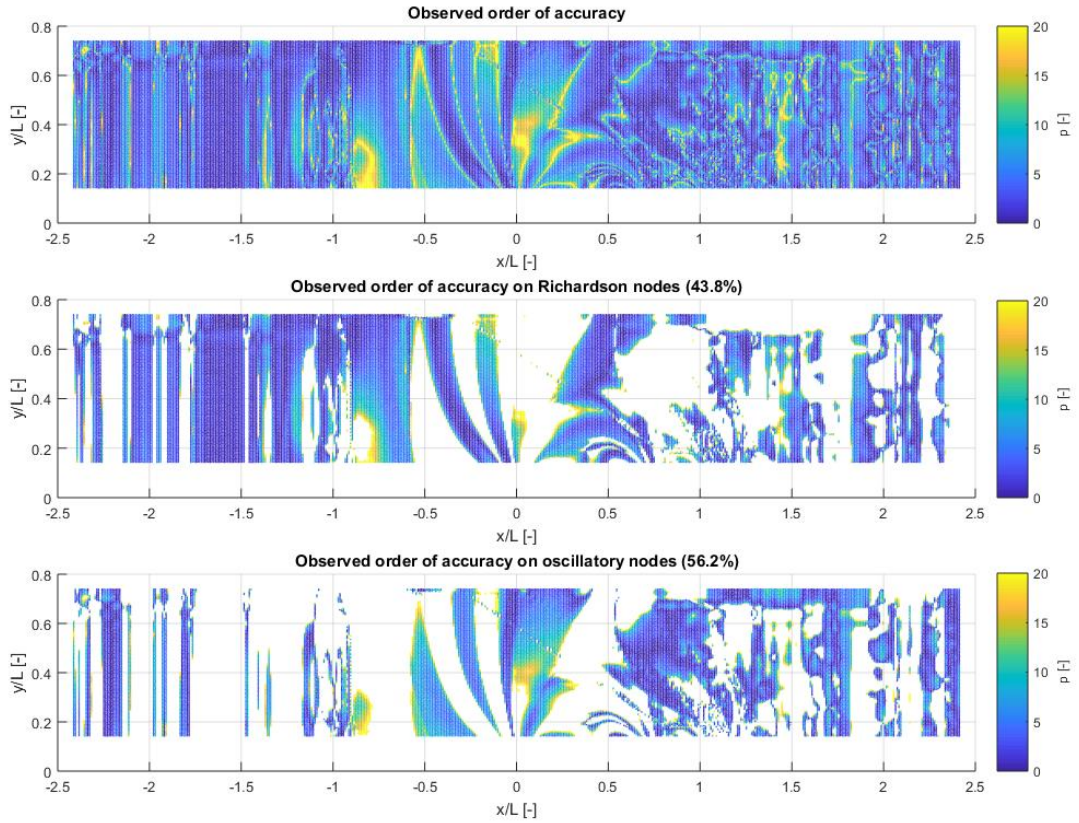

Figure 6.5. Observed local order of accuracy on the free surface nodes.

The observed local order of accuracy based on the skin friction distribution on the ship hull is shown in Figure 6.6. Here, the maximum p has been maintained as p_{max}=20 to retain consistency across the different parameters. However, as was previously observed, few points approach this limiting value.

The pattern of patches of similar behaviour seems to be largely maintained in Figure 6.6. To elaborate, it is apparent that nodes tend to switch from Richardson to oscillatory behaviour in patches along the ship hull, although this is not as easily observed as was the case in Figure 6.5. Many of the nodes previously highlighted as potentially problematic – near the parallel midbody of the hull – are shown to be characterised as of Richardson type. In the case of skin friction, fewer than half of all sampled nodes exhibit oscillatory behaviour. This shift, with respect the free surface highlights that different

parameters may require separate consideration in examinations of the type presented herein.

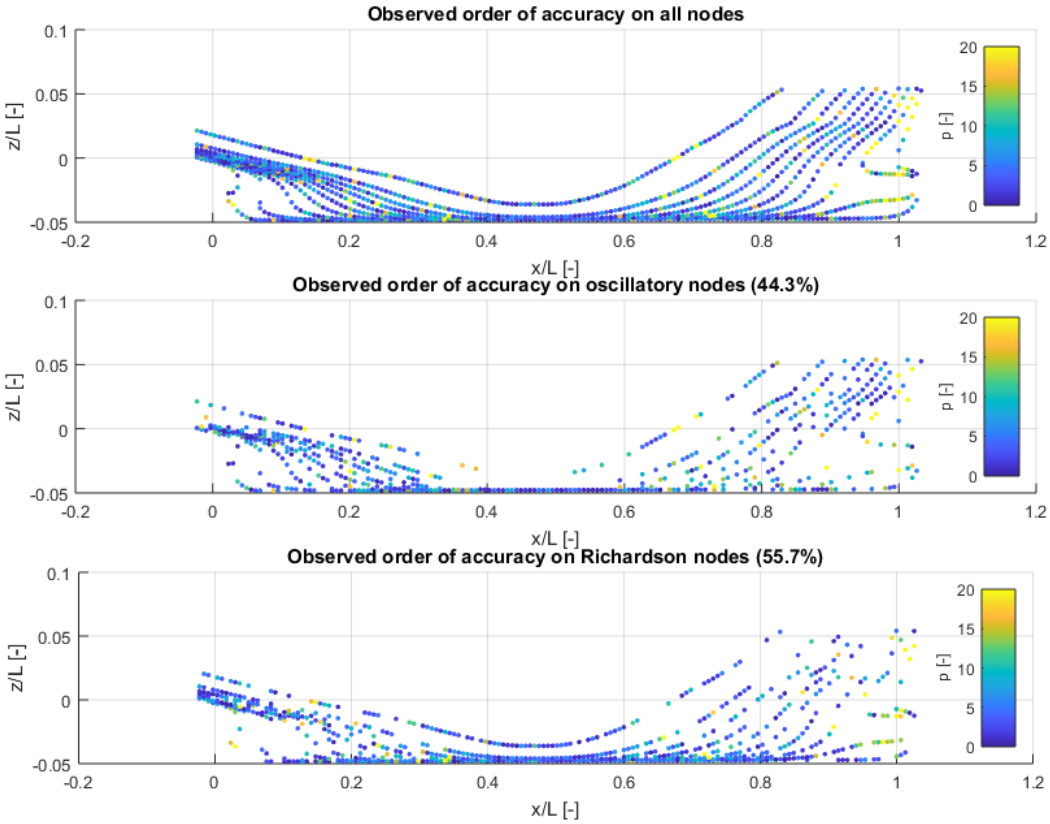

Figure 6.6. Local observed order of accuracy on the ship hull

6.4.2 Error analysis and decomposition

It is now prudent to examine the behaviour of the error constants on the free surface. These are calculated following the proposition of Roy (2008), and are shown in Eq. (6.11) and Eq. (6.12) for the linear and quadratic components, respectively. As stated in section 6.2.1, there are two possibilities for the computed error constants. The 1st and 2nd order components either amplify or attenuate the overall error once summed. The first case can occur regardless of the sign of each constant, provided they approach the asymptotic range from the same side. The contribution of these nodes in the case of the free surface is demonstrated in Figure 6.7. Here, it is evident that the vast majority of error contributions are a consequence of linear and quadratic terms of opposite sign. Those with identical sign, i.e. approaching the asymptotic range from the top, or bottom are coloured in red, and account for a small fraction of the overall (less than 1% of all samples). Clearly, they can only exist in the narrow range where the two constants cross over to a different quadrant in Figure 6.7. Thus,

leaving the vast majority of nodes to be classed as having opposite linear and quadratic signs.

Therefore, all points, located near the extremities of Figure 6.7 contribute little to the overall error, and consequently uncertainty. In the same figure, the distribution of the error constants with respect to each other is also included. This is done to demonstrate the fact that most predictions are located near the centre of the plot. In other words, one should not expect excessive errors arising from misalignment of the linear and quadratic components of the error.

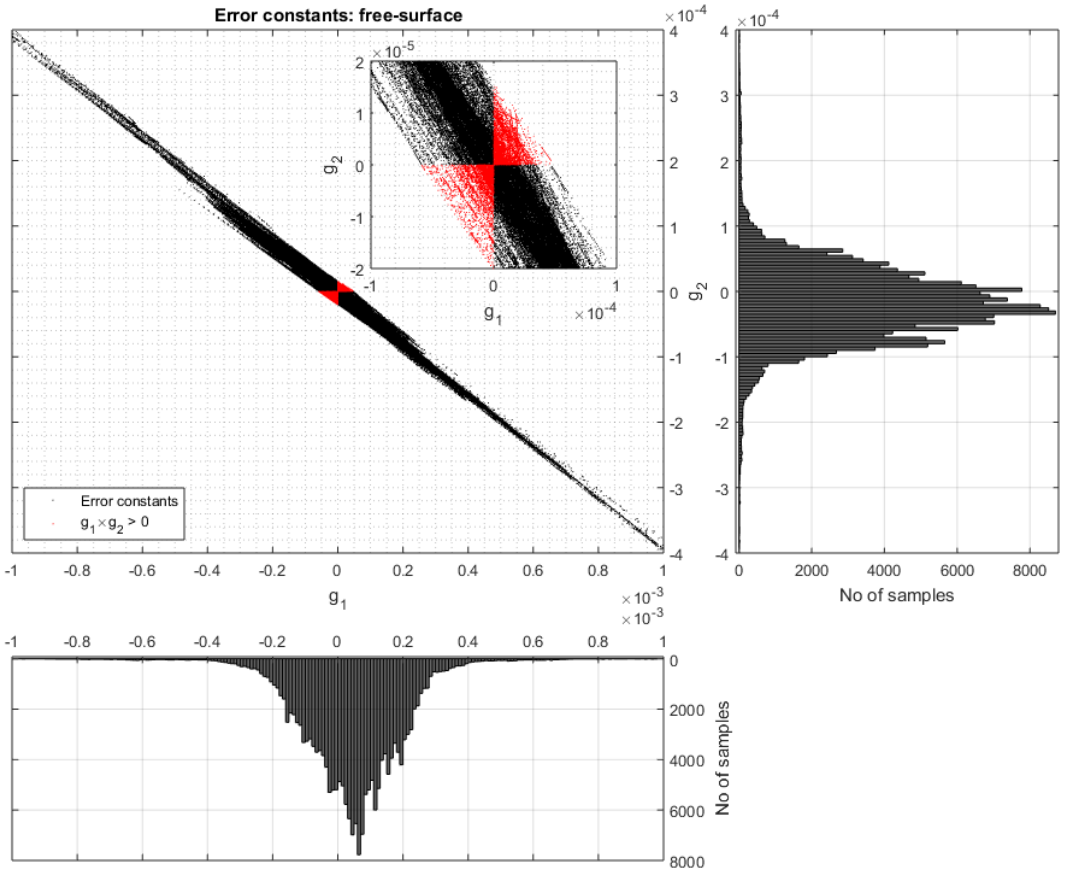

Figure 6.7. Free surface error constants.

In the case of skin friction distribution, the error constants magnitude is not similar to that of Figure 6.7, where the free surface error constants are given. The skin friction error constants are depicted in Figure 6.8, which replicates what was previously shown in the case of the free surface. Clearly, the number of samples in Figure 6.8 is significantly smaller than in Figure 6.7. Although this makes observations on the overall behaviour slightly more difficult, several general trends can be identified.

In Figure 6.8, the range of both error constants is several orders of magnitude higher than was the case for the free surface points. This is a direct consequence of the fact that the latter were normalised by ship length prior being decomposed into 1st and 2nd order contributions. Therefore, the range of the axes should not be taken as an indicator of a problem in the assessment *per se*. Secondly, as was the case in Figure 6.7, the error is distributed along the diagonal of the plot in Figure 6.8. This observation, coupled with the small number of points where the error is reinforced in the process of summation, has several implications.

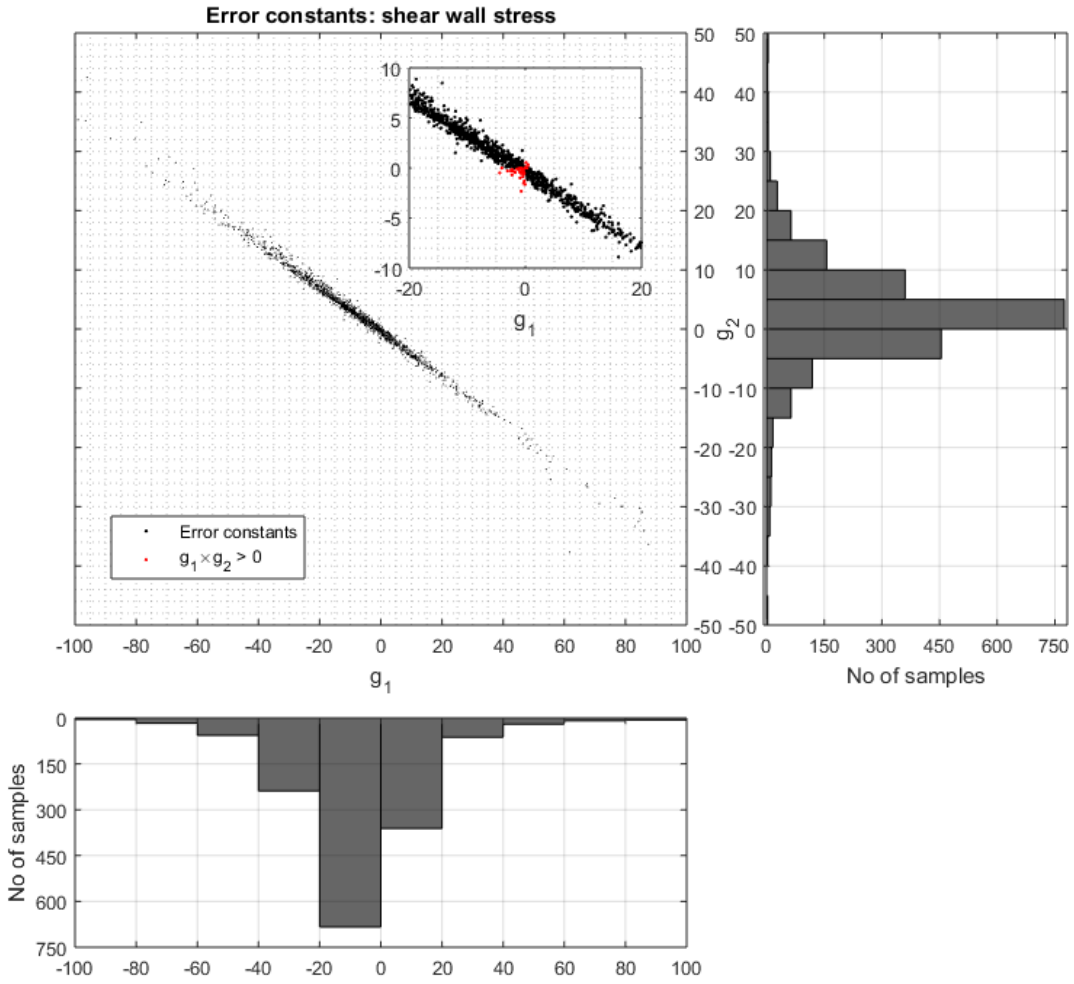

Figure 6.8. Skin friction error constants.

Primarily, the alignment of points along the aforementioned diagonal of Figure 6.8 suggests that most points will exhibit a small error, resulting from the cancellation of linear and quadratic components. Additionally, the error

amplifying points are constrained within a small wedge near the origin, implying a small numerical error can be expected to stem from these samples.

In the following section, the spatial distribution of the error is assessed for both parameters. For consistency, the free surface is examined first.

6.4.2.1 Spatial distribution of the error

The spatial distribution of the error constants (in the $x - y$ plane) is depicted in Figure 6.9 for the free surface. In the first sub-plot of the figure, the locations where the linear and quadratic components reinforce the overall error have been removed. With the exception of a line of samples near the outlet, the nodes where the error is amplified exhibit no discernible pattern. Thus, it may be postulated that such samples are a random occurrence, or are associated with a type of numerical error that is not known at present. In any event, the number of such points on the free surface is sufficiently small to be discounted.

The remaining sub-plots ($2^{nd} - 4^{th}$), shown in Figure 6.9 highlight the absolute values of the error constants. These allow one to pinpoint the specific locations, contributing to increased numerical error. Although any error estimation technique could have been used, Roy's (2008) breakdown is preferable because it allows a more detailed analysis. Moreover, since the same input is used for all uncertainty estimators, the predicted locations will remain constant, regardless of the method, as will be demonstrated later. The differences will arise in terms of magnitude, rather than relative error distribution in the domain.

Figure 6.9 can also be examined from a different viewpoint. There are two distinctive features that are shown in all three possible error contributions (1^{st}, 2^{nd}, and 3^{rd} order accurate solutions). Specifically, the locations where the Kelvin wedge approaches the side wall exhibit elevated levels of numerical error. It may be suggested that this is due to abrupt changes in mesh density. However, no such pattern can be seen over the remainder of the boundaries of the Kelvin wedge, whose arrangement can be consulted in Figure 6.2. Therefore, it may be speculated that the elevated levels of error are attributable to a combination of the change in mesh density, coupled with the proximity of a solid wall. In fact, such an observation is supported by the presence of nearly concentric semi-circles in the immediate vicinity of the ship hull (i.e. between $0 < x/L < 1$).

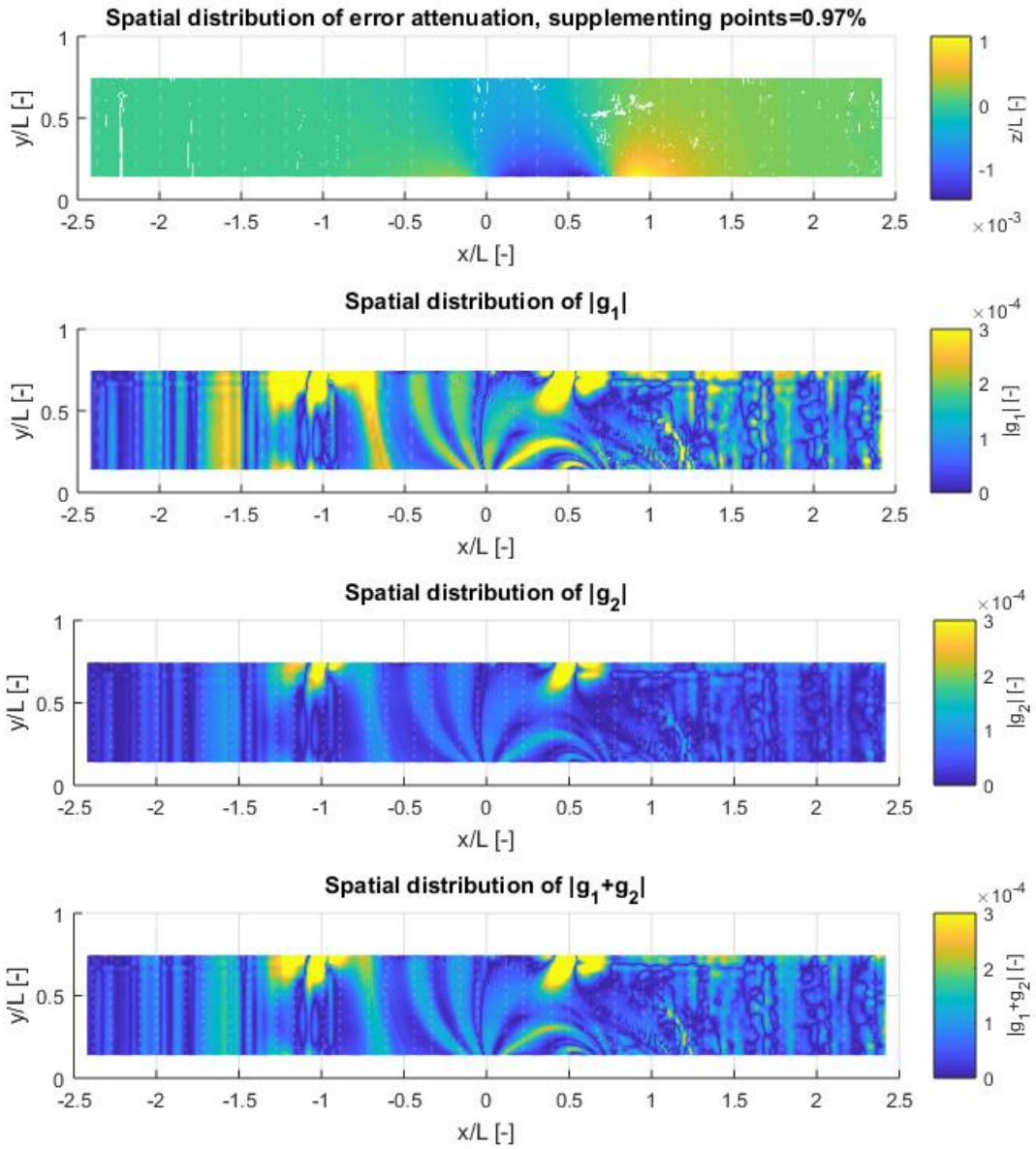

Figure 6.9. Spatial distribution of the linear and quadratic terms of the error in the free surface, computed via Eq. (6.11) and Eq. (6.12).

However, the argument that an abrupt mesh density change in proximity of a no-slip wall may not be sufficient to describe the entirety of the 'error field' shown in Figure 6.9. In other words, the arcs of elevated error, located entirely within the Kelvin wedge do not fall within the above category. That is unless the interpretation of extended influence of the solid boundary onto the flow is adopted. To elaborate, it is possible that the hull's direct influence as a numerical error generator is greater than that of the side wall. This issue may require further study to accurately pinpoint the cause of these arcs.

The same argument in terms of method used to assess the error applies to the distribution of the skin friction on the ship hull, whose decomposed error distribution is depicted in Figure 6.10. As before, the first step is to examine the relative locations where the error is augmented versus those where it is attenuated. In the present case, 3.11% of all samples fall within the former category – a significant increase when compared to the free surface. As was the case for the fee surface, no discernible pattern can be identified in the spatial distribution of these points at present.

In Figure 6.10, the error constants are limited to a maximum magnitude of 60 to avoid skewing the axes too much because few points approach the limit. This also allows the identification of the points with elevated values with ease: almost the entire bulbous bow. On the other hand, locations near the parallel midbody show low levels of error. This is also the case for locations above the waterline. Such a remark may be interpreted as an indication that surface curvature creates elevated errors. To examine this claim further, the skewness angle of the first near-wall cell, along with its aspect ratio are shown in Figure 6.11.

Although significant skewness angles and aspect ratios are observed in Figure 6.11, no correlation can be identified between either of the above mesh properties and the observed error distribution. At the onset, it was stated that an attempt is to be made to correlate the abovementioned characteristics of the numerical simulation. This was done in view of the fact that it has been demonstrated to be possible for simple cases (Salas, 2006). This may not have been achieved because a single mesh set-up was used and refined to produce the three solutions.

Therefore, as a piece of future work, the aspect ratio of near-wall cells, could be varied in a systematic manner to produce recommendations in this respect. A problem worth considering in the course of such a study would be whether the y^+ values on the hull are targeted at the same value. In the event where they are, the change in aspect ratio must stem from a lengthwise reduction, i.e. grid refinement. Conversely, if the y^+ values are not maintained constant across cases, the grid can be coarsened to achieve different case-studies. In the present case, the first near-wall cell's spanwise and lengthwise dimensions are a function of the base size. The base size represents the largest cell in the domain, and is found near the outlet and inlet. It is important to maintain the same aspect ratio across generated grids, because otherwise the procedure of Richardson extrapolation is invalid (Salas and Atkins, 2009).

Figure 6.9 and Figure 6.10 reveal two important aspects of the numerical simulation. Firstly, the linear contribution to the error is dominant in both figures. This observation, coupled with the fact that the majority of samples do not exhibit a behaviour of error amplification when summed suggests good performance of the numerical simulation. Such a conclusion can be drawn because the dominant error behaviour is known to be of 1st order as the grid is refined past a certain point, and of second order in coarser grids. This is exemplified in the following sub-section.

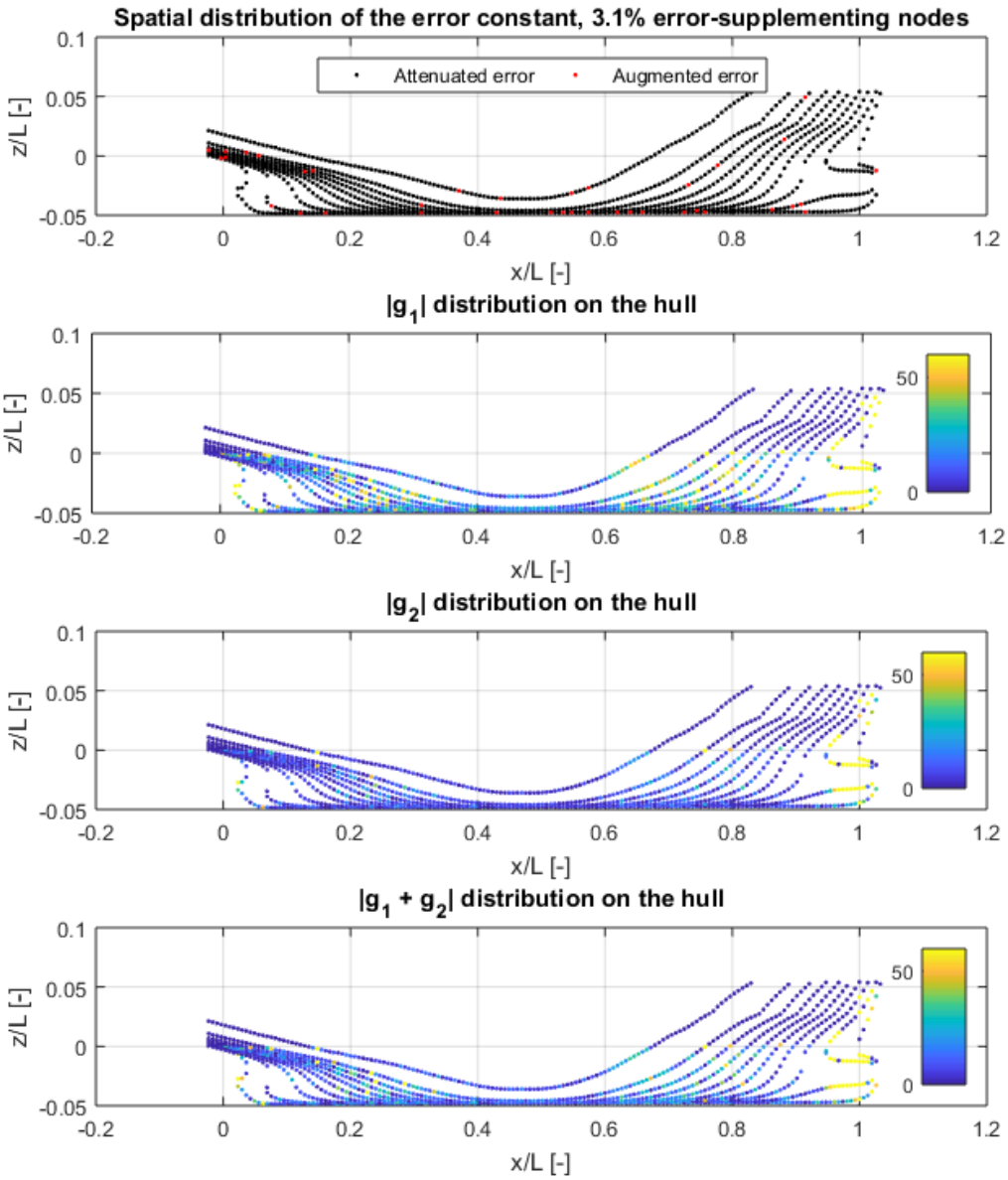

Figure 6.10. Spatial distribution of the linear and quadratic terms of the error in the skin friction, computed via Eq. (6.11) and Eq. (6.12).

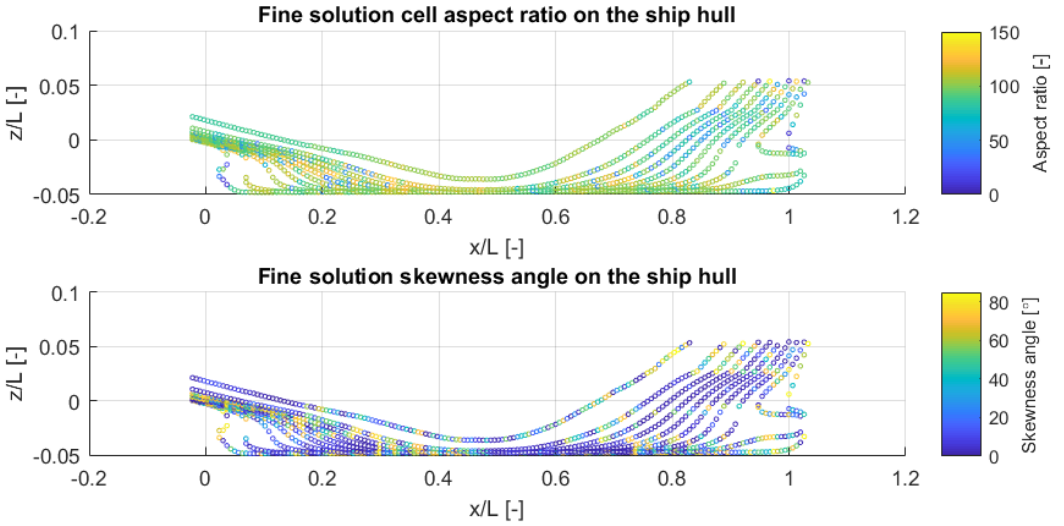

Figure 6.11. Cell aspect ratio and skewness angle on ship hull: fine solution

6.4.3 Error behaviour considerations

For this sub-section, samples from the free surface are considered only. This is done because of the greater number of available points. Regardless, the discussions and conclusions reached in what follows are equally valid for both parameters.

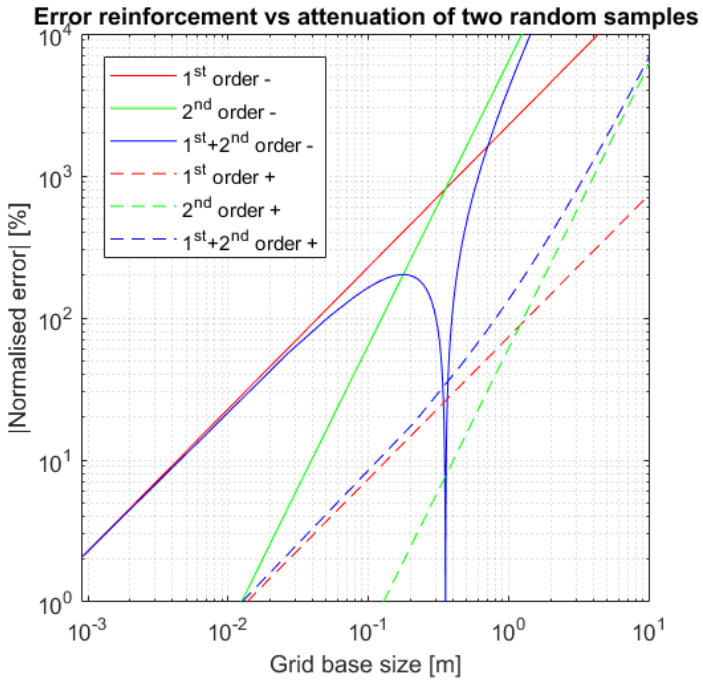

Figure 6.12. Example of error reinforcement and attenuation

The error behaviour, shown in Figure 6.12 is assembled by randomly taking two samples from each error category depicted in Figure 6.7. Specifically, a node where the 1st and 2nd order normalised error approach the asymptotic range from different sides, and a node where they approach the asymptotic range from the same side are extracted. These are classified with '-' and '+' in Figure 6.12, respectively. To simplify the figure, the logarithm of each term is used. This choice is made to allow the error line's slope to depict the order to which the term is raised. In other words, the line with slope one represents the first term of the Taylor series expansion shown in Eq. (6.10).

As referred to previously, Figure 6.12 depicts the presence of a hiatus when the first and second order error contributions intersect. This only occurs in cases where the asymptotic range is approached from opposite sides. Such a scenario is, as established in Figure 6.7, representative of the vast majority of all samples of the free surface and skin friction. Points near the hiatus are to be avoided, because of the possibility of spurious behaviour upon employing a grid in the proximity of the cusp. This is because Richardson extrapolation assumes smooth error derivatives, which is not the case in error attenuating scenarios near the cusp (Celik et al., 2005).

It is worthwhile to examine what would happen if, by chance, a solution were to be produced at precisely the grid size corresponding to the hiatus. In a typical Richardson extrapolation, for sufficiently fine grids the dominant error is raised to the lowest power, i.e. p. Thus, setting the order of accuracy as the lowest, dominant component of the Taylor series expansion and neglecting higher order terms is justifiable (Salas and Atkins, 2009). However, as h is increased, multiple errors of different behaviour begin competing in the Taylor series expansion. Thus, setting p as any one value and neglecting higher order terms is not correct in the vicinity of the hiatus.

The reason why Figure 6.12 is incorporated is to demonstrate a fact concerning the error's behaviour with grid refinement. Specifically, second order convergence, or more precisely, error reduction, can only be expected for coarse grids. This is independent of whether the error is reinforced or attenuated by its separate contributions.

On the other hand, once the hiatus (if one is present) has been overcome, the cumulative error exhibits first order convergence. This follows as a consequence of the second order term's contribution decreasing at a much faster rate than the remainder of the error. Therefore, if one observes a global

error with convergence properties that are close to linear, it can be claimed that the simulation is characterised by acceptable numerical error. It is important to note that no claim of whether a particular grid is asymptotic or not is made based on the above criterion. Instead, it is suggested that little improvement, i.e. reduction in numerical error can be achieved with grid refinement.

To elaborate, depending on the case, it may be justifiable to reject further grid refinement if the predicted numerical error will not decrease noticeably. Such an argument could be made if the error is shown to be located in the range where linear convergence dominates. On the other hand, if the specific grid produces errors in the quadratically convergent region, further grid refinement may be warranted. Further supporting evidence to this observation can be extracted from several works on numerical uncertainty estimation. In particular, the least-squares (LSQ) estimator of Eca and Hoekstra (2009, 2006). The LSQ method was designed to treat solutions with $0.5 < p < 2.1$ as asymptotic.

Another aspect of Figure 6.12 worth bearing in mind relates to the apparent order of convergence with grid refinement. It has already been stated that for fine grids, p is close to unity, while for coarse grids, it attains a value of in the vicinity of two. However, it is important to consider the manner in which such a transition occurs. In the case where the error is supplemented by the two components of the Taylor series, the error smoothly transitions from 1st to 2nd order. This can be easily deduced by an examination of the slope of the dashed blue line in Figure 6.12. There are no discontinuities, and its slope varies from 1 in the fine mesh region to 2 in the coarse mesh region. On the other hand, when the error is attenuated, the slope of the solid blue line exhibits a different behaviour. Although it too is of 1st order in the fine mesh range, the transition to 2nd order occurs though $-\infty$ and $+\infty$. In the course of this transition, the order of convergence attains all values except those between 1 and 2 (Salas and Atkins, 2009).

Combining the findings of Figure 6.9 and Figure 6.10 with those of Figure 6.12 suggests that the linear error has a much greater magnitude than its quadratic counterpart for the computed free surface and skin friction. Therefore, the locations where the majority of the error is expected to be found in the log-log plane of Figure 6.12 is to the left of the hiatus. That is, for most points, whose error approaches the asymptotic range from opposite directions. The error supplementing cases also follow a similar trend, albeit without the presence of a hiatus, which may produce spurious solutions.

In the context of asymptotic behaviour of the grid, there is one final angle from which the solution may be considered. As explained previously, the above method decomposes the error into first and second order components. Naturally, these are not dependent on the local observed order of accuracy, which is estimated via Eq. (6.14). This is true because p (nor $\hat{p}$) is not used in Roy's (2008) method. However, the order of accuracy can be interpreted as a measure of the convergence mode. That is to say, if p contains a real part only, then the solutions supplied into the equation converge monotonically. This is analogous to maintaining the convergence ratio between 0 and 1.

To exemplify the behaviour of the error constants versus each component of a typical Richardson extrapolation, Figure 6.13 depicts the behaviour of the error constants against the convergence ratio, whereas Figure 6.14 – the error constants against the observed order of accuracy. Figure 6.13 is characterised by distinct asymptotes, located at a different R value for each error constant. The prediction of where this location will lie depends exclusively on the refinement ratio. Specifically, no solutions can exist outside the boundaries defined by Eq. (6.20):

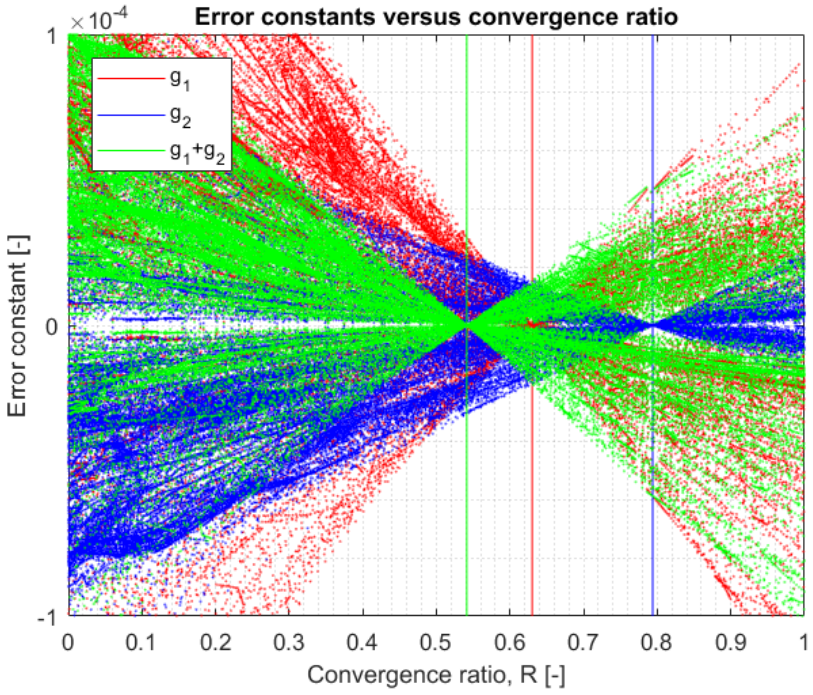

Figure 6.13. Error constants vs. convergence ratio

$$\text{Asymptote locations} \begin{cases} 1/r & for\ 1^{st}\ order \\ 1/r^2 & for\ 2^{nd}\ order \\ 1/(r^2+r-1) & for\ 1^{st}+2^{nd}\ order \end{cases} \quad (6.20)$$

Having employed $r = 2^{1/3}$, the asymptotes are located at $R = 0.7937$, 0.6300, and 0.5413 for the linear, quadratic terms, and their sum, respectively. Since one would ideally seek to obtain solutions that exhibit solely monotonic convergence, the x – axis has been limited between 0 and 1 for R. Having established that the prediction of the relative location of the asymptotes is trivial, one could employ this information before conducting the numerical simulations. The choice of r could be dictated so as to maximise the available area in Figure 6.13. In the present case, the choice of convergence ratio was governed exclusively by the rapid increase in cell numbers. Had a larger convergence ratio been selected, the cell numbers would have increased beyond a manageable size, whereas the idea was to allow for a large number of sequentially refined sets of simulations to be achieved.

Figure 6.14 demonstrates that although Roy's (2008) method does not explicitly depend on the order of accuracy, discernible patterns can be identified by combining the two. The error constant's behaviour on monotonically convergent samples shows clear trends, whereas the non-monotonic nodes do not. The former are characterised by a sharp cusp. The linear component shows that this cusp is located at p=2, the quadratic at p=1, while their sum: p=2.654. Figure 6.14 also confirms that the error due to the 2nd order term attains a smaller magnitude over the entire range examined. The 1st order term also grows at a greater rate than the quadratic term as the distance from the cusp is increased. The relative location of where this occurs is again governed exclusively by the refinement ratio. To demonstrate this, one may simply substitute the terms of Eq. (6.20) into Eq. (6.14). In the non-monotonic case, all points seem to have a tendency of increased error when compared to the monotonic samples. Therefore, despite the fact that the method does not take into account the convergence ratio, nor the order of accuracy *per se*, clear relationships can be established based on these components and the error constants.

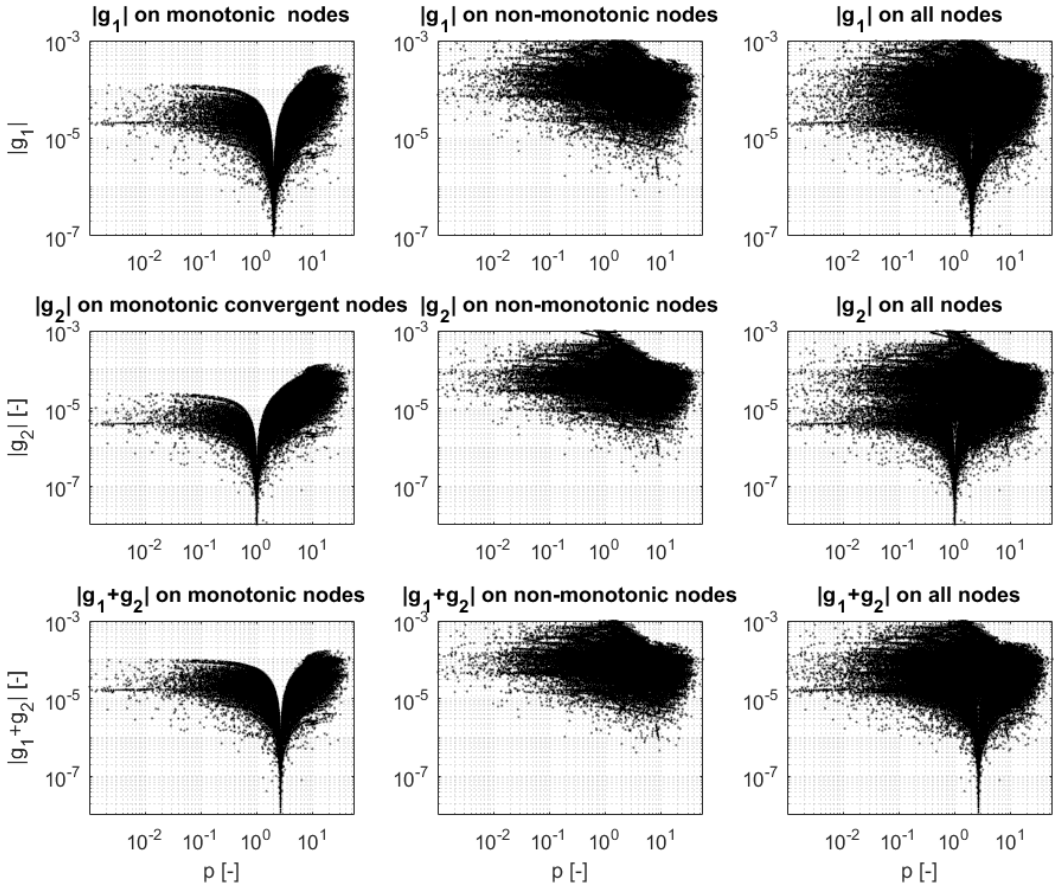

Figure 6.14. Error constants vs. local observed local of accuracy

6.4.4 Local uncertainty and extrapolated solutions

In this sub-section, the uncertainty estimates are presented for both the free surface and the skin friction data. A discussion is also given on the choice of the Factor of Safety, as well as the best choice for the order of convergence.

6.4.4.1 Factor of Safety

The first step is to determine whether the suggested FS of 1.25 as part of the GCI procedure agrees with the procedure of Phillips and Roy (2017) for estimating the FS. This is presented for both local parameters in Figure 6.15.

The results reveal that the skin friction data is asymptotic based on the criterion of Eq. (6.17), which exhibit a Factor of Safety of 1.2532 with a distance from the asymptotic range of 0.0209. The reader is reminded that in the present context, the distance from the asymptotic range metric is defined as the deviation from the formal order of accuracy ($p_f = 2$). Therefore, the skin friction data is highly asymptotic, suggesting that further refinement is of little

use in the present case. This is an encouraging finding considering the high aspect ratios of the near-wall cells and their skewness angles, shown in Figure 6.11.

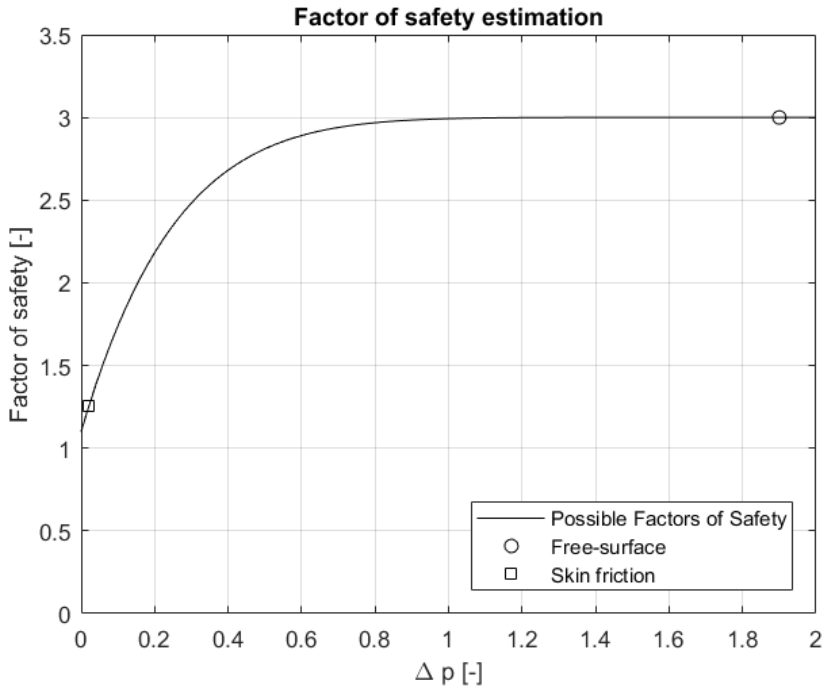

Figure 6.15. Computed Factors of Safety using Eq. (6.17).

The free surface on the other hand is highly non-asymptotic. It may seem that the point depicting its relative location on the Δp range is not at its further possible limit. However, Eq. (6.17) limits the distance from the asymptotic range to 95% of p_f, i.e. a maximum of 1.9, where the free surface Factor of Safety lies. If this limit were not imposed, the attained value along the Δp axis is predicted as 3.0571.

The remainder of the factors of safety and modified orders of convergence are not shown because they depend on simple manipulations of p and p_f. Instead, prevalence is given on the uncertainty itself in what follows.

6.4.4.2 Uncertainty spatial distribution

In this sub-section, the uncertainties for both sampled parameters are given. This is done according to all methods described in Section 2.1.

In Figure 6.16, the uncertainty of the free surface based on the method of Phillips and Roy (2017) is presented with $p = 2$ in the denominator of Eq. (6.18). This is done following the recommendation of the above authors. The uncertainty shown in second place, i.e. that due to Roy (2008) is computed

with a variable factor of safety, and the error provided by the error constants, shown in Eq. (6.11) and Eq. (6.12) multiplied by the fine grid spacing and the FS shown in Figure 6.15. This is then divided by $r^{p_f} - 1$ in line with other error estimators.

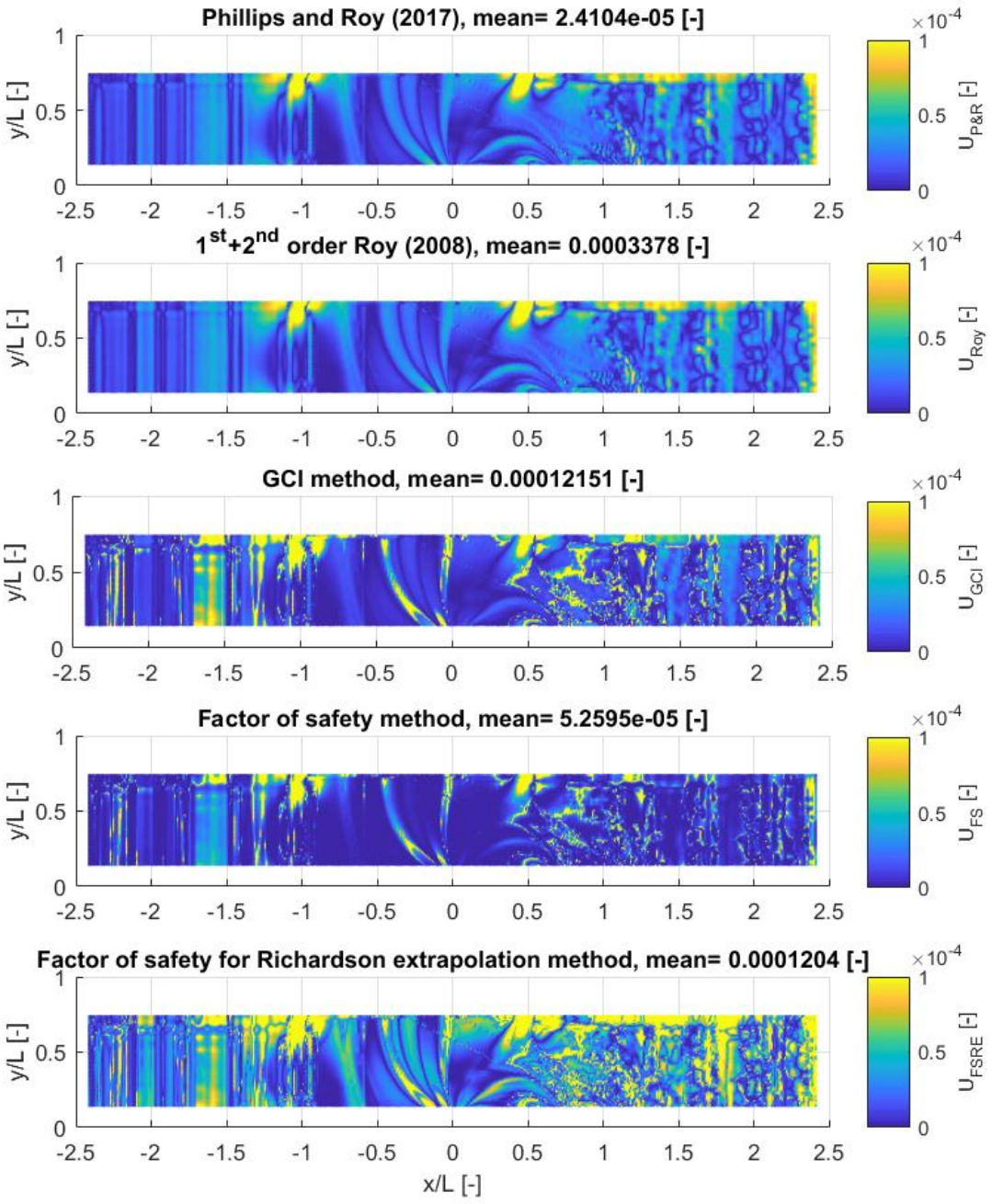

Figure 6.16. Local uncertainty spatial distribution on the free surface according to all methods.

The remainder of uncertainty estimators of Figure 6.16 follow as explained in Section 2. In other words, no modifications have been attempted on these. This

is done to avoid compromising the confidence level of each prediction. The main conclusion, drawn from Figure 6.16 is that the first two methods, due to Phillips and Roy (2017) and due to Roy (2008) exhibit similar levels of convergence, in line with other methods with a longer history of implementation. This is a promising outcome, demonstrating that their use is likely capable of providing good results. Coupling this with the in-depth assessment possible based on the abovementioned methods makes them a desirable approach to error and uncertainty estimation.

As postulated earlier, the locations of heightened uncertainty do not change across methods. However, the magnitude of the uncertainty is highly sensitive to the method employed. For instance, the GCI method predicts heightened uncertainty near y/L between -2 and -1.5. Although the decomposed linear and quadratic components also exhibit increased uncertainty in the vicinity of this region, error cancellation seems to dampen the uncertainty magnitude. Therefore, a greater level of detail can be extracted by the decomposed form of the error. Moreover, the uncertainty is highest in this type of error estimator. However, it should be employed with caution, because as stated previously, its confidence level has yet to be established. Based on the generated data the level of conservativeness predicted for the mixed order method is *circa* 51.64%.

Conservativeness is defined as the percentage of points, where $f_i - U < f_{ext} < f_i + U$ is satisfied. In other words, points where the predicted extrapolated solution lies within the uncertainty band. Since the mixed order method of Roy (2008) is designed for specific orders of magnitude, it is not capable of providing a sufficiently large band of uncertainty to accommodate an extrapolated solution with an observed order of accuracy far from 1^{st} and 2^{nd} powers of the grid spacing. Alternatively, the extrapolation itself may not be a good estimate if the observed order of accuracy is far from the pre-defined powers of the grid spacing. On the other hand, the method of (Phillips and Roy, 2017) provided a coverage of 73.60%.

A confidence interval below 95% is to be expected, since nearly half of all points were not classified as 'Richardson nodes', which is a precondition for the procedure itself. It is likely that the Factor of Safety's value (FS =3) is in part the reason why 73.60% coverage is achieved, rather than a confidence interval equal to the fraction of Richardson nodes. If the present exercise were to be repeated on a structured solver, one may expect that a greater confidence level would be achieved. Unstructured solvers tend to deteriorate the convergence

properties of the solution (Thomas and Langley, 2008). Due to the small number of skin friction samples, confidence bounds are not predicted for τ_w.

The skin friction uncertainty is shown in Figure 6.17 according to the same methods as done for the free surface. In this case, the limits of the uncertainty have been increased for two methods: Roy's (2008) and the FSRE method. This is done to accommodate the larger predictions provided by these estimators. The degree to which the grid is asymptotic, demonstrated in the previous section (Figure 6.15), has rendered the uncertainty prediction due to Phillips and Roy (2017) the smallest. Such behaviour is justified, because the near-wall grid was shown to be highly asymptotic of all methods. The difference between the abovementioned technique and the GCI method is that the former uses the theoretical order of accuracy. The GCI method on the other hand employs the locally observed order, which is in large parts of the domain larger than two. This can be consulted in Figure 6.14.

One final aspect of Figure 6.17 worth considering relates to the distinction of wet and dry areas of the hull. In all methods, the above distinction is clearly visible, with submerged points tending towards greater uncertainty. To provide a more intuitive representation of the uncertainty, Figure 6.18 is constructed to show the fine solution along with the uncertainty computed by each method. In the plot it is more evident which locations along the $x-$ axis are culpable for greater uncertainty levels. It is also manifest that points located near the origin of the abscissa contribute virtually nothing to the overall levels of uncertainty. As stated previously, these points represent the dry parts of the ship hull.

The representation used in Figure 6.18 highlights the existence of several locations where certain uncertainty estimators predict a significantly greater level of uncertainty than others. For example, the GCI method shows that few points in the stern area of the ship are characterised by large errors. On the other hand, Roy's (2008) method predicts a greater number of points behaving in this manner. This is suspected to be due to the interaction of error constants, used by the latter method. Since the GCI method does not distinguish between different orders of convergence in this respect, the decomposition approach can unveil greater detail. At this stage, no comment in terms of robustness is possible, due to the previously examined reasons.

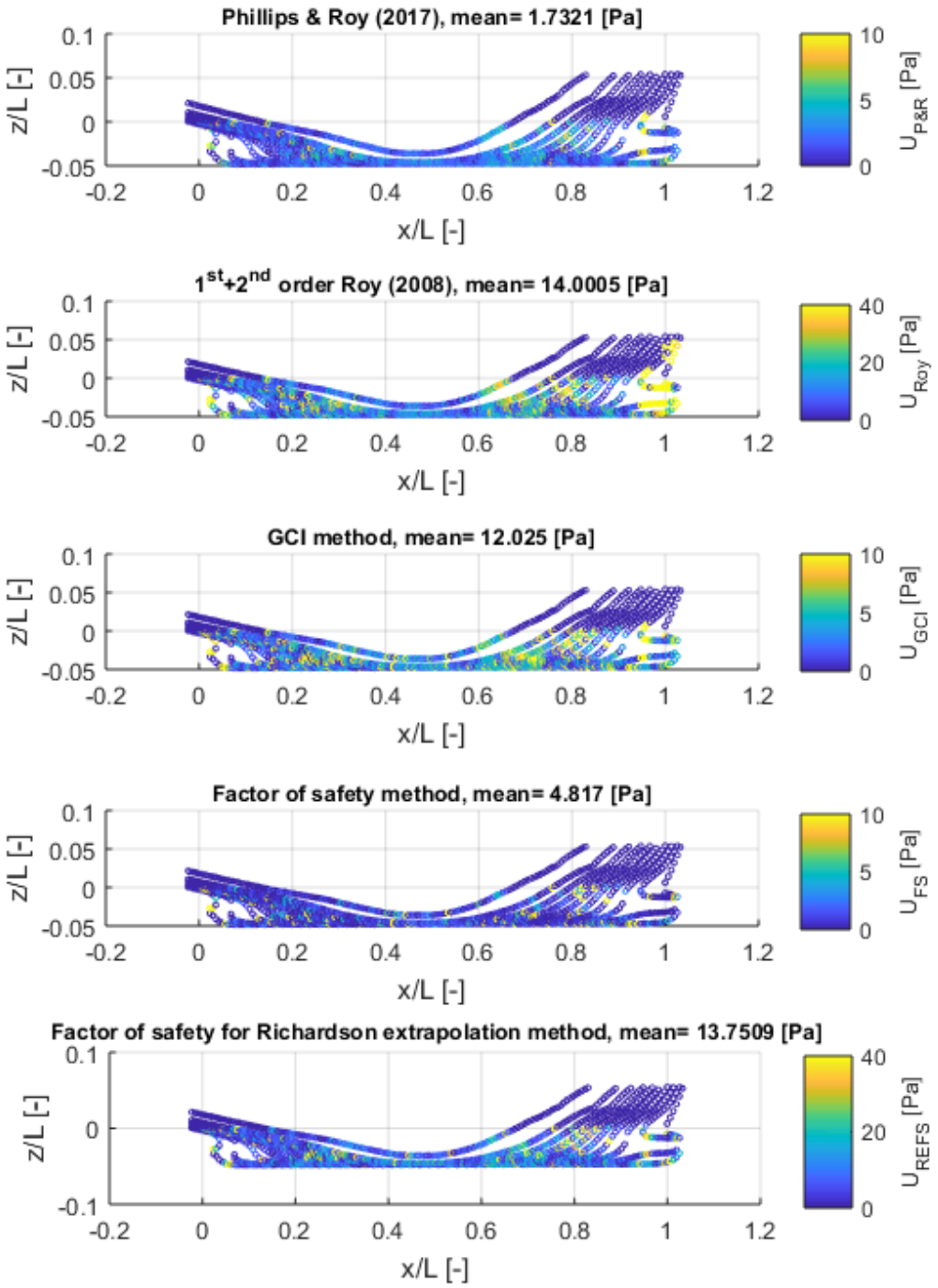

Figure 6.17. Local uncertainty spatial distribution skin friction on the ship hull according to all methods

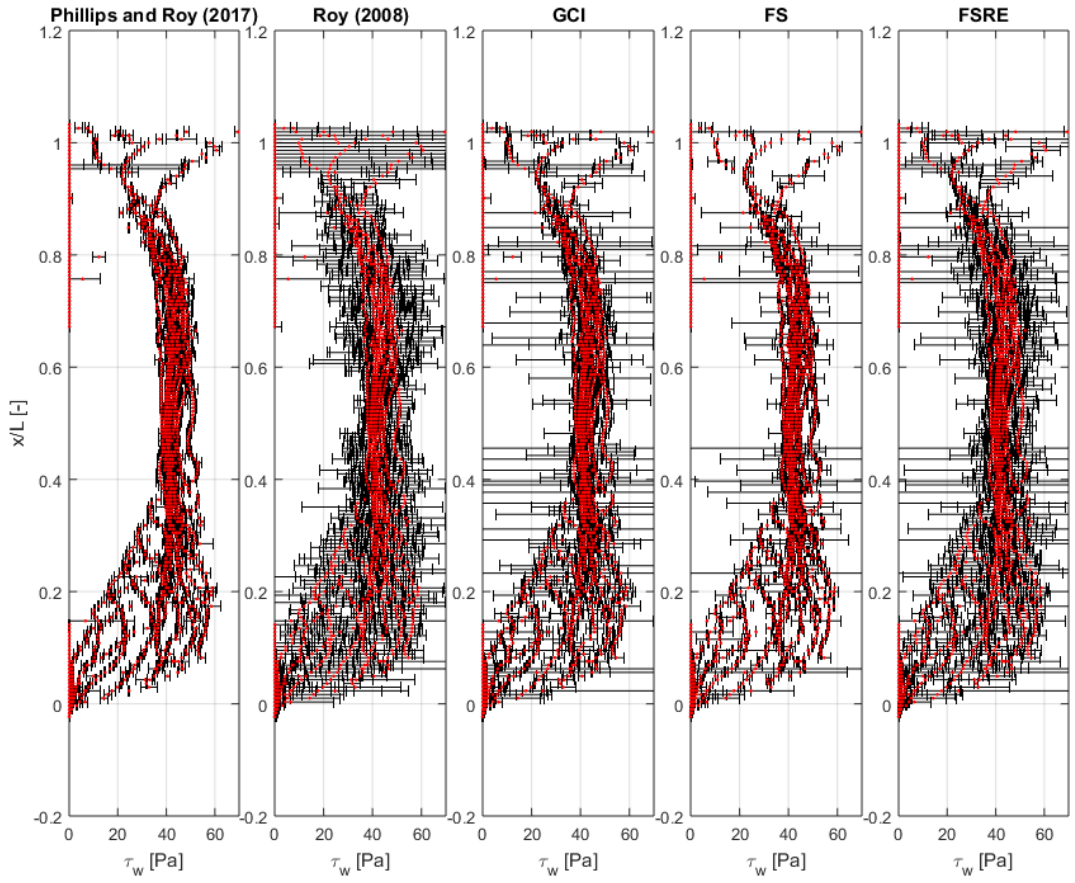

Figure 6.18. Skin friction with error bars.

6.4.4.3 Extrapolated solutions

This section examines the final aspect of the numerical verification procedure. Namely, the extrapolated solutions. There are two such solutions for each sampled point in each parameter (free surface and skin friction). These are the GCI and Roy's (2008) extrapolated solutions. A comparison between the two enables the analyst to confirm the locations of heightened error. Such locations will register in the extrapolated solution as large deviations from the fine solution. Furthermore, upon comparing extrapolated solutions achieved by different methods, it is possible to show which method can cope with non-monotonic input better. This is the case, because such a method would allow for oscillatory samples, providing an extrapolated solution that resembles the input to a greater extent.

For consistency, the free surface is examined first in Figure 6.19, where the two extrapolated solutions are accompanied by the ratio of the fine and respective extrapolated solution. This is done to better highlight the differences between

the separate solutions, and their interaction with the fine solution. The figure serves to demonstrate that both methods predict a discontinuous line emanating from the aft perpendicular and progressing towards the centre of the domain. However, they disagree on its shape and extent. The same is true for a line in the forward part of the hull.

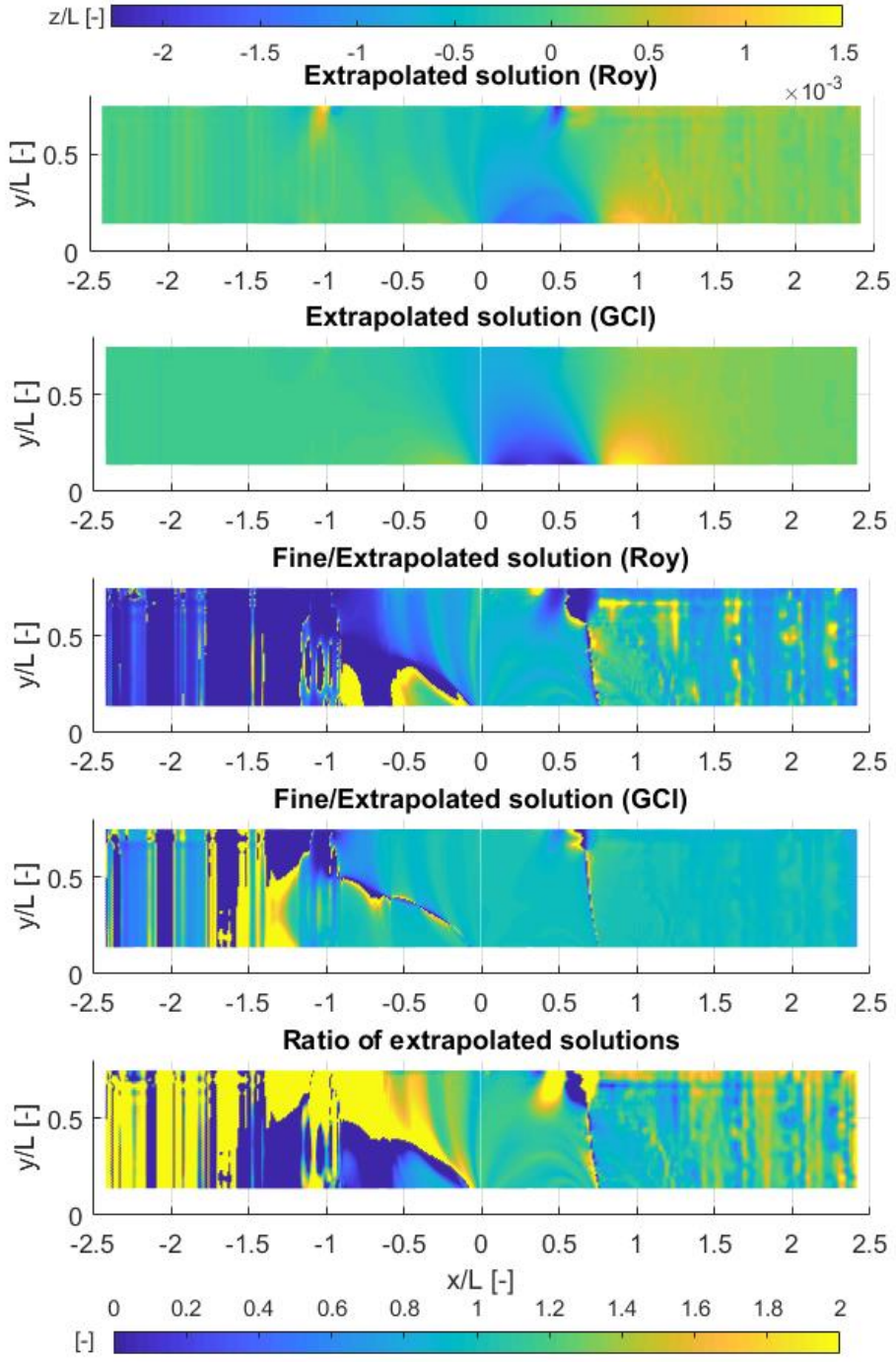

Figure 6.19. Extrapolated free surfaces

Figure 6.19 also reveals patches of differences forward of the ship, the origin of which can only be speculated at. The relative discrepancies between the two methods also highlight that the GCI method predicts to a lesser extent the semi-circular arcs in the proximity of the ship. The elevated levels of error at the side wall are also shown to be of different magnitude. More importantly, the region prescribed to provide the VOF damping seems to be a major source of disagreement between the two methods. This observation indicates that a wide range of numerical parameters simultaneously influence, and therefore compete for the dominant contribution in the error and uncertainty estimate. Splitting these from the grid-induced errors and bifurcating them as separate components may therefore not be the best approach in non-asymptotic grids.

The next step is to examine how the two extrapolated solutions compare in terms of skin friction. This is depicted in Figure 6.20 in the same order as was previously done for the free surface. Here, the GCI method is shown to provide solutions that are practically indistinguishable from the fine solution itself. This can be verified by consulting the plot representing the ratio of the GCI solution and fine solution. Almost all points in this category have attained a value of either one, or are sufficiently close to one. The mixed order method on the other hand does not resemble the fine solution as closely. This causes differences in the predicted solution by the aforementioned approach to be evident when considering its ratio with the fine solution.

Upon comparing the ratio of the two extrapolated solutions in terms of skin friction, further differences emerge. These are visible primarily near the extremities of the ship, suggesting that areas of high curvature may cause disagreement between the two methods. It is likely that the cause of this observation once again stems from the interaction of linear and quadratic components. Figure 6.10 points towards the existence of large errors in both the linear and quadratic terms of the error in this region. Even a small error misalignment will create heightened levels of uncertainty, which may be responsible for the observed levels of disagreement in Figure 6.20.

In summary, this section demonstrated that each error and uncertainty estimator has a distinct tendency when it comes to predictions. The formulation of each distinct approach governs which regions of the sampled domain are highlighted with an increased concentration of numerical problems. In many cases, different aspects of the numerical solution may, and do interact in unpredictable ways. This may be the error itself, exhibiting discontinuities in terms of value as well as order, or other aspects, such as free

surface modelling, convection properties or separate unexamined effects. These include sharpening factors in the VoF scheme, convection order, as well as the grid resolution. On the other hand, the interplay of cell aspect ratio, skewness angle, y^+ value, turbulence model, and convection scheme order generate a distinct problem. In many cases, this interplay may be fortuitously favourable, but unknown, as is probably the case in terms of skin friction. On the other hand, the level of complexity of all components influencing the free surface make it impossible to accurately pinpoint the specific cause-effect relationship, leading to the observed error and uncertainty. However, by attempting to isolate separate aspects of the numerical solution, such as grid density, it is possible to provide recommendations relating to best practices.

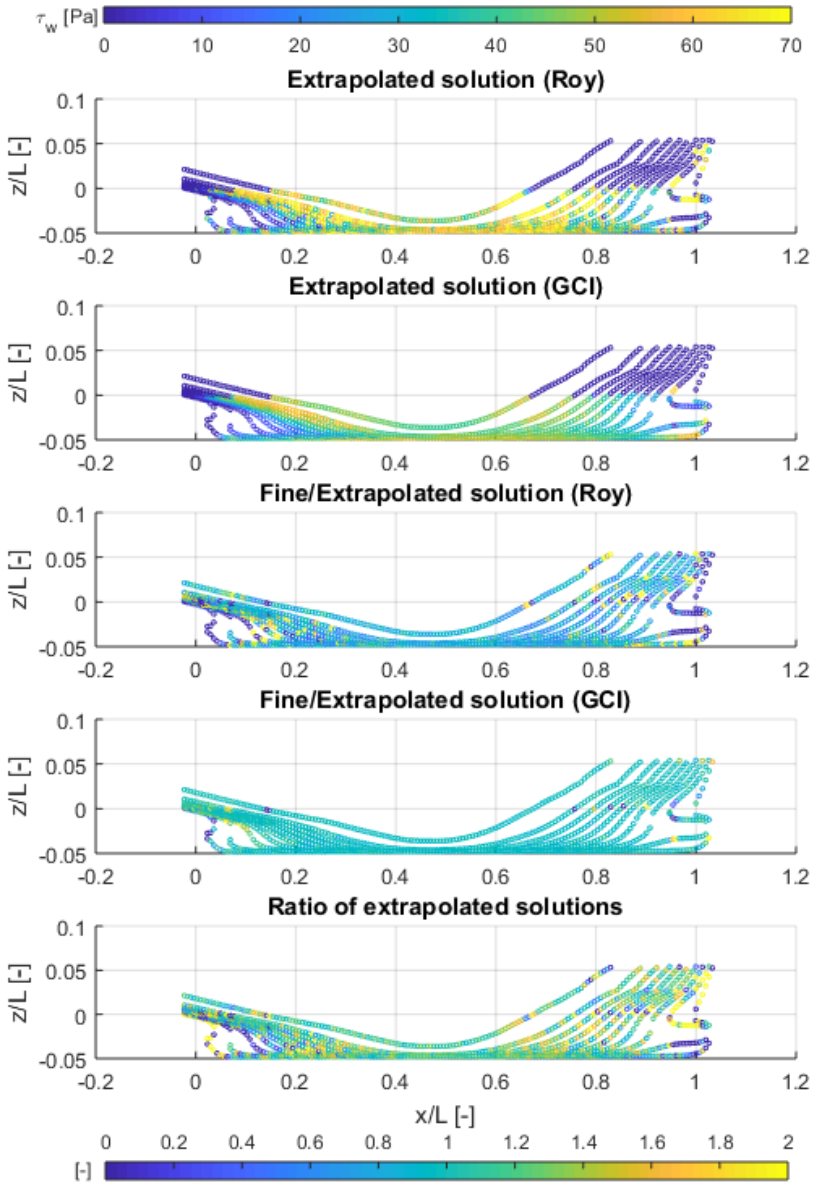

Figure 6.20. Extrapolated skin friction distribution on the hull.

It was demonstrated that in full-scale applications, a y^+ value below one is not a necessary precondition to classifying the near-wall grid as asymptotic. On the other hand, a highly dense grid, encompassing the area where the free surface deforms was shown to be insufficient to brand the sampled points as generated by an asymptotic grid. This also highlights the fact that depending on the grid arrangement and numerical set-up, vastly different behaviours in terms of error can be achieved in separate aspects of the simulation. It should be borne in mind that an asymptotic solution does not necessarily translate into a low validation error. Therefore, the next step would be to compare the solution, generated by a study similar to that presented herein, with experimental data. Recently emerging methods to capture free surface deformations experimentally show potential in this respect (Caplier et al., 2016).

6.4.5 Effect on sampling density

The present assessment used 25×10^4 points to sample the free surface. It is not reasonable to expect such level of detail be used in industrial applications. This is the case for two reasons. Primarily, because exporting 25×10^4 points requires both time and care. But also, one would ideally like to know what is the minimal sample density, required to produce a reliable result. This section will attempt to answer the above question by taking a different number of samples, randomly from the available points.

The present sampling study is performed in steps. Firstly, statistical measures are used to determine the error due to sample size, assuming the exact number of Richardson nodes is known. Then, the available free surface is randomly sampled repeatedly at different levels of density.

The error due to sample size (E) is estimated as shown in Eq. (6.21) for a 95% confidence level, which is depicted graphically in Figure 6.21.

$$E = 1.96 \times \sqrt{m \times (m-1)/n} \tag{6.21}$$

where m is the currently estimated percentage of Richardson nodes (43.9696% of all free surface points), and n is the total number of available points. This procedure implicitly assumes that the above fraction of the total represents the *true* number of Richardson nodes in the domain. Such an assertion should be made with caution, because there is no manner to determine the *exact* number of nodes in each category. Moreover, the classification of nodes may change if the grid is refined further

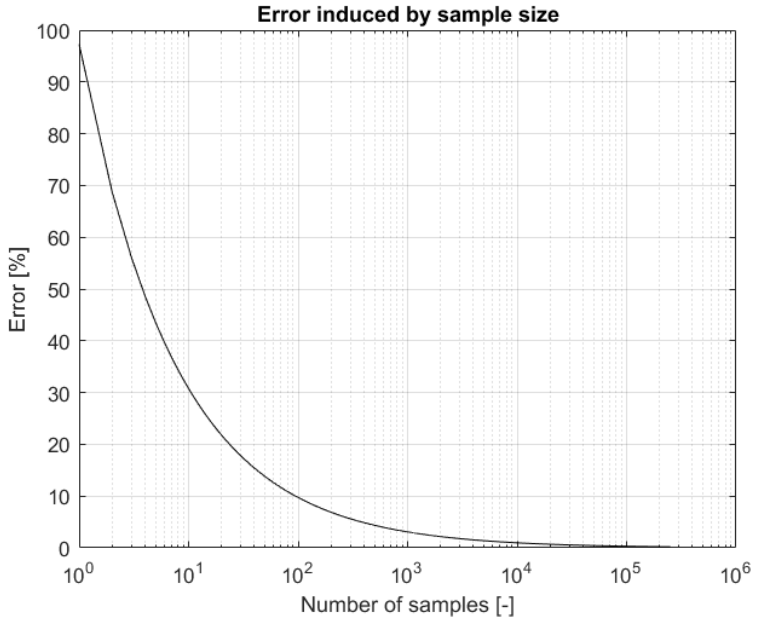

Figure 6.21. Error induced by sample size as predicted by Eq. (6.21).

For the reasons explained above, the free surface is also sampled using random, uniformly distributed points 25×10^4 times. This is performed at the density depicted in the title of each sub-plot of Figure 6.22, i.e. by taking [50%, 25%, 12.5%, 6.25%, 3%, 1%, 0.1%, 0.01%] of all samples. The results from this are presented in Figure 6.23. Here, the Factor of safety and fraction of Richardson nodes are monitored at each sampling iteration. Then, the standard deviation and mean values are used to construct the plot. No individual sample revealed a FS value other than 3, which is why no standard deviation of the Factor of Safety is included. The only varying metric was determined as the % of Richardson nodes. The sample independent solution is also estimated in Figure 6.23 using the GCI procedure to extrapolate a point, based on the final three solutions. Since these exhibit oscillatory convergence, the absolute value modification is employed in the estimation of the order of convergence. The sample-independent solution is shown as a filled circle at the end of the abscissa.

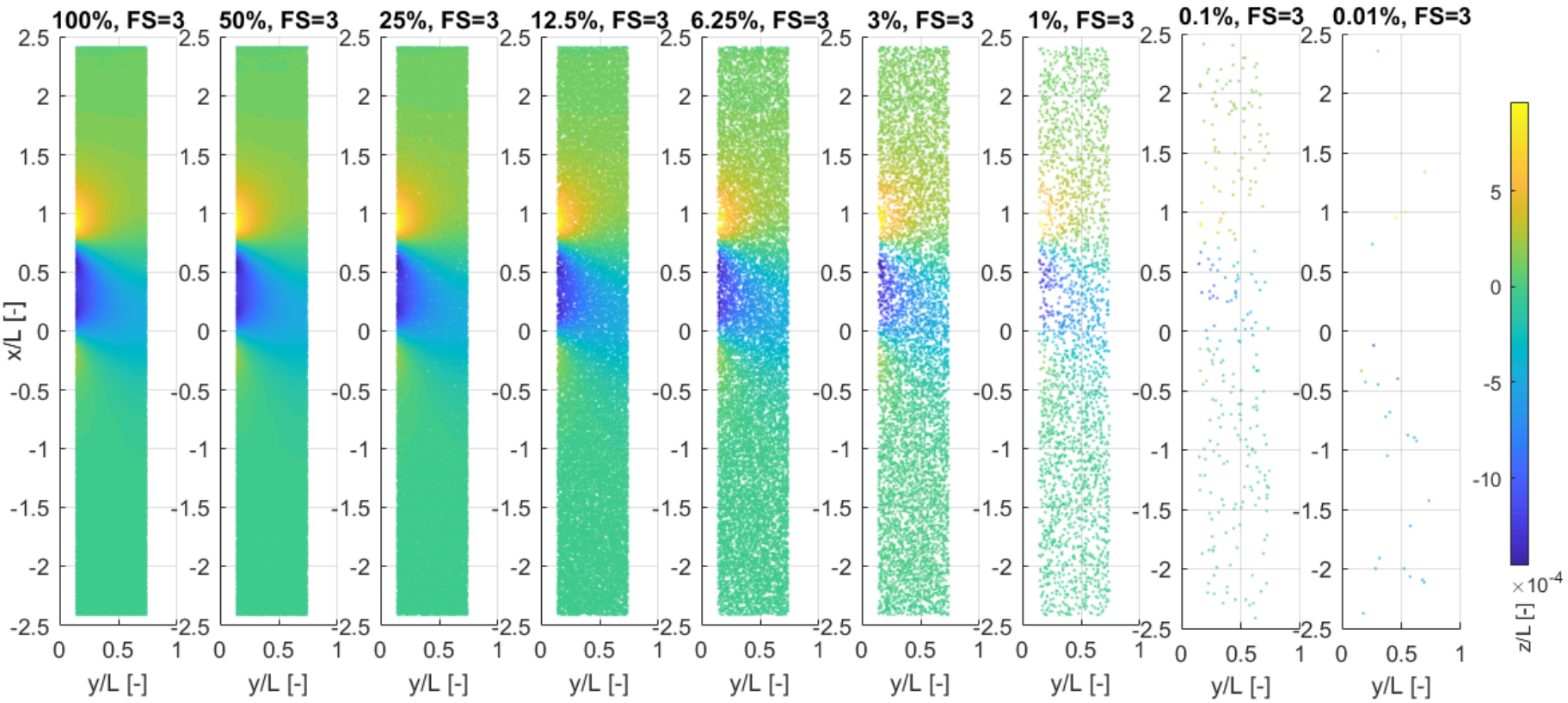

Figure 6.22. Sampling of the free surface. Each sampling, featuring less than 100% of all points is repeated 25×10^4 times.

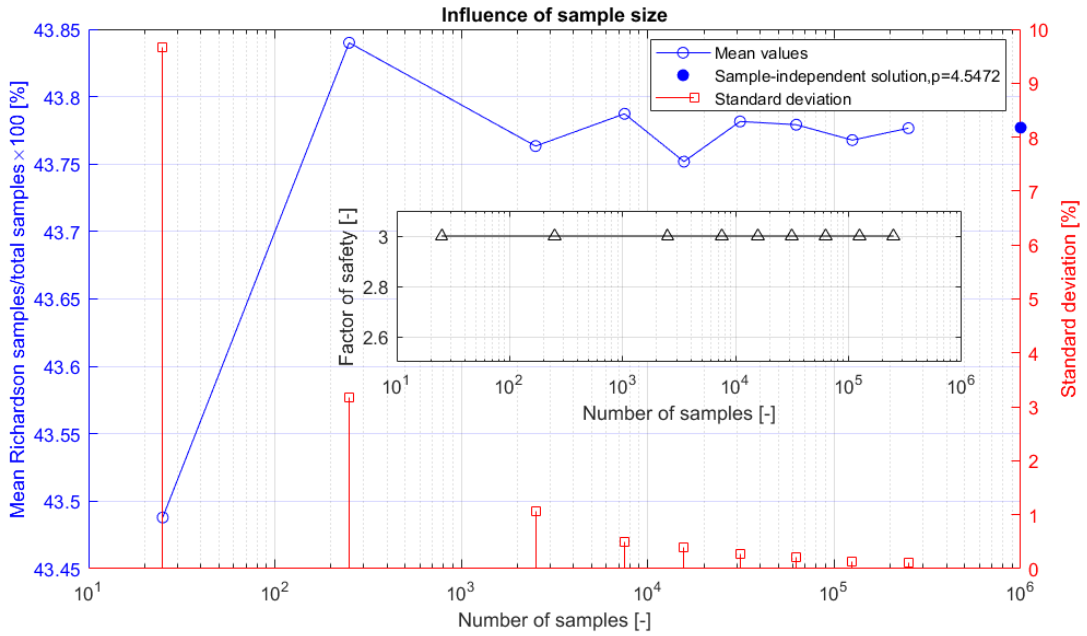

Figure 6.23. Influence of sample size.

The results presented in this Section suggest that 10^4 samples should be sufficient to estimate the Factor of Safety and fraction of Richardson nodes with sufficient confidence. The first part of the assessment performed here suggests that such a sampling density would induce errors smaller than 1%. The second assessment agrees with this conclusion, showing a standard deviation below 1% in the region of 10^4 samples. Since both types of assessments show similar behaviour, it is concluded that the aforementioned number of samples in full-scale is sufficient to accurately estimate the parameters of interest.

6.5 Conclusion and recommendations for future work

The importance of verification of CFD work has gained increased importance and attention, with many influential academic journals and institutes revising their editorial policies to reject any papers not featuring such assessments (American Institute of Aeronautics and Astronautics (AIAA), 1994; Celik et al., 2008; Roache et al., 1986). This fact, coupled with the increased reliance on simulation-based design in all fields of engineering suggests that numerical verification will only increase in importance. It is therefore paramount that new methods are assimilated within all fields of engineering soon after their inception.

This chapter presented the application of non-intrusive *a posteriori* methods to assess the numerical performance of a set of CFD simulations. The main goal was to introduce some well-known local methods of numerical verification to the field of ship hydrodynamics. To increase the practical applicability of the work presented herein, a set of full-scale simulations of the KCS advancing in a canal were adopted. Then, the numerical verification procedures were applied on local parameters, specifically, the free surface elevation and the non-dimensional shear stress, i.e. the skin friction.

The obtained results were presented in terms of several parameters of interest, including the decomposed error, uncertainty as well as the extrapolated solutions. In the case of the free surface, the assessment revealed semi-circular arcs of heightened numerical uncertainty emanating from the hull. The numerical damping beach implemented aft of the ship was also identified as a definite source of uncertainty. More importantly, it was demonstrated that the numerical uncertainty predictions in the damping region were in disagreement between the examined methods. Thus, suggesting that numerous aspects of the numerical simulation likely compete for the dominant error contribution. The grid, containing the free surface was also demonstrated to be far from asymptotic. This is likely due to interaction of different numerical parameters involving the definition of the free surface, which may affect the observed order of convergence.

In terms of skin friction, the assessment revealed that the near-wall grid is highly asymptotic. Regardless of the proximity of the generated grid to the asymptotic range, several uncertainty estimators were tested. These revealed significant disagreements in the magnitude of the uncertainty depending on the adopted approach. Based on the above findings it can be stated that the uncertainty is expected to be highly dependent on the parameter used in its prediction. Different parts of the computational domain are governed by distinct numerical schemes and approaches, thereby increasing the complexity of the problem at hand significantly.

The viscous-dominated part of the domain, located near impermeable boundaries, can be refined sufficiently to bring it in line with the asymptotic range. That is even though this particular part of the computational domain features uncertainties stemming from the choice of turbulence model, y^+ strategy, as well as a phase interphase (to name but a few aspects of the solution). On the other hand, the free surface grid resolution, containing the majority of the cells in the domain was not near the asymptotic range. The

distinction of the grid's performance with respect to the asymptotic range is important, because verification procedures implicitly contain the above requirement. Therefore, the determined uncertainty is a function of grid performance in this respect.

7. VIRTUAL REPLICA OF A TOWING TANK EXPERIMENT TO DETERMINE THE KELVIN HALF-ANGLE OF A SHIP IN RESTRICTED WATER

This chapter presents a virtual towing tank that is consistent with physical towing facilities. This is achieved by removal of all open boundaries within the computational domain. The adopted case studies represent long, narrow canals. The resistance of the ship in the New Suez Canal and a rectangular canal are compared with experimental data. The generated wavefield, including the predicted Kelvin half-angle are validated by means of a Fourier approach. The assessment suggests it may be possible to validate numerical free surfaces even in the absence of experimental data.

7.1 Introduction

Computational Fluid Dynamics (CFD) has become widely accepted as a useful tool to predict flow around a ship. This is facilitated by the increase in available computational power, which has allowed practitioners to re-create the flow around a vessel even on a standard computer. Thus, the number of cells, or more generally, the computational effort required to perform a numerical simulation in model-scale is not thought to be prohibitive for practical applications.

Regardless of the advances in every field of numerical modelling, CFD is not yet considered a replacement of model-scale experimentation. This is because it is not possible to guarantee that a particular numerical model will perform with the same level of accuracy across all possible case studies. For example, new energy-saving devices, or novel underwater shapes may require research into the best applicable modelling approaches. Additionally, the consequences of implementing modelling assumptions may not be fully understood. Specifically, although in model-scale computations, a significant portion of the ship hull is covered by a laminar layer, most turbulence models assume the flow is fully turbulent. Yet, results with accuracy of a few percentage error can be found in the open literature (Bašić et al., 2017; Bechthold and Kastens, 2020; Farkas et al., 2018; Larsson et al., 2014; Razgallah et al., 2018; Simonsen et al., 2013; Toxopeus, 2013).

There are also different aspects of the problem of modelling ship flows that can be validated with different levels of confidence. For instance, the resistance of a ship can be measured accurately. However, velocities in the wake of the ship, or free surface elevations require complex and expensive equipment. Thus, in the course of validating a numerical result, researchers typically analyse the error in observed integral quantities (resistance, motions, etc.), but tend to assume that other flow features are also accurately modelled as a consequence. Although this may be the true in many cases, an approach to validate aspects of the flow around a ship, such as the generated wave field, is necessary. Ideally, such a method would not rely on expensive equipment, nor complex mathematics, in other words, it should be accessible. It is important to mention that some experimental campaigns report on a wide range of features of the flow around the ship, for instance, the flow properties in the wake (Longo and Stern, 2002; Tahara et al., 2002b).

The research presented in this chapter is motivated primarily by the manner in which the problem of ship resistance is typically solved. That is, the principle of Galilean relativity is invoked (also called frame invariance; further information can be found in Kundu et al. (2012)). Namely, the water is flowing over a stationary ship (in the direction of the incoming flow). This assumption has several consequences. Those particularly important to the naval architect are:

1. **Levels of inlet turbulence.**
   This can have an impact on the overall properties of the flow (Wang et al., 2015) and may require calibration in some cases. For example, according to Lopes et al. (2017), the onset of transition from laminar to turbulent boundary layer is strongly dependent on the level of free-stream turbulence. Some two-equation models, such as the SST $k-\omega$ model (which is widely used in marine hydrodynamics), are known to predict excessive decay of free-stream turbulence, which may affect the results. More recently, Lopes et al. (2019) examined the same topic. According to them, even if one were to employ a more advanced eddy-viscosity model, capable of accounting for transition, the location of where laminar-turbulent transition occurs is highly dependent on the level of inlet turbulence.
2. **Wave reflections and their damping.**
   In cases where the Volume of Fluid (VoF) method is used (Wackers et al., 2011), a damping length is often prescribed. That is, a length over which all waves are damped, extending from the boundary it is applied to in the normal direction. Setting an inappropriate damping length can have severe consequences to the predicted parameters (Perić and Abdel-Maksoud, 2016).
3. **The temporal dependency of free surface flows.**
   The simulation of free surface flows via CFD cannot be solved using steady-state solvers (except in rare academic cases), because they require that properties are convected through the domain (Wackers et al., 2011). Theoretically, in the frame of reference of the ship, the flow – once converged – is steady (provided no separation and wave breaking occur). Therefore, ship resistance is frequently classed as a pseudo-steady problem. In reality, towing takes place over time, and is a fundamentally unsteady process. Here, the presence of turbulence, which is by definition time-dependent (Durbin and Pettersson Reif, 2011), should also be kept in mind.

A second aspect, inspiring this Chapter partly stems from point (2) above. Although these may be of less interest to the naval architect, they carry their own importance, nonetheless. Specifically, the destruction of ship waves, regardless of whether or not damping is prescribed. Once a ship-generated wave reaches the outlet, it is irreversibly destroyed, and the information it carries – lost. In shallow and restricted waters, ship waves are of great importance because they cause bank erosion, and may even lead to destruction

of coastal features/infrastructure (Grue, 2017; Sorensen, 1997). In extreme cases, they may even be the cause of loss of life, as stated by Soomere (2007). Therefore, the accurate modelling of ship waves and their interactions with riverbeds, or canal sides is important. Soomere (2007) also advances a criticism of ship-induced flow predictions. Namely, that the flow is only described at a distance of few ship lengths.

Clearly, ship waves are both of practical and research interest. Therefore, the validation of numerical ship-generated waves is of high importance. In this respect, the work of Caplier et al. (2016), Fourdrinoy et al. (2019), and Gomit et al. (2014) is important to mention. The authors of the aforementioned references systematically developed and implemented a technique to capture and analyse ship-generated waves from a model experiment. Of interest to the present research is the fact that in their studies, the authors proved the dispersion relation in deep and shallow water and demonstrated its validity for ships experimentally. Since the developed technique relies primarily on spectral representation of the wave field, it is thought prudent to attempt its application to numerically generated free surface disturbance caused by a ship. It is expected that, if applied correctly, it is possible to validate a numerical wave field simply by means of processing a virtual free surface, which would be undoubtedly of practical use. Such a method has the potential to change how numerical solutions of surface piercing bodies are treated.

The present chapter will attempt to apply the aforementioned spectral technique on a different type of numerical towing tank. Instead of relying on Galilean relativity, the present paper will present a numerical replica of a towing tank, where the ship advances over a stationary fluid. This is achieved via the overset domain method, where the ship is encased in what is essentially a moving box. To perform the numerical simulations, the commercial Reynold Averaged Navier-Stokes (RANS) solver, Star-CCM+ version 13.06, is used. The specific case studies adopted in this chapter are selected to maximise the practical relevance of the present work. Specifically, the New Suez Canal is replicated, alongside a standard rectangular canal, which were investigated experimentally by Elsherbiny et al. (2019). The KRISO container ship (KCS) with a scale factor of 1:75, following available experimental data is used for all simulations.

The aim of this chapter is primarily to demonstrate that it is possible to create a virtual towing tank where the ship is towed using the overset method, i.e. a virtual towing tank that does not rely on Galilean relativity. The generated

wave field will then be used to estimate the Kelvin half-angle for an example case. The adopted approach also allows one to split the near- and far-field wave systems, which is used on the fully non-linear disturbance, generated by the KCS at a variety of speeds in two different canals.

This chapter is organised as follows. Section 7.2 contains a description of the adopted case studies, while section 7.3 explains the adopted methodology, which is split into the two techniques used in this chapter. Namely, the computational set-up and the spectral representation techniques. Section 7.4 is dedicated to results and their discussion, whereas section 7.5 contains conclusions and summary.

7.2 Case studies

As mentioned in the previous section, the adopted case studies are taken from the experimental work of Elsherbiny et al. (2019). The rationale behind this choice relates to the particular objective of this chapter. To elaborate, shallow water studies are a natural choice for the examination of ship-generated waves. This is because they present several features, absent in deep water ship-generated waves. Shallow water waves are nonlinear, and their Kelvin half-angle is speed-dependent (Tunaley, 2014; Yang et al., 2011). This is illustrated in Figure 7.1, which is constructed via Havelock's (1908) linear method. Here, the Kelvin wake angle increases from its deep-water value of ≈19.47° to 90°. The theory predicts that at a depth Froude number ($F_h = U/\sqrt{gh}$, where U is the ship speed in m/s, g is the gravitational acceleration, and h is the water depth) of one, $F_h = 1$, the ship-generated waves will travel at the same speed as the disturbance, indicating the Kelvin wedge fills the entire half-plane aft of the disturbance, i.e. at a half-angle of $\theta = 90°$. The relationships derived by Havelock (1908) are omitted in the present work, as they are available in the open literature.

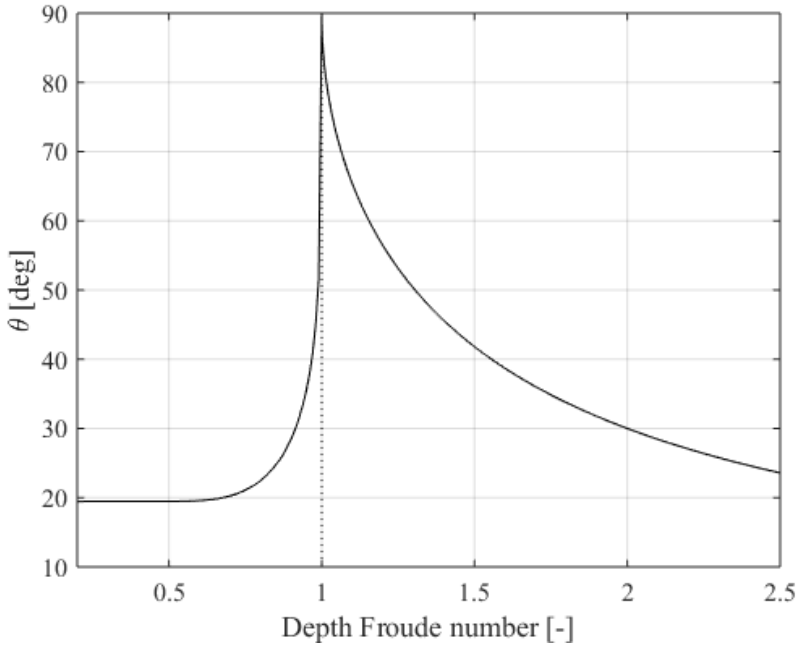

Figure 7.1. Kelvin half-angle of ship-generated waves in shallow waters as a function of the depth Froude number (Havelock, 1908).

Ship-generated waves are also of greater concern in restricted areas than in deep waters, because they may affect the surrounding environment detrimentally. In navigational fairways, bank erosion is of particular concern, which has led to authorities restricting the speed with which vessels are legally allowed to operate (Suez Canal Authority, 2019). Such a restriction simultaneously guards against groundings.

The case studies adopted herein are chosen to reflect the aforementioned points. In this respect, the recent work of Elsherbiny et al. (2019b) is used as a benchmark. From their experimentally investigated cases, two different canal cross sections are selected: The New Suez Canal, and a standard rectangular canal. These are graphically depicted in Figure 7.2.

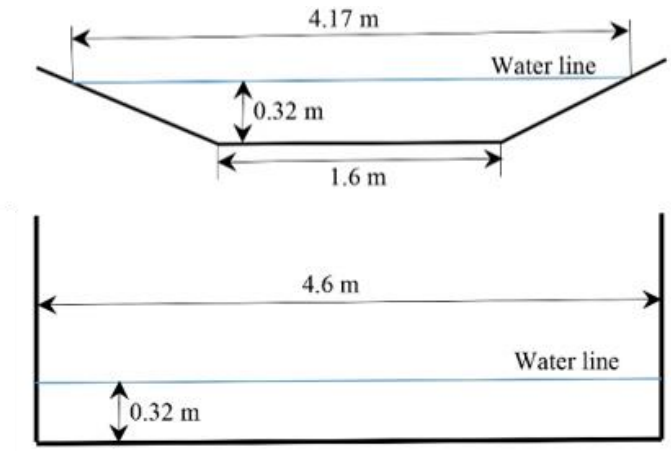

Figure 7.2. Graphical depiction of the cross-section of the selected case-studies. Top: New Suez Canal, bottom: rectangular canal.

The ship used also follows from the experimental campaign of Elsherbiny et al. (2019b). Namely, the KCS hull form is used, scaled by a factor of 1:75. This translated into a depth-to-draught ratio of 2.2, based on the ship's design draught. In order to ensure that a well-defined Kelvin wake is simulated, the selected depth Froude numbers are towards the high end of the experimentally available conditions. The ship's particulars are given in Table 7.1, whereas test matrix alongside the predicted Kelvin half-angles (via Havelock's (1908) method) are described in Table 7.2. It should be noted that Havelock's (1908) method was originally devised for point sources, and is therefore not expected to be perfectly accurate for non-linear three-dimensional surface piercing bodies. Nonetheless, it is a useful starting point. Additionally, turbulence, viscosity and vorticity may influence ship-generated waves, particularly in the near-field (Lee and Lee, 2019).

The relatively high depth Froude numbers ensure the numerically generated wave field will be discernible. The spectral method used also performs best at high speeds, where the near and far-field disturbances generated by the ship are well visible. This can be seen by consulting the results of Caplier et al. (2016).

7.3 Methodology

This section is presented in two major parts. These reflect the methodologies used within this chapter. The first section presents the numerical set-up, which is followed by an explanation of the spectral method in the second sub-section.

Table 7.1. Ship characteristics.

Quantity	Symbol	Value	Unit
Scale Factor	λ	75	-
Length	L	3.067	m
Beam	B	0.429	m
Draught	T	0.144	m
Depth	D	0.253	m
Water depth	h	0.32	m
Block coefficient	C_B	0.651	-
Longitudinal Centre of Gravity	LCG	1.488	m
Wetted area	S	1.694	m^2

Table 7.2. Test matrix and resultant Kelvin half-angles according to Havelock's (1908) method.

Canal	Case No	Depth-to-draught (h/T)	Depth Froude number (F_h)	Ship speed (m/s)	Kelvin half-angle (°) (Havelock, 1908)
Rectangular canal	1	2.2	0.57	1.01	19.52
	2		0.77	1.364	21.58
New Suez Canal	3		0.47	0.815	19.47
	4		0.57	1.01	19.52

7.3.1 Numerical aspects

The solver, Star-CCM+ version 13.06, employs the finite volume method to model the flow, which uses the integral form of the incompressible RANS equations and divides the computational domain into a finite number of adjoining cells. Continuity and momentum are linked via a predictor-corrector approach. Further details pertaining to the implementation and algorithms used can be accessed in Siemens (2018) and Ferziger and Peric (2002)

To account for turbulence within the fluid, the k–ω model due to (Wilcox, 2008) is used. This choice is made following the findings of Chapter 4, which showed the particular model to be stable and provide the fastest solution time of all two-equation variants. Benefits of using the k–ω model include its seamless application to low y^+ type meshes ($y^+ < 1$). This is a desirable feature, because it avoids the use of wall functions, or any other bifurcations of the solution, as is the case with the k–ε model (Siemens, 2018). Although wall functions can predict the forces acting on a body with good accuracy, they may introduce errors in the modelling of hydrodynamic properties in the wake of a ship. For instance, they are unable to account for flow separation (Pettersson Reif et al., 2009). To facilitate a good representation of turbulent properties, a second order convection scheme is applied throughout all simulations.

To characterise the fluid interphase, the Volume of Fluid (VoF) method is used (Hirt and Nichols, 1981). Moreover, Star-CCM+ offers a High Resolution Interphase Capturing (HRIC) scheme to enhance the definition of the free surface, which is applied to all numerical simulations (Muzaferija and Peric, 1999). Vertical ship movement, i.e. sinkage and trim, are not accounted for to reduce the complexity of the simulations. Instead, the ship's position in the x – z plane is adjusted prior to initiating the simulation (by manually changing the ship's position). This is done in an attempt to reduce the discrepancy between the experimental results, and those derived herein. However, some difference is expected to persist since the experimental data, reported by Elsherbiny et al. (2019b) was determined for a free to sink and trim KCS model.

7.3.1.1 Computational domain

As stated previously, frame invariance is not used. Instead, the ship is given the corresponding velocity, which can be consulted in Table 7.2 for each canal. To model the motion of the ship along the canal, the overset domain approach is used. Thus, the ship is towed in the virtual environment over a static fluid. This has two main consequences. Firstly, the computational domain can no longer conform to the recommendations of the ITTC (2014) relating to the positioning and dimensions of the computational boundaries. Instead, an attempt is made to replicate the towing tank used for the experimental work, used as a benchmark. Specifically, the Kelvin Hydrodynamics laboratory at the University of Strathclyde. Naturally, the width and depth of the computational domain must satisfy the test cases (given in Table 7.2). On the other hand, the length of the computational domain is set as 60 m long. The

dimensions are kept the same across case studies (pertaining to the overset domain and the length of the tank). These are shown in Figure 7.3. The height of the static domain is set as 1.23 ship lengths from the undisturbed water surface in all cases to eliminate any possible effects stemming from the height of the domain.

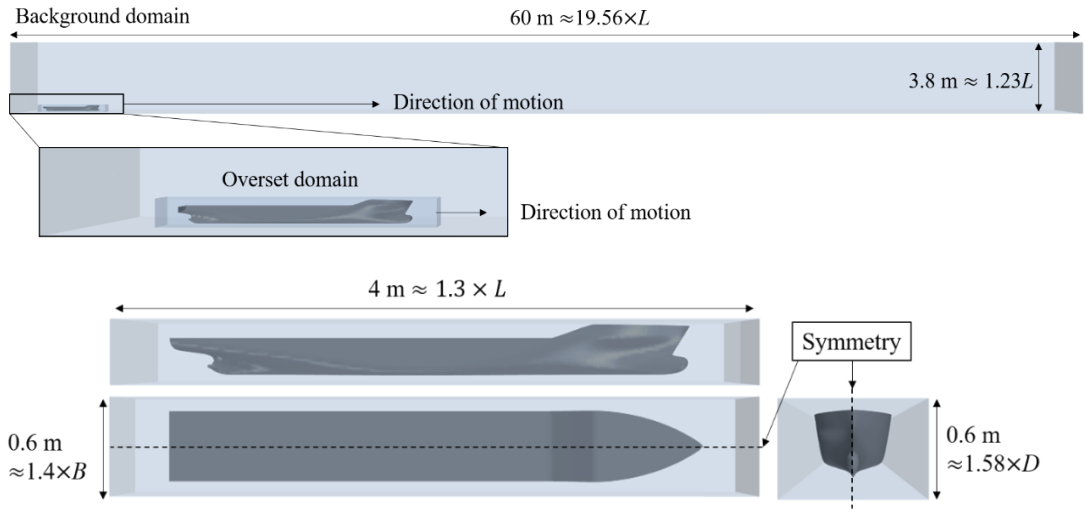

Figure 7.3. Length of the computational domain and dimensions of the overset domain.

The dimensions of the overset domain, which are maintained identical across case studies are also shown in Figure 7.3. It should be noted that for visualisation purposes, the figures have been mirrored about the central plane. Other than the boundary, coincidental with the canal and ship centrelines, where a symmetry condition is imposed, all other boundaries within the background domain are no-slip walls. This is in line with the goal of designing a more realistic representation of a towing tank. Specifically, so-called 'open boundaries' do not exist in reality (Oberkampf and Blottner, 1998). Examples of such boundaries include velocity inlets and pressure outlets. Although it is easier to define the conditions at such boundaries mathematically, they are a definite source of modelling error as discussed earlier.

The manner in which the computational domain is constructed allows the removal of wave damping. Moreover, the definition of turbulent properties on boundaries (such as levels of inlet turbulence) of the fluid is not necessary since there are no inlets nor outlets present. However, it should be noted that the initial conditions in terms of turbulence in the fluid follow the recommendations of the software developers, namely that a turbulent

viscosity ratio of 10 should be used. This decays rapidly and is close to zero in the non-disturbed region of the domain at the end of the acceleration phase.

7.3.1.2 Computational mesh

The computational mesh is generated entirely within the automatic facilities of Star-CCM+. As stated earlier, the near-wall mesh is generated so that $y^+ < 1$ over the wetted area of the ship. This is achieved via the prism layer mesher, offered by Star-CCM+. The choice of background and overset mesh is of critical importance. This must be done in a way that enables the solver to adequately capture flow properties as they transition from the background into the overset mesh. The cell distribution of each domain is depicted graphically in Figure 7.4, whereas Figure 7.5 depicts the y^+ distribution on the hull at a physical time of 40s for the F_h =0.77 case.

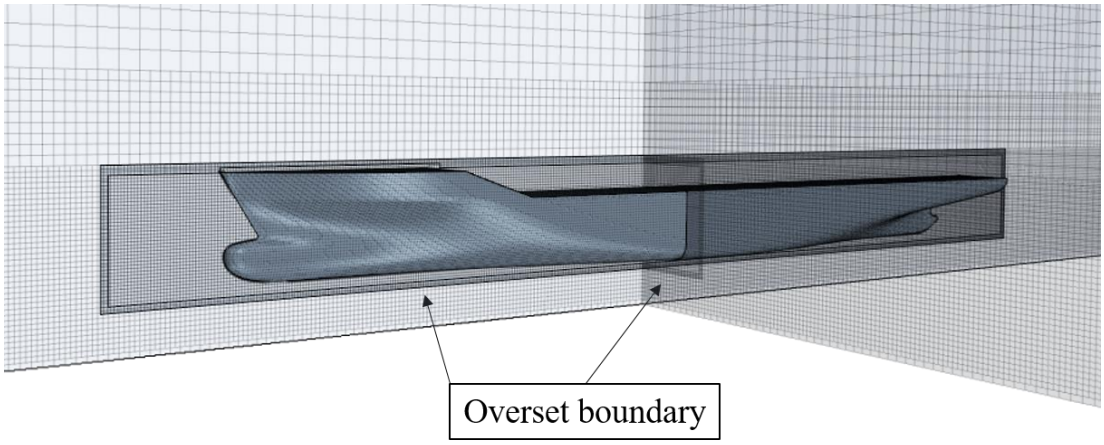

Figure 7.4. 3D depiction of the computational mesh.

The arrangement of the mesh does not vary across case studies; the total cell numbers for each canal are shown in Table 7.3. The circa 8 million cell difference between the two adopted canals is a direct result of the smaller wetted volume occupied by the Suez Canal.

Figure 7.4 also depicts the manner in which the mesh coarsens as the distance from the waterline is increased. This gradual coarsening is implemented to reduce the overall number of computational cells.

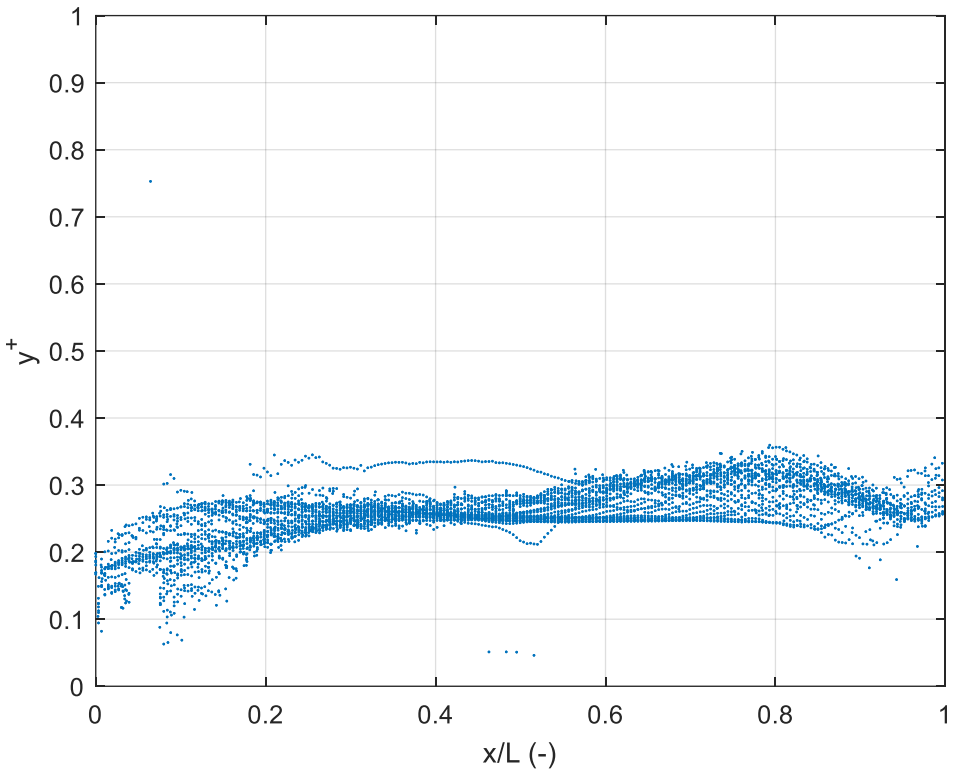

Figure 7.5. The y^+ distribution of the ship hull at F_h =0.77, sampled at 40s physical time.

Table 7.3. Cell numbers for both canals.

Canal	Background cells	Overset cells	Total
Rectangular canal	29,312,452	766,402	30,078,854
Suez Canal	21,496,179	766,402	22,262,581

7.3.1.3 Time-step selection

Time-step selection is of high importance in CFD. In this respect, the Courant–Friedrichs–Lewy (CFL) number may be used as an assessment criterion. The CFL number is defined as the product of the flow speed and time-step, divided by the mesh size (Ferziger and Peric, 2002). As a fluid parcel propagates through a mesh, one would ideally aim to capture its properties at each cell. This is satisfied when CFL<1. Since the mesh is kept identical for all cases, the highest speed can be used to assess the CFL condition. Moreover, a CFL condition onto the background domain is not a meaningful metric, since the

majority of the fluid is static. Instead, the CFL number within the overset box is monitored throughout the duration of the simulation.

Typically, when solid body motion is present, the time-step requirements are relatively low. Here, a trial with a time-step of $0.0035L/U$, where L is the ship length and U is the ship speed in m/s was used. The results indicated good agreement with experimental data, as will be demonstrated in the following section. For this reason, the time-step is set at $0.0035L/U$ for all simulations. In all RANS solution, there is a trade-off between computational resource consumption and turn-around time. For the highest speed, the average CFL within the overset domain did not exceed 0.7, which is considered adequate for a first order temporal discretisation scheme. It should also be born in mind that if the time-step is too low, severe numerical noise may be noticed in the solution time-history (Yuan, 2019).

7.3.1.4 Time-history of the solution

An example time-history of the resistance of the ship is given in Figure 7.6. The figure is characterised by two distinct regions. Firstly, the ship is accelerated linearly up to the target velocity. This is done by linking the time-step and velocity. The specific approach adopted requires the ship speed to reach its steady value at the end of the first 1000 time-steps. In other words, the ship's velocity is increased by $U_{target}/1000$ each time-step. Thus, after an initial oscillatory behaviour, the resistance time-history exhibits oscillatory convergence towards its steady-state value. The oscillations are liked with the reflections of waves from the side walls, which also impact the observed resistance (Yuan et al., 2018). All final values, reported in are obtained by averaging over one period of oscillation of the resistance curve. The specific point where averaging is performed is chosen to be sufficiently far from the acceleration phase to eliminate its effect.

Figure 7.6 is characterised by a sharp cusp at the end of the acceleration phase. This stems from the approach adopted to towing the ship through the domain. Once the velocity of the ship has reached its final value, the simulation is stopped, and the towing speed altered. It is thought that this change induces a shock on the ship, which causes the observed cusp. This is likely not the observed in physical towing. Nevertheless, the results, used for the present analysis are taken a considerable time after this shock occurs. Therefore, the results are not thought contaminated by this cusp.

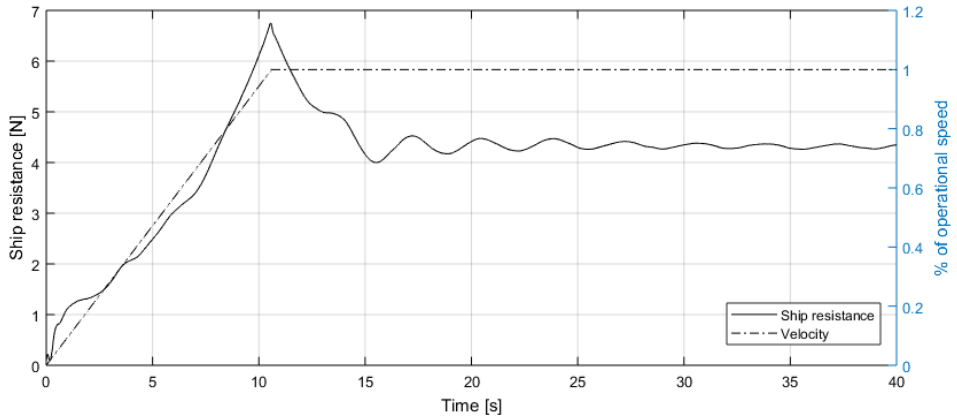

Figure 7.6. Example time-history of the solution (depicted: F_h=0.57).

7.3.1.5 Verification

This section contains the numerical verification of the case study in the rectangular canal, F_h=0.57. The numerical uncertainties are estimated via the Grid Convergence Index (GCI) method. This is the standard way to report numerical uncertainties in ship CFD (ITTC, 2002). It is assumed that the remaining cases are characterised by similar levels of numerical uncertainty.

The GCI method requires three systematically coarsened solutions for the same case. The recommendations of the ITTC (2002) are followed. Specifically, the refinement ratio, $r = \sqrt{2}$ is adopted. The refinement ratio is used to coarsen and lessen the grid size and time step, respectively. The GCI method assumes that all three solutions are close to the asymptotic range, and are sufficiently different, which may be difficult to achieve in practice. The proximity to the asymptotic range is typically characterised by the convergence ratio, p, which is shown in Eq. (7.1).

$$p = \ln(\varepsilon_{32}/\varepsilon_{21}) / \ln r \tag{7.1}$$

where ε_{32}=f_3 – f_2, and $\varepsilon_{21} = f_2 - f_1$. Here, f_i represents the i^{th} solution, generated by a systematic coarsening/lessening of the input parameter (grid or time-step). If $p = 2$, then the grid or time-step can be deemed asymptotic (Roy, 2005). The convergence properties, however, can be determined in a different manner, which also carries information on what type of convergence/divergence is achieved with refinement. This is known as the convergence ratio, R=$\varepsilon_{21}/\varepsilon_{32}$ (Stern et al., 2006). Based on the value of R, the following may be interpreted:

- Monotonic convergence is observed if $0 < R < 1$
- Oscillatory convergence is observed if $R < 0$
- Divergence is observed if $R > 1$

The GCI method is only applicable in case (1). Next, an error estimate (ε_{21}) is defined as (Celik et al., 2008):

$$\varepsilon_{21}=(f_1 - f_2)/f_1 \quad (7.2)$$

Once the error is known, the numerical uncertainty can be calculated as shown in Eq. (7.3) (Roache, 1997):

$$GCI=1.25\ \varepsilon_{21}/(r_k^p - 1) \quad (7.3)$$

where k represents the k^{th} input variable (grid or time-step). The factor 1.25 in the numerator of the expression, defining the numerical uncertainty represents a Factor of Safety. This has been devised to ensure that the true solution lies within the bracket provided by the *GCI* with 95% confidence. The results from the convergence study can be seen in Table 7.4

The successive grid coarsening resulted in 10,955,825 and 4,155,326 cells for the medium and coarse solutions, respectively. In terms of spatial dependence, the solution exhibited rapid ranges with reduction in cell numbers. This 'superconvergence' can be deduced by examining the order of accuracy, p. While in the case of grid coarsening it is approximately 9, when the time-step is lessened, the solution changes according to p_{time}=0.463. According to Eca and Hoekstra (2009), orders of accuracy between in the range 0.5 and 2 can still be treated as asymptotic.

Eca and Hoekstra (2009) devised a procedure based on a least-squares fit to estimate the numerical uncertainty. Their method is not employed here, because it requires a minimum of four solutions. Further coarsening of the computational mesh resulted in divergent behaviour in the simulation. The consequence of the time-step exhibiting the above order of accuracy means that the *GCI* method predicts large numerical uncertainties. That is, even though the overall change between the coarse and fine solution is less than 3% of the fine solution's value.

It should be noted that the time-step as kept at the smallest value while coarsening the grid. Conversely, the finest grid was maintained throughout the temporal convergence analysis. To ensure that the ratio of overset cell to background cell dimension is kept constant, both domains were coarsened

simultaneously. It is assumed that all examined cases will exhibit similar levels of spatial and temporal dependence. For this reason, the above procedure is not repeated.

Table 7.4. Grid and time independence (rectangular canal, F_h=0.57). EFD result: 4.5047 N.

Parameter	Mesh	Time-step	Units
r	$\sqrt{2}$	$\sqrt{2}$	-
f_1	4.325 (29,312,452 cells)	4.325	N
f_2	4.356 (10,955,825 cells)	4.381	N
f_3	5.045 (4,155,326 cells)	4.446	N
R	0.044	0.852	-
p	9.005	0.463	-
GCI (%)	0.6704	19.609	-

7.3.2 Spectral representation of the wave field

In this section, the method devised by Caplier et al. (2016) and Gomit et al. (2014) is briefly examined. This method has previously been used to determine a ship's speed via satellite imagery (Arnold-Bos et al., 2007; Wu, 1992). The essence of the approach is to process an available water surface in Fourier space. To achieve this, a 2D Fourier transform is used to represent the disturbance in the spectral space (k_x, k_y). These arise by defining the angular wavenumber, k, as a vector containing x and y components, $k = \sqrt{k_x^2 + k_y^2}$. The spatial equivalent of these components are used to calculate the extents of the spectrum. The x-direction length of the entire water surface (L_x) becomes $k_{x,max}$, similarly, using the extent in the y-direction (L_y) one obtains $k_{y,max}$, as shown in Eq. (7.4). Likewise, the resolution of the water surface in real space dictates the steps in Fourier space Δk_x and Δk_y in the x and y directions, respectively (Eq. (7.5)).

$$k_{x,max} = 2\pi/L_x \, , \, k_{y,max} = 2\pi/L_y \tag{7.4}$$

$$\Delta k_x = \frac{1}{2} \times \frac{2\pi}{\Delta X}, \, \Delta k_y = \frac{1}{2} \times \frac{2\pi}{\Delta Y} \tag{7.5}$$

where ΔX and ΔY are the resolutions in the x and y directions, respectively.

If surface tension is ignored, the dispersion relation in shallow water may be expressed via the angular frequency (ω) of the waves as shown in Eq. (7.6). This is justified, because surface tension becomes important only in waves, characterised by wavelengths smaller than 7cm. Alternatively, the travelling disturbance should propagate with a speed higher than 0.23 m/s (Lighthill, 1990).

$$\omega(k) = \pm\sqrt{gk\tanh kh} \tag{7.6}$$

A moving ship will cause the waves to be Doppler-shifted, and setting ω'=ω, and $k' = k$, the resulting dispersion relation becomes (Caplier et al., 2016):

$$\omega'(k) = \pm\sqrt{gk\tanh kh} - Uk_x \tag{7.7}$$

To obtain the locus of the dispersion relation, Eq. (7.7) is solved for $\omega'(k) = 0$ (Carusotto and Rousseaux, 2013), which yields:

$$U^2k_x^2 - g\sqrt{k_x^2 + k_y^2}\tanh\left(h\sqrt{k_x^2 + k_y^2}\right) = 0 \tag{7.8}$$

Eq. (7.8) is symmetrical with respect to both axes (Crapper, 1964). This is demonstrated in Figure 7.7, which includes to computed loci (this is used to represent the solutions of Eq. (7.8)) for F_h=0.57, 0.77, according to the adopted cases. Alongside these, the critical depth Froude number is depicted to demonstrate the effect of ship speed on the dispersion relation in shallow water. It should be noted that, the dispersion relation is speed independent in deep water (Caplier et al., 2016). The arms of the loci always begin at $k_{y,x}/(g/U^2)$ =1 in deep water. This is also the cut-off wavenumber. In shallow waters on the other hand, the cut-off wavenumber varies with speed. This can be seen by consulting Figure 7.7, specifically, where the loci cross the abscissa. Here, the case for F_h=0.47 is not shown, as it is practically impossible to distinguish it from the F_h=0.57 case. Deep and shallow water cases are essentially identical when $kh \gg 1$.

The cut-off wavenumber separates the near-field disturbance from the far-field waves, generated by the ship (Caplier et al., 2016). Thus, useful analysis with applications to loads on coastal structures may be performed by removing the near-field disturbance, which does not propagate away from the ship. To determine the cut-off wavenumber (k_x^c) in shallow water, Caplier et al. (2016) solved Eq. (7.9).

$$U^2k_x^c - gk_x^c\tanh(hk_x^c) = 0 \tag{7.9}$$

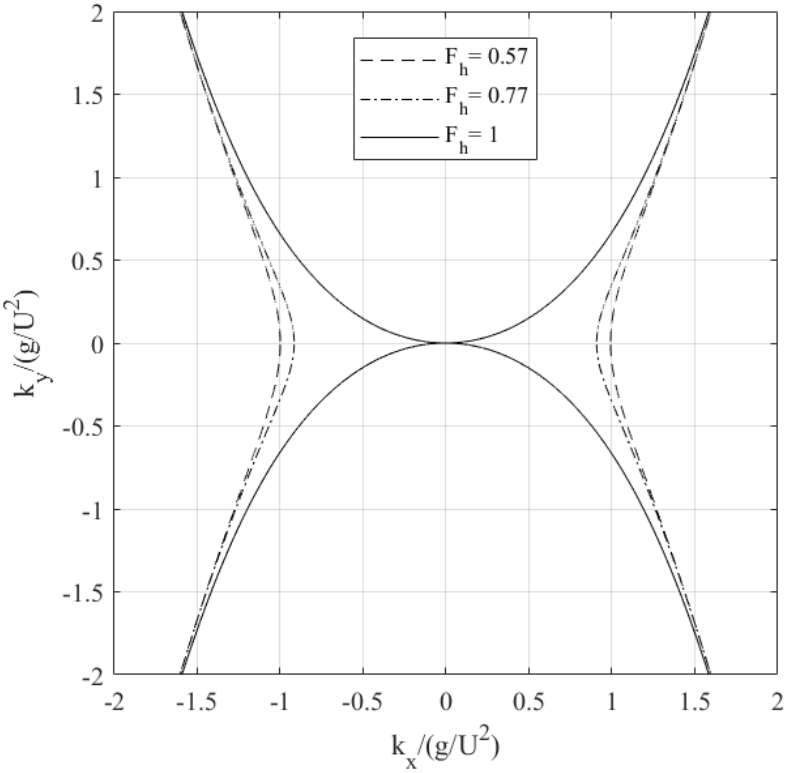

Figure 7.7. Solutions to Eq. (7.8). Figure depicts the examined loci, alongside the critical depth Froude number (F_h=1) to demonstrate the effect of speed.

Finally, the Kelvin half-angle may be determined by computing $\tan\theta = \left(dk_y/dk_x\right)^{-1}$ at the inflection point. According to Nakos and Sclavounos (1989), numerical errors will manifest near cut-off wavenumbers. This can be deduced by examining Figure 7.7. Even a small deviation in the intersection between the locus and the abscissa will lead to large errors. The specific example given demonstrates the relatively low distance between the intersection point of F_h=0.57 and 0.77. On the other hand, as the speed is increased further, the locus approaches the origin. At the critical depth Froude number, the locus will transition into crossing the origin and progressing into a quadrant characterised by opposite signs of the abscissa and ordinate.

The manner in which a numerical free surface generates this pattern is in terms of maxima of the spectrum in Fourier space. This can be extracted and compared to the theoretical prediction, provided by Eq. (7.8). (Caplier et al., 2016) demonstrated that the relationship holds well despite its neglect of non-linear and three-dimensional terms. Thus, if one can prove that a numerically generated free surface (once processed to the spectral domain) provides

maxima, near the locus, then the free surface can be considered validated. This is explored in the following section. The analysis method can be summarised as follows:

1. Using the required input in terms of ship geometry, speed and underwater topography, solve the governing equations and obtain a numerical free surface.
2. Compute the locus using Eq. (7.8).
3. Predict the location of the cut-off wave number using Eq. (7.9).
4. Export the numerical free surface and transform it using a Fast Fourier Transform.
5. Filter the matrix, resulting from step 4 into two parts:
    a. The far field wave components are given by locations of the matrix, obtained during step 4 which lie in the region $|k_x| > |k_x^c|$ (high pass filter).
    b. The near field wave components are given by locations of the matrix obtained during step 4 which lie in the region $|k_x| < |k_x^c|$ (low pass filter).
6. Extract the coordinates (k_x, k_y) of the maxima of each column of the matrix obtained in step 5.a.
7. Fit a curve through the points obtained in step 6 and compare with the locus, computed in step 2.
8. Compute the inflection point of the curve fit obtained in step 7 with the locus' inflection point (obtained in step 2) by using $\tan\theta = \left(dk_y/dk_x\right)^{-1}$, computed at the inflection point.
9. Represent each component of the free surface (near and far field waves) by using an Inverse fast Fourier Transform on the components 5.a and 5.b.

7.4 Results and discussion

The presentation and analysis of the results are split into two major parts. The first relates to the computed ship resistance coefficients, while the second sub-section relates to the spectral analysis of ship waves.

7.4.1 Ship resistance

In this sub-section, the resistance, obtained numerically is briefly discussed and compared to the experimental data. To begin with, the total resistance coefficients are presented in Figure 7 for all cases. The experimental data of

Elsherbiny et al. (2019b) is included alongside each numerical result to enable comparison. Figure 7.8 clearly indicates the numerical prediction has a well-defined tendency to slightly underpredict the experimental data. Here, the subscripts refer to depth Froude number. As one might expect, the ship's resistance at higher speeds becomes more challenging to predict by CFD. This is evident, especially in the resistance characteristics at the highest depth Froude number for each case.

The overall agreement between the experimental and numerical data is encouraging. This is the first sign that the constructed towing tank is capable of providing good predictions for the resistance of a ship. Possible sources of discrepancy are suspected to stem from the fact that the numerical approach did not model sinkage and trim. In shallow waters, their combined effect, termed ship squat, is attributed greater relative importance than in deep waters. Thus, the imperfect modelling adopted may have been partly the cause of the observed levels of discrepancy between the experimental and numerical results. Moreover, as the ship speed is increased, the difference also grows. This matches the pattern observed in the sinkage and trim curves for a ship, both theoretically (Tuck, 1967, 1966), as well as numerically (Jachowski, 2008).

In practice, the cell numbers used tend towards being prohibitively high. As stated earlier, a virtual towing tank, where the principle of Galilean invariance has been utilised will consist of no more than 2-3 million cells. Such simulations can be performed within a few days on a standard computer. Thus, the adopted approach of virtually towing the ship may not become widespread soon. Nevertheless, the additional information that may be extracted from a case such as this can be useful. An example of this is given in the following sub-section.

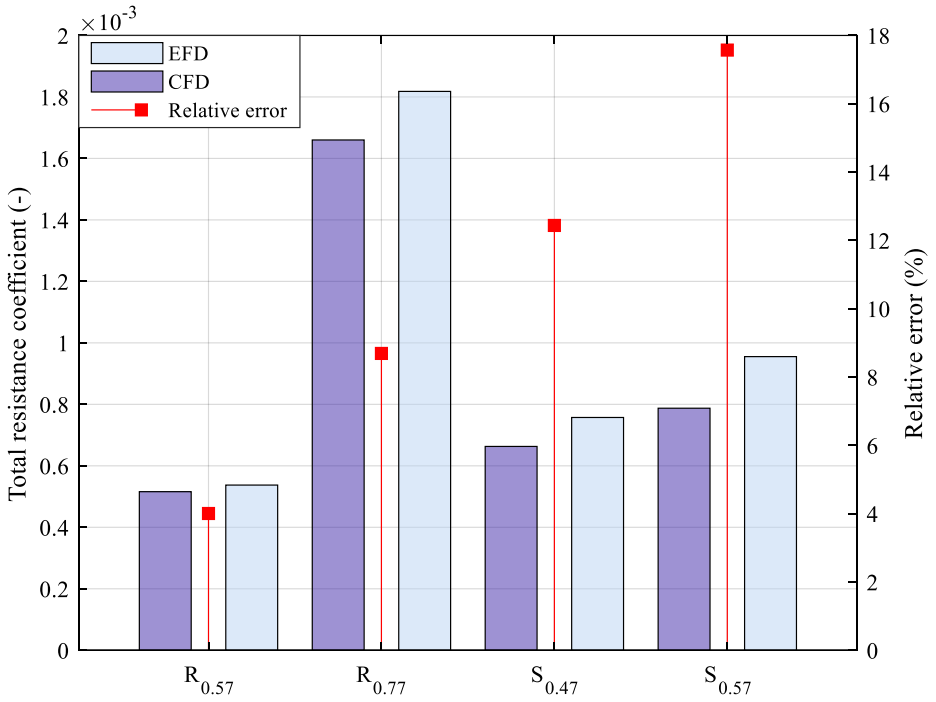

Figure 7.8. Comparison of total resistance coefficients for all cases (R indicates the rectangular canal case, whereas S – the Suez Canal). Subscripts refer to depth Froude number.

7.4.2 Spectral analysis of the numerical free surface

The highest speed is examined to begin with, simulated in the virtual towing tank, F_h=0.77 in the rectangular canal. The numerical free surface is depicted in Figure 7.9. Here, the far field waves, generated by the ship are clearly visible. Due to the lateral restriction, waves have reflected approximately 2.5 ship lengths aft of the ship. It should be noted that Figure 7.9, and other figures henceforth, are reflected around the central symmetry plane to enable a better visualisation.

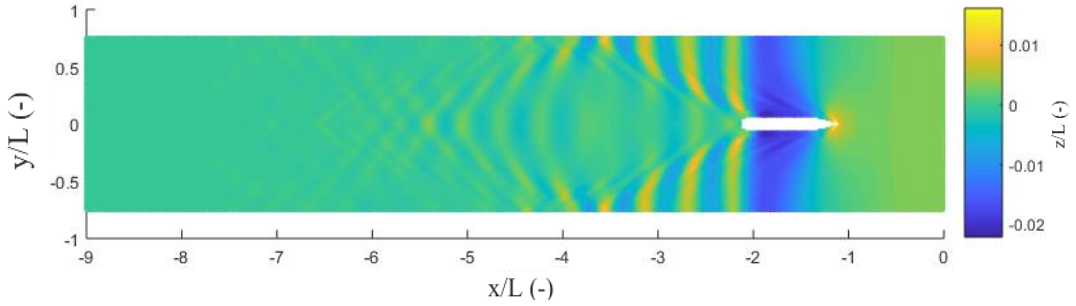

Figure 7.9. Generated wave field in the rectangular canal at F_h=0.77.

At this point, it is useful to attempt to determine the wave angle. According to Havelock's (1908) method, the Kelvin half-angle is θ=21.58°. Figure 7.10 depicts an attempt at solving this problem by projecting a (dashed) straight line form the forward perpendicular to the sides (and its reflection) at an angle of 21.58°. The line 'lands' at a wave trough on the canal wall – clearly, this is not the correct approach. The solid line in Figure 7.10 represents the same process, but beginning from the nearest peak downstream at the wall, and projecting in both directions. The line intersects the ship approximately ¼L from the forward perpendicular. Then, the broken line is initiated at the highest peak at the wall, where wave reflection occurs. This intersects the ship approximately ¾L from the FP. Finally, the dotted line shows the same process. It originates at the point [min(x), max(y)], representing the point where the aft wave system is generated.

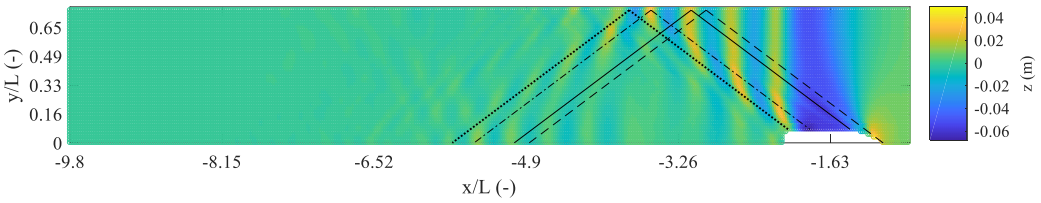

Figure 7.10. Generated wave field in the rectangular canal at F_h=0.77 and corresponding half angle according to Havelock (1908). Dashed line originates at FP, solid line originates at the nearest downstream peak, where the dashed line is reflected. Broken line originates at the highest wave elevation on the wall, dotted line originates at the ship coordinates representing the point where the aft wave system is generated.

Clearly, neither line in Figure 7.10 accounts for the wave angle well. This is not surprising since the method used to estimate the half angle is linear and devised for a point source. In this case, the spectral representation may be used to approach the problem. As explained earlier, the first step is to calculate the Fourier transform of the wave field. This is performed in MATLAB, which uses grayscale images. For this reason, the images used henceforth to represent the free surface will be shown in the grayscale format, used to perform the analysis. By doing so, other researchers may cross-reference results obtained herein by analysing the provided images.

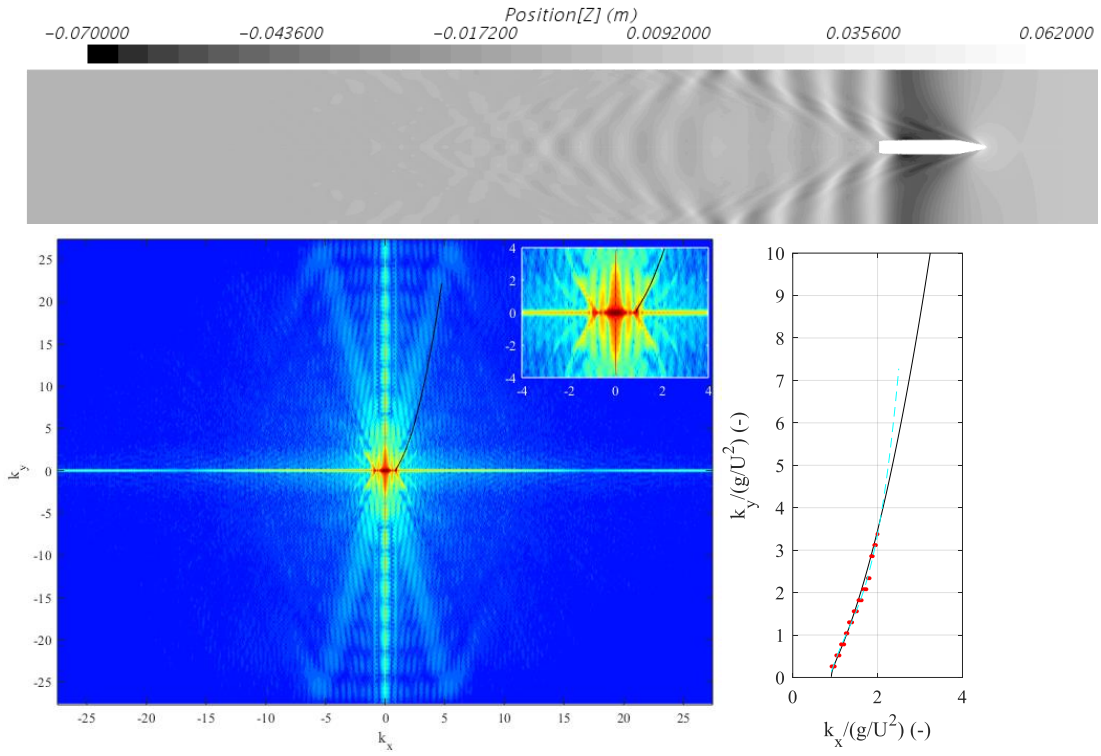

Figure 7.11. Processing of the wave field. Depicted: F_h=0.77 in the rectangular canal. Top: the raw image – real space extents are 32m in the stream wise and 4.6m in the span wise directions. Bottom left: the Fourier representation of the wave field. Bottom right: detected maxima (red points) and fit (dashed line), superimposed onto the theoretical relationship (solid line), Eq. (7.8).

Figure 7.11 depicts the adopted method of analysis. Specifically, the free surface is first represented in Fourier space. Then, for each column of the matrix defining the Fourier transform, a maximum is identified. The k_x, k_y components of these maxima are then compared to the theoretical relationship provided by Eq. (7.8). A polynomial fit is constructed from these points to demonstrate the accuracy of large and small k_x on the fit. In the present case, it is apparent that as one progresses in the k_x range to higher values, agreement deteriorates quickly. According to Nakos and Sclavounos (1989), insufficient grid resolution will be manifest as numerical dispersion in the k_x, k_y plane being curved towards high values of k_x, eventually forming closed curves. Since this is not what is observed in the present study, it may be concluded that the numerical wave field is represented with sufficient grid resolution. Nonlinear phenomena will be revealed in the appearance of additional branches in the spectrum. In each quadrant, a branch, emanating from the origin and propagating linearly to the edge of the plot, where it reflects, is observed. Moreover, smaller branches of the dispersion relation are

observed, with origins at higher k_x values, indicating nonlinearity (Fourdrinoy et al., 2019). These lead to deformation of the wake in the real space.

Now, it is important to deduce the origin of the apparent disagreement in the high k_x region, as well as its effect on the predicted Kelvin half-angle. One source of disagreement inevitably stems from the fact that the dispersion relation used for comparison is linear (Whitham, 2011). Ship waves, particularly in shallow water are nonlinear. Even in deep waters, Ma et al. (2018) found significant nonlinear influence on the dynamic pressure of the KCS. On the other hand, the experimental data presented in Caplier et al. (2016) suggest that the theory approximates real ship waves very well for the Wigley hull. This may not be a fair comparison, because nonlinear effects for the Wigley hull are known to be small (Chen et al., 2016; Ma et al., 2018; Wu et al., 2019). In other words, using the parabolic hull plays to the method's strengths.

The neglect of nonlinear terms is chiefly manifest in the near-field disturbance, close to the ship. Although a modification to the Kelvin half-angle may be produced as a consequence of modified pressure in the near field, the magnitude of such an effect is not known. Interference between of transverse and divergent waves, generated at the ship's bow may be one cause in the observed disagreement (Noblesse et al., 2014). Such an effect, coupled with nonlinearity exhibited by the KCS and influence of viscosity are thought to be the dominant sources of discrepancy.

There is one more aspect of the solution one should consider carefully. This relates to the curve fit used to approximate the numerical dispersion for higher k_x values than maxima were detected for. In shallow waters, the arms of the locus are typically not well developed (Caplier et al., 2016). Thus, it is difficult to extract sufficiently many points to perform the analysis. For this reason, the only fair assessment recommended is within the range where maxima have been detected from the Fourier transform. The range, $k_x/(g/U^2) \in [1, 2.5]$, is used to perform all subsequent analysis. This includes part of the fit over which no maxima have been detected to illustrate the effect of limited data samples.

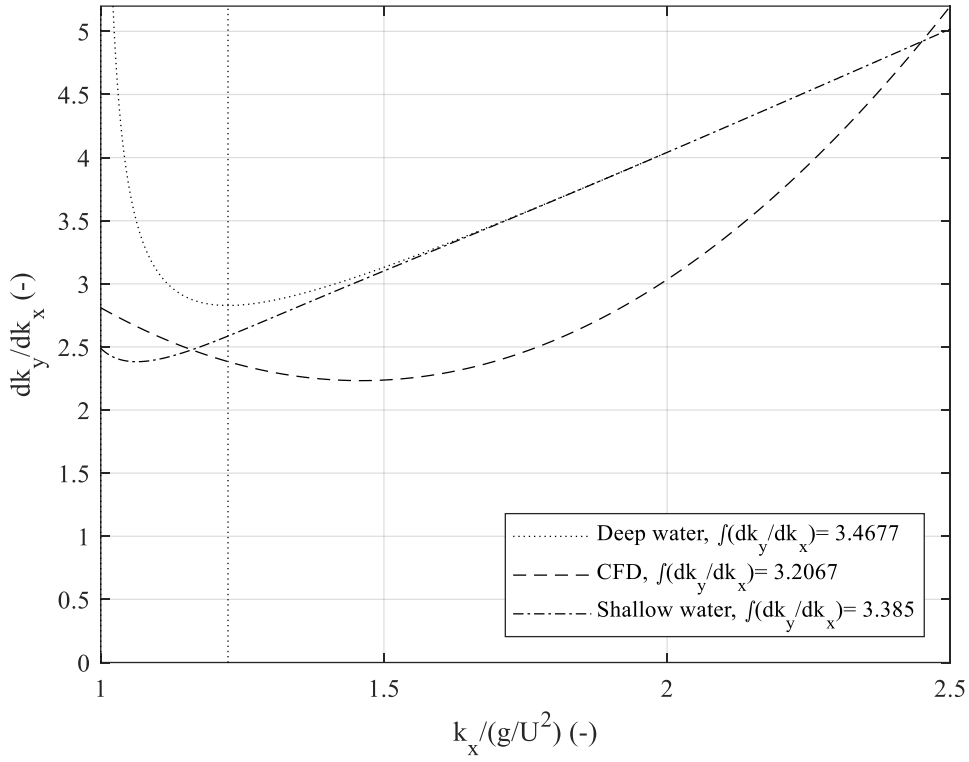

Figure 7.12. Derivatives dk_y/dk_x for deep water, shallow water, and numerical shallow water cases.

Figure 7.12 contains the derivatives dk_y/dk_x for deep and shallow water based on the dispersion relation, alongside the numerically generated fit from CFD. This is shown because upon evaluating dk_y/dk_x at the inflection point, the Kelvin half-angle can be obtained. Moreover, Nakos and Sclavounos (1990) recommend the examination of these derivatives to highlight differences between numerical and theoretical dispersion relations. Figure 7.12 also includes the area under each curve for reference. Clearly, assessing solely the area under each curve is not a good approach to determine an apparent disagreement, or error, which is -3.901% in this case. This is the case because different parts of the k_x range over which the derivative is shown may attenuate or reinforce the total favourably. On the other hand, the RMS (Root-Mean-Square) of the difference between the theoretical and numerical curve is predicted as 0.456. The effect of this on the predicted half-angle is illustrated in Figure 7.13, where the consequences of the previously examined differences are highlighted.

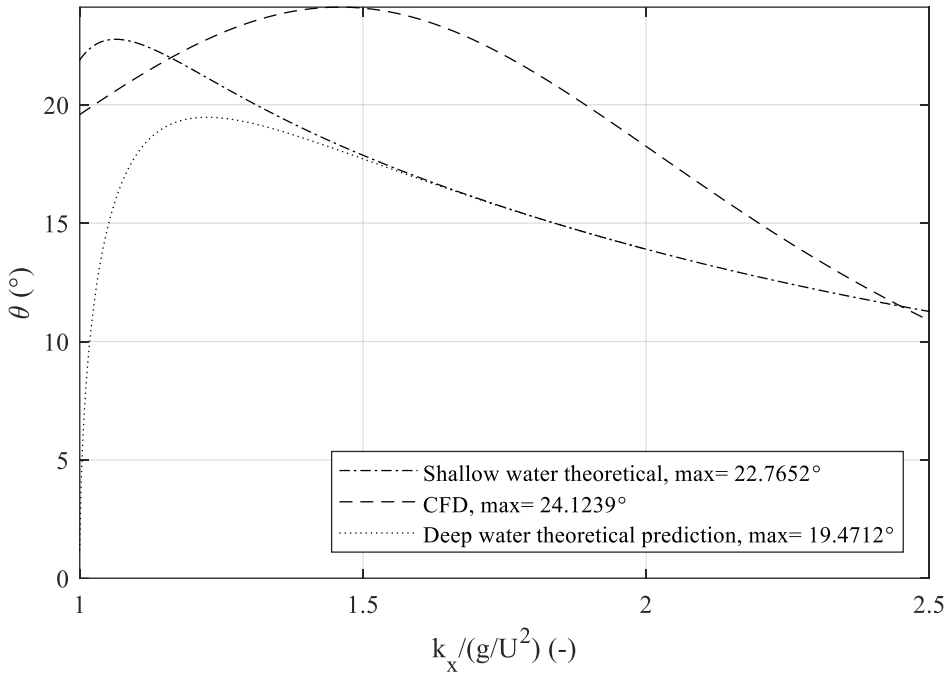

Figure 7.13. Predicted and theoretical half-angles.

The net effect of the difference between the fit and theoretical curves is translated into a difference of approximately 2.6° in the predicted half-angle. This is not considered as a substantial discrepancy. However, the location, where inflection occurs is significantly different between the two sets of data. This occurs at $k_{x,theory}/(g/U^2)$=1.06 according to the theoretical relationship, whereas CFD predicts this at $k_{x,CFD}/(g/U^2)$ ≈1.46. The identification of this half-angle does not help in visualising the wake better. Plotting a line with origins at the bow with an angle of 24.1° causes an intersection with the wall earlier than what is shown in Figure 7.10.

There are several aspects of this technique that should be improved. Firstly, the range, over which it is acceptable to find maxima of the Fourier transform should be defined. The only way to accomplish this is via an extensive experimental campaign. If such an interval is known, then it may be possible to define a metric expressing the degree to which waves are correctly modelled. It may also be possible to link specific parts of the computational free surface with increased error in the representation of ship waves. The only manner in which this can be achieved is via experimental work, which should demonstrate the validity of the assumptions as they apply to waves generated by a ship, rather than point sources. Specifically, ships causing highly nonlinear flows, and thereby – waves.

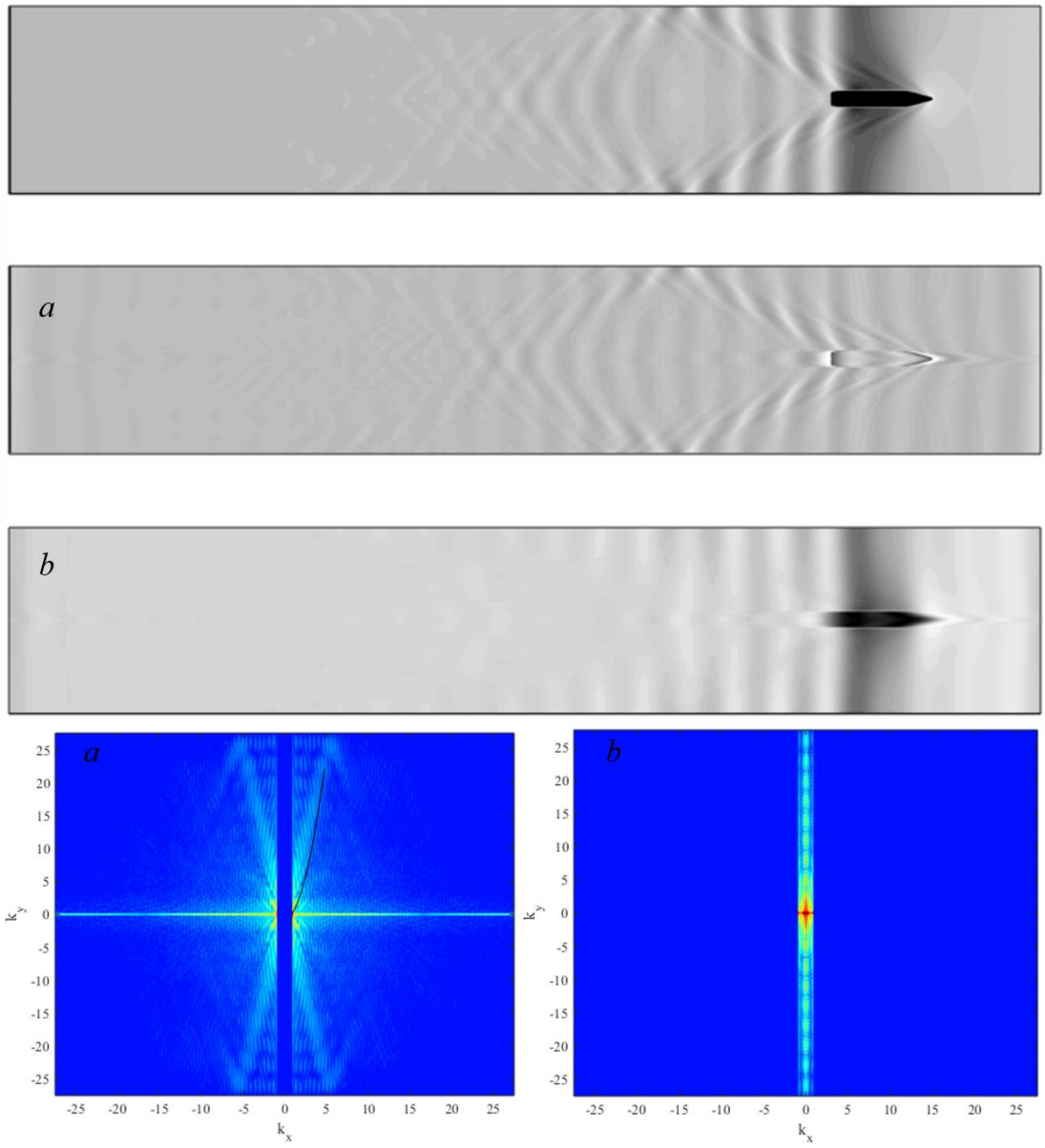

Figure 7.14. Splitting of near and far field components via manipulations of the spectrum (cut-off wave number k_x^c= 4.7885). Top: original free surface, (a) indicates the far field component, whereas (b) indicates the near-field disturbance and their corresponding Fourier representations. Longitudinal extent: 32 m.

This section proceeds with the next aspect of the solution, which one may obtain via the spectral representation. Specifically, splitting the near field from the far field components. This is illustrated for the rectangular case study at F_h =0.77 in Figure 7.14, where the cut-off wave number is k_x^c = 4.7885. Here, the shape of the ship leaves a small effect onto the corresponding near and far field systems because the outline of the vessel forms part of the free surface

itself. The intensity of the spectrum depends on the input, and can be changed based on the brightness of the supplied input. The range of the spectrum is therefore not shown.

The near field disturbance is not confined in the immediate vicinity of the ship in Figure 7.14, contrary to expectations. Instead, it is shed from the ship downstream, with its influence being clearly visible near the domain walls. This representation also allows the detection of the far field waves, as well as their reflection form the side walls with ease. It is apparent that the wave system is convex with respect to the ship centreline. Once reflected, this is not as clearly visible. The full spectrum for this case can be consulted in Figure 7.11.

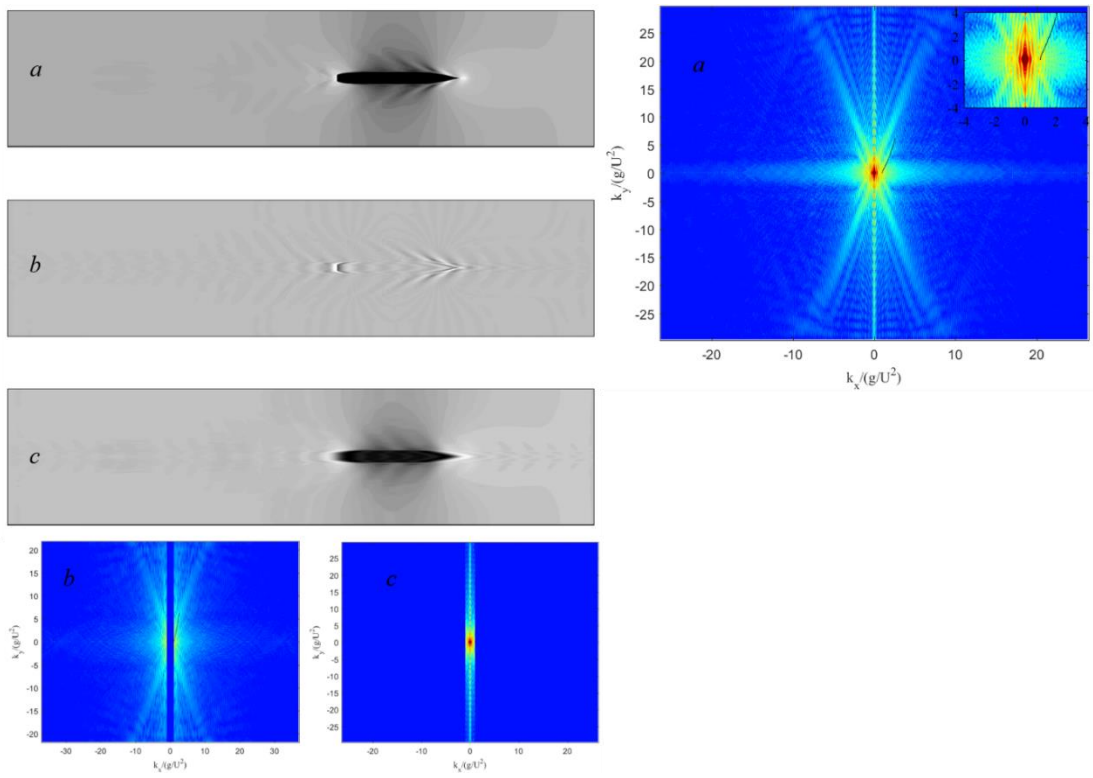

Figure 7.15. Computed free surface in the rectangular canal, F_h=0.57. (a), far field (b), and near field (c) representations in the real and spectral space (k_x^c=9.5796). Longitudinal extent: 16.5 m.

Figure 7.15 shows the spectral decomposition process as applied to the rectangular canal for F_h=0.57. Here, the arms of the spectrum, previously used to extract maxima and compare with the theoretical relationship are not clearly formed. This is consistent with findings of other researchers (Caplier et al., 2016). Specifically, the higher the depth Froude number is, the more clearly the arms of the spectrum are formed. The physical origins of this relate to the

relatively small far field disturbance generated by the ship in the examined speed range. Simultaneously, speeds corresponding to $F_h \geq 1$ are impractical, which is why they have not been investigated. Experimental data in terms of resistance is also not available for the adopted case studies at the aforementioned speeds. In any case, several features of the spectrum can be observed. Firstly, the low-intensity arms, observed in Figure 7.11 and Figure 7.14, extending into the far field are reproduced. However, in Figure 7.14, the arms are not reflected from the boundaries of the plot, instead, they exhibit periodic structures, which vanish near the limits.

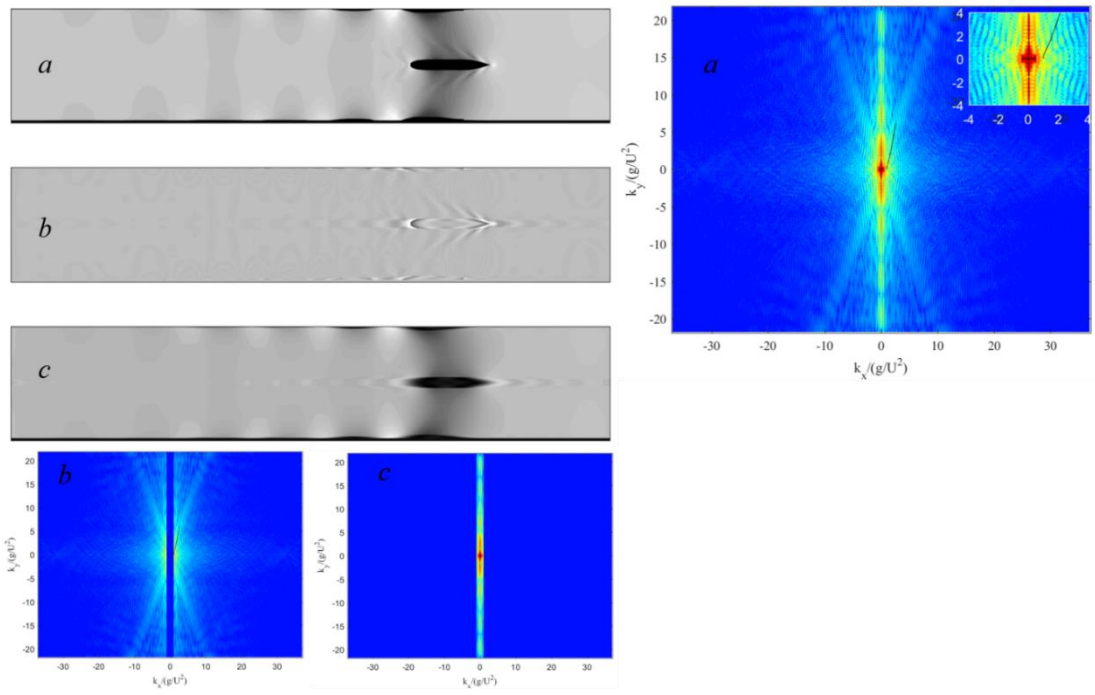

Figure 7.16. Computed free surface in the Suez Canal, F_h=0.57. (*a*), far field (*b*), and near field (*c*) representations in the real and spectral space (k_x^c=9.5796). Longitudinal extent: 13 m.

It is now appropriate to shift the focus onto the Suez Canal and the spectral representation of the wave field obtained. As before, the higher speed (F_h=0.57) is examined first, shown in Figure 7.16. An immediately apparent difference relates to the structure of the wave field. Specifically, the slopped canal banks have caused a rundown of the water surface. Since the theoretical relationship used to plot the solid line in Figure 7.16a (top right) can only account for a single depth, it is not seen to represent the Fourier representation of the numerical wave field well. Interestingly, the spectrum contains maxima, arranged in semi-circular arcs. An interpretation of this is not attempted at present, instead, leaving this for a more theoretical piece of work. Such a

research would need to determine the form of the dispersion relation in non-constant water depths. The cut-off wave number, used to produce Figure 7.15 and Figure 7.16 is same (k_x^c=9.5796 m-1), for this reason. As was the case for F_h=0.77, the near field disturbance is trapped near the canal walls, and over a great distance downstream.

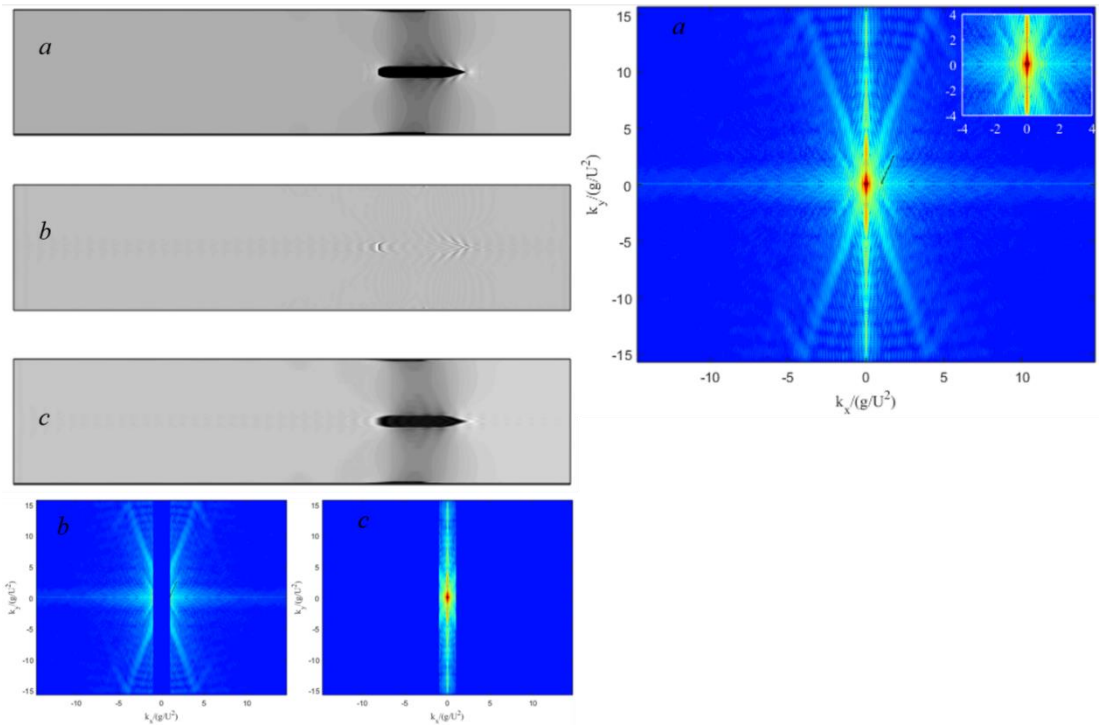

Figure 7.17. Computed free surface in the Suez Canal, F_h=0.47. (a), far field (b), and near field (c) representations in the real and spectral space (k_x^c= 14.1833). Longitudinal extent: 20 m.

The lower speed investigated in the Suez Canal, and the Fourier representation of its wave field is depicted in Figure 7.17. As expected, the disturbance generated by the ship at F_h =0.47 is significantly smaller than that produced at F_h =0.57 (Figure 7.16). The spectrum exhibits a similar structure to what was previously observed for F_h =0.57. For both results shown in Figure 7.16 and Figure 7.17, the near field hydrodynamic response has caused bright parts of the spectrum, which are periodically broken. These correspond to what is identified as a near field wave by the method, trapped at the lateral extents of the tank. This is primarily the case due to the relative size of these disturbances. Namely, their wavelength is of the order of magnitude of the ship itself. Whether this classification itself is correct probably requires further research. However, their effect onto the Fourier representation is clearly

visible, especially in Figure 7.16, where a high intensity patch can be seen undulating along the ordinate.

The lower speed investigated in the Suez Canal, and the Fourier representation of its wave field is depicted in Figure 7.18. As expected, the disturbance generated by the ship at F_h=0.47 is significantly smaller than that produced at F_h=0.57 (Figure 7.17). The spectrum exhibits a similar structure to what was previously observed for F_h=0.57. For both results shown in Figure 7.16 and Figure 7.18, the near field hydrodynamic response has caused bright parts of the spectrum, which are periodically broken. These correspond to what is identified as a near field wave by the method, trapped at the lateral extents of the tank. This is primarily the case due to the relative size of these disturbances. Namely, their wavelength is of the order of magnitude of the ship itself. Whether this classification itself is correct probably requires further research. However, their effect onto the Fourier representation is clearly visible, especially in Figure 7.17, where a high intensity patch can be seen undulating along the ordinate.

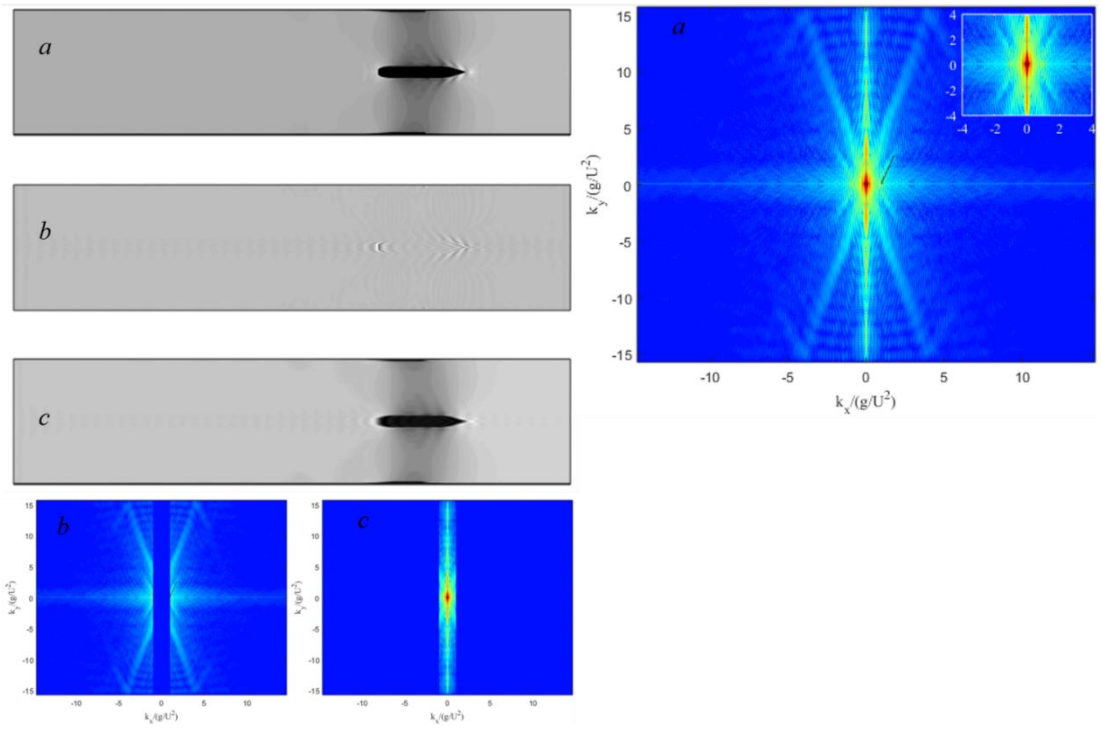

Figure 7.18. Computed free surface in the Suez Canal, F_h=0.47. (a), far field (b), and near field (c) representations in the real and spectral space (k_x^c= 14.1833). Longitudinal extent: 20 m.

7.5 Summary and conclusion

This chapter presented a towing tank which does not reply on the principle of Galilean relativity. This was accomplished via the overset method, which was used to actually 'tow' the KCS model in a virtual environment. The main benefits of adopting such an approach were identified in terms of the reduced number of assumptions needed to perform the analysis. Specifically, all boundaries (except those prescribed as symmetries or overset boundaries) are no-slip walls, which is more physically consistent than 'traditional' virtual towing tanks. Since the ship advances over a static fluid, the approach presented in this thesis does not require the definition of inlet turbulent properties, as is usually the case. Thereby, removing one major source of modelling error and uncertainty.

The adopted case studies numerically replicated recently published results in a rectangular canal and in the New Suez Canal (Elsherbiny et al., 2019b). The computed resistance of the ship was compared to the experimentally obtained values. Good agreement was found, although some discrepancy persisted in the highest speeds examined. The source of the difference between the experimental and numerical results is primarily attributed to the fixed sinkage and trim used in the virtual towing tank. The study was supplemented by a method to decompose the wave field and determine the Kelvin wake angle. In terms of the former, it was discovered that near field disturbances propagate outwards towards the canal sides and are shed by the ship downstream. Their effect persisted over a significant distance. This is of practical interest, because near field disturbances are typically linked with strong pressure variations. Thus, information extracted via the spectral decomposition method may be used to assess the optimum slope and positioning of canal sides to avoid excessive forces, linked with bank erosion.

On the other hand, it was shown that in a narrow canal, it is difficult to identify the boundaries of the Kelvin wake. Values for the half-angle computed via linear point-source methods were compared with those obtained by CFD. The effects of nonlinearity and interference of wave systems shed by the bow and stern were identified potential sources of discrepancy. However, the numerical (θ_{CFD}=24.1°) and theoretical (θ_{Theory}=22.756°) Kelvin wake half-angles for F_h=0.77 in the rectangular canal were found to compare reasonably well. The inflection point, which governs the value of the half-angle however was found to be in some disagreement. According to the theory, this should

occur at approximately k_x =1.06, whereas CFD suggests the inflection point is located at k_x = 1.46. The potential sources of this discrepancy likely pertain to limitations in terms of mesh size, time step in CFD, but also, and likely more importantly, the theoretical assumptions.

8. MODELLING THE HYDRODYNAMIC EFFECT OF ABRUPT WATER DEPTH CHANGES ON A SHIP TRAVELLING IN RESTRICTED WATERS USING CFD

This chapter examines the hydrodynamics of ships advancing past depth discontinuities in restricted waters. Numerical simulations are performed using two speeds and four different levels of water depth reduction. To gauge the effects of transcritical flows, the case studies are specifically designed to result in such conditions. The assessment suggests a strong influence in the relative change of parameters of interest depending on the initial speed.

8.1 Introduction

Although there is a significant body of literature devoted to the study of ship hydrodynamics in confined waters, several open research questions remain. Contemporary interest in the field is driven by the fact that according to EMSA (European Maritime Safety Agency, 2019, 2018, 2017, 2016, 2015), a large proportion of all ship incidents occur in restricted waters. Although human factors are predominantly thought to be the root cause of this, counter-intuitive ship behaviour can occur in shallow waters, magnifying the overall risk (Tuck, 1978). Therefore, understanding the hydrodynamic phenomena occurring in shallow, and more generally, restricted waters, is of practical relevance.

In some cases, the ship operator may not be aware of the consequences caused by their operation in shallow water. An excellent example of this is described and analysed at length by Grue (2017), who investigated waves caused by ships sailing past abrupt depth transitions. He demonstrated that long waves can be generated at the depth transition, which the author termed "mini-tsunamis". The resulting waves were shown to cause substantial damage to coastal infrastructure several kilometres from their inception point. An even more extreme case is reported to have caused the loss of life (Soomere, 2007).

The present chapter takes inspiration form Grue's (2017) work and seeks to explore the associated effects further, using numerical methods. A survey of the literature revealed that studies model similar problems using potential-flow-based methods. These generally fall within three categories including slender body methods (Gourlay, 2003; Plotkin, 1977, 1976; Tuck, 1967), Green function-based methods (Yang et al., 2001; Yuan, 2014; Yuan et al., 2018; Yuan and Incecik, 2016), methods based on the Boussinesq approach (Dam et al., 2008; David et al., 2017; Grue, 2017; Jiang et al., 2002; Torsvik et al., 2006; Wu and Wu, 1982), methods based on the Korteweg-de Vries equation (Cole, 1987; Hur, 2019; Katsis and Akylas, 1987, 1984), and methods based on the Kadomtsev-Petviashvili equation (Beji, 2018; Mathew and Akylas, 1990; Sharma, 1995).

Most methods mentioned previously can be thought of as long wave theories. The long wave family of theories can be arrived at by applying a combination of assumptions and appropriate boundary conditions to the Euler equations, which are known to model ship waves with adequate accuracy. However, as is often the case, there is some disparity between different approaches as illustrated by Torsvik (2009) in terms of dispersive properties exhibited by generated waves. Neglecting viscosity may not be a valid assumption, based on the findings of recent numerical and experimental studies, which observed the formation of a boundary layer on the seabed in very shallow conditions (Böttner et al., 2020; Shevchuk et al., 2016).

By contrast, studies have shown that the fully nonlinear Reynolds averaged Navier-Stokes (RANS) equations can model the present class of problems well (Bechthold and Kastens, 2020; Elsherbiny et al., 2020; Shevchuk et al., 2016; Terziev et al., 2018; Tezdogan et al., 2016a). It is therefore prudent to attempt to construct a fully nonlinear viscous towing tank with a varying bathymetry. The specific object of this chapter is thus to simulate the hydrodynamic effects caused by a ship passing over a step change in the water depth using CFD. To

the best of the author's knowledge, such towing tanks have only been constructed via the use of the family of long wave theories, described previously.

According to Jiang et al. (2002), the unsteadiness and three-dimensionality of the problem to be investigated herein precludes the use of many methods. Even the applicable methods rely on the assumption of inviscid flow, which may not hold for near-critical speeds or very shallow waters. Therefore, provided one can cope with the computational effort, it is desirable to investigate the effects of depth changes via a RANS method.

This chapter presents an attempt at modelling the above scenario using the commercial RANS solver Star-CCM+, version 14.06. As a starting point, the experimentally investigated rectangular canal of Elsherbiny et al. (2019) is used. In their study, the authors of the aforementioned work performed an experimental investigation into the hydrodynamics of the KCS containership in a rectangular canal and the Suez Canal. Their findings indicate a strong dependence of the canal cross-sectional area on all examined parameters. Their study featured a depth-to-draught ratio of 2.2 and a width of 4.6m for the rectangular canal.

To examine phenomena other methods may not be well-suited for, the chosen speed range for the present work is trans-critical and is applied to the rectangular canal of Elsherbiny et al. (2019). Specifically, two subcritical ($F_h < 1$) depth Froude numbers are chosen to begin with. As the ship advances through the domain, it encounters a step decrease in the water depth, rendering a higher value of F_h. To model the longitudinal motion of the ship along the canal, the overset domain approach is utilised, which follows from the preceding chapter. To simplify the numerical simulations, the ship is not allowed to move in any direction, other than along the canal's length. Therefore, ship squat is not modelled in this chapter.

The specific cases examined here are detailed in the following section. Section 8.3 presents the numerical implementation, which also contains estimates for the numerical uncertainty. Then, the generated results and their analysis are given in Section 8.4. Finally, Section 8.5 contains a summary and conclusion.

8.2 Case studies

This section is devoted to an overview of selected case studies. To begin with, justification is given in terms of the selected conditions.

As stated previously, transitions past the critical depth Froude number are sought. This is to demonstrate that RANS solvers are well-equipped to handle such problems, that present significant difficulties for several theoretical methods as reported in the literature. For example, the slender body theory has a singularity at $F_h = 1$. Several studies have devised approaches to handle the behaviour of the theory around this depth Froude number, but none has become widely used (Alam and Mei, 2008; Gourlay and Tuck, 2001; Lea and Feldman, 1972; Miles, 1986; Tuck, 1967, 1966). Therefore, the decision to simulate conditions where the critical speed is met and exceeded was taken. Alongside these, subcritical conditions are also modelled.

To achieve a high depth Froude number, a relatively high ship speed is required. Although it may be the case that few vessels would operate under such conditions, Grue (2017) reported fast ferries travelling at $F_h = 0.7$ prior to the depth transition. Therefore, the high-speed choice is deemed both acceptable and practically relevant for ship operations. Since ship waves are of greater concern in restricted waterways due to bank erosion, such as rivers and canals, a corresponding case study is sought.

As mentioned earlier, the work of Elsherbiny et al. (2019) is used as a starting point for three reasons. Firstly, they investigated a canal case, which matches the requirements set out previously. Secondly, the groundwork in constructing and validating the wavefield of this case study was laid out in chapter 7. Finally, replicating the towing conditions allows other researchers to compare resistance and wavefield data against the work presented herein. This could be done by other researchers using numerical methods. Alternatively, an experimental version of the case studies presented here should also be carried out.

Initial speeds are selected based on the highest available F_h explored by Elsherbiny et al. (2019), namely, $F_{hi} = 0.77$. Since one of the objectives is to model a critical case, the water depth restricted so that when the ship crosses the step at a constant speed, the resulting depth Froude number, $F_{hs} = 1$. Henceforth, the subscripts i and s will be used to denote the initial condition, and the condition past the step, respectively. Naturally the same ship as used in the work of Elsherbiny et al. (2019) is utilised, namely the KCS, whose principal characteristics are shown in Table 8.1.

Table 8.1. KCS principal characteristics (in model scale).

Quantity	Symbol	Value	Unit
Scale factor	λ	75	-
Length	L	3.067	m
Beam	B	0.429	m
Draught	T	0.144	m
Block coefficient	C_B	0.651	-
Longitudinal Centre of Gravity	LCG	1.488	m
Wetted area	S	1.694	m^2

Making the above choice while maintaining a constant velocity requires the depth to change from h_i/T=2.2 to $h_s/T \approx 1.3$ (note that the width is maintained constant w=4.6m). Further cases to gauge the sensitivity of the flow to water depth are specified at three equal intervals between the two extremities in terms of the depth Froude number. Moreover, to include additional supercritical cases, a second initial depth Froude number is selected as $F_{hi} = 0.9$ and investigated for the same depths. The resulting test matrix is given in Table 8.2. Further reductions in the water depth are not implemented to avoid numerical problems in the implementation of the overset domain approach, used to tow the ship. A schematic drawing of the different steps investigated can be seen in Figure 8.1.

Table 8.2. Text matrix

No	U (m/s)	F_{hi}	h_i (m)	h_i/T	F_{hs}	h_s (m)	h_s/T	h_i/h_s
1	1.364	0.77	0.32	2.2	1	0.190	1.304	1.687
2					0.943	0.214	1.468	1.500
3					0.885	0.242	1.665	1.321
4					0.826	0.277	1.905	1.155
5	1.595	0.9			1.169	0.190	1.304	1.687
6					1.102	0.214	1.468	1.500
7					1.034	0.242	1.665	1.321
8					0.967	0.277	1.905	1.155

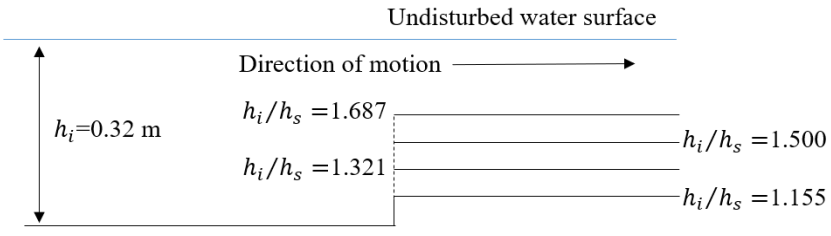

Figure 8.1. Schematic drawing of the step changes in water depth. Not drawn to scale.

8.3 Numerical implementation

This section is devoted to the numerical implementation, with subsections assigned to different aspects of the simulations.

8.3.1 The numerical environment

As stated in the earlier, the commercial solver, Star-CCM+, version 14.06 is used. The solver is based on the Finite Volume Method (FVM). To avoid deviating from the core topic of this chapter, specific details in terms of algorithms and subroutines are not discussed. Instead, the reader is referred to the user manual (Siemens, 2018) and texts containing detailed information of the numerics used (Ferziger and Peric, 2002).

There are two main aspects of the solution in the present CFD modelling requiring particular attention. The first relates to the definition of the free surface. The disturbance caused by the ship may be significant and will influence the solution substantially, therefore, an accurate representation is necessary. The definition of the water surface is modelled via the Volume of Fluid (VoF) method (Hirt and Nichols, 1981), with the High Resolution Interphase Capturing (HRIC) scheme to enhance its sharpness (Muzaferija and Peric, 1999, 1997). The grid on which the problem at hand is discretised is discussed in the following subsections.

The second aspect of the numerical implementation that is of importance relates to turbulence. The k-ω model of Wilcox (2008) is used, which has been utilised to obtain consistently good predictions in terms of computational resources and resistance predictions, as demonstrated in recent studies (Eca and Hoekstra, 2008; Elsherbiny et al., 2020). The two-equation eddy-viscosity turbulence closure is also selected due to its seamless application to all types of meshes. This is an advantage because the model does not require modifications independent on whether a wall function is used or not. Although a low y^+ mesh is constructed on the ship hull, as will be demonstrated at a later stage, this is not the case for the canal sides and bottom. Therefore, wall functions are used at all domain boundaries. Finally, to ensure a good representation of turbulent properties, all simulations are run with a second order accurate convection scheme.

To model the ship's longitudinal motion along the domain, the overset domain approach is used. In essence, this results in the creation of a box, enveloping the hull. To re-create the ship's motion in the x direction, the overset domain

is assigned the ship's velocity, which appears in Table 8.2. Adopting the overset domain allows the efficient modelling of the problem at hand. The alternative would involve re-meshing at each time-step, which would cause considerable increase in the computational load.

8.3.2 Computational domain and boundary conditions

The computational domain dimensions and arrangement are depicted in Figure 8.2. The location labelled as "Step" represents where the water depth transition is located. The values used can be consulted in Table 8.2 and Figure 8.1.

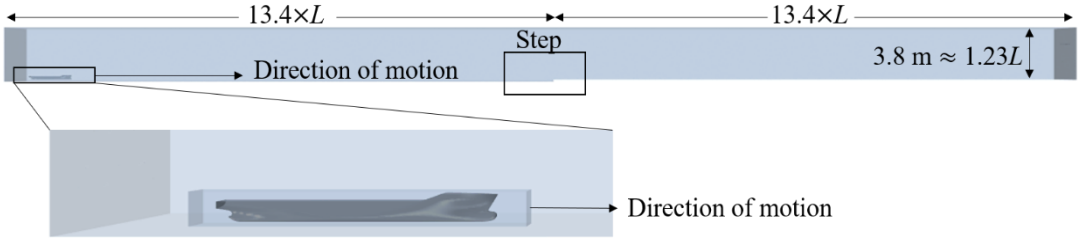

Figure 8.2. Depiction of the computational domain (depicted: h_i/h_s=1.687).

The main dimensions of both the background and overset domains are unaltered across case studies. The only change stems from the difference in the water depth after the midpoint of background domain. This is also set as the global origin of the coordinate system to simplify the representation of the results. To further simplify the results, the ship is modelled with an even keel, and ship squat is not accounted for. The reason behind this relates to the restricted water depth. If the overset domain were to collide with the background domain, the simulation could fail or cause unreasonable results. Since a shock is expected as the ship transits past the step, ship squat is not modelled to avoid the aforementioned effects.

The modelling of the KCS with an even keel results in substantially different resistance values to those recorded in the article by Elsherbiny et al. (2019), precluding the possibility of a validation study. However, using an identical set-up, the resistance and wavefield have been validated in Chapter 4 and Chapter 7 (Elsherbiny et al., 2019a; Terziev et al., 2020, 2019b; Tezdogan et al., 2016b, 2015).

The manner in which the numerical towing tank is constructed allows the removal of all open boundary conditions. This carries positive and negative impacts on the solution simultaneously. Specifically, the modelling

assumptions related to inlets and outlets, damping lengths and clearances between an open boundary and the ship, inlet turbulence, etc. are no longer of consequence because they no longer exist in the CFD simulations. Therefore, the modelling assumptions and sources of uncertainty are significantly reduced. On the other hand, from a mathematical point of view, open boundaries are easier to implement. Their removal may destabilise the solution in some cases. This is particularly the case when performing grid refinement studies – if the grid is too coarse, the simulation diverges during the early stages of the solution.

The numerical implementation of the domain requires in three types of boundary conditions. Symmetry planes are instituted in the overset and background domains, coincident with the centreline to reduce the computational effort. The overset domain requires the appropriate boundaries to imposed on the moving box, encasing the ship. All other boundaries are set as no-slip walls, as would be the case in a physical towing tank. Therefore, the numerical tank is physically consistent with real towing facilities.

8.3.3 Computational mesh

The computational mesh onto which the RANS equations are discretised is generated within the automatic facilities of the software package utilised to run the analysis. To ensure a good representation of the water surface, the mesh used in Chapter 7 is duplicated, due to the fact that those results are already validated. The prism layer mesher, offered by Star-CCM+ is used to create near-wall cells at the ship hull, with the average y^+ not exceeding 0.8 for the highest speed examined. This is used to construct the near-wall cells on the ship hull, responsible for accounting for the high velocity gradients within the boundary layer. On the other hand, the y^+ values on the side walls and bottom are allowed to exceed 1, resulting in the use of wall functions on these boundaries. A close-up of the generated grid on the undisturbed free surface prior to initiating the simulation is shown in Figure 8.3.

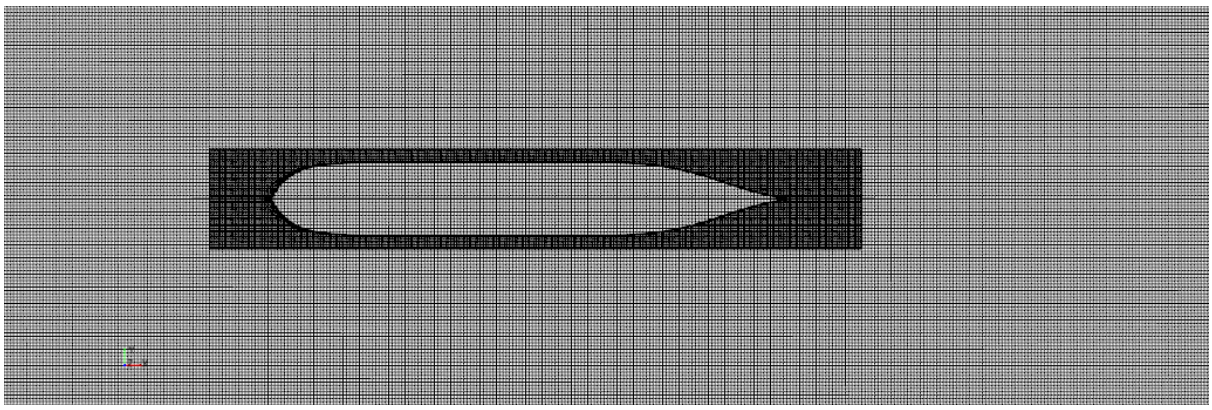

Figure 8.3. Close-up of the computational mesh on the free surface.

Table 8.3 contains the numbers of cells, generated for each case. It should be noted that these do not vary with F_{hi}. Therefore, both $F_{hi} = 0.77, 0.9$ are simulated with the same numbers of cells for their corresponding cases.

Table 8.3. Cell numbers for all four depth transitions

Cases	h_i/h_s	Number of cells
1 and 5	1.687	25,248,501
2 and 6	1.500	25,632,314
3 and 7	1.321	26,392,544
4 and 8	1.155	26,776,892

8.3.4 Time-step selection

Making an adequate choice for the time-step (Δt) in unsteady simulations is of critical importance. If the Δt value is too large, the numerical solution may become unstable, or give unrealistic results. This is to be balanced with computational time, i.e. it is not practical for a simulation to run over unnecessary long periods of time while consuming computational resources. Numerical noise may also manifest itself in the solution if the time-step is not chosen correctly. Based on the results of Chapter 7, $\Delta t = 0.0035 L/U$ is chosen with a first order discretisation scheme. To ensure an adequate representation of the physics, the Courant number is monitored throughout the simulation, with a stopping criterion imposed to end the simulation if the Courant number equals or exceeds unity within the overset domain.

The overset domain is chosen instead of the background to represent the Courant number criteria because in the former, the majority of the flow is accelerated. Had this been applied to the background domain, where the majority of the fluid is static, the results in terms of the Courant number would

be misleadingly low. The generated grid succeeded in preserving a Courant number, CFL>1.

8.3.5 Numerical verification

This subsection contains estimates of the numerical uncertainty, induced by the discretisation of the RANS equations in time and space. The approach used follows the recent work of Bechthold and Kastens (2020), who followed the guide of Celik et al. (2008). This begins with the definition of a refinement factor, *r*. According to ASME (American Society of Mechanical Engineers, 2009), acceptable values of *r* range between 1.1 and 1.5. The value of $\sqrt{2}$ is adopted for the refinement ratio for the present set of simulations. This is applied as a multiplicative factor to the mesh and time-step, which are magnified successively, creating a medium (*i*=2) and coarse (*i*=3) solution for each metric (mesh and time-step). To simplify the analysis, the refinement ratio is kept constant, i.e. $r_{21} = r_{32} = \sqrt{2}$. Nevertheless, the relationships used to perform the analysis with non-uniform *r* are adopted to enable comparison of results with other studies.

Once the medium and coarse solutions have been obtained, the observed order of accuracy can be determined as shown in Eq. (8.1):

$$p = \frac{|\ln|\varepsilon_{32}/\varepsilon_{21}| + q(p)|}{\ln(r_{21})}, \tag{8.1}$$

with

$$q(p) = \ln\left(\frac{r_{21}^{p} - s}{r_{32}^{p} - s}\right), \tag{8.2}$$

and

$$s = sgn\left(\frac{\varepsilon_{32}}{\varepsilon_{21}}\right), \tag{8.3}$$

where $\varepsilon_{32} = f_3 - f_2$, and $\varepsilon_{21} = f_2 - f_1$, with f_i denoting the i^{th} solution. For a constant refinement case, the function $q(p) = 0$. In the case of mesh independence, the medium and coarse solution featured 8,684,955 and 3,167,970 cells, respectively.

The next step is to estimate the uncertainty, denoted *GCI* (Grid Convergence Index), after Roache (1998), shown in Eq. (8.4):

$$GCI = 1.25 \times \left|\frac{f_1 - f_2}{f_1}\right| / \left(r_{21}^{p} - 1\right) \tag{8.4}$$

In the present case, the resistance of the ship before and after the step change in depth is used in the assessment. Therefore, two different estimates of the uncertainty are obtained for the mesh and two for the time-step. The specific case to which this is applied is case 1, $F_{hi} = 0.77, F_{hs} = 1$, as shown in Table 8.4.

Table 8.4. Numerical uncertainty study results (results are given for the ship resistance).

	Before step (F_{hi}=0.77)		After step (F_{hs}=1)	
	Mesh	Time-step	Mesh	Time-step
Fine (N)	19.74	19.74	64.43	64.43
Medium (N)	23.09	23.05	53.40	65.76
Coarse (N)	23.85	23.04	47.64	65.76
GCI	6.20%	0.03%	10.94%	0.01%
U_c	0.06%		0.11%	

In Table 8.4, the GCI value before and after the step is reported. Then, the combined uncertainty, U_c is estimated for each case as shown in Eq. (8.5):

$$U_c = \sqrt{GCI_{mesh}^2 + GCI_{time}^2} \tag{8.5}$$

It is apparent from the results of Table 8.4 that the results of the study are more sensitive to variations in the mesh than they are to variations in the time-step. Although the uncertainty exceeds 10% for the mesh in the critical region, this is considered a tolerable level of uncertainty considering the challenging case to which the analysis is applied to. The results from this subsection can be interpreted as follows. The mesh requirements for critical depth Froude number cases are considerably higher than those for subcritical cases. This serves to highlight that the examination of critical speeds is not a trivial problem even for RANS solvers. However, results with the given uncertainty can be obtained, whereas many potential flow-based methods predict singularities at $F_h = 1$.

Finally, it should be noted that while coarsening the grid, the finest time-step was maintained. The mesh was magnified by the same factor ($r = \sqrt{2}$) in both the overset and background domains to preserve the transitional ratio between the two. Conversely, the temporal dependence study was carried out on the finest mesh only.

8.4 Results and discussion

This section presents the obtained results, their analysis and discussion. To begin with, the resistance characteristics of the ship are given. For convenience, the percentage increase in resistance as the water depth changes is presented. This is thought to be a more suitable way to enable other researchers to compare different hull forms subjected to similar conditions. The initial resistance recorded for the model-scale ship at F_{hi}=0.77 was 19.74N, while at F_{hi}=0.9 the value was 55.891 N.

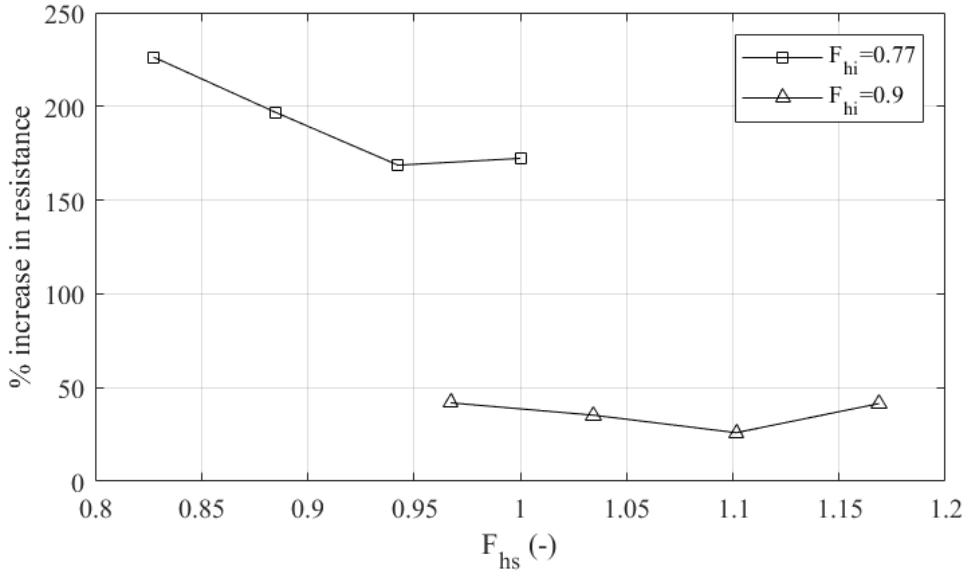

Figure 8.4. Resistance increase resulting from the depth change.

Figure 8.4. demonstrates that the initial velocity is critically important for the relative increase in resistance. To elaborate, the cases where the initial speed is $F_{hi} = 0.77$ exhibit several times the increase in resistance when compared to the cases with initial speed corresponding to $F_{hi} = 0.9$. More importantly, no jumps or sharp cusps are observed, as predicted by linear potential flow theory. The results in Figure 8.4 also point towards the possibility to minimise the total drag by small variations in the ship speed. For example, case 3 (F_{hs}=0.885) is considerably more favourable than case 1 (F_{hs}=1).

For both initial depth Froude numbers, the resistance does not peak at $F_h = 1$. This is in line with experimental data for a family of hulls given in Benham et al. (2020) and Benham et al. (2019), where the authors predicted that wave resistance peaks well before the critical depth Froude number. The reason why ship resistance is thought to exhibit a peak near $F_h = 1$ is strictly related to the sustained generation of waves, which is widely considered an independent

component of the total resistance. Linear potential flow theories place the peak at the critical depth Froude number; however, nonlinear phenomena are known to deform the wave resistance curve's peak towards the lower F_h range. A similar effect can be observed in other experimental data, in terms of the Kelvin wake angle (θ). For example, Johnson's (1957) experiments showed that the peak in θ can occur at around $F_{h,\theta=max}$ =0.9. Therefore, the trend exhibited by both curves in Figure 8.4 matches expectations.

In the cases where $F_{hs} \geq 1.1$, one might expect to observe a reduction in the resistance. This is a well-known phenomenon and has recently been demonstrated by Benham et al. (2020, 2019). There are two possible explanations as to why this is not observed in the presented results, which suggest the resistance increases in each case. One way to look at the data would be to suggest that the expected decrease in resistance is too narrow over the depth Froude number range. In such a scenario, the dip would be observed if further simulations were carried out between $1.09 < F_{hs} < 1.15$. Evidence to suggest that this may be the case can be found in Benham et al. (2019). The decrease in resistance for their hull forms is narrow. It is also worth noting that in their study, a family of simple hull shapes were examined. Similar hulls, for example, the Wigley hull, are known to produce a predominantly linear flow field (Chen et al., 2016).

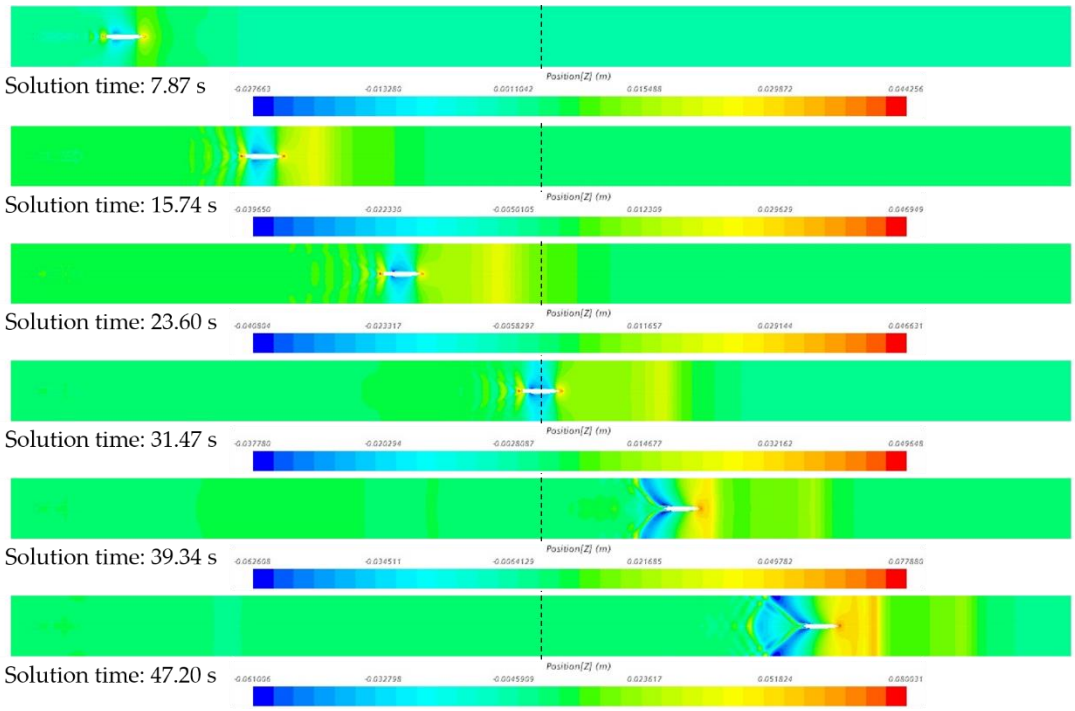

Figure 8.5. Wavefield for case 1, F_{hi} =0.77 and F_{hs} =1. The solution time and increment interval unit at which the free surface is shown is based on the end

of the acceleration phase (shown in the first tile). The dashed line indicates the position of the step change in water depth.

A second way of interpreting these results may be in terms of the wavefield. When the depth Froude number past the step exceeds or is equal to unity, any solitons generated by the ship may not be shed sufficiently quickly, to the forward part of the tank. Therefore, the ship may be trapped sailing against a wave. One way to determine whether this is the case would be to examine the wave field. This is shown in Figure 8.6 and Figure 8.6 for cases 1 and 7, respectively ($F_{hi} = 0.77$ with $F_{hs} = 1$, and $F_{hi} = 0.9$ with $F_{hs} = 1.03$, respectively).

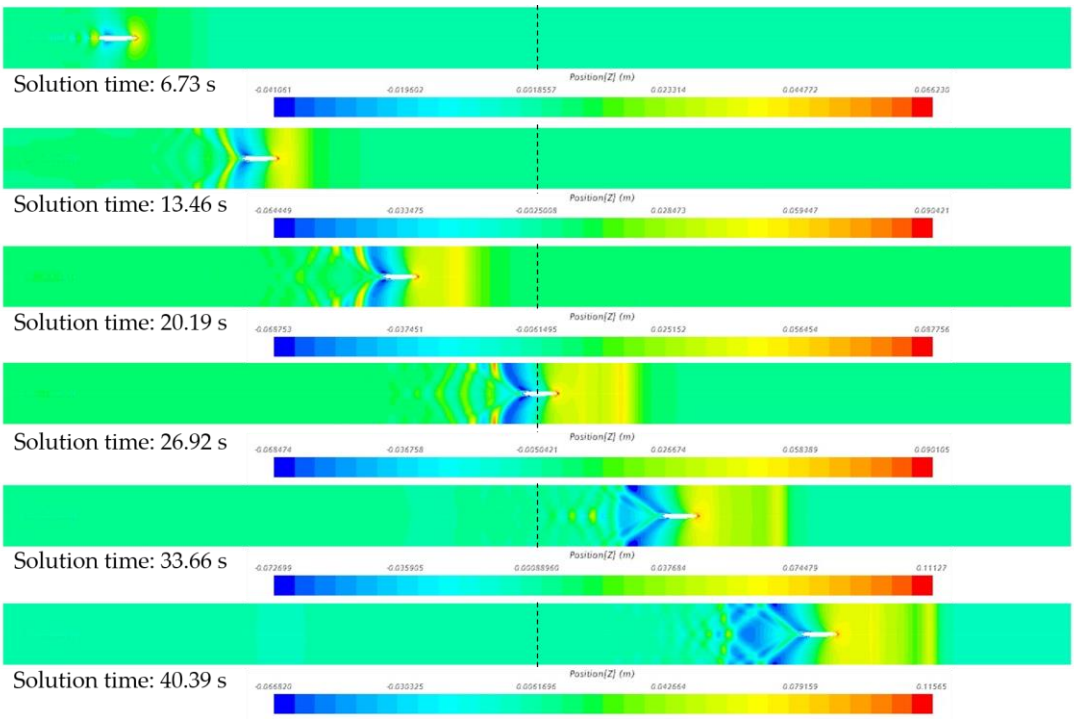

Figure 8.6. Wavefield for case 7, F_{hi} =0.9 and F_{hs} = 1.03. The solution time and increment interval unit at which the free surface is shown is based on the end of the acceleration phase (shown in the first tile). The dashed line indicates the position of the step change in water depth.

The wave elevation carried in front of the ship is longer for F_{hi} =0.9 and F_{hs} =1.03 (case 7). Thus, it is conceivable that this is could be the root cause for the elevated resistance. The second main difference between Figure 8.5 and Figure 8.6 relates to the generated soliton. While the soliton is clearly visible in Figure 8.5, it has not detached from the bow wave elevation in Figure 8.6. This is the case because the ship speed is close to the wave speed (F_{hi} =0.9),

therefore, the soliton would require a much longer domain to be properly shed. Solitons are also known to be essentially two-dimensional (Gourlay, 2001). To check whether the wavefield is 2D on the step, the time-history of the wave elevation on the step is recorded and shown in Figure 8.7. The free surface is monitored at four points next to the ship to provide a picture of the generated disturbance with distance in the y direction. Since the towing tank is symmetrical about the centreline, the probes are not mirrored. For comparison, the time-history of the same probes shown in Figure 8.7 for F_{hi} =0.77, are shown for F_{hs}=0.9 in Figure 8.8. These demonstrate that the wavefield in the latter case is 2D to a much greater extent and that the change in step height (h_s) has a smaller relative influence on the deformations of the free surface.

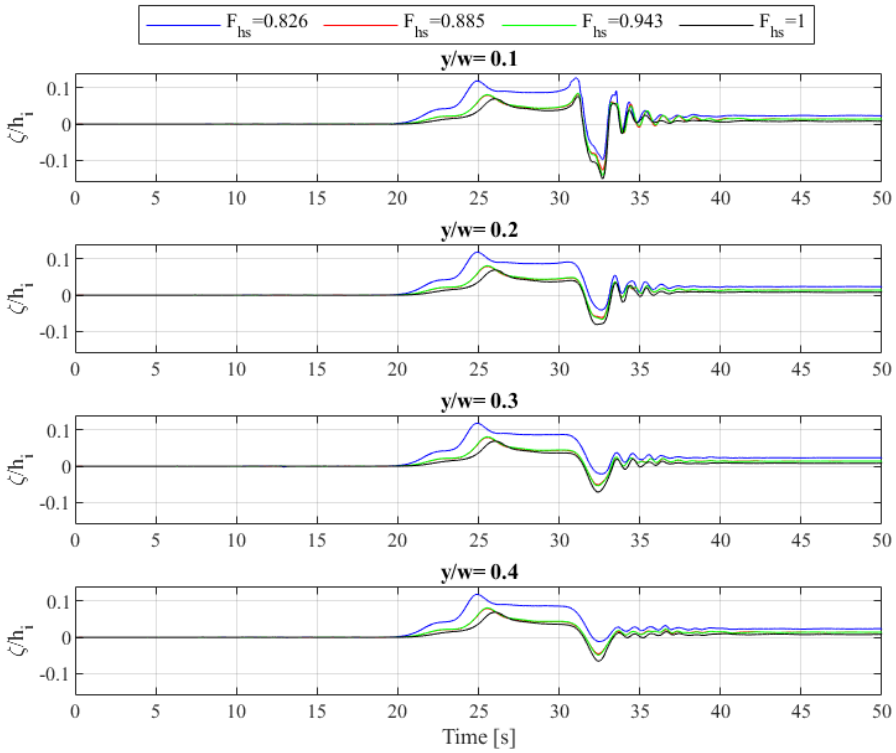

Figure 8.7. Wave probes at the step for F_{hi} =0.77.

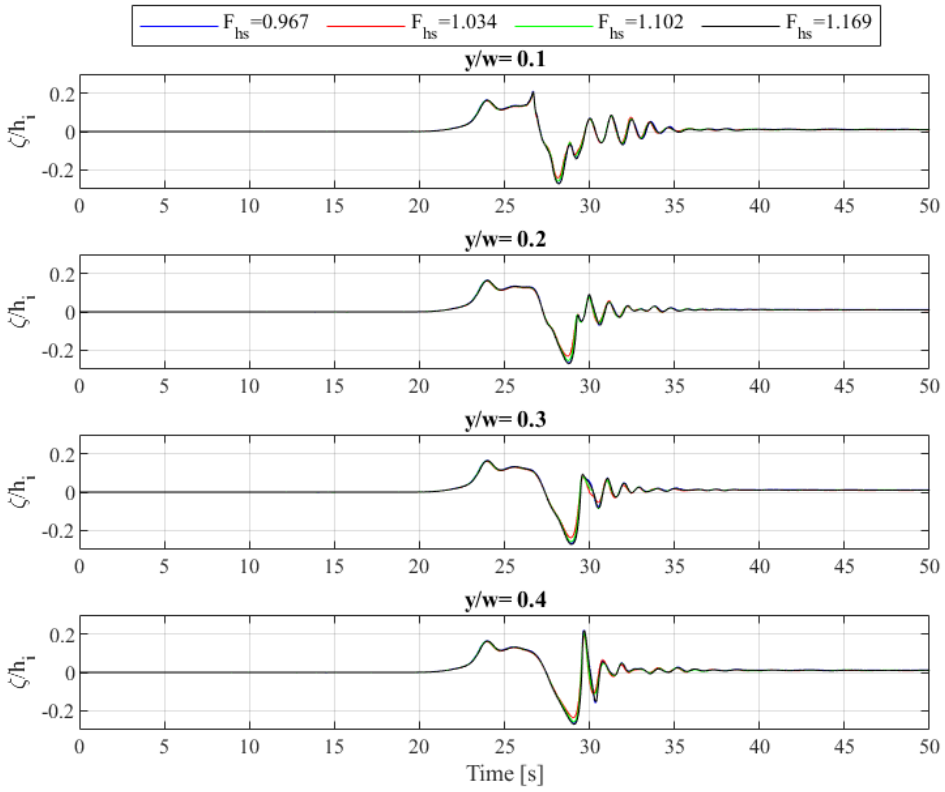

Figure 8.8. Wave probes at the step for F_{hi} =0.9.

Figure 8.7 indicates that the wave field is only uniform along the y axis prior to the ship's interaction with the step. This can be seen by referring to the wave elevation between 20 and 30 seconds of physical time in Figure 8.7 and Figure 8.8. The interactions differ with F_{hs} due to the physics of wave reflection and transition from a submerged step. Since the wave speed in the deeper region is higher than that of the shallower region, past the step, the wave profile must transform upon transiting from one depth to the other. There have been many studies into how this occurs. The first such work is thought to be that of Lamb (1932), who derived an expression for the ratio of transmitted and incident waves. His assumption of zero vertical velocity at the step seemed inappropriate to Bartholomeusz (1958), who presented a more in-depth study. However, the end result was identical to Lamb's (1932). Later, both of these studies were put under question by Newman (1965), who also ended up with Lamb's (1932) formulation for very shallow water cases.

The contribution of Newman (1965) however was expressed in the fact that he obtained an expression for an infinitely deep incident wave transforming into a shallow region. He provided a physical interpretation as to why a transmitted wave asymptotically tends to a wave height ζ_s =2× ζ_i (where ζ is the wave elevation, whereas the subscripts maintain their earlier designation)

as $h_s \to 0$. Newman's (1965) interpretation is that as the shallower region's depth vanishes, two phenomena occur. Firstly, the entire incident wave's amplitude is reflected, which is physically consistent. Secondly, that as the wave transits to much shallower regions, the energy transmitted into the region of depth h_s reduces at a rate proportional to the that depth (h_s), causing the transmitted component to be twice the incident wave's height. Newman (1965) then presents experimental results, which show that the theory is consistent, although some scatter in the tank data is observed around the theory. To check whether the physical phenomena occur in agreement with the aforementioned studies, the wave elevation is recorded along the entire tank at different times.

To simplify the discussion of the results, the obtained wavecuts are split into different phases of the simulation as follows (Figure 8.6 and Figure 8.6 can also be consulted in this respect):

I. **End of acceleration** – this occurs when the ship has reached its target speed. The wavefield at this stage is not yet fully developed and differs from its pseudo-steady state in several important ways. Discussion of these can be found in Doctors (1975) and Day et al. (2009).
II. **Subcritical wavefield development** – this phase of the simulation contains the time required by the wavefield to approach its steady state. This process occurs in all towing tanks, whether virtual or physical. In numerical tanks where the ship's position in the x direction is maintained constant, this phase is equivalent to the time allowed for convergence.
III. **Prior to the step** – at this stage, the ship begins to interact with the step. Initially, this is indirectly via the bow wave, which is partially compressed by the additional blockage.
IV. **Transiting the step** – this phase occurs while the step is located under the ship itself.
V. **After the step** – this phase begins as soon as the stern of the ship has cleared the step. Interactions between the depth transition and the step do not cease here. Instead, the accelerated fluid aft of the ship, interacts with the step continuously for a considerable time. This effect is subsequently demonstrated.
VI. **Critical wavefield development** – once the ship has cleared the step and advanced about one ship length along the canal, the wavefield

corresponding to the depth h_s has begun developing. This can be thought of in similar terms as explained in II, i.e. a convergence stage.

The development of the wavefield is split into the above stages and given in Figure 8.9 and Figure 8.10 for case 1 (F_{hi} =0.77, F_{hs} =1) along y/w=0.1 and y/w =0.2. In these figures, the maximum and minimum wave elevation for each phase are recorded and marked. Evidently, for y/w =0.2, shown in Figure 8.10, the disturbance caused by the ship decays in the y direction, allowing the soliton to assume the maximum value in phases II, III, and IV. For y/w =0.1 (Figure 8.9), this is only the case in phase II.

An interesting property, observed in Figure 8.9 and Figure 8.10 relates to the difference of the wave field aft of the ship in phases III and IV (prior and in transit of the step) when compared to phase V (after the step). The oscillatory pattern observed in the earlier phases, corresponding to the Kelvin wake (refer to Figure 8.6 for a top view) is transformed as the ship enters the region of depth h_s. The oscillatory pattern are replaced by a substantial depression, following the ship, as evident in the final stage, given in Figure 8.9 and Figure 8.10 along each wavecut. The length and height of the wave, trapped at the ship's stern is seen to decrease substantially, while the bow wave is considerably stronger in both respects. This observation partly explains the increase in resistance, shown in Figure 8.4. Namely, the ship carries with it a greater volume of water at its bow.

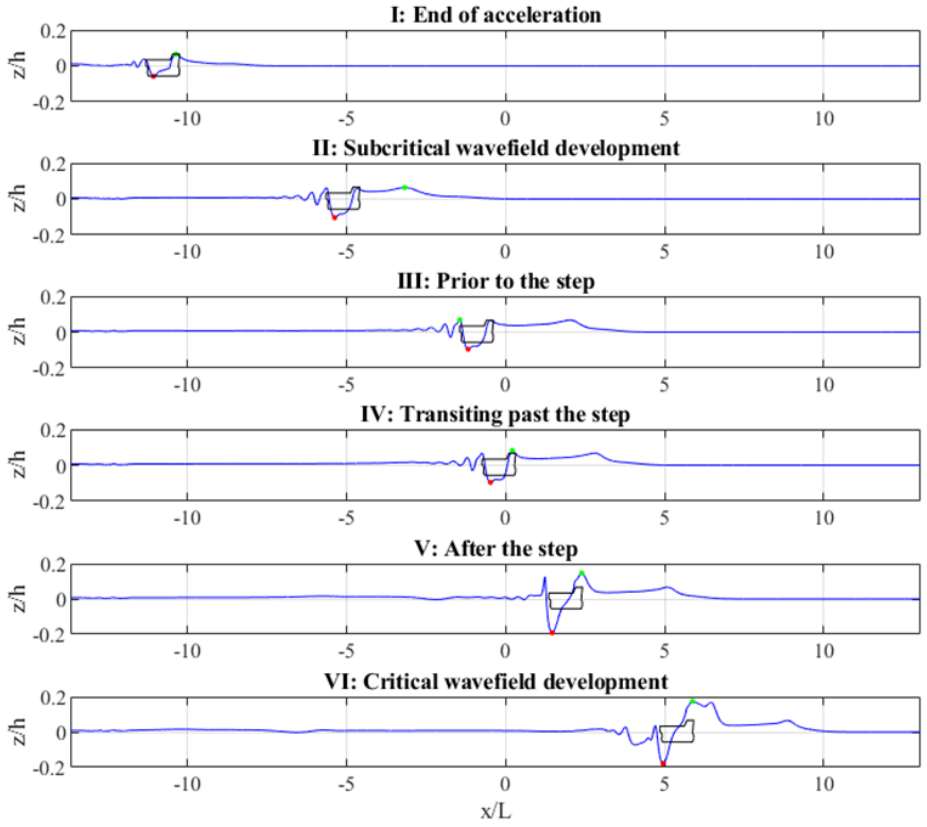

Figure 8.9. Wavecut 1 (y/w=0.1) evolution for case F_{hi} =0.77, F_{hs} =1, made dimensionless by the initial depth h_i =0.32. Maxima and minima are marked with green and red points, respectively. The outline of the ship is scaled down in the vertical direction by a factor of 8 to enable a visualisation of the ship's position.

In investigating the wavefield, it is important to keep in mind that the RANS solver models the flow in a fully nonlinear manner. In Chapter 7, it was demonstrated that the present set-up models the dispersive properties of the Kelvin wake in good agreement with the linear dispersion relation. In this chapter the opportunity to compare the evolution of the numerical wavefield with linear potential flow approximations of wave transmission past different steps, is used to provide a form of validation.

As stated earlier, Lamb (1932), Bartholomeusz (1958), and Newman (1965) all arrived at the same relationship describing the transmission coefficient, expressed as shown in Eq. (8.6):

$$T_R = \frac{2\sqrt{h_i}}{\sqrt{h_i}+\sqrt{h_s}} \tag{8.6}$$

where T_R is the ratio of transmitted and incident wave height. This relationship follows directly from the wave speed in each shallow water region, whose linear form is $\sqrt{gh}$, with g being the gravitational acceleration. Lamb (1932) showed that this relationship can be arrived at simply by imposing continuity and equivalence of the two waves (transmitted and reflected component) at the point directly above the step. All possible values of T_R are shown in Figure 8.11 alongside the numerical predictions for cases 1-4 using this method. Here, the theoretical predictions are marked along each line representing the possible coefficient values to enable a better visualisation of the numerical results and their deviation from the theory.

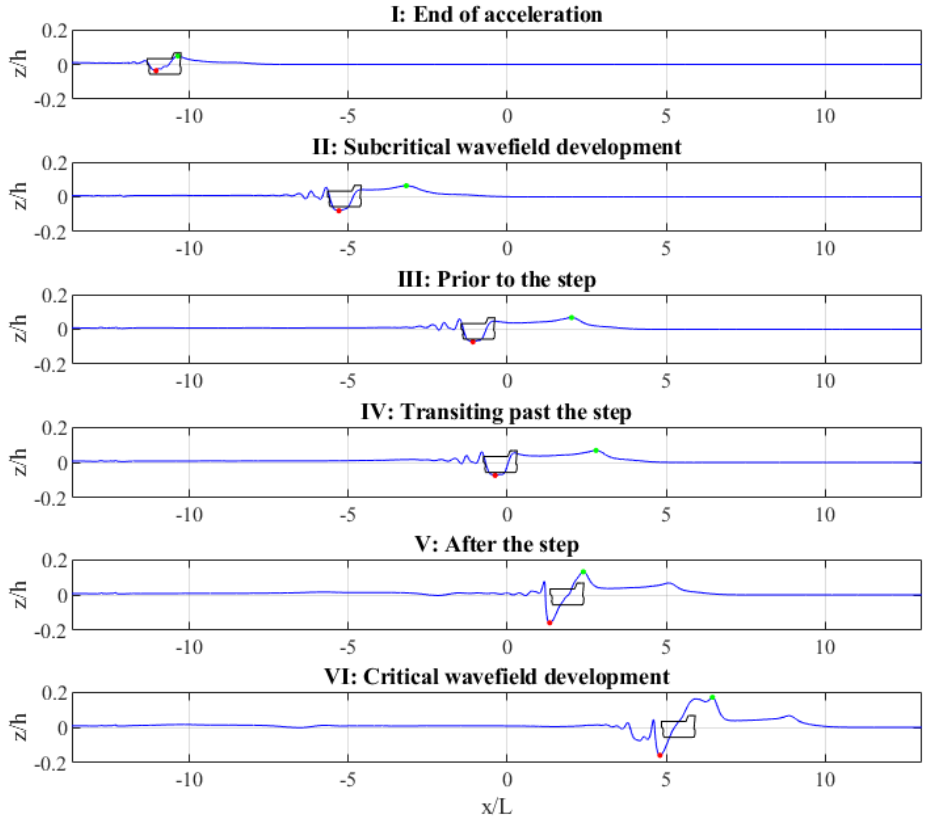

Figure 8.10. Wavecut 2 (y/w=0.2) evolution for case F_{hi} =0.77, F_{hs} =1, made dimensionless by the initial depth h_i =0.32. Maxima and minima are marked with green and red points, respectively. The outline of the ship is scaled down in the vertical direction by a factor of 8 to enable a visualisation of the ship's position.

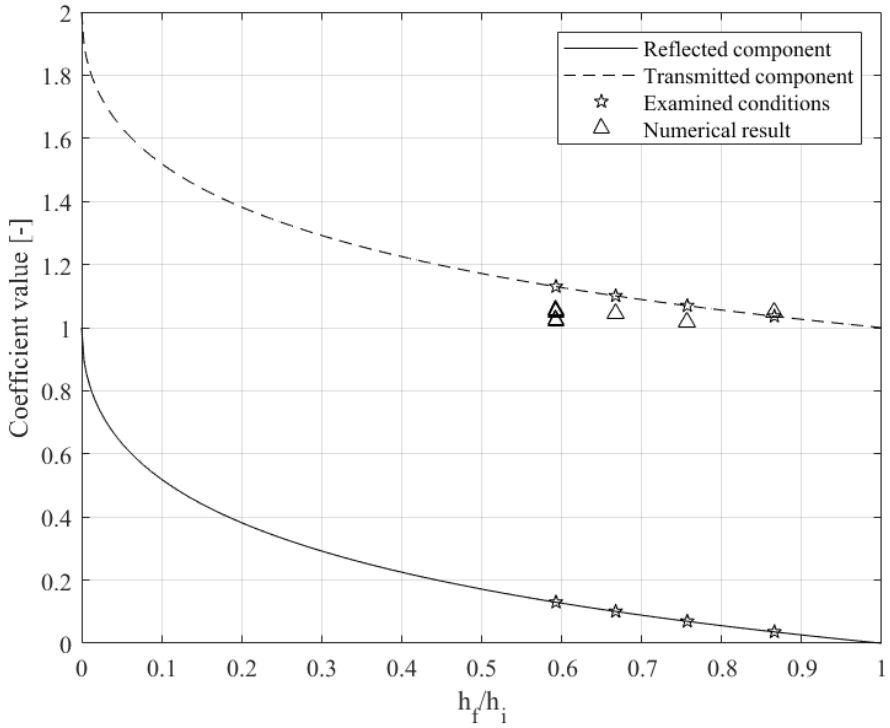

Figure 8.11. Transition and reflection coefficients for cases 1-4 (F_{hi} =0.77).

Figure 8.11 also contains the reflected coefficient values for the entire range of depth ratios. In this case, no numerical predictions are given because a reflected wave elevation is not observed. The suspected cause of this is the ship's interaction with the wavefield. To elaborate, any reflected wave will be disturbed almost as soon as it is created by the passing of the ship. On the other hand, the numerical results for T_R (transmission coefficient) show good agreement with the theoretical line. In fact, the present datapoints are less scattered than the experimental results shown in Newman (1965). It should be noted that in the aforementioned work, the author used the infinitely deep initial region theory to construct his line. Nevertheless, he demonstrated that the experimental data are scattered around the line, providing a form of validation for the present wavefield.

The reason why several closely positioned datapoints are shown in Figure 8.11 relates to the manner in which the wavefield is sampled. Specifically, Figure 8.9 and Figure 8.10 show that one has a range of choices when it comes to taking the incident wave height and transmitted wave height. Therefore, it is thought important to demonstrate that this particular choice is of little importance on the positioning of the calculated transmission coefficients. For this reason, only one datapoint is given for cases II ~ IV. To further investigate the significance of the location over which the soliton is taken, the wavefield

maximum and minimum along the wavecuts given in Figure 8.9 and Figure 8.10 are shown in Figure 8.12.

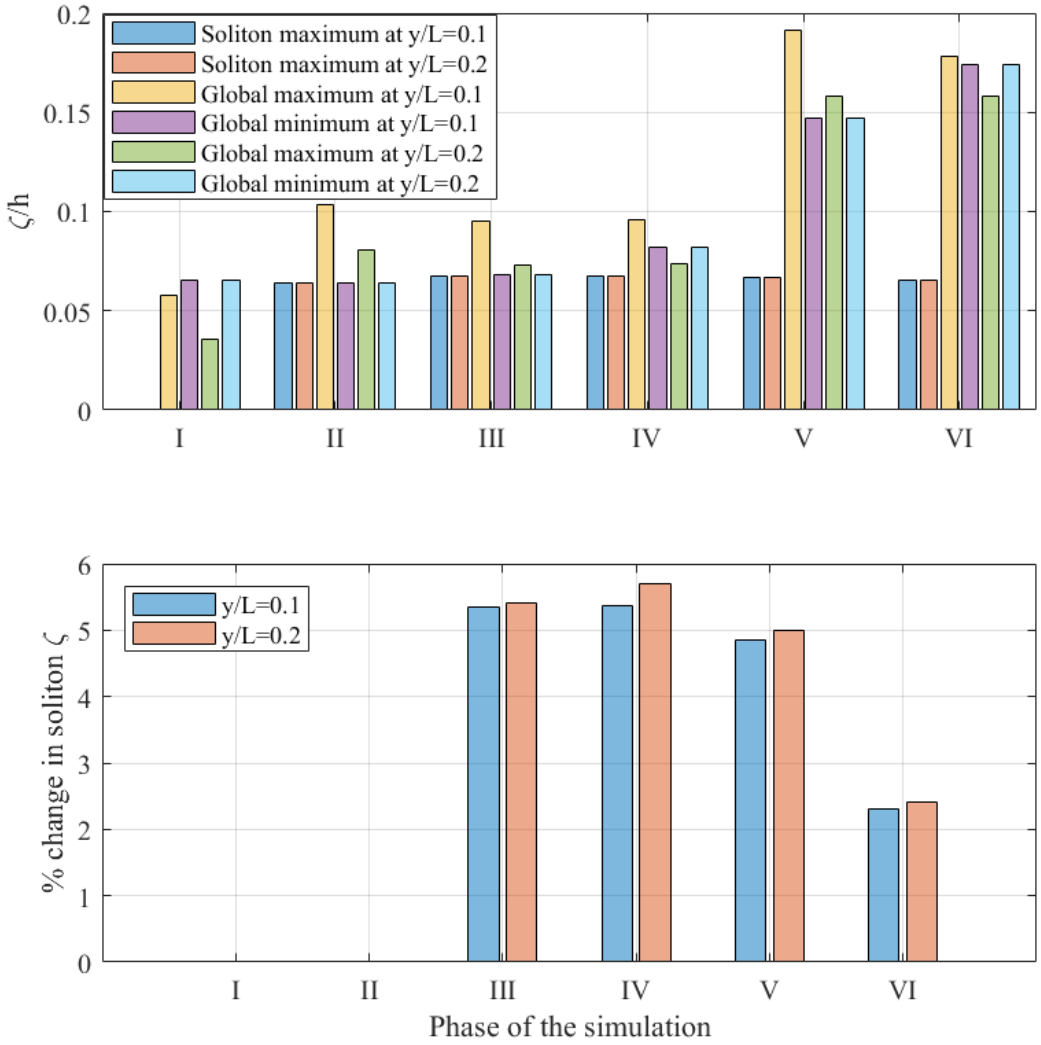

Figure 8.12. Analysis of the wavefield for F_{hi} =0.77, F_{hs} =1 along wavecuts y/w=0.1 and y/w=0.2

Here, a simple relation was used to predict the transmitted component of the soliton, which was shown to agree well with the numerical results. However, it also important to state that following the work of Newman (1965), Lamb (1932), and Bartholomeusz (1958), considerable developments have been made in the field of predicting the behaviour of waves at depth transitions. Some recent studies include Bender and Dean, (2003), and discussions thereof (Bender and Dean, 2005; Liu and Lin, 2005), which can give the reader a much more in-depth appreciation of the complexities encountered in the related field. Many methods, such as that of Marshall and Naghdi (1990) use the wavenumber, k, in each region to arrive at an expression for T_R.

To estimate the wavenumber, Lee and Lee (2019) give several methods. Guo (2002), and Newman (1990) can be consulted as well. In this chapter, the approaches of Hunt (1979) and Havelock (1908) are used. These techniques agree well for the examined range (F_{hi} =0.77), as shown in Figure 8.13.

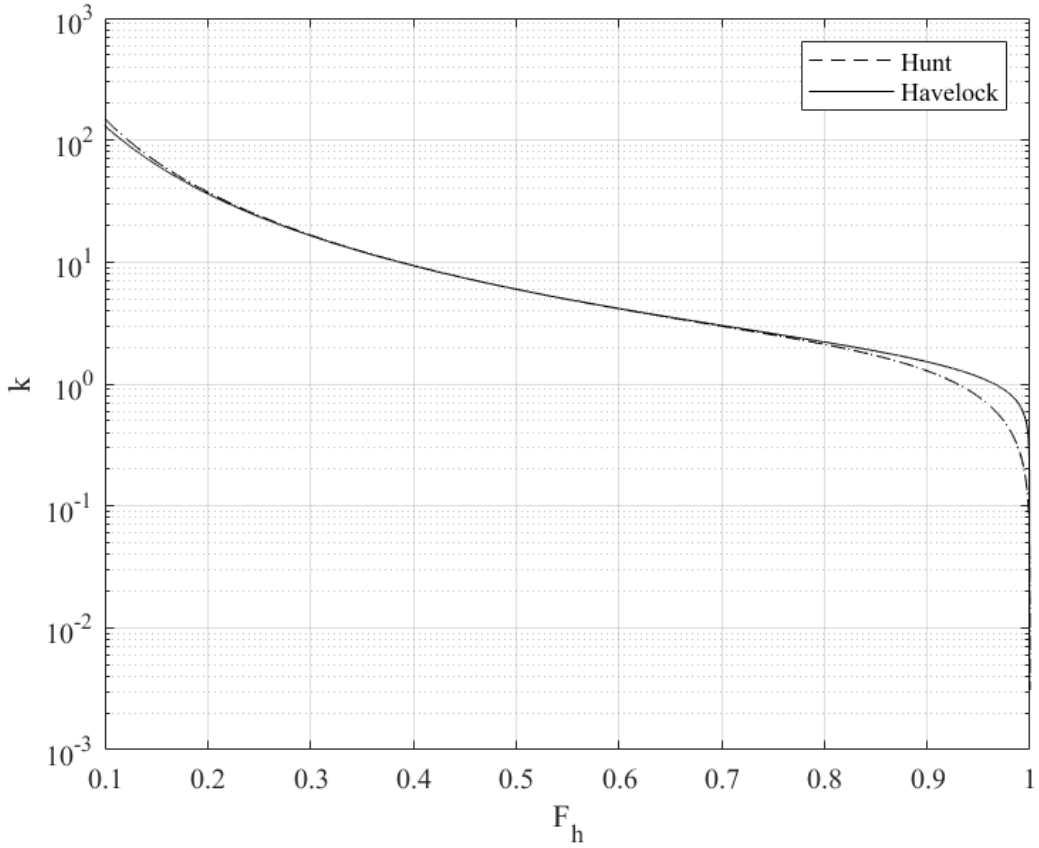

Figure 8.13. Predicted wavenumber (k_i) for each depth Froude number

Clearly, one runs into problems using these methods when predicting the wavenumber in the region past the step if F_{hs} =1. In this respect, Marshall and Naghdi (1990) proposed the following relationships between the two regions' wavenumbers:

$$k_i \tanh(k_i h_i) = k_{s1} \tanh(k_{s1} h_s) \tag{8.7}$$

$$k_{s2} = \sqrt{\frac{h_i k_i^2}{h_s(1+k_i^2 h_i^2/3 - k_i^2 h_i h_s/3)}} \tag{8.8}$$

$$k_{s3} = k_i \sqrt{h_i/h_s} \tag{8.9}$$

Then, the reflected and transmitted and coefficients are given in Eq. (8.10) and Eq. (8.11), respectively:

$$R_R = \frac{k_s - k_i}{k_2 + k_i} \tag{8.10}$$

$$T_R = \frac{2k_s}{k_s + k_i} \tag{8.11}$$

In Eq. (8.7) – Eq. (8.9), the subscripts 1, 2, 3 are used to differentiate the wavenumber predictions. To examine the predictions graphically, Figure 8.14 was constructed showing the relationships between k_{s1-3} and the wavenumber, as predicted by Hunt's (1979) method.

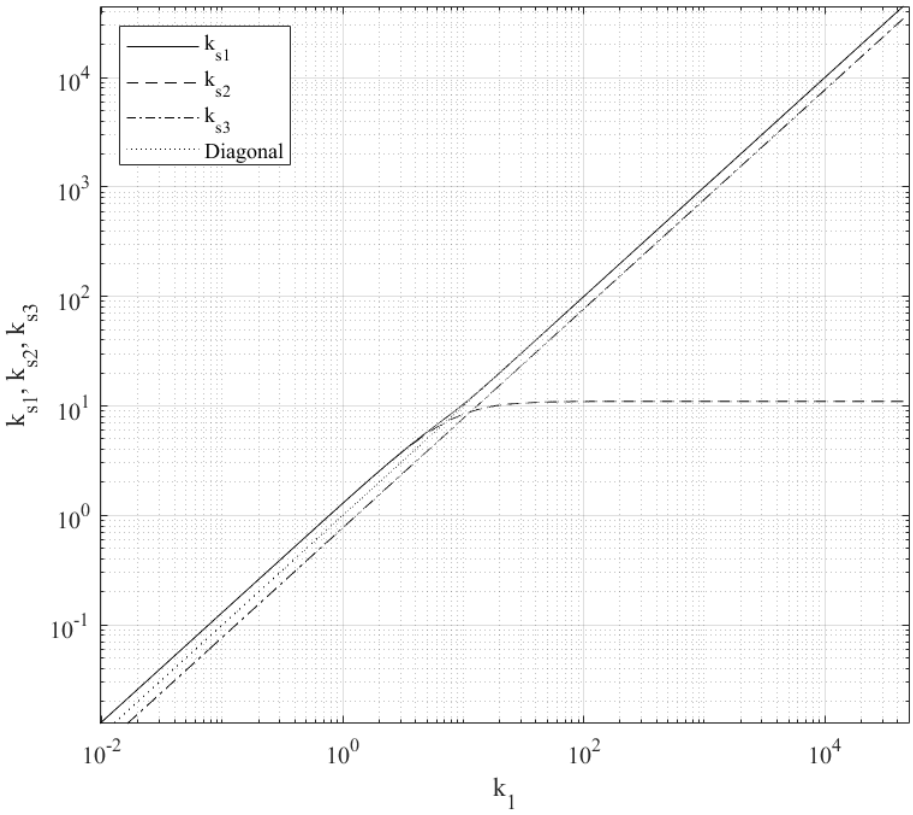

Figure 8.14. Wavenumber predictions for the region past the step. Depicted: case 1, F_{hi} =0.77 and F_{hs} =1.

As k_{s2} increases past a value of 100, it essentially ceases to grow. Fortunately, the values of interest are far from this boundary. The predicted wave numbers using the aforementioned methods are summarised in Table 8.5.

Table 8.5. Summary of wavenumbers for cases 1 ~ 4 (F_{hi} =0.77).

Method	Description		Wavenumber value
Havelock (1908)	F_{hi} =0.77	Initial region	7.591
Hunt (1979)			7.367
Relative difference			-3.04%
Eq. (8.7)		F_{hs} =1	7.974
		F_{hs} =0.943	7.777
		F_{hs} =0.885	7.608
		F_{hs} =0.826	7.470
Eq. (8.8)		F_{hs} =1	7.224
		F_{hs} =0.943	7.093
		F_{hs} =0.885	7.031
		F_{hs} =0.826	7.085
Eq. (8.9)		F_{hs} =1	5.672
		F_{hs} =0.943	6.018
		F_{hs} =0.885	6.409
		F_{hs} =0.826	6.855

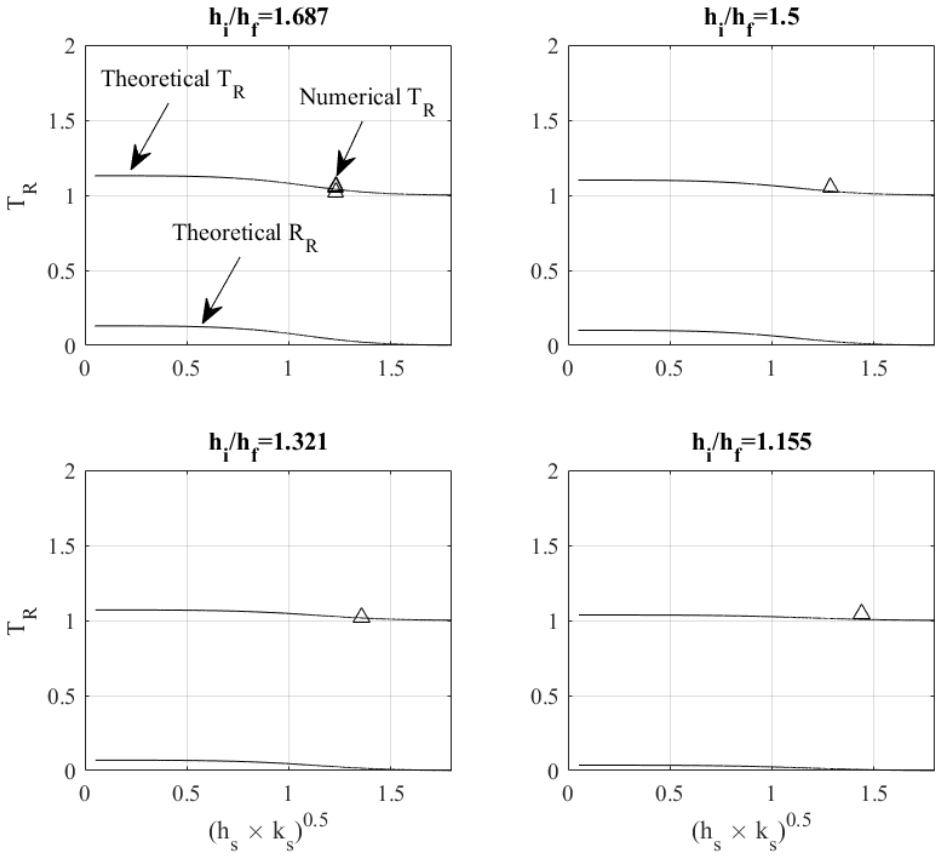

Figure 8.15. Transmission and reflection coefficients based on Marshall and Naghdi's (1990) method (F_{hi} =0.77).

Since Marshall and Naghdi (1990) derived Eq. (8.7) without additional assumptions, it is used to construct transmission coefficients shown in Figure 8.15 for cases 1~4 (F_{hi} =0.77). Here, the range has been retained from Figure 8.11 for consistency. Figure 8.15 demonstrates that the much simpler approach given in Figure 8.11 can be used to quickly estimate the values, with essentially the same accuracy in the transmission coefficients. This is valid due to the particular case studies selected. Had a deeper water region been chosen, the approach of Marshall and Naghdi (1990) would have been recommended.

At this stage it is also worthwhile to mention that the decrease in height of the soliton with distance, given in Figure 8.12 is also physically sound. As stated earlier, the height of the wave in front of the ship was shown to decay. This was given as a justification to the question why, there are several datapoints for F_{hs} =1 in terms of transmission coefficients. The dissipation of the wave is due to a combination of viscous action in the fluid and friction at the edges and bottom of the tank. Here, the reader is reminded that all boundary conditions, with the exception of the symmetry plane and overset box are no-slip walls. Therefore, the dissipation of the wave is an expected outcome.

The dissipation in the present context can be approximated as shown in Figure 8.16. Here, Eq. (8.12) and Eq. (8.13) are used to construct the dissipation and amplitude-change parts of the plot, as reported in Lamb (1932). Further discussion of these equations can be found in the relevant literature (Denner et al., 2017; Dorn, 1966; Hunt, 1964; Keulegan, 1948; Liang and Chen, 2019).

$$D = \frac{2k}{b}\sqrt{\frac{\nu}{2\omega}}\frac{kw+\sinh(2kh)}{2kh+\sinh(2kh)} \tag{8.12}$$

$$\delta = \zeta e^{-Dx} \tag{8.13}$$

where D is the dissipation, $\omega^2 = gk\tanh(kh)$, ν is the kinematic viscosity, δ is the amplitude of the wave having travelled x metres, and ζ is the elevation of the initial wave. It should be noted that k_{s1}, as given in Table 8.5 and Eq. (8.7) are used throughout for consistency.

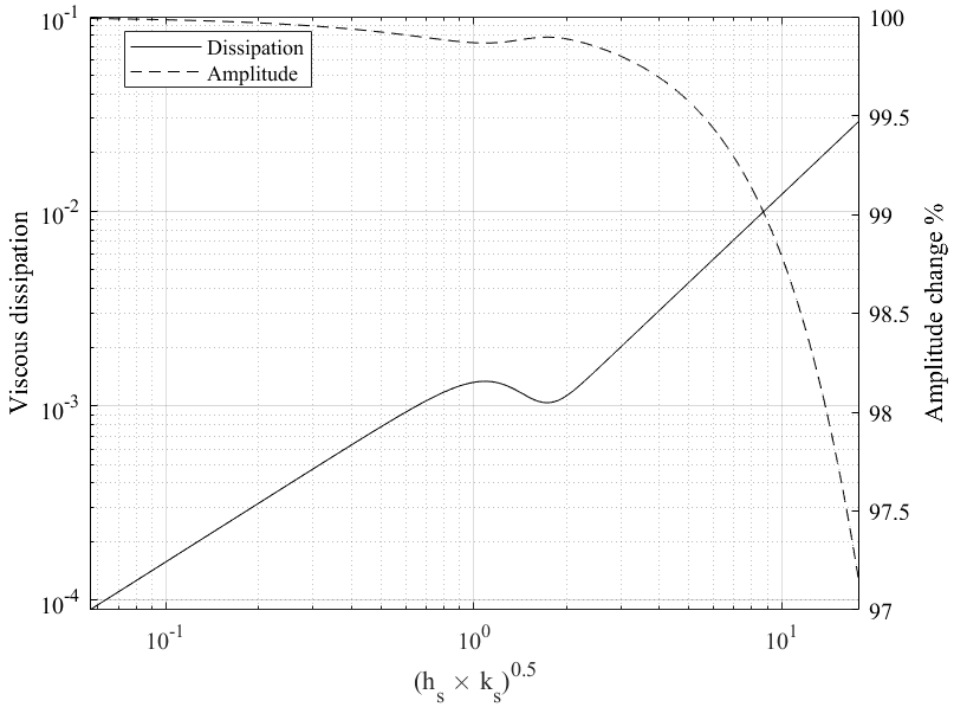

Figure 8.16. Viscous dissipation on a unit wave with different dispersive properties travelling a unit distance.

In the present set of simulations, it is not immediately obvious where the origins of the soliton lie. It is therefore difficult to determine an exact damped amplitude. Thus, tracing the soliton's decay continuously and comparing it with the analytical solution is not attempted. Instead, the value of the soliton after it has transferred onto the step is used. Then, the damping relations given in Eq. (8.12) and Eq. (8.13) are applied to arrive at a decrease in magnitude by 2.923%. Similarly, the numerical result is that the soliton reduced in magnitude by 2.994% between phases III (prior to the step) to VI (critical wavefield development). Note that the soliton has already cleared the step at phase III. This agreement is excellent and indicates that the present solution has captured the physics of wave propagation and transmission well, as indicated by the results given here and in Figure 8.11 and Figure 8.15.

The numerical modelling of the wavefield, including the friction on the side walls and bottom was shown to agree well with analytical solutions. Therefore, the use of wall functions at the boundaries of the tank is shown to provide sufficient accuracy. This result also suggests that numerical diffusion, incurred by the grid density is minimal for the soliton. To check whether the solitary wave propagates with a speed, consistent with theoretical predictions, the formulation given in Ertekin et al. (1986), Eq. (8.14) is used.

$$C = \sqrt{gh \times (1 + \zeta/h)} \tag{8.14}$$

where C is the solitary wave speed in a region of depth h. The formulation is used for case 1 to obtain $C = 1.44$ m/s, which compares well with the numerically observed 1.46 m/s, exhibiting a relative difference of 1.71%. In this calculation, the average ζ value is used form the final two measurements, given in Figure 8.9 and Figure 8.12.

Another aspect of the generated data considered here relates to the velocity field produced by the soliton, and the ship and its wave system as they interact with the step. As was the case earlier, focus is placed on the critical transition case (case 1, F_{hi} =0.77 and F_{hs} =1). To examine the velocity field, the proportion of the domain beneath the undisturbed free surface is plotted at various times in Figure 8.17. The symmetry plane is used as a reference in this case throughout. Longitudinally, one ship length before and after the step is included in the plots.

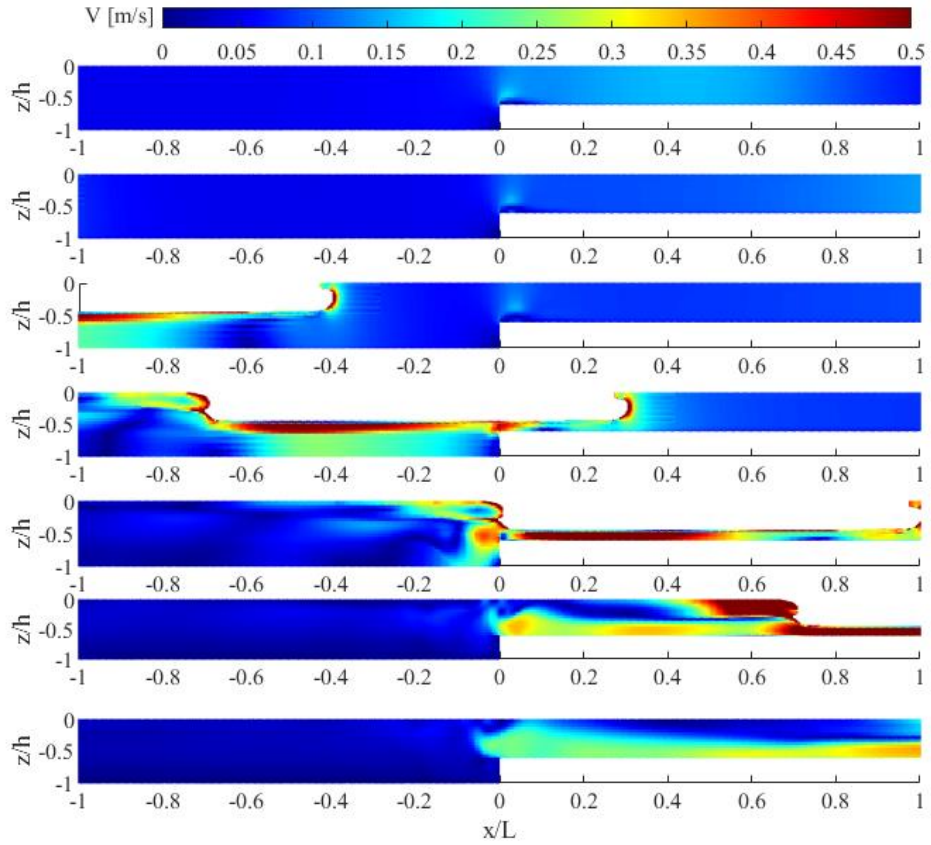

Figure 8.17. Generated velocity field for case 1, F_{hi} =0.77 and F_{hs} =1 as the ship and soliton interact with the step.

The first part of Figure 8.17 shows the process of the soliton as it has cleared the step. Here, the step causes a region of elevated velocity magnitude to persist even after the soliton has propagated a full ship length past the depth reduction. This would likely persist for a long time had the ship not disturbed the flow field. The most surprising aspect of the solution is that a significant proportion of the fluid maintains its velocity a significant time after the ship has cleared the step. The flow field in the final part of Figure 8.17 is in the direction of the ship, with a vortex persisting at the step's edge.

The observations made in Figure 8.17 are in agreement with recent numerical and experimental work, which demonstrated that a boundary layer will form on the seabed in very shallow conditions (Böttner et al., 2020; Shevchuk et al., 2016). In this Chapter it is also demonstrated that this effect persists in the final part of Figure 8.17. However, as mentioned earlier, the domain does not feature any inlets or outlets. Therefore, any fluid, accelerated in the ship's direction must return to equalise the pressure and water elevation behind the ship. Ship-generated waves would also contribute to this, but they diffuse by a combination of sides/bottom friction, numerical and viscous dissipation. Indeed, the smaller the waves, the greater the action of numerical dissipation.

To investigate the mechanism by which the fluid returns after being accelerated in the direction of the ship, the velocity field at the step is taken at the end of the simulation (i.e. once the ship's bow is about 1 m from the end boundary) and shown in Figure 8.18. Although the magnitude of velocity is given in the contour of the plot, the x-direction velocity is also shown as a vector field. This reveals that fluid is returning at a palpable rate to the step. However, once the step is cleared, the velocity diminishes rapidly. Such an effect may explain the elevated time-history of the free surface in Figure 8.7 and Figure 8.8. Specifically, these indicate that considerable volumes of water have been swept along with the ship and are subsequently returning to equilibrium.

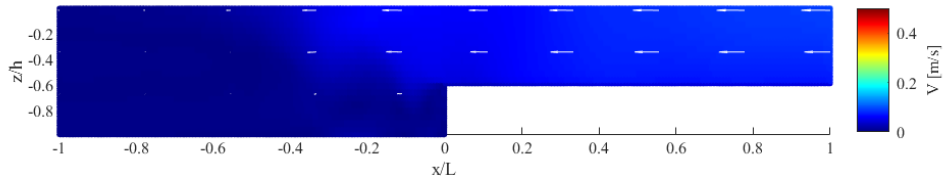

Figure 8.18. Example velocity field near the step at the end of the simulation for case 1: F_{hi} =0.77, F_{hs} =1.

A final consideration is given to the wavecuts shown in Figure 8.9 and Figure 8.10. Although difficult to spot, in phase VI (critical wavefield development), a wave trough can be seen propagating in the direction, opposite that of the ship's. This is not a purely numerical phenomenon. Grue's (2017) theory and observations in a Norwegian fjord demonstrated that this is a key feature of depth transitions. In the case depicted in Figure 8.9 and Figure 8.10, the depression is of approximately –40cm height when converted to full-scale. This consequence of depth transitions is clearly an important part of the physics and has the potential to cause severe infrastructure damage.

8.5 Conclusion and summary

This chapter examined the impact of a step change in the water depth on ship performance using the commercial RANS solver Star-CCM+. The adopted case studies reflected a narrow canal, along the length of which, the water depth changes abruptly. This scenario was modelled to reflect recent work performed experimentally (Elsherbiny et al., 2019c) over a constant canal cross-section, and subsequently validated in Chapter 7. Four depth reductions were modelled with two constant speeds. These were deliberately selected to provide transcritical depth Froude numbers, with one case targeted specifically at the critical speed.

The results were reported in terms of percentage increase of the base resistance encountered by the ship prior to, and after the step. These indicated that a resistance increase of up to approximately 226% may occur if the transition results in subcritical depth Froude numbers approaching the critical speed. On the other hand, it was shown that when the ship has a high initial speed, close to the sub-supercritical boundary, the resistance increase is considerably milder. Results indicated in this case a change of less than 50% for the model scale ship.

In cases where the initial speed is near F_h =1, it was shown that the wavefield is largely two-dimensional and unaffected by the height of the step. On the other hand, when the speed is lower, the interaction of the ship's wavefield with the depth transition is highly sensitive to the step height. For this reason, the transition of waves past shallow water depth discontinuities were examined in some detail. Two theories with varying complexity were employed, both of which agreed well with the numerical results. This suggested that the shallow water celerity approximation $\sqrt{gh}$ holds well even

when the critical depth Froude number is reached in water depths of up to h/T =2.2.

Simultaneously, the damping of the soliton was shown to be in excellent agreement with analytical relations for viscous dissipation of waves in canals. The theoretical result for damping in the amplitude of the soliton was 2.923%, whereas the numerically obtained decrease in amplitude was 2.994%. This suggests that the present RANS approach can model the dissipation of solitons with high accuracy. It was also shown that a boundary layer is formed on the canal bottom, which persisted long after the ship has passed through. The accelerated fluid also requires considerable time to return to its quiescent state.

In terms of numerical uncertainty, it was observed that the requirements for the grid are considerably higher. The numerical uncertainty analysis was performed for both regions, i.e. before and after the step. This revealed that as the depth Froude number decreased, the requirements in terms of mesh increased noticeably, resulting in an elevated uncertainty. On the other hand, both regions showed relatively low temporal dependency.

9. CONCLUSIONS AND FUTURE WORK

9.1 Introduction

This chapter summarises the work performed in this thesis. The completion of the aims and objectives is assessed based on the contents of each chapter. Future work is then suggested based on the findings of the thesis.

9.2 Conclusions

This thesis presented examinations on a variety of subjects within the field of ship hydrodynamics. Each chapter presented an assessment, designed to allow a better understanding of the underlying phenomena. These were defined at the onset of this thesis in terms of research aims and objectives, and were met as follows.

The first objective, listed in Chapter 1 was:

- ✓ *To perform a thorough review of the literature on computational ship hydrodynamics and identify open research questions.*

This objective was met in Chapter 2, which presented a literature review on a variety of issues within the field of ship hydrodynamics. It included scale effects in unrestricted and restricted waters. The survey revealed several key characteristics of investigations in the area. For instance, assumptions, such as that of the double body flow are frequently applied, as well as the high popularity of linear and potential flow methods is noteworthy. Until recently, this was justified with the scarcity of computational resources. However, double body simulations of ship hydrodynamics can also be beneficial in

revealing underlying physics. For example, the interaction between frictional and wave resistance, as pointed out in Chapter 3.

The following objectives, listed in Chapter 1 were:

- ✓ *To perform a geosim analysis in deep and shallow waters.*
- ✓ *To investigate the scale effects on ship resistance and identify the sources of these scale effects.*

These objectives were addressed in two parts. Firstly, a geosim analysis was performed in deep, unrestricted waters, where the physics of the problem are simpler (Chapter 3). Then, the analysis was performed for the shallow water equivalent (Chapter 5). Both of these assessments revealed an interaction between different components of ship resistance, specifically, wave and frictional resistance. Moreover, the existence of scale effects was demonstrated on the wave resistance and form factor. Therefore, the choice of the scale factor was shown to be one of the important aspects determining the value of the extrapolated full-scale resistance of a ship. It was also demonstrated that one should account for interactions between the components of ship resistance, and that neglecting these can have a palpable influence on the extrapolated value.

The sources of scale effects were shown to be rooted in the complexity of the problem. The disparity between the Reynolds number of the model and full-scale ships are chiefly responsible as causing scale effects. Specifically, the action of viscosity and vorticity, which largely defy analytical description, were identified as the responsible factors. This is due to their non-linear variations with the Reynolds number, which changes several orders of magnitude between the experimental and full-scale conditions.

The scale effects on the wave field were analysed from two points of view. Firstly, the observed numerical wave profiles were shown to vary with scale. In the deep-water case, this was done for the far-field waves, which are assumed geometrically similar and inviscid. In the case of shallow water, the wave elevation on the hull was examined due to the fact that the adopted case produced near-field waves only. Both examinations revealed a change in the wave elevation with variations in Reynolds number. The second point of view, from which the wave field was examined was to seek the origin of the observed scale effect. In both cases, this was identified as the boundary layer, and its viscous and vortical action on the surrounding fluid.

The next objectives, listed in Chapter 1 were:

- ✓ *To identify the best turbulence model to close the RANS equations, providing consistent predictions over a range of parameters, at a small computational cost.*

The approach to addressing these objectives was designed to maximise their practical relevance. To achieve this, Chapter 4 presented a turbulence dependence study in restricted waters. Firstly, an overview was given to familiarise the reader with the fundamental concepts, strengths, and outstanding problems of the field of turbulence modelling. These were placed in context by reference to workshops on numerical ship hydrodynamics and current trends in the field. Then, four case studies in restricted waters were adopted to demonstrate the relative effect of turbulence closure on sinkage, trim, and resistance, since all of these parameters are magnified in confined waters.

A consequence of the complexity of the problem of turbulence modelling was found to preclude a straightforward ranking of the models. For this reason, a statistical approach, originally devised to determine consistency in experimental facilities was implemented with a small variation in the methodology. This revealed that it is possible to obtain both qualitative and quantitative characteristics of the turbulence models in terms of consistency and accuracy across a range of different case studies. The assessment suggested that the standard k-ω model provides the best compromise between accuracy and consistency. Moreover, it was demonstrated that the k-ω model requires the least computational resources of all two-equation eddy-viscosity turbulence closures examined. Thus, the k-ω model was identified as a good choice for studies in ship hydrodynamics.

The following objectives were listed in Chapter 1 as:

- ✓ *To demonstrate the application of numerical uncertainty estimators on different parameters and their use in full-scale ship hydrodynamics.*
- ✓ *To determine the performance of computational grids in terms of proximity to the asymptotic range.*

To maximise the practical relevance of the work and meet the above objectives, a full-scale set of simulations was adopted in Chapter 6, where the objectives were addressed. This choice was made in line with the fact that high Reynolds number flows are difficult and expensive to measure, making them scarce in

the open literature and allowing little room for validation. In such cases, numerical uncertainty estimators are frequently the only manner in which one can assess the performance of a simulation. Therefore, an in-depth study into the application of numerical uncertainty estimators, both local and global, was performed. To facilitate the interpretation of data, generated as part of the uncertainty study, a variety of methods were adopted. The resulting data was shown to be able to aid the analyst in making decisions regarding the performance of the simulation in terms of proximity to the asymptotic range.

The importance of choice of a parameter for the assessment was demonstrated by sampling the free surface around the ship and the skin friction it experiences. The assessment showed that despite the use of wall functions in the latter case, the grid behaved in close proximity to the asymptotic range, and was therefore associated with a relatively low numerical uncertainty. On the other hand, the free surface was highly non-asymptotic, rendering the uncertainty which was observed to be found higher. These contradicting outcomes within the same simulation demonstrated that it is of high importance to assess different parameters to determine the performance of a numerical grid.

The next objectives, given in Chapter 1 read as follows:

- ✓ *To determine the Kelvin half-angle of a ship in restricted waters based on a numerical free surface analysis method.*

These objectives were met within Chapter 7, where a virtual towing tank was constructed, featuring no open boundaries (inlets or outlets), thereby being consistent with physical experiments. In this towing tank, Galilean relativity was not invoked to assign a velocity to the fluid to flow past a static hull. Instead the ship propagates over a static fluid by use of the overset domain method. It was demonstrated that via this approach, it is possible to achieve reasonable accuracy in terms of ship resistance in model scale.

On the other hand, the wave field was analysed via a Fourier representation of the numerical free surface. Despite the anticipated nonlinearities, resulting from the solver and hullform, good agreement was established between a theoretical prediction of the wave field in the tank and the numerical observation. The numerically modelled Kelvin half-angle was shown to differ in magnitude by a reasonably small amount when compared with the theoretical approach (less than 2° deviation).

The final objective, listed in Chapter 1 was:

- ✓ *To predict the impact of an abrupt change in the water depth on the resistance of a ship and its wavefield in shallow waters.*

To achieve this objective, Chapter 8 presented a numerical model of the hydrodynamic effect of abrupt water depth changes on a ship travelling in restricted waters using CFD. The virtual approach to tow the ship within the computational tank, developed in Chapter 7, was applied. The resistance was shown to vary substantially depending on the chosen depth Froude numbers, both initial and those resulting after the step.

Significant interactions between the wave field and submerged depth discontinuity were observed in the wave elevation time-history. The wave field was analysed using two methods. Firstly, transmission coefficients were calculated using two theories. One assuming the limit of very shallow water has been achieved, and one taking into account the linear dispersion relation for intermediate depths. Both theories showed agreement amongst themselves, and with the numerical data. Secondly, the viscous dissipation, resulting due to the friction with the side walls and inherent properties of the fluid were analysed. These showed excellent agreement with an analytical approximation.

9.3 Discussion

This thesis relied almost exclusively on the Computational Fluid Dynamics approach to analysing ship hydrodynamics in deep and shallow waters. Nevertheless, several theoretical methods were included to either augment the discussions, provide room for comparison, or offer a type of validation. The author of this thesis believes that it is justifiable to expect that CFD will become the norm in hydrodynamic analysis and simulation-based design. However, the utility of theories, relying on a number of well-posed assumptions should not be discounted.

It was demonstrated in Chapter 2 that scientific papers concerning ship CFD analysis have been increasing exponentially in recent years (Figure 2.3). Open research questions in the field have persisted, presenting both researchers and practitioners with several highly relevant unresolved issues. In Chapter 2 the unresolved issues were identified as the resistance extrapolation procedures, the approaches to modelling turbulence, shallow water effects on ship performance, particularly as they relate to full-scale studies, the sensitivity of

the solution to grid density and topography, the representation of ship waves, and the modelling of depth transitions in shallow waters. This thesis has showed that each of these problems can be solved with the CFD approach. Moreover, it was shown that the conceptual problems plaguing simpler methods are largely overcome in this way. However, useful information can be obtained from potential flow approaches, which can increase the confidence in numerical approaches.

Specifically, Chapter 5 showed that theoretical analysis predicts the correct behaviour of scale effects. Chapter 7 demonstrated that a fully nonlinear towing tank produces a wavefield in agreement with linear methods, whereas Chapter 8 validated the transmission coefficients and viscous dissipation on ship-induced disturbances.

Alongside the successes of numerical approaches in modelling a variety of phenomena, their limitations should also be borne in mind. These were examined in Chapter 4, where turbulence dependence was reviewed. On the other hand, Chapter 6 presented a detailed application and interpretation of numerical uncertainty, induced as a result of mapping the governing equations onto a discrete grid. Therefore, there are many aspects in which the work presented in this thesis could be extended. These are examined in the following section.

9.4 Future work

Without a doubt, the field of ship hydrodynamics presents many opportunities of both theoretically engaging and practically relevant work. Some specific examples for further research are given in this section.

It is hoped that the work presented in Chapter 3 and Chapter 5 will create an interest in wave resistance changes with scale, a topic largely ignored in the study of ship resistance. A more scientific extrapolation procedure is required to replace the experience-based approach most facilities seem to have adopted. While the ITTC's procedure has been widely criticised for years, little progress has been made towards its improvement, largely stagnating new developments in this direction. The problems associated with scale effects do not necessarily come from the decomposition and extrapolation procedure itself, rather the assumptions imposed as a part of it. Were these to be relaxed or re-examined with modern computational tools, progress could be achieved.

In this thesis, the presence of a rotating propeller was not modelled. This is justifiable due to the scarcity such of studies performed even for un-appended hulls where the complexity is much smaller compared to modelling a hull with its appendages (propeller). Therefore, the studies presented in this thesis should be used as a stepping stone to lead to research where self-propulsion is considered.

A different aspect of ship hydrodynamics that is currently popular amongst researchers is the estimation of roughness and fouling effects on ship hulls. Although several studies have already been performed in this area, the combined effect of shallow waters and fouling is yet unexamined. A related study could also examine the effect of roughness on the canal walls or seabed on ship performance. As demonstrated in Chapter 8, a boundary layer forms on the ship and domain bottom surfaces. If both of these feature a degree of fouling, it is justifiable to expect different performance characteristics.

Fouling and surface roughness should also be examined under different turbulence models and their wider effect on ship performance. Ideally, such a work would model the propeller's action. The assessment of numerical uncertainty should be extended to propellers. Since the wave field would be fundamentally time-dependent, one could focus on the pressure pulses on the ship hull, the friction experienced by the propeller blades, or the position and volume of sheets of cavitation.

Finally, it would be of practical interest to determine which acceleration profile results in the smallest unsteadiness and therefore quickest convergence of the resistance curve. In both Chapter 7 and Chapter 8, a constant acceleration was used to ramp up the velocity until the target speed is achieved. Determining a manner of achieving the target speed with the smallest possible soliton magnitude would be undoubtedly of interest to the towing tank community.

REFERENCES

Abe, K., Kondoh, T., Nagano, Y., 1994. A new turbulence model for predicting fluid flow and heat transfer in separating and reattaching flows-l. Flow field calculations. Int. J. Heat Mass Transf. 37, 139–151. https://doi.org/10.7566/JPSJ.84.054710

Abu-Ghannam, B.J., Shaw, R., 1980. Natural Transition of Boundary Layers - The Effects of Turbulence, Pressure Gradient, and Flow History. J. Mech. Eng. Sci. 22, 213–228. https://doi.org/https://doi.org/10.1243/JMES_JOUR_1980_022_043_02

Alam, M.R., Mei, C.C., 2008. Ships advancing near the critical speed in a shallow channel with a randomly uneven bed. J. Fluid Mech. 616, 397–417. https://doi.org/10.1017/S0022112008004035

American Institute of Aeronautics and Astronautics (AIAA), 1994. Editorial policy statement on numerical accuracy and experimental uncertainty. AIAA J. 32, 3. https://doi.org/10.2514/3.48281

Andrun, M., Blagojević, B., Bašić, J., 2018. The influence of numerical parameters in the finite-volume method on the Wigley hull resistance. Proc. Inst. Mech. Eng. Part M J. Eng. Marit. Environ. https://doi.org/10.1177/1475090218812956

Argyropoulos, C.D., Markatos, N.C., 2015. Recent advances on the numerical modelling of turbulent flows. Appl. Math. Model. 39, 693–732. https://doi.org/10.1016/j.apm.2014.07.001

Arnold-Bos, A., Martin, A., Khenchaf, A., 2007. Obtaining a ship's speed and direction from its Kelvin wake spectrum using stochastic matched filtering, in: International Geoscience and Remote Sensing Symposium (IGARSS). pp. 1106–1109. https://doi.org/10.1109/IGARSS.2007.4422995

ASME (American Society of Mechanical Engineers), 2009. Standard for Verification and Validation in Computational Fluid Dynamics and Heat Transfer - ASME V&V 20-2009, ASME International.

Atencio, B.N., Chernoray, V., 2019. A resolved RANS CFD approach for drag characterization of antifouling paints. Ocean Eng. 171, 519–532. https://doi.org/10.1016/j.oceaneng.2018.11.022

Axtmann, G., Rist, U., 2016. Scalability of OpenFOAM with Large EddySimulations and DNS on High-PerformanceSystems, in: Nagel W., Kröner D., Resch M. (Eds) High Performance Computing in Science and Engineering ´16. Springer, Cham. https://doi.org/10.1109/CAHPC.2005.27

Bailly, C., Comte-Bellot, G., 2004. Turbulence, Springer. Springer, Cham. https://doi.org/https://doi.org/10.1007/978-3-319-16160-0

Bakica, A., Gatin, I., Vukčević, V., Jasak, H., Vladimir, N., 2019. Accurate assessment of ship-propulsion characteristics using CFD. Ocean Eng. 175, 149–162. https://doi.org/10.1016/j.oceaneng.2018.12.043

Baldwin, B.S., Lomax, H., 1978. Thin Layer Approximation and Algebraic Model for Separated Turbulent Flows, In 16th aerospace sciences meeting.

Baldwin, B.S., Timothy, B., 1990. A one-equation turbulence transport model for high Reynolds number wall-bounded flows, National Aeronautics and Space Administration. https://doi.org/10.2514/6.1991-610

Banks, J.B., Phillips, B., Bull, W., Turnock, S.R., 2010. RANS Simulations of the Multiphase Flow Around the KCS Hullform, in: Gothenburg 2010 Workshop on Numerical Ship Hydrodynamics. pp. 601–606.

Bartholomeusz, B.Y.E.F., 1958. Reflexion of long waves at a step. Math. Proc. Cambridge Philos. Soc. 54, 106–118.

Bašić, J., Degiuli, N., Dejhalla, R., 2017. Total resistance prediction of an intact and damaged tanker with flooded tanks in calm water. Ocean Eng. 130, 83–91. https://doi.org/10.1016/j.oceaneng.2016.11.034

Bechthold, J., Kastens, M., 2020. Robustness and quality of squat predictions in extreme shallow water conditions based on RANS-calculations. Ocean Eng. 197, 106780. https://doi.org/10.1016/j.oceaneng.2019.106780

Beck, R.F., 1977. Forces and Moments on a Ship Moving in a Shallow Channel. J. Sh. Res. 21, 107–119.

Beck, R.F., Newman, J.N., Tuck, E.O., 1975. Hydrodynamic forces on ships in dredged channels. J. Sh. Res. 19, 166–171.

Beck, R.F., Reed, A.M., 2001. Modern Computational Methods for Ships in a Seaway. SNAME Trans. 109, 1–55.

Begovic, E., Day, A.H., Incecik, A., Mancini, S., Pizzirusso, D., 2015. Roll damping assessment of intact and damaged ship by CFD and EFD methods. Proc. 12th Int. Conf. Stab. Ships Ocean Veh. 501–512.

Beji, S., 2018. Kadomtsev-Petviashvili type equation for entire range of relative water depths. https://doi.org/10.1080/21664250.2018.1436241org/10.1080/21664250.2018.1436241

Bellafiore, D., Zaggia, L., Broglia, R., Ferrarin, C., Barbariol, F., Zaghi, S., Lorenzetti, G., Manfè, G., De Pascalis, F., Benetazzo, A., 2018. Modeling ship-induced waves in shallow water systems: The Venice experiment. Ocean Eng. 155, 227–239. https://doi.org/10.1016/j.oceaneng.2018.02.039

Bender, C.J., Dean, R.G., 2005. Reply to discussion of "Wave transformation by two-dimensional bathymetric anomalies with sloped transitions" [Coast. Eng. 50 (2003) 61-84]. Coast. Eng. 52, 201. https://doi.org/10.1016/j.coastaleng.2004.11.003

Bender, C.J., Dean, R.G., 2003. Wave transformation by two-dimensional bathymetric anomalies with sloped transitions. Coast. Eng. 50, 61–84. https://doi.org/10.1016/j.coastaleng.2003.08.002

Benham, G.P., Bendimerad, R., Benzaquen, M., Clanet, C., 2020. Hysteretic wave drag in shallow water. Phys. Rev. Fluids 5, 64803. https://doi.org/10.1103/physrevfluids.5.064803

Benham, G.P., Boucher, J.P., Labbé, R., Benzaquen, M., Clanet, C., 2019. Wave drag on asymmetric bodies. J. Fluid Mech. 878, 147–168. https://doi.org/10.1017/jfm.2019.638

Bertram, V., 2012. Resistance and Propulsion, Practical Ship Hydrodynamics. https://doi.org/10.1016/B978-0-08-097150-6.10003-X

Bhushan, S., Alam, M.F., Walters, D.K., 2013. Evaluation of hybrid RANS/LES models for prediction of flow around surface combatant and Suboff geometries. Computers and Fluids 88, 834–849. https://doi.org/10.1016/j.compfluid.2013.07.020

Bhushan, S., Xing, T., Carrica, P., Stern, F., 2009. Model- and Full-Scale URANS Simulations of Athena Resistance, Powering, Seakeeping, and 5415 Maneuvering. J. Sh. Res. 53, 179–198.

Bhushan, S., Xing, T., Carrica, P., Stern, F., Des, U., 2007. Model- and Full-Scale

URANS / DES Simulations for Athena R / V Resistance , Powering , and Motions, in: 9th International Conference on Numerical Ship Hydrodynamics Ann Arbor, Michigan. pp. 5–8.

Billard, F., Laurence, D., 2012. A robust k-ε-v2/k elliptic blending turbulence model applied to near-wall, separated and buoyant flows. Int. J. Heat Fluid Flow 33, 45–58. https://doi.org/10.1016/j.ijheatfluidflow.2011.11.003

Blasius, H., 1908. The boundary layers in fluids with little friction. National Advisory Committee for Aeronautics. Technical Memorandum 1256.

Böttner, C.U., Anschau, P., Shevchuk, I., 2020. Analysis of the flow conditions between the bottoms of the ship and of the waterway. Ocean Eng. 199. https://doi.org/10.1016/j.oceaneng.2020.107012

Bourne, J., 2000. Louisiana's Vanishing Wetlands: Going, Going ... Science (80-.). 289, 1860 LP – 1863. https://doi.org/10.1126/science.289.5486.1860

Brard, R., 1970. Viscosity, Wake, and Ship Waves. J. Sh. Res. 14, 1–34.

Bugalski, T., 2007. An overview of the selected results of the European Union Project EFFORT. Arch. Civ. Mech. Eng. 7, 55–67. https://doi.org/10.1016/S1644-9665(12)60013-2

Cadafalch, J., Pérez-Segarra, C.D., Cònsul, R., Oliva, A., 2002. Verification of finite volume computations on steady-state fluid flow and heat transfer. J. Fluids Eng. Trans. ASME 124, 11–21. https://doi.org/10.1115/1.1436092

Cakici, F., Sukas, O.F., Kinaci, O.K., Alkan, A.D., 2017. Prediction of the vertical motions of the dtmb 5415 ship using different numerical approaches. Brodogradnja 68, 29–44. https://doi.org/10.21278/brod68203

Caplier, C., Rousseaux, G., Calluaud, D., David, L., 2016. Energy distribution in shallow water ship wakes from a spectral analysis of the wave field. Phys. Fluids 28. https://doi.org/10.1063/1.4964923

Caris, A., Limbourg, S., Macharis, C., van Lier, T., Cools, M., 2014. Integration of inland waterway transport in the intermodal supply chain: A taxonomy of research challenges. J. Transp. Geogr. 41, 126–136. https://doi.org/10.1016/j.jtrangeo.2014.08.022

Carlson, J.A., Jaffe, A., Wiles, A., 2014. The Millenium Prize Problems, American Mathematical Society.

Carrica, P.M., Huang, J., Noack, R., Kaushik, D., Smith, B., Stern, F., 2010. Large-scale DES computations of the forward speed diffraction and pitch and heave problems for a surface combatant. Computers and Fluids 39,

1095–1111. https://doi.org/10.1016/j.compfluid.2010.02.002

Carrica, P.M., Wilson, R. V., Noack, R.W., Stern, F., 2007. Ship motions using single-phase level set with dynamic overset grids. Computers and Fluids 36, 1415–1433. https://doi.org/10.1016/j.compfluid.2007.01.007

Carusotto, I., Rousseaux, G., 2013. The Cerenkov effect revisited: From swimming ducks to zero modes in gravitational analogues, in: Analogue Gravity Phenomenology. Cham, pp. 109–144.

Castiglione, T., Stern, F., Bova, S., Kandasamy, M., 2011. Numerical investigation of the seakeeping behavior of a catamaran advancing in regular head waves. Ocean Eng. 38, 1806–1822. https://doi.org/10.1016/j.oceaneng.2011.09.003

Castro, A.M., Carrica, P.M., Stern, F., 2011. Full scale self-propulsion computations using discretized propeller for the KRISO container ship KCS. Computers and Fluids 51, 35–47. https://doi.org/10.1016/j.compfluid.2011.07.005

Cazalbou, J.B., Spalart, P.R., Bradshaw, P., 1994. On the behavior of two-equation models at the edge of a turbulent region. Phys. Fluids 6, 1797–1804. https://doi.org/10.1063/1.868241

Celik, I.B., Ghia, U., Roache, P.J., Freitas, C.., 2008. Procedure for Estimation and Reporting of Uncertainty Due to Discretization in CFD Applications. J. Fluids Eng. 130, 078001. https://doi.org/10.1115/1.2960953

Celik, I.B., Karatekin, O., 1997. Numerical Experiments on Application of Richardson Extrapolation With Nonuniform Grids. J. Fluids Eng. 119, 584–590. https://doi.org/10.1115/1.2819284

Celik, I.B., Li, J., Hu, G., Shaffer, C., 2005. Limitations of Richardson Extrapolation and Some Possible Remedies. J. Fluids Eng. 127, 795. https://doi.org/10.1115/1.1949646

Chen, H.C., Patel, V.C., 1988. Near-wall turbulence models for complex flows including separation. AIAA J. 26, 641–648. https://doi.org/10.2514/3.9948

Chen, X.-N., Grounarz, A., List, S., 2001. Flow Around Ships Sailing in Shallow Water—Experimental and Numerical Results, in: Twenty-Second Symposium on Naval Hydrodynamics Office of Naval Research Bassin d'Essais Des CarenesNational Research Council. pp. 968–982. https://doi.org/10.17226/9771

Chen, X., Zhu, R., Ma, C., Fan, J., 2016. Computations of linear and nonlinear ship waves by higher-order boundary element method. Ocean Eng. 114,

142–153. https://doi.org/10.1016/j.oceaneng.2016.01.016

Chien, K.Y., 1982. Predictions of Channel and Boundary-Layer Flows with a Low-Reynolds-Number Turbulence Model. AIAA J. 20, 33–38. https://doi.org/10.2514/3.51043

Choi, J.E., Kim, J.H., Lee, H.G., Choi, B.J., Lee, D.H., 2009. Computational predictions of ship-speed performance. J. Mar. Sci. Technol. 14, 322–333. https://doi.org/10.1007/s00773-009-0047-4

Choi, J.E., Min, K.S., Kim, J.H., Lee, S.B., Seo, H.W., 2010. Resistance and propulsion characteristics of various commercial ships based on CFD results. Ocean Eng. 37, 549–566. https://doi.org/10.1016/j.oceaneng.2010.02.007

Chou, P.Y., 1945. On velocity correlations and the solutions of the equations of turbulent fluctuation. Q. Appl. Math. 3, 38–54. https://doi.org/10.1090/qam/11999

Chun, H.H., Park, I.R., Lee, S.K., 2001. Analysis of Turbulence Free-Surface Flow around Hulls in Shallow Water Channel by a Level-set Method, in: Twenty-Second Symposium on Naval Hydrodynamics Office of Naval Research Bassin d'Essais Des CarenesNational Research Council. pp. 941–956. https://doi.org/10.17226/9771

Ciappi, E., Magionesi, F., 2005. Characteristics of the turbulent boundary layer pressure spectra for high-speed vessels. J. Fluids Struct. 21, 321–333. https://doi.org/10.1016/j.jfluidstructs.2005.07.006

Cifani, P., Kuerten, J.G.M., Geurts, B.J., 2018. Highly scalable DNS solver for turbulent bubble-laden channel flow. Computers and Fluids 172, 67–83. https://doi.org/10.1016/j.compfluid.2018.06.008

Cole, S.L., 1987. Transient waves produced by a moving pressure distribution. Q. Appl. Math. 45, 51–58. https://doi.org/10.1090/qam/885167

Crapper, G.D., 1964. Surface waves generated by a travelling pressure point. Proc. R. Soc. London. Ser. A. Math. Phys. Sci. 282, 547–558. https://doi.org/10.1098/rspa.1964.0250

Dam, K.T., Tanimoto, K., Fatimah, E., 2008. Investigation of ship waves in a narrow channel. J. Mar. Sci. Technol. 13, 223–230. https://doi.org/10.1007/s00773-008-0005-6

Dand, W.I., 1967. The wavemaking resistance of ships: Vertical force and form resistance of a hull at uniform velocity. PhD Thesis. University of Glasgow.

Darrigol, O., 2017. Joseph Boussinesq's legacy in fluid mechanics. Comptes Rendus - Mec. 345, 427–445. https://doi.org/10.1016/j.crme.2017.05.008

Darrigol, O., 2003. The spirited horse, the engineer, and the mathematician: Water waves in nineteenth-century hydrodynamics. Arch. Hist. Exact Sci. 58, 21–95. https://doi.org/10.1007/s00407-003-0070-5

Darrigol, O., Frisch, U., 2008. From Newton's mechanics to Euler's equations. Phys. D Nonlinear Phenom. 237, 1855–1869. https://doi.org/10.1016/j.physd.2007.08.003

Darrigol, O., Turner, J.S., 2006. Worlds of flow: A history of hydrodynamics from the bernoullis to prandtl, Physics Today. https://doi.org/10.1063/1.2349735

Date, C.J., Turnock, S., 1999. A study into the techniques needed to accurately predict a skin friction using RANS solvers with validation against Froude's historical flat place experimental data, Ship science report No. 114.

David, C.G., Roeber, V., Goseberg, N., Schlurmann, T., 2017. Generation and propagation of ship-borne waves - Solutions from a Boussinesq-type model. Coast. Eng. 127, 170–187. https://doi.org/10.1016/j.coastaleng.2017.07.001

Davidson, L., Nielsen, P. V, Sveningsson, A., 2003. Modifications of the V2F Model for Computing the Flow in a 3D Wall Jet. Turbul. Heat Mass Transf. 4, 577–584.

Day, A.H., Clelland, D., Doctors, L.J., 2009. Unsteady finite-depth effects during resistance tests on a ship model in a towing tank. J. Mar. Sci. Technol. 14, 387–397. https://doi.org/10.1007/s00773-009-0057-2

Demirel, Y.K., Khorasanchi, M., Turan, O., Incecik, A., Schultz, M.P., 2014. A CFD model for the frictional resistance prediction of antifouling coatings. Ocean Eng. 89, 21–31. https://doi.org/10.1016/j.oceaneng.2014.07.017

Demirel, Y.K., Turan, O., Incecik, A., 2017. Predicting the effect of biofouling on ship resistance using CFD. Appl. Ocean Res. 62, 100–118. https://doi.org/10.1016/j.apor.2016.12.003

Deng, G., Duvigneau, R., Queutey, P., Visonneau, M., 2004. Assessment of turbulence models for ship flow at full scale, in: Comp. Mech., WCCM VI. Beijing, China.

Deng, G., Nantes, E.C. De, Guilmineau, E., Queutey, P., Visonneau, M., 2014. Simulation of Container Ship in Shallow Water at Model Scale and Full

Scale, in: Proceedings of the 3rd National CFD Workshop for Ship and Offshore Engineering.

Deng, G.B., Queutey, P., Visonneau, M., 2010. RANS prediction of the KVLCC2 tanker in head waves. J. Hydrodyn. 22, 476–481. https://doi.org/10.1016/S1001-6058(09)60239-0

Deng, R., Li, C., Huang, D., Zhou, G., 2015. The Effect of Trimming and Sinkage on the Trimaran Resistance Calculation, Procedia Engineering. Elsevier B.V. https://doi.org/10.1016/j.proeng.2015.11.199

Denner, F., Paré, G., Zaleski, S., 2017. Dispersion and viscous attenuation of capillary waves with finite amplitude. Eur. Phys. J. Spec. Top. 226, 1229–1238. https://doi.org/10.1140/epjst/e2016-60199-2

Dhinesh, G., Murali, K., Subramanian, V.A., 2010. Estimation of hull-propeller interaction of a self-propelling model hull using a RANSE solver. Ships Offshore Struct. 5, 125–139. https://doi.org/10.1080/17445300903231109

Dias, F., 2014. Ship waves and Kelvin. J. Fluid Mech. 746, 1–4. https://doi.org/10.1017/jfm.2014.69

Diskin, B., Thomas, J.L., 2010. Notes on accuracy of finite-volume discretization schemes on irregular grids. Appl. Numer. Math. 60, 224–226. https://doi.org/10.1016/j.apnum.2009.12.001

Doctors, L.J., 2007. A Numerical Study of the Resistance of Transom-Stern Monohulls. Sh. Technol. Res. 54, 134–144. https://doi.org/10.1179/str.2007.54.3.005

Doctors, L.J., 1975. The experimental wave resistance of an accelerating two-dimensional pressure distribution. J. Fluid Mech. 72, 513–527. https://doi.org/10.1017/S0022112075003114

Doctors, L.J., Macfarlane, G.J., Young, R., 2007. A study of transom-stern ventilation. Int. Shipbuild. Prog. 54, 145–163.

Dorn, W.G.V., 1966. Boundary dissipation of oscillatory waves. J. Fluid Mech. 24, 769–779. https://doi.org/10.1017/S0022112066000995

Duffy, J., 2008. Modelling of Ship-Bank Interaction and Ship Squat for Ship-Handling Simulation by.

Durbin, P.A., 2017a. Some Recent Developments in Turbulence Closure Modeling. Annu. Rev. Fluid Mech. 50, 77–103. https://doi.org/10.1146/annurev-fluid-122316-045020

Durbin, P.A., 2017b. Perspectives on the Phenomenology and Modeling of

Boundary Layer Transition. Flow, Turbul. Combust. 99, 1–23. https://doi.org/10.1007/s10494-017-9819-9

Durbin, P.A., 1996. On the k-3 stagnation point anomaly. Int. J. Heat Fluid Flow 17, 89–90. https://doi.org/10.1016/0142-727X(95)00073-Y

Durbin, P.A., 1995. Separated flow computations with the k-epsilon-v-squared model. AIAA J. 33, 659–664. https://doi.org/10.2514/3.12628

Durbin, P.A., 1993a. Application of a near-wall turbulence model to boundary layers and heat transfer. Int. J. Heat Fluid Flow 14, 316–323. https://doi.org/10.1016/0142-727X(93)90004-7

Durbin, P.A., 1993b. A Reynolds stress model for near-wall turbulence. J. Fluid Mech. 249, 465–498. https://doi.org/10.1017/S0022112093001259

Durbin, P.A., 1991. Near-wall turbulence closure modeling without "damping functions." Theor. Comput. Fluid Dyn. 3, 1–13. https://doi.org/10.1007/BF00271513

Durbin, P.A., Pettersson Reif, B.A., 2011. Statistical theory and modelling for turbulent flow, Second Edi. ed. Wiley.

Duvigneau, R., Visonneau, M., Deng, G.B., 2003. On the role played by turbulence closures in hull shape optimization at model and full scale. J. Mar. Sci. Technol. 8, 11–25. https://doi.org/10.1007/s10773-003-0153-8

Eca, L., Hoekstra, M., 2009. Evaluation of numerical error estimation based on grid refinement studies with the method of the manufactured solutions. Computers and Fluids 38, 1580–1591. https://doi.org/10.1016/j.compfluid.2009.01.003

Eca, L., Hoekstra, M., 2008. The numerical friction line. J. Mar. Sci. Technol. 13, 328–345. https://doi.org/10.1007/s00773-008-0018-1

Eca, L., Hoekstra, M., 2006. Discretization Uncertainty Estimation based on a Least Squares version of the Grid Convergence Index. Proc. Second Work. CFD Uncertain. Anal. 1–27.

Eca, L., Hoekstra, M., 2001. Numerical Prediction of Scale Effects in Ship Stern Flows with Eddy-Viscosity Turbulence Models, in: Twenty-Second Symposium on Naval Hydrodynamics Office of Naval Research Bassin d'Essais Des CarenesNational Research Council. pp. 553–568. https://doi.org/10.17226/9771

Eca, L., Hoekstra, M., Beja Pedro, J.F., Falcao de Campos, J.A.C., 2013. On the characterization of grid density in grid refinement studies for

discretization error estimation. Int. J. Numer. Methods Fluids 72, 119–134. https://doi.org/https://doi.org/10.1002/fld.3737

Eca, L., Pereira, F.S., Vaz, G., 2018. Viscous flow simulations at high Reynolds numbers without wall functions: Is y+≃1 enough for the near-wall cells? Computers and Fluids 170, 157–175. https://doi.org/10.1016/j.compfluid.2018.04.035

Eca, L., Saraiva, G., Vaz, G., Abreu, H., 2015. The Pros and Cons of Wall Functions. OMAE2015, St.Johns, Newfoundland, Canada 0–11. https://doi.org/10.1115/OMAE2015-41518

El-Behery, S.M., Hamed, M.H., 2011. A comparative study of turbulence models performance for separating flow in a planar asymmetric diffuser. Computers and Fluids 44, 248–257. https://doi.org/10.1016/j.compfluid.2011.01.009

el Moctar, O., Lantermann, U., Mucha, P., Höpken, J., Schellin, T.E., 2015. RANS-Based Simulated Ship Maneuvering Accounting for Hull-Propulsor-Engine Interaction. Sh. Technol. Res. 61, 142–161. https://doi.org/10.1179/str.2014.61.3.003

Elsherbiny, K., Terziev, M., Tezdogan, T., Incecik, A., Kotb, M., 2020. Numerical and experimental study on hydrodynamic performance of ships advancing through different canals. Ocean Eng. 195. https://doi.org/10.1016/j.oceaneng.2019.106696

Elsherbiny, K., Terziev, M., Tezdogan, T., Incecik, A., Kotb, M., 2019a. Numerical and experimental study on hydrodynamic performance of ships advancing through different canals. Ocean Eng. 106696. https://doi.org/10.1016/j.oceaneng.2019.106696

Elsherbiny, K., Tezdogan, T., Kotb, M., Incecik, A., Day, A.H., 2019b. An experimental investigation of the trim effect on the behaviour of a containership in shallow water, in: Proceedings of the ASME 2019 38th International Conference on Ocean, Offshore and Arctic Engineering OMAE2019, Glasgow, UK.

Elsherbiny, K., Tezdogan, T., Kotb, M., Incecik, A., Day, S., 2019c. Experimental analysis of the squat of ships advancing through the New Suez Canal. Ocean Eng. 178, 331–344. https://doi.org/10.1016/j.oceaneng.2019.02.078

EMSA (European Maritime Safety Agency), 2019. Annual Overview of Marine Casualties and Incidents 2019.

EMSA (European Maritime Safety Agency), 2018. Annual Overview of Marine Casualties and Incidents 2018.

EMSA (European Maritime Safety Agency), 2017. Annual overview of marine casualties and incidents 2017.

EMSA (European Maritime Safety Agency), 2016. Annual overview of marine casualties and incidents 2016.

EMSA (European Maritime Safety Agency), 2015. Annual overview of marine casualties and incidents 2011-2015.

Ertekin, R.C., Webster, W.C., Wehausen, J. V., 1986. Waves caused by a moving disturbance in a shallow channel of finite width. J. Fluid Mech. 169, 275–292. https://doi.org/10.1017/S0022112086000630

European Commission, 2018. Inland waterways [WWW Document]. Mobil. Transp. URL https://ec.europa.eu/transport/modes/inland_en (accessed 5.17.19).

Farkas, A., Degiuli, N., Martić, I., 2018. Assessment of hydrodynamic characteristics of a full-scale ship at different draughts. Ocean Eng. 156, 135–152. https://doi.org/10.1016/j.oceaneng.2018.03.002

Farkas, A., Degiuli, N., Martić, I., 2017. Numerical investigation into the interaction of resistance components for a series 60 catamaran. Ocean Eng. 146, 151–169. https://doi.org/10.1016/j.oceaneng.2017.09.043

Ferguson, A.M., 1977. Factors affecting the components of ship resistance. PhD Thesis. University o Glasgow, Department of Naval Architecture. University of Glasgow.

Ferziger, J.H., Peric, M., 2002. Computational Methods for Fluid Dynamics, Springer. https://doi.org/10.1016/S0898-1221(03)90046-0

Fourdrinoy, J., Caplier, C., Devaux, Y., Rousseaux, G., et. al., 2019. The naval battle of actium and the myth of the ship-holder : the effect of bathymetry, in: 5th MASHCON, Ghent University, May 2019.

Fox, R., McDonald, A., Prichard, P., 2015. Introduction to fluid mechanics, 6th ed, Hoboken, NJ. Wiley.

Freitas, C.J., 2002. The issue of numerical uncertainty. Appl. Math. Model. 26, 237–248. https://doi.org/10.1016/S0307-904X(01)00058-0

Froude, W., 1874. Report to the lords commissioners of the admiralty on experiments for the determination of the frictional resistance of water on a surface, under various conditions, performed at Chelston cross, under

the authority of their lordships.

Fujino, M., 1976. Maneuverability in restricted waters, state of the art. National Science Foundation Report No. 184. Department of Naval Architecture and Marine Engineering, College of Engineering, University of Michigan, Ann Arbor, Michigan. Ann Arbor, Michigan.

Fukagata, K., Iwamoto, K., Kasagi, N., 2002. Contribution of Reynolds stress distribution to the skin friction in wall-bounded flows. Phys. Fluids 14, L73–L76. https://doi.org/10.1063/1.1516779

Fureby, C., Toxopeus, S.L., Johansson, M., Tormalm, M., Petterson, K., 2016. A computational study of the flow around the KVLCC2 model hull at straight ahead conditions and at drift. Ocean Eng. 118, 1–16. https://doi.org/10.1016/j.oceaneng.2016.03.029

Gadd, G.E., 1967. A new turbulent friction formulation based on a reappraisal of Hughes' results. Trans. RINA 109, 109–511.

Gaggero, S., Villa, D., Viviani, M., 2015. The Kriso container ship (KCS) test case: An open source overview. Comput. Methods Mar. Eng. VI, Mar. 2015 735–749.

García-Gómez, A., 2000. On the form factor scale effect. Ocean Eng. 27, 97–109. https://doi.org/10.1016/S0029-8018(98)00042-0

Golbraikh, E., Eidelman, A., Soloviev, A., 2013. On helical behavior of turbulence in the ship wake. J. Hydrodyn. 25, 83–90. https://doi.org/10.1016/S1001-6058(13)60341-8

Gomit, G., Rousseaux, G., Chatellier, L., Calluaud, D., David, L., 2014. Spectral analysis of ship waves in deep water from accurate measurements of the free surface elevation by optical methods. Phys. Fluids 26. https://doi.org/10.1063/1.4902415

Gorji, S., Seddighi, M., Ariyaratne, C., Vardy, A.E., O'Donoghue, T., Pokrajac, D., He, S., 2014. A comparative study of turbulence models in a transient channel flow. Computers and Fluids 89, 111–123. https://doi.org/10.1016/j.compfluid.2013.10.037

Gotman, A., 2007. A history of ship resistance evaluation. J. Ocean Technol. 2, 74–96.

Gotman, A., 2002. Study Of Michell's Integral And Influence Of Viscosity And Ship Hull Form On Wave Resistance. Ocean. Eng. Int. 6, 74–115.

Gourlay, T., 2014. Duisburg Test Case Containership Squat Prediction using

ShallowFlow Software, in: , PreSquat - Numerische Vorhersagen von Dynamischem Squat in Begrenzten Gewässern, Bericht F005/2014. pp. 1–6.

Gourlay, T., 2006. Flow beneath a ship at small underkeel clearance. J. Sh. Res. 50, 250–258.

Gourlay, T., 2003. Ship Squat In Water of Varying Depth. Int. J. Marit. Eng. 145, 12. https://doi.org/10.3940/rina.ijme.2003.a1.1031

Gourlay, T., 2001. The supercritical bore produced by a high-speed ship in a channel. J. Fluid Mech. 434, 399–409. https://doi.org/10.1017/S002211200100372X

Gourlay, T., Tuck, E.O., 2001. The maximum sinkage of a ship. J. Sh. Res. 45, 50–58.

Grigson, C.W.B., 1999. A planar friction algorithm and its use in analysing hull resistance. Trans. RINA.

Grue, J., 2017. Ship generated mini-tsunamis. J. Fluid Mech. 816, 142–166. https://doi.org/10.1017/jfm.2017.67

Guo, B.J., Deng, G.B., Steen, S., 2013. Verification and validation of numerical calculation of ship resistance and flow field of a large tanker. Ships Offshore Struct. 8, 3–14. https://doi.org/10.1080/17445302.2012.669263

Guo, C., Zhang, Q., Shen, Y., 2015. A non-geometrically similar model for predicting the wake field of full-scale ships. J. Mar. Sci. Appl. 14, 225–233. https://doi.org/10.1007/s11804-015-1316-8

Guo, J., 2002. Simple and explicit solution of wave dispersion equation. Coast. Eng. 45, 71–74. https://doi.org/10.1016/S0378-3839(02)00039-X

Haase, M., Davidson, G., Binns, J., Thomas, G., Bose, N., 2016a. Full-scale resistance prediction in finite waters: A study using computational fluid dynamics simulations, model test experiments and sea trial measurements. Proc. Inst. Mech. Eng. Part M J. Eng. Marit. Environ. 231, 316–328. https://doi.org/10.1177/1475090216642467

Haase, M., Zurcher, K., Davidson, G., Binns, J.R., Thomas, G., Bose, N., 2016b. Novel CFD-based full-scale resistance prediction for large medium-speed catamarans. Ocean Eng. 111, 198–208. https://doi.org/10.1016/j.oceaneng.2015.10.018

Hai-Long, S., Obwogi, E.O., Yu-Min, S., 2016. Scale effects for rudder bulb and rudder thrust fin on propulsive efficiency based on computational fluid

dynamics. Ocean Eng. 117, 199–209. https://doi.org/10.1016/j.oceaneng.2016.03.046

Havelock, T., 1908. The Propagation of Groups of Waves in Dispersive Media, with Aplication to Waves on Water produced by a Travelling Disturbance 422–451. https://doi.org/10.1098/rspa.1933.0074

Hawkes, J., Vaz, G., Phillips, A.B., Cox, S.J., Turnock, S.R., 2018. On the strong scalability of maritime CFD. J. Mar. Sci. Technol. 23, 81–93. https://doi.org/10.1007/s00773-017-0457-7

Hirt, C.. W., Nichols, B.. D., 1981. Volume of fluid (VOF) method for the dynamics of free boundaries. J. Comput. Phys. 39, 201–225. https://doi.org/10.1016/0021-9991(81)90145-5

Hochkirch, K., Mallol, B., 2000. On the Importance of Full-Scale CFD Simulations for Ships. Numeca 85–95.

Hoekstra, M., Eca, L., Windt, J., Raven, H.C., 2000. Viscous flow calculations for KVLCC2 and KCS models using the PARNASSOS code, in: Gotenburg 2000: A Workshop on Numerical Ship Hydrodynamics.

Hofmann, H., Lorke, A., Peeters, F., 2008. The relative importance of wind and ship waves in the littoral zone of a large lake. Linnol. Ocean. 53, 368–380. https://doi.org/10.1029/2010WR010012

Hou, Y. hang, Li, Y. jia, Liang, X., 2019. Mixed aleatory/epistemic uncertainty analysis and optimization for minimum EEDI hull form design. Ocean Eng. 172, 308–315. https://doi.org/10.1016/j.oceaneng.2018.12.003

Hughes, G., 1954. Friction and form resistance in turbulent flow and a proposed formulation for use in model and ship correlation. Trans. Inst. Nav. Arch. 96.

Hunt, J.N., 1979. Direct solution of wave dispersion equation. J. Waterw. Port, Coastal, Ocean Eng. 106, 457–459.

Hunt, J.N., 1964. The viscous damping of gravity waves in shallow water. La Houille Blanche 685–691. https://doi.org/10.1051/lhb/1964038

Hur, V.M., 2019. Shallow water models with constant vorticity. Eur. J. Mech. B/Fluids 73, 170–179. https://doi.org/10.1016/j.euromechflu.2017.06.001

Iaccarino, G., 2002. Predictions of a Turbulent Separated Flow Using Commercial CFD Codes. J. Fluids Eng. 123, 819. https://doi.org/10.1115/1.1400749

IMO, 2011. Annex 19: Resolution MEPC.203(62).

Inui, T., 1954. Wave-Making Resistance in Shallow Sea and in Restricted Water, with Special Reference to its Discontinuities. J. Zosen Kiokai 76, 1–10.

Inui, T., 1936a. On Deformation, Wave Patterns and Resoncance Phenomenon of Water Surface due to a Moving Disturbance. II. Proc. Physico-Mathematical Soc. Japan 18.

Inui, T., 1936b. On Deformation, Wave Patterns and Resoncance Phenomenon of Water Surface due to a Moving Disturbance. I. Proc. Physico-Mathematical Soc. Japan 18.

Irkal, M.A.R., Nallayarasu, S., Bhattacharyya, S.K., 2019. Numerical prediction of roll damping of ships with and without bilge keel. Ocean Eng. 179, 226–245. https://doi.org/10.1016/j.oceaneng.2019.03.027

Ishihara, T., Ogasawara, H., Hunt, J.C.R., 2015. Analysis of conditional statistics obtained near the turbulent/non-turbulent interface of turbulent boundary layers. J. Fluids Struct. 53, 50–57. https://doi.org/10.1016/j.jfluidstructs.2014.10.008

ITTC, 2017a. Recommended Procedures 1978 ITTC Performance Prediction Method, 4th revision, 7.5 – 02 03 – 01.4. 28th Int Towing Tank Conf.

ITTC, 2017b. ITTC-Recommended Procedures and Guidelines Uncertainty Analysis, Instrument Cali-bration ITTC Quality System Manual Recommended Procedures and Guidelines Procedure.

ITTC, 2014. ITTC – Recommended Procedures and Guidelines - Practical guidelines for ship CFD applications. 7.5-03-02-03 (Revision 01). ITTC – Recomm. Proced. Guidel. 19.

ITTC, 2011. Recommended Procedures and Guidelines: Practical Guidelines for Ship CFD. 26th Int. Towing Tank Conf.

ITTC, 2008. Uncertainty Analysis in CFD Verification and Validation Methodology and Procedures. 25th ITTC 2008, Resist. Comm. 12.

ITTC, 2002. ITTC – Recommended Procedures and Guidelines Uncertainty Analysis , Example for Resistance Test.

ITTC, 1999. 1978 ITTC Performance Prediction Method 7.5 - 02 - 03 - 01.4.

Jachowski, J., 2008. Assessment of ship squat in shallow water using CFD. Arch. Civ. Mech. Eng. 8, 27–36. https://doi.org/10.1016/S1644-9665(12)60264-7

Jagadeesh, P., Murali, K., 2010. Rans Predictions of Free Surface Effects on

Axisymmetric Underwater Body. Eng. Appl. Comutational Fluid Mech. 4, 301–313. https://doi.org/10.1080/19942060.2010.11015318

Janson, C.-E., Spinney, D., 2004. A Comparison of Four Wave Cut Analysis Methods for Wave Resistance Prediction. Sh. Technol. Res. 51, 173–184. https://doi.org/10.1179/str.2004.51.4.004

Jasak, H., 1996. Error analysis and estimation for finite volume method with applications to fluid flow. PhD Thesis. Imperial College of Science, Technology and Medicine.

Jasak, H., Vukčević, V., Gatin, I., Lalović, I., 2018. CFD validation and grid sensitivity studies of full scale ship self propulsion. Int. J. Nav. Archit. Ocean Eng. https://doi.org/10.1016/j.ijnaoe.2017.12.004

Jiang, T., 2001. A New Method For Resistance and Propulsion Prediction of Ship Performance in Shallow Water, in: Proceedings of the Eighth International Symposium on Practical Design of Ships and Other Floating Structures 16 – 21 September 2001 Shanghai, Chaina. pp. 509–515.

Jiang, T., Henn, R., Sharma, S.D., 2002. Wash waves generated by ships moving on fairways of varying topography. 24th Symp. Nav. Hydrodyn. 2, 8–13.

Johnson, D.A., King, L.S., 1984. A mathematically simple turbulence closure model for attached and separated turbulent boundary layers. AIAA J. 23, 1684–1692. https://doi.org/10.2514/3.9152

Johnson, J.W., 1957. Ship Waves in Navigation Channels. Coast. Eng. Proc. 1, 40. https://doi.org/10.9753/icce.v6.40

Jones, D.A., Clarke, D.B., 2010. Fluent Code Simulation of Flow around a Naval Hull: the DTMB 5415. Def. Sci. Technol. Organ. Victoria (Australia), Marit. platforms Div.

Jones, W.P., Launder, B.E., 1972. The Prediction of Laminarization with a Two-Equation Model of Turbulence. Int. J. Heat Mass Transf. 15, 301–314. https://doi.org/10.1016/0017-9310(72)90076-2

Jongen, T., 1998. Simulation and Modeling of Turbulent Incompressible Flows.

Kaidi, S., Smaoui, H., Sergent, P., 2017. Numerical estimation of bank-propeller-hull interaction effect on ship manoeuvring using CFD method. J. Hydrodyn. 29, 154–167. https://doi.org/10.1016/S1001-6058(16)60727-8

Katsis, C., Akylas, T.R., 1987. On the excitation of long nonlinear water waves by a moving pressure distribution. part 2. three dimensional effects. J.

Fluid Mech. 177, 49–65. https://doi.org/10.1017/S0022112087000855

Katsis, C., Akylas, T.R., 1984. On the excitation of long nonlinear water waves by a moving pressure distribution. J. Fluid Mech. 177, 49–65. https://doi.org/10.1017/S0022112087000855

Katsui, T., Asai, H., Himeno, Y., Tahara, Y., 2005. The proposal of a new friction line, in: Fifth Osaka Colloquium on Advanced CFD Applications to Ship Flow and Hull Form Design, Osaka, Japan.

Kellett, P., Turan, O., Incecik, A., 2013. A study of numerical ship underwater noise prediction. Ocean Eng. 66, 113–120. https://doi.org/10.1016/j.oceaneng.2013.04.006

Keulegan, G.H., 1948. Gradual damping of solitary waves. J. Res. Natl. Bur. Stand. (1934). 40, 487. https://doi.org/10.6028/jres.040.041

Kianejad, S.S., Enshaei, H., Duffy, J., Ansarifard, N., 2019. Prediction of a ship roll added mass moment of inertia using numerical simulation. Ocean Eng. 173, 77–89. https://doi.org/10.1016/j.oceaneng.2018.12.049

Kim, M., Hizir, O., Turan, O., Day, S., Incecik, A., Day, A.H., 2017a. Estimation of added resistance and ship speed loss in a seaway. Ocean Eng. 141, 1–12. https://doi.org/10.1016/j.oceaneng.2017.06.051

Kim, M., Hizir, O., Turan, O., Incecik, A., 2017b. Numerical studies on added resistance and motions of KVLCC2 in head seas for various ship speeds. Ocean Eng. 140, 466–476. https://doi.org/10.1016/j.oceaneng.2017.06.019

Kim, W.J., Van, S.H., Kim, D.H., 2001. Measurement of flows around modern commercial ship models. Exp. Fluids 31, 567–578. https://doi.org/10.1007/s003480100332

Kim, Y.C., Kim, K.S., Kim, J., Kim, Y., Park, I.R., Jang, Y.H., 2017. Analysis of added resistance and seakeeping responses in head sea conditions for low-speed full ships using URANS approach. Int. J. Nav. Archit. Ocean Eng. 9, 641–654. https://doi.org/10.1016/j.ijnaoe.2017.03.001

Kinaci, O.K., Gokce, M.K., 2015. A computational hydrodynamic analysis of duisburg test case with free surface and propeller. Brodogradnja 66, 23–38.

Kinaci, O.K., Sukas, O.F., Bal, S., 2016. Prediction of wave resistance by a Reynolds-averaged Navier-Stokes equation-based computational fluid dynamics approach. Proc. Inst. Mech. Eng. Part M J. Eng. Marit. Environ. 230, 531–548. https://doi.org/10.1177/1475090215599180

Kiš, P., Herwig, H., 2012. The near wall physics and wall functions for turbulent natural convection. Int. J. Heat Mass Transf. 55, 2625–2635. https://doi.org/10.1016/j.ijheatmasstransfer.2011.12.031

Kok, Z., Duffy, J., Chai, S., Jin, Y., Javanmardi, M., 2020. Numerical investigation of scale effect in self-propelled container ship squat. Appl. Ocean Res. 99. https://doi.org/10.1016/j.apor.2020.102143

Kok, Z., Jin, Y., Chai, S., Denehy, S., Duffy, J., 2018. URANS prediction of berthed ship–passing ship interactions. Ships Offshore Struct. 13, 561–574. https://doi.org/10.1080/17445302.2018.1429136

Kolmogorov, A.N., 1942. Equations of turbulent motion of an incompressible fluid. Izv. Acad. Sci. USSR Phys 6, 56–58.

Kolmogorov, A.N., 1941. The local structure of turbulence in incompressible viscous fluid for very large Reynolds numbers. Cr Acad. Sci. URSS 30, 301–305.

Kooij, G.L., Botchev, M.A., Frederix, E.M.A., Geurts, B.J., Horn, S., Lohse, D., van der Poel, E.P., Shishkina, O., Stevens, R.J.A.M., Verzicco, R., 2018. Comparison of computational codes for direct numerical simulations of turbulent Rayleigh–Bénard convection. Computers and Fluids 166, 1–8. https://doi.org/10.1016/j.compfluid.2018.01.010

Korkmaz, K.B., Werner, S., Bensow, R.E., 2019. Numerical friction lines for CFD based form factor determination, in: VIII International Conference on Computational Methods in Marine Engineering MARINE 2019.

Kornev, N., Abbas, N., 2018. Vorticity structures and turbulence in the wake of full block ships. J. Mar. Sci. Technol. 23, 567–579. https://doi.org/10.1007/s00773-017-0493-3

Kornev, N., Shevchuk, I., Abbas, N., Anschau, P., Samarbakhsh, S., 2019. Potential and limitations of scale resolved simulations for ship hydrodynamics applications. Sh. Technol. Res. 7255. https://doi.org/10.1080/09377255.2019.1574965

Kouh, J.S., Chen, Y.J., Chau, S.W., 2009. Numerical study on scale effect of form factor. Ocean Eng. 36, 403–413. https://doi.org/10.1016/j.oceaneng.2009.01.011

Kundu, P., Cohen, I.M., Dowling, D.R., 2012. Fluid Mechanics. Elsevier.

Lam, W.H., Hamill, G.A., Robinson, D.J., 2013. Initial wash profiles from a ship propeller using CFD method. Ocean Eng. 72, 257–266. https://doi.org/10.1016/j.oceaneng.2013.07.010

Lamb, H., 1932. Hydrodynamics. Cambridge Univ. Press 6th revise, 262–264. https://doi.org/10.1017/CBO9781107415324.004

Landweber, L., Patel, V.C., 1979. Ship Boundary Layers. Annu. Rev. Fluid Mech. 11, 173–205. https://doi.org/10.1146/annurev.fl.11.010179.001133

Langtry, R.B., 2006. A Correlation-Based Transition Model using Local Variables for Unstructured Parallelized CFD codes. Univ. Stuttgart. https://doi.org/10.1115/1.2184352

Larsson, L., Stern, F., Visonneau, M., 2014. Numerical Ship Hydrodynamics: An assessment of the Gothenburg 2010 Workshop. Springer. https://doi.org/10.1007/978-94-007-7189-5

Launder, B.E., Sharma, B.I., 1974. Application of the energy-dissipation model of turbulence to the calculation of flow near a spinning disc. Lett. Heat Mass Transf. 1, 131–137. https://doi.org/10.1016/0094-4548(74)90150-7

Laurence, D., Uribe, J.C., Utyuzhnikov, S.V., 2004. A robust formulation of the v2-f model and its applications. Int. J. Numer. Methods Fluids 00, 1–6.

Lax, P.D., Richtmyer, R.D., 1956. Survey of the stability of linear finite difference equations. Commun. Pure Appl. Math. 9, 267–293. https://doi.org/10.1002/cpa.3160090206

Lazauskas, L. V, 2009. Resistance, Wave-Making and Wave-Decay of Thin Ships, with Emphasis on the Effects of Viscosity.

Lea, G.K., Feldman, J.P., 1972. Transcritical flow past slender ships, in: 9th Symposium on Naval Hydrodynamics. Washington DC, pp. 1527–1542.

Lee, B.W., Lee, C., 2019. Equation for ship wave crests in the entire range of water depths. Coast. Eng. 153, 103542. https://doi.org/10.1016/j.coastaleng.2019.103542

Lee, S.J., Kim, H.R., Kim, W.J., Van, S.H., 2003. Wind tunnel tests on flow characteristics of the KRISO 3,600 TEU containership and 300K VLCC double-deck ship models. J. Sh. Res. 47, 24–38.

Lee, Y.G., Ha, Y.J., Lee, S.H., Kim, S.H., 2018. A study on the estimation method of the form factor for a full-scale ship. Brodogradnja 69, 71–87. https://doi.org/10.21278/brod69105

Lesieur, M., 2008. Turbulence in fluids, 4th ed, Physics of Fluids. Springer. https://doi.org/10.1063/1.1711203

Li, T., 2003. Computation of turbulent free-surface flows around modern ships. Int. J. Numer. Methods Fluids 43, 407–430.

https://doi.org/10.1002/fld.580

Liang, H., Chen, X., 2019. Viscous effects on the fundamental solution to ship waves. J. Fluid Mech. 879, 744–774. https://doi.org/10.1017/jfm.2019.698

Liefvendahl, M., Fureby, C., 2017. Grid requirements for LES of ship hydrodynamics in model and full scale. Ocean Eng. 143, 259–268. https://doi.org/10.1016/j.oceaneng.2017.07.055

Lien, F.S., Kalitzin, G., Durbin, P.A., 1998. RANS modeling for compressible and transitional flows. Cent. Turbul. Res. Summer Progr. 1998 1–20.

Lighthill, M.J., 1990. Waves in Fluids.

Lilek, Ž., Peric, M., 1995. A fourth-order finite volume method with colocated variable arrangement. Computers and Fluids 24, 239–252. https://doi.org/10.1016/0045-7930(94)00030-3

Linde, F., Ouahsine, A., Huybrechts, N., Sergent, P., 2016. Three-Dimensional Numerical Simulation of Ship Resistance in Restricted Waterways: Effect of Ship Sinkage and Channel Restriction. J. Waterw. Port, Coastal, Ocean Eng. 143, 06016003. https://doi.org/10.1061/(asce)ww.1943-5460.0000353

Liu, H.W., Lin, P.Z., 2005. Discussion of "Wave transformation by two-dimensional bathymetric anomalies with sloped transitions" [Coast. Eng. 50 (2003) 61-84]. Coast. Eng. 52, 197–200. https://doi.org/10.1016/j.coastaleng.2004.11.002

Liu, W., Demirel, Y.K., Djatmiko, E.B., Nugroho, S., Tezdogan, T., Kurt, R.E., Supomo, H., Baihaqi, I., Yuan, Z.M., Incecik, A., 2018. Bilge Keel Design for the Traditional Fishing Boats of Indonesia's East Java. Int. J. Nav. Archit. ure Ocean Eng.

Liu, Y., Zou, L., Zou, Z.J., 2017. Computational fluid dynamics prediction of hydrodynamic forces on a manoeuvring ship including effects of dynamic sinkage and trim. Proc. Inst. Mech. Eng. Part M J. Eng. Marit. Environ. https://doi.org/10.1177/1475090217734685

Longo, J., Huang, H.P., Stern, F., 1998. Solid/free-surface juncture boundary layer and wake. Exp. Fluids 25, 283–297. https://doi.org/10.1007/s003480050232

Longo, J., Stern, F., 2002. Effects of drift angle on model ship flow. Exp. Fluids 32, 558–569. https://doi.org/10.1007/s00348-001-0397-0

Lopes, R., Eca, L., Vaz, G., 2019. On the Numerical Behavior of Rans-based Transition Models. J. Fluids Eng. 142, 1–14.

https://doi.org/10.1115/1.4045576

Lopes, R., Eca, L., Vaz, G., 2017. On the Decay of Free-stream Turbulence Predicted by Two-equation Eddy-viscosity Models. NuTTS-2017, Wageningen, the Netherlands 1–6.

Ma, C., Zhu, Y., He, J., Zhang, C., Wan, D.C., Yang, C., Noblesse, F., 2018. Nonlinear corrections of linear potential-flow theory of ship waves. Eur. J. Mech. B/Fluids 67, 1–14. https://doi.org/10.1016/j.euromechflu.2017.07.006

Ma, S.J., Zhou, M.G., Zou, Z.J., 2013. Hydrodynamic interaction among hull, rudder and bank for a ship sailing along a bank in restricted waters. J. Hydrodyn. 25, 809–817. https://doi.org/10.1016/S1001-6058(13)60428-X

Maasch, M., Mizzi, K., Atlar, M., Fitzsimmons, P., Turan, O., 2019. A generic wake analysis tool and its application to the Japan Bulk Carrier test case. Ocean Eng. 171, 575–589. https://doi.org/10.1016/j.oceaneng.2018.12.030

Magionesi, F., Di Mascio, A., 2016. Investigation and modelling of the turbulent wall pressure fluctuations on the bulbous bow of a ship. J. Fluids Struct. 67, 219–240. https://doi.org/10.1016/j.jfluidstructs.2016.09.008

Majidian, H., Azarsina, F., 2019. Numerical simulation of container ship in oblique winds to develop a wind resistance model based on statistical data. J. Int. Marit. Safety, Environ. Aff. Shipp. 2, 67–88. https://doi.org/10.1080/25725084.2018.1564471

Maki, K.J., Broglia, R., Doctors, L.J., Di Mascio, A., 2013. Numerical investigation of the components of calm-water resistance of a surface-effect ship. Ocean Eng. 72, 375–385. https://doi.org/10.1016/j.oceaneng.2013.07.022

Manceau, R., 2015. Recent progress in the development of the Elliptic Blending Reynolds-stress model. Int. J. Heat Fluid Flow 51, 195–220. https://doi.org/10.1016/j.ijheatfluidflow.2014.09.002

Manceau, R., Hanjalić, K., 2002. Elliptic blending model: A new near-wall Reynolds-stress turbulence closure. Phys. Fluids 14, 744–754. https://doi.org/10.1063/1.1432693

Manceau, R., Wang, M., Laurence, D., 2001. Inhomogeneity and anisotrophy effects on the redistribution term in Reynolds-averaged Navier-Stoke modelling. J. Fluid Mech. 438, 307–338. https://doi.org/10.1017/S0022112001004451

Mancini, S., Begovic, E., Day, A.H., Incecik, A., 2018. Verification and validation of numerical modelling of DTMB 5415 roll decay. Ocean Eng. 162, 209–223. https://doi.org/10.1016/j.oceaneng.2018.05.031

Markatos, N.C., 1986. The mathematical modelling of turbulent flows. Appl. Math. Model. 10, 190–220. https://doi.org/https://doi.org/10.1016/0307-904X(86)90045-4

Marquardt, M.W., 2009. Effects of waves and the free surface on a surface-piercing flat-plate turbulent boundary layer and wake. University of Iowa.

Marshall, J.S., Naghdi, P.M., 1990. Wave reflection and transmission by steps and rectangular obstacles in channels of finite depth. Theor. Comput. Fluid Dyn. 1, 287–301. https://doi.org/10.1007/BF00271583

Mathew, J., Akylas, T.R., 1990. On three-dimensional long water waves in a channel with sloping sidewalls. J. Fluid Mech. 215, 289–307. https://doi.org/10.1017/S0022112090002658

Menter, F.R., 1994. Two-equation eddy-viscosity turbulence models for engineering applications. AIAA J. 32, 1598–1605. https://doi.org/10.2514/3.12149

Menter, F.R., Smirnov, P.E., Liu, T., Avancha, R., 2015. A One-Equation Local Correlation-Based Transition Model. Flow, Turbul. Combust. 95, 583–619. https://doi.org/10.1007/s10494-015-9622-4

Michell, J.H., 1898. The wave-resistance of a ship. London, Edinburgh, Dublin Philos. Mag. J. Sci. 45, 106–123.

Mihic, S., Golusin, M., Mihajlovic, M., 2011. Policy and promotion of sustainable inland waterway transport in Europe - Danube River. Renew. Sustain. Energy Rev. 15, 1801–1809. https://doi.org/10.1016/j.rser.2010.11.033

Miles, J.W., 1986. Stationary, transcritical channel flow. J. Fluid Mech. 162, 489–499. https://doi.org/10.1017/S0022112086002136

Millward, A., 1996. A review of the prediction of squat in shallow water. J. Navig. 77–88. https://doi.org/10.1017/S0373463300013126

Milne-Thomson, L.M., 1962. Theoretical hydrodynamics, MacMillan & Co LTD.

Min, K.-S., Kang, S.-H., 2010. Study on the form factor and full-scale ship resistance. J. Mar. Sci. Technol. 15, 108–118.

https://doi.org/10.1007/s00773-009-0077-y

Molland, A.F., Turnock, S.R., Hudson, D.A., 2017. Model-Ship Extrapolation, in: Ship Resistance and Propulsion: Practical Estimation of Ship Propulsive Power. Cambridge University Press, Cambridge, pp. 70–85. https://doi.org/10.1017/9781316494196.006

Moore, G.E., 1965. Cramming more components onto integrated circuits, in: Proceedings Of The IEEE. pp. 82–85. https://doi.org/10.1109/N-SSC.2006.4785860

Morton, K.W., Mayers, D.F., 2005. Numerical Solution of Partial Differential Equations: An Introduction. Cambridge University Press, Cambridge. https://doi.org/10.1017/CBO9780511812248

Mucha, P., 2017. On Simulation-based Ship Maneuvering Prediction in Deep and Shallow Water.

Mucha, P., Deng, G., Gourlay, T., Moctar, O. el, 2016. Validation studies on numerical prediction of ship squat and resistance in shallow water. Proc. 4th MASHCON 83–92. https://doi.org/10.18451/978-3-939230-38-0

Mucha, P., el Moctar, B., 2014. Numerical Prediction of Resistance and Squat for a Containership in Shallow Water.

Mucha, P., El Moctar, O., Böttner, C.U., 2014. Technical note: PreSquat - Workshop on numerical prediction of ship Squat in restricted waters. Sh. Technol. Res. 61, 162–165. https://doi.org/10.1179/str.2014.61.3.004

Müller, C., Herbst, F., 2014. Modelling of crossflow-induced transition based on local variables, in: 6th European Conference on Computational Fluid Dynamics (ECFD). Barcelona, Spain, pp. 20–25.

Muzaferija, S., Peric, M., 1999. Computation of free-surface ows using interface- tracking and interface-capturing methods, in: Chap. 2 in O. Mahrenholtz and M. Markiewicz (Eds.), Nonlinear Water Wave Interaction, Computational Mechanics Publications, WIT Press, Southampton.

Muzaferija, S., Peric, M., 1997. Computation of free-surface flows using the finite-volume method and moving grids. Numer. Heat Transf. Part B Fundam. 32, 369–384. https://doi.org/10.1080/10407799708915014

Nakos, D.E., Sclavounos, P.D., 1990. On steady and unsteady ship wave patterns. J. Fluid Mech. 215, 263–288. https://doi.org/10.1017/S0022112090002646

Newman, J.N., 1992. Panel methods in marine hydrodynamics. 11th Australas. Fluid Mech. Conf.

Newman, J.N., 1990. Numerical solutions of the water-wave dispersion relation. Appl. Ocean Res. 12, 14–18. https://doi.org/10.1016/S0141-1187(05)80013-6

Newman, J.N., 1970. Recent research on ship waves, in: Proceedings of the 8th Symposium on Naval Hydrodynamics, August 24-28. Rome, Italy, pp. 519–545.

Newman, J.N., 1965. Propagation of water waves over an infinite step. J. Fluid Mech. 23, 399–415. https://doi.org/10.1017/S0022112065001453

Niklas, K., Pruszko, H., 2019a. Full-scale CFD simulations for the determination of ship resistance as a rational, alternative method to towing tank experiments. Ocean Eng. 190, 106435. https://doi.org/10.1016/j.oceaneng.2019.106435

Niklas, K., Pruszko, H., 2019b. Full scale CFD seakeeping simulations for case study ship redesigned from V-shaped bulbous bow to X-bow hull form. Appl. Ocean Res. 89, 188–201. https://doi.org/10.1016/j.apor.2019.05.011

Noblesse, F., He, J., Zhu, Y., Hong, L., Zhang, C., Zhu, R., 2014. Why can ship wakes appear narrower than Kelvin's angle ? Eur. J. Mech. B/Fluids 46, 164–171. https://doi.org/10.1016/j.euromechflu.2014.03.012

Nwogu, O., 1993. Alternative form of Boussinesq equations for nearshore wave propagation. J. Waterw. Port, Coast. Ocean Eng. 119, 618–638. https://doi.org/10.1061/(ASCE)0733-950X(1993)119:6(618)

Oberkampf, W.L., Blottner, F.G., 1998. Issues in computational fluid dynamics code verification and validation. AIAA J. 36, 687–695. https://doi.org/10.2514/2.456

Oggiano, L., Pierella, F., Nygaard, T.A., De Vaal, J., Arens, E., 2017. Reproduction of steep long crested irregular waves with CFD using the VOF method, in: Energy Procedia. https://doi.org/10.1016/j.egypro.2017.10.351

Oh, K.J., Kang, S.H., 1992. Full scale Reynolds number effects for the viscous flow around the ship stern. Comput. Mech. 9, 85–94. https://doi.org/10.1007/BF00370064

Ohashi, K., Kobayashi, H., Hino, T., 2018. Numerical simulation of the free-running of a ship using the propeller model and dynamic overset grid method. Sh. Technol. Res. 65, 153–162.

https://doi.org/10.1080/09377255.2018.1482610

Ozdemir, Y.H., Barlas, B., 2017. Numerical study of ship motions and added resistance in regular incident waves of KVLCC2 model. Int. J. Nav. Archit. Ocean Eng. 9, 149–159. https://doi.org/10.1016/j.ijnaoe.2016.09.001

Ozdemir, Y.H., Cosgun, T., Dogrul, A., Barlas, B., 2016. A numerical application to predict the resistance and wave pattern of KRISO containership. Brodogradnja 67, 47–65.

Pacuraru, F., Domnisoru, L., 2017. Numerical investigation of shallow water effect on a barge ship resistance. IOP Conf. Ser. Mater. Sci. Eng. 227. https://doi.org/10.1088/1757-899X/227/1/012088

Parneix, S., Durbin, P.A., Behnia, M., 1998. Computation of 3-D turbulent boundary layers using the V2F model. Flow, Turbul. Combust. 60, 19–46. https://doi.org/10.1023/A:1009986925097

Patel, V.C., Rodi, W., Scheuerer, G., 1984. Turbulence models for near-wall and low Reynolds number flows - A review. AIAA J. 23, 1308–1319. https://doi.org/10.2514/3.9086

Patel, V.C., Sarda, O.P., 1990. Mean-flow and turbulence measurements in the boundary layer and and wake of a ship double model. Exp. Fluids 8, 319–335. https://doi.org/https://doi.org/10.1007/BF00217197

Peltier, L.J., Hambric, S.A., 2007. Estimating turbulent-boundary-layer wall-pressure spectra from CFD RANS solutions. J. Fluids Struct. 23, 920–937. https://doi.org/10.1016/j.jfluidstructs.2007.01.003

Pena, B., Muk-Pavic, E., Ponkratov, D., 2019. Achieving a high accuracy numerical simulations of the flow around a full scale ship, in: Proceedings of the International Conference on Offshore Mechanics and Arctic Engineering - OMAE. pp. 1–10. https://doi.org/10.1115/OMAE2019-95769

Peregrine, D.H., 1967. Long waves on a beach. J. Fluid Mech. 27, 815–827. https://doi.org/10.1017/S0022112067002605

Pereira, F.S., Eca, L., Vaz, G., 2017. Verification and Validation exercises for the flow around the KVLCC2 tanker at model and full-scale Reynolds numbers. Ocean Eng. 129, 133–148. https://doi.org/10.1016/j.oceaneng.2016.11.005

Peric, M., 2019. White paper: Full-scale simulation for marine design. Siemens White Pap.

Perić, R., Abdel-Maksoud, M., 2016. Reliable damping of free-surface waves in

numerical simulations. Sh. Technol. Res. 63, 1–13. https://doi.org/10.1080/09377255.2015.1119921

Pethiyagoda, R., McCue, S.W., Moroney, T.J., 2017. Spectrograms of ship wakes: Identifying linear and nonlinear wave signals. J. Fluid Mech. 811, 189–209. https://doi.org/10.1017/jfm.2016.753

Pethiyagoda, R., McCue, S.W., Moroney, T.J., 2014. What is the apparent angle of a Kelvin ship wave pattern? J. Fluid Mech. 758, 468–485. https://doi.org/10.1017/jfm.2014.530

Pethiyagoda, R., Moroney, T.J., Macfarlane, G.J., Binns, J.R., McCue, S.W., 2018. Time-frequency analysis of ship wave patterns in shallow water: modelling and experiments. Ocean Eng. 158, 123–131. https://doi.org/10.1016/j.oceaneng.2018.01.108

Pettersson Reif, B.A., 2006. Towards a nonlinear eddy-viscosity model based on elliptic relaxation. Flow, Turbul. Combust. 76, 241–256. https://doi.org/10.1007/s10494-006-9013-y

Pettersson Reif, B.A., Mortensen, M., Langer, C.A., 2009. Towards sensitizing the nonlinear v 2-f model to turbulence structures. Flow, Turbul. Combust. 83, 185–203. https://doi.org/10.1007/s10494-008-9194-7

Phillips, O.M., 1955. The irrotational motion outside a free turbulent boundary. Math. Proc. Cambridge Philos. Soc. 51, 220–229. https://doi.org/10.1017/S0305004100030073

Phillips, T., 2014. Residual-based Discretization Error Estimation for Computational Fluid Dynamics 148.

Phillips, T., 2012. Extrapolation-based Discretization Error and Uncertainty Estimation in Computational Fluid Dynamics.

Phillips, T., Roy, C.J., 2017. A New Extrapolation-Based Uncertainty Estimator for Computational Fluid Dynamics. J. Verif. Valid. Uncertain. Quantif. 1, 041006. https://doi.org/10.1115/1.4035666

Phillips, T., Roy, C.J., 2012. Evaluation of Extrapolation-Based Discretization Error and Uncertainty Estimators, AIAA 2011-215. 49th AIAA Aerosp. Sci. Meet. Incl. New Horizons Forum Aerosp. Expo. Orlando, F, 1–18. https://doi.org/10.2514/6.2011-215

Piomelli, U., Balaras, E., 2002. Wall Layer Models for Large Eddy Simulations. Annu. Rev. Fluid Mech. 34, 349–374. https://doi.org/10.1146/annurev.fluid.34.082901.144919

Plotkin, A., 1977. Slender-ship shallow-water flow past a slowly varying bottom. J. Eng. Math. 11, 289–297. https://doi.org/10.1007/BF01537089

Plotkin, A., 1976. The flow due to a slender ship moving over a wavy wall in shallow water. J. Eng. Math. 10, 207–218. https://doi.org/10.1007/BF01535383

Ponkratov, D., 2016. Lloyd's Register workshop on ship scale hydrodynamics, in: Ponkratov, D. (Ed.), 2016 Workshop on Ship Scale Hydrodynamic Computer Simulation. p. 2016. https://doi.org/10.1002/ejoc.201200111

Posa, A., Broglia, R., Felli, M., Falchi, M., Balaras, E., 2019. Characterization of the wake of a submarine propeller via Large-Eddy simulation. Computers and Fluids 184, 138–152. https://doi.org/10.1016/j.compfluid.2019.03.011

Prakash, S.M.N., Chandra, B., 2013. Numerical Estimation of Shallow Water Resistance of a River-Sea Ship using CFD. Int. J. Comput. Appl. 71, 33–40. https://doi.org/https://doi.org/10.5120/12357-8670

Prandtl, L., 1925. Report on the investigation of developed turbulence, Translation of " Bericht über Untersuchungen zur ausgebildeten Turbulenz." Zeitschrift für angewandte Mathematik und Mechanik, vol. 5, no. 2, April 1925.

Quérard, A., Temarel, P., Turnock, S.R., 2008. Influence of viscous effects on the hydrodynamics of ships-like sections undergoing symmetric and anti-symmetric motions, using RANS, in: Proceedings of the ASME 27th International Confer Ence on Offshore Mechanics and Arctic Engineering OMAE2008, Estoril, Portugal. pp. 1–10. https://doi.org/10.1115/OMAE2008-57330

Queutey, P., Visonneau, M., 2015. Free-Surface Capturing RANSE Simulations for a Ship at Steady Drift. Sh. Technol. Res. 51, 106–122. https://doi.org/10.1179/str.2004.51.3.003

Rabaud, M., Moisy, F., 2013. Ship wakes: Kelvin or mach angle? Phys. Rev. Lett. 110, 1–5. https://doi.org/10.1103/PhysRevLett.110.214503

Raven, H.C., 2019. Shallow-water effects in ship model testing and at full scale. Ocean Eng. 189, 106343. https://doi.org/10.1016/j.oceaneng.2019.106343

Raven, H.C., van der Ploeg, A., Starke, A.R., Eca, L., 2008. Towards a CFD-based prediction of ship performance—progress in predicting full-scale resistance and scale effects. Int. J. Marit. Eng. 150.

Razgallah, I., Kaidi, S., Smaoui, H., Sergent, P., 2018. The impact of free surface modelling on hydrodynamic forces for ship navigating in inland

waterways: water depth, drift angle, and ship speed effect. J. Mar. Sci. Technol. 1–22. https://doi.org/10.1007/s00773-018-0566-y

Revell, A.J., Benhamadouche, S., Craft, T., Laurence, D., Yaqobi, K., 2005. A Stress-Strain Lag Eddy Viscosity Model for Unsteady Mean Flow. Eng. Turbul. Model. Exp. 6 27, 117–126. https://doi.org/10.1016/B978-008044544-1/50010-8

Richardson, L.F., 1927. Deferred approach to the limit. Trans. R. Soc. London, Ser. A 226, 299–361.

Richardson, L.F., 1922. Weather prediction by numerical process, 1st ed. Cambridge University Press.

Richardson, L.F., 1911. The Approximate Arithmetical Solution by Finite Differences of Physical Problems involving Differential Equations, with an Application to the Stresses in a Masonry Dam. Philos. Trans. th R. Soc. London,Containing Pap. a Math. Phys. Character 210, 307–357.

Roache, P.J., 2016. Verification and Validation in Fluids Engineering: Some Current Issues. J. Fluids Eng. 138, 101205. https://doi.org/10.1115/1.4033979

Roache, P. J., 1998. Validation and Verification in computational science and engineering. Hermosa Albuquerque, NM.

Roache, Patrick J., 1998. Verification of codes and calculations. AIAA J. 36, 696–702. https://doi.org/10.2514/2.457

Roache, P.J., 1997. Quantification of Uncertainty in Computational Fluid Dynamics. Annu. Rev. Fluid Mech. 29, 123–160. https://doi.org/10.1146/annurev.fluid.29.1.123

Roache, P.J., Ghia, K.N., White, F., 1986. Editorial Policy Statement on the Control of Numerical Accuracy. J. Fluids Eng. 108, 2.

Roache, P.J., Knupp, P.M., 1993. Completed richardson extrapolation. Commun. Numer. Methods Eng. 9.

Robertson, E., Choudhury, V., Bhushan, S., Walters, D.K., 2015. Validation of OpenFOAM numerical methods and turbulence models for incompressible bluff body flows. Computers and Fluids 123, 122–145. https://doi.org/10.1016/j.compfluid.2015.09.010

Rotta, J., 1951. Statistical Theory of Inhomogeneous Turbulence. NASA Tech. Doc.

Rotteveel, E., Hekkenberg, R.G., 2015. The Influence of Shallow Water and

Hull Form Variations on Inland Ship Resistance 2, 220–236.

Roy, C.J., 2008. Grid Convergence Error Analysis for Mixed-Order Numerical Schemes. AIAA J. 41, 595–604. https://doi.org/10.2514/2.2013

Roy, C.J., 2005. Review of code and solution verification procedures for computational simulation. J. Comput. Phys. 205, 131–156. https://doi.org/10.1016/j.jcp.2004.10.036

Roy, C.J., Blottner, F.G., 2006. Review and Assessment of Turbulence Models for Hypersonic Flows: 2D/Asymmetric Cases. 44th AIAA Aerosp. Sci. Meet. Exhib. https://doi.org/10.2514/6.2006-713

Roy, C.J., Blottner, F.G., 2001. Assessment of One- and Two-Equation Turbulence Models for Hypersonic Transitional Flows. J. Spacecr. Rockets 38, 699–710. https://doi.org/10.2514/2.3755

Rozman, S., 2009. Wake pattern of a boat. (Doctoral Diss. Ljubljana, Slov. Univ. Ljubliana).

Saaty, L.T., Bram, J., 1964. Nonlinear mathematics, Vol 12. ed. McGraw-Hill.

Saffman, P.G., 1970. A Model for Inhomogeneous Turbulent Flow. Proc. R. Soc. A Math. Phys. Eng. Sci. 317, 417–433. https://doi.org/10.1098/rspa.1970.0125

Saffman, P.G., Wilcox, D.C., 1974. Turbulence-Model Predictions for Turbulent Boundary Layers. AIAA J. 12, 541–546. https://doi.org/10.2514/3.49282

Salas, M.D., 2006. Some observations on grid convergence. Computers and Fluids 35, 688–692. https://doi.org/10.1016/j.compfluid.2006.01.003

Salas, M.D., Atkins, H.L., 2009. Problems associated with grid convergence of functionals. Comput. Fluid Dyn. 2008 38, 309–314. https://doi.org/10.1016/j.compfluid.2008.01.015

Salim, M., Cheah, S.C., 2009. Wall y + strategy for dealing with wall-bounded turbulent flows. Int. MultiConference Eng. Comput. Sci. II, 1–6. https://doi.org/10.1.1.149.722

Saric, W.S., Reed, H.L., White, E.B., 2002. Stability and Transition of three - Dimensional Boundary Layers. Annu. Rev. Fluid Mech. 35, 413–440. https://doi.org/10.1146/annurev.fluid.35.101101.161045

Sarkar, S., Lakshmanan, B., 1991. Application of a Reynolds stress turbulence model to the compressible shear layer. AIAA J. 29, 743–749. https://doi.org/10.2514/3.10649

Saydam, A.Z., Taylan, M., 2018. Evaluation of wind loads on ships by CFD analysis. Ocean Eng. 158, 54–63. https://doi.org/10.1016/j.oceaneng.2018.03.071

Schlichting, H., 1979. Boundary-Layer Theory, 7th ed. McGraw-Hill. https://doi.org/10.1007/978-3-662-52919-5

Schoellhamer, D.H., 1996. Anthropogenic sediment resuspension mechanisms in a shallow microtidal estuary. Estuar. Coast. Shelf Sci. 43, 533–548. https://doi.org/10.1006/ecss.1996.0086

Schoenherr, K., 1932. Resistance of flat surfaces moving through a fluid. Trans. Soc. Nav. Arch. Mar. Eng. 40, 279–313.

Schweighofer, J., 2004. Numerical Investigation of the Turbulent Free-Surface Flow around the Series 60 Ship at Model- and Full-Scale Ship Reynolds Numbers. Yearb. Soc. Nav. Archit. Ger. STG Summer Meet. Pol. 1–10.

Schweighofer, J., Regnstr, B., 2005. Viscous-Flow Computations of Two Existing Vessels At Model- and Full-Scale Ship Reynolds Numbers - a Study Carried Out Within the European Union Project , Effort ., in: International Conference on Computational Methods in Marine Engineering. pp. 1–11.

Sezen, S., Cakici, F., 2019. Numerical Prediction of Total Resistance Using Full Similarity Technique. China Ocean Eng. 33, 493–502. https://doi.org/10.1007/s13344-019-0047-z

Sharma, S.D., 1995. A Slender Ship Moving at a Near-Critical Speed in a Shallow Channel. J. Fluid Mech. 291, 263–285. https://doi.org/10.1017/S0022112095002692

Shenoi, R.R., Krishnankutty, P., Panneer Selvam, R., 2016. Study of manoeuvrability of container ship by static and dynamic simulations using a RANSE-based solver. Ships Offshore Struct. 11, 316–334. https://doi.org/10.1080/17445302.2014.987439

Shevchuk, I., Bottner, C.-U., Kornev, N., 2019. Numerical investigation of scale effects on squat in shallow water, in: 5th MASHCON, Ostend, Belgium. pp. 410–422.

Shevchuk, I., Böttner, C.U., Kornev, N., 2016. Numerical Analysis of the Flow in the Gap Between the Ship Hull and the Fairway Bottom in Extremely Shallow Water. Proc. 4th Int. Conf. Sh. Manoeuvring Shallow Confin. Water (MASHCON), 23 - 25 May 2016, Hamburg, Ger. 0, 37–42. https://doi.org/10.18451/978-3-939230-38-0

Shevchuk, I., Kornev, N., 2017. Study of unsteady hydrodynamic effects in the stern area of river cruisers in shallow water. 7th Int. Conf. Comput. Methods Mar. Eng. Mar. 2017 2017-May, 440–448. https://doi.org/10.1080/09377255.2017.1349599

Shi, A., Wu, M., Yang, B., Wang, X., Wang, Z., 2012. Resistance calculation and motions simulation for free surface ship based on CFD. Procedia Eng. 31, 68–74. https://doi.org/10.1016/j.proeng.2012.01.992

Shih, T., 1990. An improved k-epsilon model for near-wall turbulence and comparison with direct numerical simulation. NASA STI/Recon Tech. Rep. N 0–21.

Shih, T.H., Liou, W.W., Shabbir, A., Yang, Z., Zhu, J., 1995. A new k-ε eddy viscosity model for high reynolds number turbulent flows. Computers and Fluids 24, 227–238. https://doi.org/10.1016/0045-7930(94)00032-T

Shivachev, E., Khorasanchi, M., Day, A.H., 2017. Trim influence on KRISO container ship (KCS); an experimental and numerical study, in: Proceedings of the ASME 2017 36th International Conference on Ocean, Offshore and Arctic Engineering. pp. 1–7. https://doi.org/10.1115/OMAE2017-61860

Siemens, 2018. Star-CCM+ User Guide version 13.04.

Sigmund, S., Moctar, O., 2018. Numerical and experimental investigation of added resistance of different ship types in short and long waves. Ocean Eng. 147, 51–67. https://doi.org/10.1016/j.oceaneng.2017.10.010

Simonsen, C.D., Otzen, J.F., Joncquez, S., Stern, F., 2013. EFD and CFD for KCS heaving and pitching in regular head waves. J. Mar. Sci. Technol. 18, 435–459. https://doi.org/10.1007/s00773-013-0219-0

Slotnick, J., Khodadoust, A., Alonso, J., Darmofal, D., Gropp, W., Lurie, E., Mavriplis, D., 2014. CFD Vision 2030 Study: A Path to Revolutionary Computational Aerosciences, NASA/CR–2014-218178. https://doi.org/10.1017/CBO9781107415324.004

Song, K., Guo, C., Wang, C., Sun, C., Li, P., Zhong, R., 2019. Experimental and numerical study on the scale effect of stern flap on ship resistance and flow field. Ships Offshore Struct. 0, 1–17. https://doi.org/10.1080/17445302.2019.1697091

Song, S., Demirel, Y.K., Atlar, M., 2019. An investigation into the effect of biofouling on the ship hydrodynamic characteristics using CFD. Ocean Eng. 175, 122–137. https://doi.org/10.1016/j.oceaneng.2019.01.056

Soomere, T., 2007. Nonlinear components of ship wake waves. Appl. Mech. Rev. 60, 120–138. https://doi.org/10.1115/1.2730847

Soomere, Tarmo, 2009. Long ship waves in shallow water bodies, in: Quak, E., Soomere, T. (Eds.), Applied Wave Mathematics: Selected Topics in Solids, Fluids, and Mathematical Methods. pp. 193–228. https://doi.org/10.1007/978-3-642-00585-5_12

Sorensen, R.M., 1997. Prediction of Vessel-Generated Waves with Reference to Vessels Common to the Upper Mississippi River System, US Army Corps of Engineers, Waterways Experiment Station, ENV Report 4.

Spalart, P., Allmaras, S., 1992. A one-equation turbulence model for aerodynamic flows. 30th Aerosp. Sci. Meet. Exhib.

Srividya, K., Thandaveswara, B.S., 2005. CFD analysis for sea-chest design. ISH J. Hydraul. Eng. 11, 58–72. https://doi.org/10.1080/09715010.2005.10514781

St Denis, M., Pierson, W.J., 1953. On the Motions of Ships in Confused Seas. Trans. Soc. Nav. Archit. Mar. Eng. 61, 280–357.

Starke, A.R., Drakopoulos, K., Toxopeus, S.L., Turnock, S.R., 2017. RANS-based full-scale power predictions for a general cargo vessel, and comparison with sea-trial results. 7th Int. Conf. Comput. Methods Mar. Eng. Mar. 2017 2017-May, 353–364.

Stern, F., 1985. Effects of Waves on the Boundary Layer of a Surface-Piercing Body.

Stern, F., Wilson, R., Shao, J., 2006. Quantitative V&V of CFD simulations and certification of CFD codes. Int. J. Numer. Methods Fluids 50, 1335–1355. https://doi.org/10.1002/fld.1090

Stern, F., Wilson, R. V., Coleman, H.W., Paterson, E.G., 2001. Comprehensive approach to verification and validation of CFD simulations—Part 1: Methodology and procedures. J. Fluids Eng. Trans. ASME 123, 793–802. https://doi.org/10.1115/1.1412235

Stern, F., Yang, J., Wang, Z., Sadat-Hosseini, H., Mousaviraad, M., 2013. Computational ship hydrodynamics: Nowadays and way forward. Int. Shipbuild. Prog. 60, 3–105. https://doi.org/10.3233/ISP-130090

Stroh, A., 2016. Control of Spatially Developing TurbulentBoundary Layers for Skin Friction DragReduction, in: Nagel W., Kröner D., Resch M. (Eds) High Performance Computing in Science and Engineering ´16. https://doi.org/10.1109/CAHPC.2005.27

Suez Canal Authority, 2019. Suez Canal Rules of Navigation. https://doi.org/https://www.suezcanal.gov.eg/English/Navigation/Pages/RulesOfNavigation.aspx

Suez Canal Authority, 2018. Suez Canal Traffic Statistics: Annual Report 2018.

Suh, J., Yang, J., Stern, F., 2011. The effect of air-water interface on the vortex shedding from a vertical circular cylinder. J. Fluids Struct. 27, 1–22. https://doi.org/10.1016/j.jfluidstructs.2010.09.001

Sun, W., Hu, Q., Hu, S., Su, J., Xu, J., Wei, J., 2020. Numerical Analysis of Full-Scale Ship Self-Propulsion Performance with Direct Comparison to Statistical Sea Trail Results. J. Mar. Sci. Eng. 8, 1–22.

Tahara, Y., Katsui, T., Himeno, Y., 2002a. Computation of Ship Viscous Flow at Full Scale Reynolds Number. J. Soc. Nav. Archit. Japan 92, 89–101.

Tahara, Y., Longo, J., Stern, F., 2002b. Comparison of CFD and EFD for the Series 60 C B = 0.6 in steady drift motion, J Mar Sci Technol.

Tahara, Y., Stern, F., 1994. Validation of an interactive approach for calculating ship boundary layers and wakes for nonzero froude number. Computers and Fluids 23, 785–816. https://doi.org/10.1016/0045-7930(94)90066-3

Tatinclaux, B.J., 1970. Effect of a Rotational Wake on the Wavemaking Resistance of an Ogive. J. Sh. Res. 14, 84–99.

Telfer, E. V., 1927. Ship resistance similarity. Trans. R. Inst. Nav. Archit. 69, 174–190.

Terziev, M., Tezdogan, T., Incecik, A., 2019a. A geosim analysis of ship resistance decomposition and scale effects with the aid of CFD. Appl. Ocean Res. 92. https://doi.org/10.1016/j.apor.2019.101930

Terziev, M., Tezdogan, T., Incecik, A., 2019b. Application of eddy-viscosity turbulence models to problems in ship hydrodynamics. Ships Offshore Struct. 1–24. https://doi.org/10.1080/17445302.2019.1661625

Terziev, M., Tezdogan, T., Oguz, E., Gourlay, T., Demirel, Y.K., Incecik, A., 2018. Numerical investigation of the behaviour and performance of ships advancing through restricted shallow waters. J. Fluids Struct. 76, 185–215. https://doi.org/10.1016/j.jfluidstructs.2017.10.003

Terziev, M., Zhao, G., Tezdogan, T., Yuan, Z., Incecik, A., 2020. Virtual Replica of a Towing Tank Experiment to Determine the Kelvin Half-Angle of a Ship in Restricted Water. J. Mar. Sci. Appl. 8, 1–24. https://doi.org/10.3390/jmse8040258

Tezdogan, T., Demirel, Y.K., Kellett, P., Khorasanchi, M., Incecik, A., Turan, O., 2015. Full-scale unsteady RANS CFD simulations of ship behaviour and performance in head seas due to slow steaming. Ocean Eng. 97, 186–206. https://doi.org/10.1016/j.oceaneng.2015.01.011

Tezdogan, T., Incecik, A., Turan, O., 2016a. A numerical investigation of the squat and resistance of ships advancing through a canal using CFD. J. Mar. Sci. Technol. 21, 86–101. https://doi.org/10.1007/s00773-015-0334-1

Tezdogan, T., Incecik, A., Turan, O., 2016b. Full-scale unsteady RANS simulations of vertical ship motions in shallow water. Ocean Eng. 123, 131–145. https://doi.org/10.1016/j.oceaneng.2016.06.047

Tezdogan, T., Incecik, A., Turan, O., Kellett, P., 2016c. Assessing the Impact of a Slow Steaming Approach on Reducing the Fuel Consumption of a Containership Advancing in Head Seas. Transp. Res. Procedia 14, 1659–1668. https://doi.org/10.1016/j.trpro.2016.05.131

Thomas, J.L., Langley, N., 2008. Toward Verification of Unstructured-Grid Solvers. AIAA J. 46. https://doi.org/10.2514/1.36655

Thomson, W., 1887. On ship waves, in: Proceedings of the Institution of Mechanical Engineers. pp. 409–434. https://doi.org/https://doi.org/10.1243/PIME_PROC_1887_038_028_02

Tin Htwe, N.T., Hino, T., Suzuki, K., 2015. Computation of Free Surface Flows around Box-Shaped Ships by an Unstructured Navier-Stokes Solver. Sh. Technol. Res. 60, 104–117. https://doi.org/10.1179/str.2013.60.3.001

Toki, N., 2008. Investigation on Correlation Lines through the Analyses of Geosim Model Test Results. J. Japan Soc. Nav. Archit. Ocean Eng. 8, 71–79.

Torsvik, T., 2009. Modelling of ship waves from high-speed vessels, in: Applied Wave Mathematics: Selected Topics in Solids, Fluids, and Mathematical Methods. Springer Berlin Heidelberg, pp. 229–263.

Torsvik, T., Dysthe, K., Pedersen, G., 2006. Influence of variable Froude number on waves generated by ships in shallow water. Phys. Fluids 18. https://doi.org/10.1063/1.2212988

Torsvik, T., Pedersen, G., Dysthe, K., 2009. Waves Generated by a Pressure Disturbance Moving in a Channel with a Variable Cross-Sectional Topography. J. Waterw. Port Coast. Ocean Eng. 135, 120–123. https://doi.org/Doi 10.1061/(Asce)0733-950x(2009)135:3(120)

Townsin, R.L., 1971. The viscous drag of a “Victory” model—Results from

wake and wave pattern measurements. Trans. RINA 113, 307–321.

Townsin, R.L., 1968. Viscous drag from a wake survey. Measurements in the wake of a 'Lucy Ashton' mode. Trans. RINA 110.

Toxopeus, S.L., 2013. Viscous-flow calculations for KVLCC2 in deep and shallow water. Comput. Methods Appl. Sci. 29, 151–169. https://doi.org/10.1007/978-94-007-6143-8_9

Toxopeus, S.L., Simonsen, C.D., Guilmineau, E., Visonneau, M., Xing, T., Stern, F., 2013. Investigation of water depth and basin wall effects on KVLCC2 in manoeuvring motion using viscous-flow calculations. J. Mar. Sci. Technol. 18, 471–496. https://doi.org/10.1007/s00773-013-0221-6

Troesch, A., Beck, R.F., 1974. Experiments on ship motions in shallow water.

Tropea, C., Yarin, A.L., Foss, J.F., 2007. Springer handbook of experimental fluid mechanics, Springer Berlin, Heidelberg. https://doi.org/10.1007/978-3-540-30299-5

Tuck, E.O., 1978. Hydrodynamic Problems of Ships in Restricted Waters. Annu. Rev. Fluid Mech. 10, 33–46.

Tuck, E.O., 1967. Sinkage and Trim in Shallow Water of Finite Width. Schiffstechnik 14, 92–94.

Tuck, E.O., 1966. Shallow-Water Flows Past Slender Bodies. J. Fluid Mech. 26, 81–95. https://doi.org/10.1017/S0022112066001101

Tuck, E.O., Lazauskas, L. V, 2008. Drag on a ship and Michell's integral, in: 22nd Int. Congress of Theoretical and Applied Mechanics, Adelaide, South Australia, August.

Tuck, E.O., Taylor, J.P., 1970. Shallow wave problems in ship hydrodynamics, in: 8th Symposium Naval Hydrodynamics. pp. 627–659.

Tunaley, J.K.E., 2014. Ship Wakes in Shallow Waters. LRDC Rep. 6–9.

UNFCCC, 1998. Kyoto Protocol To the United Nations Framework Kyoto Protocol To the United Nations Framework, United Nations. https://doi.org/10.1111/1467-9388.00150

van der Poel, E.P., Ostilla-Mónico, R., Donners, J., Verzicco, R., 2015. A pencil distributed finite difference code for strongly turbulent wall-bounded flows. Computers and Fluids 116, 10–16. https://doi.org/10.1016/j.compfluid.2015.04.007

van Driest, E.R., 1956. On Skin Friction and Heat Transfer Near the Stagnation

Point, NACA Report, AL-2267.

van Mannen, J.D., van Oossanem, P., 1988. Principles of Naval Architecture. The Society of Naval Architects and Marine Engineers, Jersey.

Van, S.H., Ahn, H., Lee, Y.Y., Kim, C., Hwang, S., Kin, J., Kim, S.K., Park, I.R., 2011. Resistance Characteristics And Form Factor Evaluation For Geosim Models Of KVLCC2 And KCS, in: Advanced Model Measurement Technology for EU Maritime Industry - AMT'11. pp. 282–293.

van Strien, M., 2014. On the origins and foundations of laplacian determinism. Stud. Hist. Philos. Sci. Part A 45, 24–31. https://doi.org/10.1016/j.shpsa.2013.12.003

van Wijngaarden, E., 2005. Recent developments in predicting propeller-induced hull pressure pulses. Proc. 1st Int. Sh. Noise Vib. Conf. 1–8.

Vanka, S.P., 1987. Second-order upwind differencing in a recirculating flow. AIAA J. 25, 1435–1441. https://doi.org/10.2514/3.9801

Velázquez, M.J.N., Asuero, A.G., 2017. Youden Two-Sample Method, in: Quality Control and Assurance-An Ancient Greek Term Re-Mastered. IntechOpen.

Visonneau, M., 2005. A Step Towards the Numerical Simulation of Viscous Flows Around Ships at Full-Scale. Mar. CFD.

Wackers, J., Koren, B., Raven, H.C., van der Ploeg, A., Starke, A.R., Deng, G.B., Queutey, P., Visonneau, M., Hino, T., Ohashi, K., 2011. Free-Surface Viscous Flow Solution Methods for Ship Hydrodynamics. Arch. Comput. Methods Eng. 18, 1–41. https://doi.org/10.1007/s11831-011-9059-4

Wang, J., Yu, H., Zhang, Y., Xiong, X., 2016. CFD-based method of determining form factor k for different ship types and different drafts. J. Mar. Sci. Appl. 15, 236–241. https://doi.org/10.1007/s11804-016-1372-8

Wang, J., Zou, L., Wan, D.C., 2018. Numerical simulations of zigzag maneuver of free running ship in waves by RANS-Overset grid method. Ocean Eng. 162, 55–79. https://doi.org/10.1016/j.oceaneng.2018.05.021

Wang, J., Zou, L., Wan, D.C., 2017. CFD simulations of free running ship under course keeping control. Ocean Eng. 141, 450–464. https://doi.org/10.1016/j.oceaneng.2017.06.052

Wang, Z.Z., Xiong, Y., Shi, L.P., Liu, Z.H., 2015. A numerical flat plate friction line and its application. J. Hydrodyn. 27, 383–393. https://doi.org/10.1016/S1001-6058(15)60496-6

Web of Science, 2020. Publication statistics [WWW Document]. Clarivate Anal. URL https://wcs.webofknowledge.com/RA/analyze.do?product=WOS&SID=F6qCjOD5enYzEEUuVEv&field=PY_PublicationYear_PublicationYear_en&yearSort=true (accessed 4.26.20).

Weymouth, G.D., Wilson, R., Stern, F., 2005. Rans computational fluid dynamics predictions of pitch and heave ship motions in head seas. J. Sh. Res. 49, 80–97.

White, F., 2010. Fluid Mechanics. McGraw-Hill,New York 862. https://doi.org/10.1111/j.1549-8719.2009.00016.x.Mechanobiology

White, F., 2006. Viscous fluid flow, 3rd ed. McGraw-Hill.

Whitham, G.B., 2011. Linear and nonlinear waves.

Wilcox, D.C., 2008. Formulation of the k-w Turbulence Model Revisited. AIAA J. 46, 2823–2838. https://doi.org/10.2514/1.36541

Wilcox, D.C., 2006. Turbulence modeling for CFD, 3rd ed, Transportation Research Record. DCW Industries. https://doi.org/10.1016/j.aqpro.2013.07.003

Wilcox, D.C., 1988. Reassessment of the scale-determining equation for advanced turbulence models. AIAA J. 26, 1299–1310. https://doi.org/10.2514/3.10041

Wilson, R. V., Carrica, P.M., Stern, F., 2006. URANS simulations for a high-speed transom stern ship with breaking waves. Int. J. Comut. Fluid Dyn. 20, 105–125. https://doi.org/10.1080/10618560600780916

Witherden, F.D., Jameson, A., 2017. Future directions of computational fluid dynamics, in: 23rd AIAA Computational Fluid Dynamics Conference, 2017. pp. 1–16.

Wnęk, A.D., Sutulo, S., Soares, C.G., 2018. CFD Analysis of Ship-to-Ship Hydrodynamic Interaction. J. Mar. Sci. Appl. 17, 21–37. https://doi.org/https://doi.org/10.1007/s11804-018-0010-z

Wolfshtein, M., 1969. The velocity and temperature distribution in one-dimensional flow with turbulence augmentation and pressure gradient. Int. J. Heat Mass Transf. 12, 301–318. https://doi.org/10.1016/0017-9310(69)90012-X

Wolter, C., Arlinghaus, R., 2003. Navigation impacts on freshwater fish assemblages: The ecological relevance of swimming performance. Rev.

Fish Biol. Fish. 13, 63–89. https://doi.org/10.1023/A:1026350223459

Wortley, S., 2013. CFD Analysis of Container Ship Sinkage, Trim and Resistance.

Wu, C.S., Zhou, D.C., Gao, L., Miao, Q.M., 2011. CFD computation of ship motions and added resistance for a high speed trimaran in regular head waves. Int. J. Nav. Archit. Ocean Eng. 3, 105–110. https://doi.org/10.3744/JNAOE.2011.3.1.105

Wu, D.-M., Wu, T.Y., 1982. Three-Dimensional Nonlinear Long Waves Due to Moving Surface Pressure, in: 14th Symposium on Naval Hydrodynamics, Ann Arbor.

Wu, H., Wu, J., He, J., Zhu, R., Yang, C.J., Noblesse, F., 2019. Wave profile along a ship hull, short farfield waves, and broad inner Kelvin wake sans divergent waves. Phys. Fluids 31. https://doi.org/10.1063/1.5088531

Wu, Z., 1992. On the Estimation of a Moving Ship's Velocity and Hull Geometry Information from its Wave Spectra.

Xing-Kaeding, Y., Jensen, G., 2015. Simulation of Ship Motions during Maneuvers. Sh. Technol. Res. 53, 159–182. https://doi.org/10.1179/str.2006.53.4.003

Xing-Kaeding, Y., Jensen, G., Hadžić, I., Peric, M., 2015. Simulation of Flow-Induced Ship Motions in Waves using a RANSE Method. Sh. Technol. Res. 51, 56–68. https://doi.org/10.1179/str.2004.51.2.002

Xing, T., Stern, F., 2010. Factors of Safety for Richardson Extrapolation. J. Fluids Eng. 132, 061403. https://doi.org/10.1115/1.4001771

Xu, X., Li, H.A.O., Lin, Y., 2019. Mesh – Order Independence in CFD Simulation. IEEE Access 7, 119069–119081. https://doi.org/10.1109/ACCESS.2019.2937450

Yang, Q., Faltinsen, O.M., Zhao, R., 2001. Wash and Wave Resistance of Ships in Finite Water Depth. Pract. Des. Ships Other Float. Struct. 475–483. https://doi.org/10.1016/b978-008043950-1/50060-0

Yang, R., Shugan, I. V, Fang, M., 2011. Kelvin ship wake in the wind and waves fiend and on the finite sea depth. Environment 27, 71–77. https://doi.org/10.1115/OMAE2011-49872

Youden, W.J., 1972. Graphical diagnosis of inter-laboratory test results. J. Qual. Technol. 4. https://doi.org/https://doi.org/10.1080/00224065.1972.11980509

Yuan, Z.M., 2019. Ship Hydrodynamics in Confined Waterways. J. Sh. Res. 63, 1–14. https://doi.org/http://dx.doi.org/10.5957/JOSR.04170020

Yuan, Z.M., 2014. Hydrodynamic interaction between ships travelling or stationary in shallow waters. Universtiy of Strathclyde.

Yuan, Z.M., Incecik, A., 2016. Investigation of side wall and ship model interaction, in: 2016 International Conference on Maritime Technology. pp. 1–10.

Yuan, Z.M., Zhang, X., Ji, C.Y., Jia, L., Wang, H., Incecik, A., 2018. Side wall effects on ship model testing in a towing tank. Ocean Eng. 147, 447–457. https://doi.org/10.1016/j.oceaneng.2017.10.042

Zeng, Q., Hekkenberg, R., Thill, C., 2019. On the viscous resistance of ships sailing in shallow water. Ocean Eng. 190, 106434. https://doi.org/10.1016/j.oceaneng.2019.106434

Zeng, Q., Thill, C., Hekkenberg, R., Rotteveel, E., 2018. A modification of the ITTC57 correlation line for shallow water. J. Mar. Sci. Technol. 0, 0. https://doi.org/10.1007/s00773-018-0578-7

Zhang, S., Tezdogan, T., Zhang, B., Xu, L., Lai, Y., 2018. Hull form optimisation in waves based on CFD technique. Ships Offshore Struct. 13, 149–164. https://doi.org/10.1080/17445302.2017.1347231

Zhang, S., Zhang, B., Tezdogan, T., Xu, L., Lai, Y., 2017. Research on bulbous bow optimization based on the improved PSO algorithm. China Ocean Eng. 31, 487–494. https://doi.org/10.1007/s13344-017-0055-9

Zhang, Z., 2010. Verification and validation for RANS simulation of KCS container ship without/with propeller. J. Hydrodyn. 22, 932–938. https://doi.org/10.1016/S1001-6058(10)60055-8

Zou, L., Zou, Z., Liu, Y., 2019. CFD-based predictions of hydrodynamic forces in ship-tug boat interactions. Ships Offshore Struct. 0, 1–11. https://doi.org/10.1080/17445302.2019.1589963

PUBLICATIONS

The following papers have been either published, or submitted for publication. Please note that not all papers are included in this thesis.

Journal articles

1. **Terziev, M**., Tezdogan, T. and Incecik, A., 2019. A geosim analysis of ship resistance decomposition and scale effects with the aid of CFD. Applied Ocean Research, 92, p.101930.
2. **Terziev, M**., Tezdogan, T. and Incecik, A., 2019. Application of eddy-viscosity turbulence models to problems in ship hydrodynamics. Ships and Offshore Structures, pp.1-24.
3. Elsherbiny, K., **Terziev, M**., Tezdogan, T., Incecik, A. and Kotb, M., 2020. Numerical and experimental study on hydrodynamic performance of ships advancing through different canals. Ocean Engineering, 195, p.106696.
4. **Terziev, M**., Tezdogan, T. and Incecik, A., 2020. A numerical assessment of the scale effects of a ship advancing through restricted waters (s*ubmitted to Ships and Offshore Structures*).
5. **Terziev, M.**, Tezdogan, T., Incecik, A., 2020. A posteriori error and uncertainty estimation in computational ship hydrodynamics. Ocean Eng. 208, 107434. https://doi.org/10.1016/j.oceaneng.2020.107434
6. **c) Terziev, M.**, Zhao, G., Tezdogan, T., Yuan, Z. and Incecik, A., 2020. Virtual replica of a towing tank experiment to determine the Kelvin half-angle of a ship in restricted water. Journal of Marine Science and Engineering, 8(4), p.258.
7. **Terziev, M**., Tezdogan, T. and Incecik, A., 2020. Modelling the hydrodynamic effect of abrupt water depth changes on a ship travelling

in restricted waters using CFD (*submitted to Ships and Offshore Structures).*

Conference papers

1. **Terziev, M**., Tezdogan, T. and Incecik, A., 2019, February. Influence of mixed flows on ship hydrodynamics in dredged channels. In ASME 2019 38th International Conference on Ocean, Offshore and Arctic Engineering, Glasgow, UK.
2. **Terziev, M**., Elsherbiny, K., Tezdogan, T. and Incecik, A., 2020, March. Experimental and numerical study of an obliquely towed ship model in confined waters. In 39th International Conference on Ocean, Offshore & Arctic Engineering. (*In press*).

APPENDIX A

The data obtained from Web of Science (2020) reads as follows:

Publication year	Records	% of total
2020 – as of 26.04.2020	34	2.56%
2019	206	15.50%
2018	168	12.64%
2017	154	11.59%
2016	130	9.78%
2015	107	8.05%
2014	89	6.70%
2013	58	4.36%
2012	70	5.27%
2011	50	3.76%
2010	38	2.86%
2009	36	2.71%
2008	34	2.56%
2007	27	2.03%
2006	28	2.11%
2005	26	1.96%
2004	5	0.38%
2003	17	1.28%
2002	15	1.13%
2001	10	0.75%
2000	5	0.38%

1999	3	0.23%
1998	7	0.53%
1997	3	0.23%
1996	5	0.38%
1995	2	0.15%
1992	2	0.15%
Total	1329	

The fit used to extrapolate to the year 2030 with $R^2 = 0.9908$ was determined using a curve fit within MATLAB as shown in Eq. (A.1):

$$f(x) = ae^{bx} + ce^{dx} \quad \text{(A.1)}$$

where, x represents the year. The fit was performed excluding data point for year 2020.

Coefficients of Eq. (A.1):
$a = 8.718 \times 10^{-149}$
$b = 0.1715$
$c = 0$
$d = -0.1013$

APPENDIX B

The data, used to construct Figure 4.1 is listed in the table below (all citations are listed in the reference list):

Turbulence model	Reference	Count	Percentage of total
Spalart-Allmaras	(Duvigneau et al., 2003; Eca et al., 2018; Eca and Hoekstra, 2001; Hoekstra et al., 2000; Maki et al., 2013; Pereira et al., 2017; Tin Htwe et al., 2015)	7	6.31%
k-ω Wilcox	(Eca and Hoekstra, 2001; Hoekstra et al., 2000; Lam et al., 2013; Pereira et al., 2017; Weymouth et al., 2005; Wortley, 2013)	6	5.41%
k-ω SST	(Atencio and Chernoray, 2019; Banks et al., 2010; Bhushan et al., 2009, 2007; Castiglione et al., 2011; Castro et al., 2011; Demirel et al., 2017, 2014; Deng et al., 2014, 2010; Duvigneau et al., 2003; Eca et al., 2018; Eca and Hoekstra, 2001; el Moctar et al., 2015; Farkas et al., 2018; Gaggero et al., 2015; Guo et al., 2013, 2015; Haase et al., 2016a; Hoekstra et al., 2000; Irkal et al., 2019; Jasak et al., 2018; Kaidi et al., 2017; Kianejad et al., 2019; Kok et al., 2018; Liu et al., 2017; Maasch et al., 2019; Majidian and Azarsina, 2019; Mucha et al., 2016; Oggiano et al., 2017; Ohashi et al., 2018; Pacuraru and Domnisoru, 2017; Pereira et al., 2017; Prakash and Chandra, 2013; Queutey and Visonneau, 2015; Razgallah et al., 2018; Saydam and Taylan, 2018; Schweighofer and Regnstr, 2005; Shenoi et al., 2016; Shi et al., 2012; Sigmund and Moctar, 2018; Simonsen et al., 2013; S. Song et al., 2019; Toxopeus et al.,	50	45.05%

	2013; Visonneau, 2005; Wang et al., 2017, 2016; Wilson et al., 2006; Zhang, 2010; Zou et al., 2019)		
k-ε	(Bakica et al., 2019; Begovic et al., 2015; Bellafiore et al., 2018; Chen et al., 2001; Choi et al., 2009; Chun et al., 2001; Dhinesh et al., 2010; Eca and Hoekstra, 2001; Farkas et al., 2017; Hai-Long et al., 2016; Hoekstra et al., 2000; Jagadeesh and Murali, 2010; Kellett et al., 2013; M. Kim et al., 2017b, 2017a; Y. C. Kim et al., 2017; Kinaci et al., 2016; Kinaci and Gokce, 2015; Kouh et al., 2009; Lee et al., 2018; Linde et al., 2016; Liu et al., 2018; Ma et al., 2013; Mancini et al., 2018; Oh and Kang, 1992; Ozdemir and Barlas, 2017; Schweighofer, 2004; Shivachev et al., 2017; Srividya and Thandaveswara, 2005; Tahara et al., 2002a; Terziev et al., 2018; Tezdogan et al., 2016c, 2016b, 2016a, 2015; Van et al., 2011; Visonneau, 2005; Wang et al., 2016; Wu et al., 2011; Xing-Kaeding et al., 2015; Xing-Kaeding and Jensen, 2015; Zhang et al., 2018, 2017)	41	36.94%
AKN	(Jagadeesh and Murali, 2010; Pereira et al., 2017)	2	1.80%
RST	(Choi et al., 2010; Duvigneau et al., 2003; Lee et al., 2018; Visonneau, 2005; Wang et al., 2016)	5	4.50%

APPENDIX C

This Appendix details the equations used by in this thesis. Sources for the information presented herein concerning governing equations is drawn from Ferziger and Peric (2002) and Durbin and Pettersson Reif (2011). These references are omitted henceforth.

Firstly, the governing equations, describing viscous incompressible flow can be written as follows:

$$\partial_t \tilde{u} + \tilde{u}_i \partial_j \tilde{u}_i = -\frac{1}{\rho}\partial_i \tilde{p} + \nu \nabla^2 \tilde{u}_i \tag{C.1}$$

$$\partial_i \tilde{u}_i = 0 \tag{C.2}$$

Eq. (C.1) is the conservation of momentum, whereas Eq. (C.2) is the conservation of mass. In the aforementioned equations, the notation ∂_i was used to denote the partial derivative $\partial/\partial x_i$, whereas the subscript i gives the respective component of the vector. We may decompose the total velocity $\tilde{u}(x,t)$ into a mean and fluctuating component $\tilde{u}(x,t) = U(x,t) + u(x,t)$, and $U = \bar{\tilde{u}}$. Here, a bar above a variable indicates averaging.

Utilising the abovementioned decomposition, Eq. (C.1) and Eq. (C.2) become:

$$\partial_t (U_i + u_i) + (U_i + u_i)\partial_j (U_i + u_i) = -\frac{1}{\rho}\partial_i (P + p) + \nu \nabla^2 (U_i + u_i) \tag{C.3}$$

$$\partial_i (U_i + u_i) = 0 \tag{C.4}$$

In cases, such as those presented throughout the thesis, where the fluctuating component is not modelled, one may average Eq. (C.3) and Eq. (C.4), which become:

$$\partial_t U_i + U_i \partial_j U_i = -\frac{1}{\rho}\partial_i P + \nu \nabla^2 U_i - \partial_j \overline{u_j u_i} \tag{C.5}$$

$$\partial_i U_i = 0 \tag{C.6}$$

Eq. (C.5) and Eq. (C.6) are the Reynolds averaged Navier-Stokes equations. The final term in Eq. (C.5) is the derivative of the Reynolds stress tensor $\overline{u_j u_i}$, given in Eq. (C.7):

$$\overline{u_j u_i} = \begin{pmatrix} \overline{u_1 u_1} & \overline{u_1 u_2} & \overline{u_1 u_3} \\ \overline{u_2 u_1} & \overline{u_2 u_2} & \overline{u_2 u_3} \\ \overline{u_3 u_1} & \overline{u_3 u_2} & \overline{u_3 u_3} \end{pmatrix} \tag{C.7}$$

The resultant set of 4 equations contain 10 unknowns, which is why turbulence modelling is frequently referred to as providing closure, i.e. additional equations, allowing the system to form a closet set. The unknowns, present in the above equations are U_i, P, and $\overline{u_i u_j}$ with $i, j = 1, 2, 3$. The Reynolds stress term is modelled an eddy-viscosity concept, which translates into:

$$-\overline{u_i u_j} \approx v_T [\partial_j U_i + \partial_i U_j] \tag{C.8}$$

It is the purpose of all eddy-viscosity turbulence models to predict the eddy-viscosity, v_T. This may be achieved by a variety of methods.

C.1 Spalart-Allmaras model

The one-equation Spalart and Allmaras (1992) closure models the eddy-viscosity via Eq. (C.9):

$$v_T = \rho f_v(\tilde{v}/v) \tag{C.9}$$

where $\tilde{v}$ is the modified diffusivity term, and f_v is the damping function, shown in Eq. (C.10)

$$f_v(\tilde{v}/v) = \frac{(\tilde{v}/v)^3}{(\tilde{v}/v)^3 + 7.1^3} \tag{C.10}$$

Finally, the modified diffusivity is modelled via a transport equation in the form of:

$$\partial_t \tilde{v} + U \cdot \nabla \tilde{v} = \mathcal{P}_v - \varepsilon_v + \frac{1}{\sigma_v} [\nabla\big((v + \tilde{v})\nabla\tilde{v}\big) + c_{b2} |\nabla \tilde{v}|^2] \tag{C.11}$$

Where according to Spalart and Allmaras (1992), $c_{b2} = 0.622$, $\sigma_v = 2/3$, while $\mathcal{P}$ is the production term, modelled using Eq. (C.12), where $c_{b1} = 0.1355$, and S being the magnitude of the mean vorticity:

$$\mathcal{P}_v = c_{b1} S \tilde{v} \tag{C.12}$$

C.2 The $k-\varepsilon$ family of turbulence models

The $k-\varepsilon$ family of models predicts the eddy viscosity by using the turbulent kinetic energy (k) and dissipation rate (ε):

$$v_T = C_\mu f_\mu k^2/\varepsilon \tag{C.11}$$

where the standard value of C_μ is a constant, and f_μ is a damping function. These parameters are summarised in . The mean flow properties are the expressed via:

$$-\overline{u_j u_i} = 2v_T S_{ij} - \frac{2}{3}k\delta_{ij} \tag{C.12}$$

with S_{ij} being the mean rate of strain tensor, $S_{ij} = 0.5(\partial_i U_j + \partial U_i)$.

The transport equations for the turbulent kinetic energy and dissipation rate are:

$$\partial_t(k) + U_j\partial_j k = \mathcal{P} - \varepsilon + \partial_j((v + v_T/\sigma_k)\partial_j k) \tag{C.13}$$

$$\partial_t\varepsilon + U_j\partial_j\varepsilon = \frac{C_{\varepsilon1}\mathcal{P} - C_{\varepsilon2}\varepsilon}{T} + \partial_j\left(\left(v + \frac{v_T}{\sigma_\varepsilon}\right)\partial_j\varepsilon\right) \tag{C.14}$$

In the above equations, $\mathcal{P} = 2v_T|S|^2$, and $T = k/\varepsilon$ is the turbulent time scale. Eq. (C.14) is constructed by dimensional analogy, and is an assumed form. For this reason, Eq. (C.14) contains empirical constants $C_{\varepsilon1}$, $C_{\varepsilon2}$, σ_ε, while σ_k is usually taken as unity. The respective coefficient values for the models, used in this thesis (the AKN model and the realizable $k-\varepsilon$ models are given in Table 0.1.

Table 0.1. Model coefficients for AKN and $k-\varepsilon$ closures.

Coefficient	AKN	Realizable $k-\varepsilon$
$C_{\varepsilon1}$	1.5	max(0.43, $\eta/(5+\eta)$), with $\eta = Sk/\varepsilon$
$C_{\varepsilon2}$	1.9	1.9
σ_ε	1.4	1.2
σ_k	1.4	1

The (Lag) Elliptic blending and v^2-f models share their origins and are presented jointly.

Firstly, the turbulent eddy viscosity of the v^2-f model is predicted via:

$$\partial_t\overline{v^2} + U_j\partial_j\overline{v^2} + \frac{\varepsilon\overline{v^2}}{k} = kf + \partial_k\left[v_T\partial_k\overline{v^2}\right] + v\nabla^2\overline{v^2} \tag{C.15}$$

$$L^2\nabla^2 f - f = -\frac{c_2\mathcal{P}}{k} + \frac{c_1}{T}\left(\frac{\overline{v^2}}{k} - \frac{2}{3}\right) \quad \text{(C.16)}$$

with $c_2 = 0.3$, and c_1=0.4. The eddy viscosity is predicted as $v_T = C_\mu \overline{v^2} T$.

The Elliptic blending model solves the transport equations for the turbulent kinetic energy (Eq. (C.13)) and dissipation rate (Eq. (C.14)), alongside a reduced wall-normal stress component ϕ, and the elliptic blending factor α.

$$\nabla(L^2\nabla\alpha) = \alpha - 1 \quad \text{(C.17)}$$

$$\partial_t(\rho\phi) + \nabla(\rho\phi U) = \nabla\left[\left(\frac{\mu}{2} + \frac{\mu_t}{\sigma_\phi}\right)\nabla\phi\right] + \mathcal{P}_\phi + S_\phi \quad \text{(C.18)}$$

where $\mathcal{P}_\phi$ is the production term, $\sigma_\phi = 1$, and

$$L = C_L\sqrt{\frac{k^3}{\varepsilon^2} + C_\eta^2\sqrt{\frac{v^3}{\varepsilon}}} \quad \text{(C.19)}$$

with $C_L = 0.164$, $C_\eta = 75$.

The $k-\omega$ family of turbulence models

Wilcox (2006) represented the transport equation for the turbulent kinetic energy as:

$$\partial_t k + U_j\partial_j k = 2v_T|S|^2 - C_\mu k\omega + \partial_j\left(\left(v + \frac{v_T}{\sigma_k}\right)\partial_j k\right) \quad \text{(C.20)}$$

and the dissipation frequency as:

$$\partial_t\omega + U_j\partial_j\omega = 2C_{\omega1}|S|^2 - C_{\omega2}\omega^2 + \partial_j\left(\left(v + \frac{v_T}{\sigma_\omega}\right)\partial_j\omega\right) \quad \text{(C.21)}$$

where $C_{\omega1} = 5/9$, $C_{\omega2} = 3/40$, $\sigma_\omega = \sigma_k = 2$, and $C_\mu = 0.09$. The eddy-viscosity is predicted as $v_T = k/\omega$.

Menter (1994) proposed the Shear Stress Transport turbulence closure. He noted certain properties of solutions, obtained with the $k-\omega$ model, for example, overprediction of shear stress. Menter's (1994) solution was to introduce a bound on the stress-intensity ratio $|\overline{uv}|/k = a_1$. Then, by using the identity $-\overline{uv} = k\partial_k U/\omega$, he arrived at:

$$\frac{\mathcal{P}}{\varepsilon} = \frac{\overline{uv}^2\omega}{k\varepsilon} = \frac{1}{C_\mu}\left|\frac{\overline{uv}}{k}\right|^2 \quad \text{(C.22)}$$

Menter (1994) also proposed bounds on v_T in the form of:

$$v_T = \min\left[\frac{k}{\omega}, \frac{\sqrt{C_\mu}k}{|2\boldsymbol{\Omega}|}\right] \tag{C.23}$$

where $|\boldsymbol{\Omega}|$ is the mean flow rotation tensor. Next, a limiting function (F_1) is introduced:

$$F_1 = \tanh(arg_1^4) \tag{C.24}$$

with

$$arg_1 = \min\left[max\left(\frac{\sqrt{k}}{C_\mu \omega y}, \frac{500v}{\omega y^2}\right), \frac{2k\omega}{y^2\, max(\nabla k \cdot \nabla \omega, 10^{-20})}\right] \tag{C.25}$$

Finally, the transport equation for the turbulent dissipation rate is:

$$\partial_t \varepsilon + U_j \partial_j \varepsilon = \frac{C_{\varepsilon 1}\mathcal{P} - C_{\varepsilon 2}\varepsilon}{T} + \partial_j\left(\left(v + \frac{v_T}{\sigma_\varepsilon}\right)\partial_j \varepsilon\right) + F_1 S_\omega \tag{C.26}$$

which is identical to Eq. (C.14), with the exception of the final term on the right-hand side. Here, S_ω is found by:

$$S_\omega = \frac{2}{T}\left(v + \frac{v_T}{\sigma_\omega}\right)\left[\frac{|\nabla k|^2}{k} - \frac{\nabla k \cdot \nabla \varepsilon}{\varepsilon}\right] \tag{C.27}$$

The model constants are also interpolated as follows:

$$C_{\varepsilon_1} = 1 + (1 - F_1)0.44 + F_1 C_{\omega 1} \tag{C.28}$$

$$C_{\varepsilon 2} = 1 + (1 - F_1)0.92 + F_1 C_{\omega 2}/C_\mu \tag{C.29}$$

The γ (intermittency) transition model adds a transport equation to be solved alongside those stated earlier for the SST model:

$$\frac{d\gamma}{dt}(\rho\gamma) + \nabla(\rho\gamma U) = \nabla\nabla\left[\left(\mu + \frac{\mu_T}{\sigma_f}\right)\nabla\gamma\right] + P_\gamma - E_\gamma \tag{C.30}$$

where:

$$P_\gamma = 100\rho S\gamma(1 - \gamma)F_{onset} \tag{C.31}$$

$$F_{onset} = \max\left(F_{onset2} - F_{onset3}, 0\right) \tag{C.32}$$

in which

$$F_{onset2} = \min\left(F_{onset1}, 2\right) \tag{C.33}$$

$$F_{onset3} = \max\left[1 - \left(\frac{Re_t}{3.5}\right)^3, 0\right] \tag{C.34}$$

$$F_{onset1} = \frac{Re_v}{C_{onset1} Re_{\theta c}} \quad \text{(C.35)}$$

where:

- $C_{onset1} = 2.2$
- $\sigma_f = 1$
- Re_t is the turbulent Reynolds number, $Re_t = k^2/(v\varepsilon) = k/(v\omega)$
- Re_v is the strain-rate Reynolds number $Re_v = d^2 S/v$, with d being the distance from the wall
- $Re_{\theta c}$ is the correlation for the critical Reynolds number and is defined as follows:

  $$Re_{\theta c} = C_{TU1} + C_{TU2} \exp\left[-C_{TU3} Tu_L F_{PG}(\lambda_{\theta L})\right] \quad \text{(C.36)}$$

  where $C_{TU1} = 100$, $C_{TU2} = 1000$, $C_{TU3} = 1$, and

  $$Tu_L = \min\left(\frac{100\sqrt{2k/3}}{\omega d}, 100\right) \quad \text{(C.37)}$$

  $$\lambda_{\theta L} = \min\left[max\left(-7.57 \times \frac{10^{-3} d^2}{v} \nabla(nU) \times n + 0.0128, -1\right), 1\right] \quad \text{(C.38)}$$

  $$F_{PG}(\lambda_{\theta L}) = \begin{cases} \max[\min(1 + 14.68\lambda_\theta, 1.5), 0], \lambda_{\theta L} \geq 0 \\ \max[\min(1 - 7.34\lambda_\theta, 3), 0], \lambda_\theta < 0 \end{cases} \quad \text{(C.39)}$$

The production term $E_\gamma = C_{a2} \rho W \gamma F_{turb}(c_{e2}\gamma - 1)$,

where $F_{turb} = \exp[-(Re_t/2)^4]$. W is the modulus of the mean vorticity tensor, while $C_{a2} = 0.06$, and $C_{e2} = 50$.